Geodätisch-geophysikalische Arbeiten in der Schweiz

(Fortsetzung der Publikationsreihe
«Astronomisch-geodätische Arbeiten in der Schweiz»)

herausgegeben von der

Schweizerischen Geodätischen Kommission
(Organ der Akademie der Naturwissenschaften Schweiz)

Einhundertneunter Band
Volume 109

Methods for an Enhanced Co-Location of Space Geodetic Techniques

Iván Herrera Pinzón

2023

Adresse der Schweizerischen Geodätischen Kommission:

ETH Zürich
Institut für Geodäsie und Photogrammetrie
Eidg. Technische Hochschule Zürich
8093 Zürich
Switzerland

Internet: http://www.sgc.ethz.ch

ISBN 978-3-908440-56-7

Redaktion des 109. Bandes:
Dr. I. Herrera Pinzón, Prof. Dr. M. Rothacher, J. Müller-Gantenbein
Druck: Print-Atelier ADAG, Zürich

VORWORT

Das International Terrestrial Reference System (ITRS) und seine Realisierung, das International Terrestrial Reference Frame (ITRF), sind heutzutage die metrologische Basis für alle globalen Mess- und Monitoring-Aktivitäten im Systems Erde. Bei der Betrachtung von globalen Veränderungen, insbesondere des Meeresspiegelanstiegs von ungefähr 2-3 mm/Jahr, ist eine extrem stabile und hochgenaue Realisierung des ITRS von grösster Wichtigkeit. Es konnte gezeigt werden, dass die Ungenauigkeiten in der Realisierung des globalen terrestrischen Referenzsystems einer der wichtigsten Faktoren darstellt, der die zuverlässige Bestimmung des Meeresspiegelanstiegs begrenzt. Das Global Geodetic Observing System (GGOS) der International Association of Geodesy (IAG) hat daher die Forderung aufgestellt, dass die ITRF-Stationskoordinaten und die Stationsgeschwindigkeiten insgesamt mit einer Genauigkeit von besser als 1 mm respektive 0.1 mm/Jahr bekannt sein sollten. Heute hängt die Genauigkeit des ITRF weitgehend davon ab, wie gut und präzise die verschiedenen geodätischen Weltraumverfahren (GNSS, VLBI, SLR, DORIS) an Ko-lokationsstationen verknüpft werden können. Die ITRF2014-Realisierung des ITRS beinhaltet z.B. Klaffungen zwischen den Resultaten der Weltraumverfahren und den terrestrisch gemessenen lokalen Verknüpfungen von typischerweise 5-40 mm, viel zu gross um die Forderung von GGOS einzuhalten. Diese Diskrepanzen haben zwei Ursachen: a) Unzulänglichkeiten in den lokalen Verknüpfungen und b) bedeutende systematische Fehler in den individuellen Weltraumverfahren.

Genau hier setzt die Dissertation von Iván Herrera Pinzón mit dem Ziel ein, diese Diskrepanzen und deren Ursprung zu ergründen. Dazu wird die spezielle Situation auf der Fundamentalstation Wettzell genutzt, wo drei VLBI-Teleskope, zwei SLR-Teleskope und mehrere GNSS-Antennen/Empfänger am selben Ort installiert sind und die Analyse von kurzen Intra-Technik-Basislinien erlaubt sowie die Überprüfung mit den lokalen terrestrischen Messungen. Zudem studiert Iván Herrera Pinzón auch die rigorose Kombination von VLBI- und GNSS-Beobachtungen während der CONT'17-VLBI-Kampagne, wo alle verfügbaren Radioteleskope während 15 Tagen durchgängig beobachtet haben. In dieser Kombinationsstudie hat Iván Herrera Pinzón nicht nur alle gemeinsamen Parameter zur Verknüpfung der zwei Verfahren eingeschlossen, sondern auch die Effekte bewertet, die durch die Einführung der lokalen terrestrischen Koordinaten und der lokalen Troposphärenkorrekturen – VLBI- und GNSS-Beobachtungen werden ja von der troposphärischen Refraktion gleich beeinflusst – entstehen. Die Datenanalyse erfolgte vorwiegend mit der Bernese GNSS Software. Dieses komplexe Softwarepaket musste aber für die spezifischen Aufgaben der Doktorarbeit angepasst werden, u.a. für die Einführung von Uhrendifferenzen zwischen zwei VLBI-Teleskopen (Uhrenverknüpfung, gegeben durch den in Wettzell installierten Two-Way Optical Time Transfer (TWOTT) und die Einführung der Troposphärenverknüpfung.

Insgesamt leistet Iván Herrera Pinzón mit den umfassenden, im Rahmen seiner Dissertation durchgeführten Studien einen international bedeutenden Beitrag zum Thema der Kombination und Ko-lokation der geodätischen Weltraumtechniken.

Die SGK dankt sowohl dem Autor Iván Herrera Pinzón für den wertvollen Beitrag als auch der Schweizerischen Akademie für Naturwissenschaften (SCNAT) für die Übernahme der Druckkosten.

Prof. Dr. M. Rothacher
Institut für Geodäsie und Photogrammetrie
ETH Zürich

Prof. Dr. A. Jäggi
ETH Zürich
Präsident der SGK

PREFACE

Le Système de Référence Terrestre International (ITRS) et sa réalisation, le Cadre de Référence Terrestre International (ITRF), constituent aujourd'hui la base métrologique pour toutes les activités mondiales de mesure et de surveillance du système Terre. Lors de l'analyse des changements globaux, en particulier de l'élévation du niveau de la mer d'environ 2 à 3 mm par an, une réalisation extrêmement stable et précise de l'ITRS est d'une importance capitale. Il a été démontré que les imprécisions dans la réalisation du système de référence terrestre mondial sont l'un des facteurs les plus importants limitant la détermination fiable de l'élévation du niveau de la mer. Le Système d'Observation Géodésique Global (GGOS) de l'Association Internationale de Géodésie (IAG) a donc formulé l'exigence que les coordonnées des stations ITRF et les vitesses des stations devraient être connues avec une précision meilleure que 1 mm et 0.1 mm/an, respectivement. Aujourd'hui, la précision de l'ITRF dépend largement de la qualité et de la précision avec lesquelles les différentes techniques géodésiques spatiales (GNSS, VLBI, SLR, DORIS) peuvent être liés aux stations de co-location. La réalisation ITRF2014 de l'ITRS inclut, par exemple, des divergences entre les résultats des techniques spatiales et les liaisons locales mesurées sur terre de typiquement 5 à 40 mm, bien trop importantes pour satisfaire aux exigences du GGOS. Ces divergences ont deux causes : a) des lacunes dans les liaisons locales et b) des erreurs systématiques significatives dans les techniques spatiales individuelles.

C'est précisément là que la thèse d'Iván Herrera Pinzón intervient, dans le but d'explorer ces divergences et leur origine. Pour ce faire, la situation particulière à la station fondamentale de Wettzell est exploitée, où trois télescopes VLBI, deux télescopes SLR et plusieurs antennes/récepteurs GNSS sont installés au même endroit, permettant l'analyse de courtes lignes de base intra-techniques ainsi que la vérification avec les mesures terrestres locales. De plus, Iván Herrera Pinzón étudie également la combinaison rigoureuse des observations VLBI et GNSS lors de la campagne VLBI CONT'17, où tous les radiotélescopes disponibles ont observé de manière continue pendant 15 jours. Dans cette étude de combinaison, Iván Herrera Pinzón n'a pas seulement inclus tous les paramètres communs pour relier les deux procédés, mais a également évalué les effets résultant de l'introduction des coordonnées terrestres locales et des corrections locales de la troposphère, car les observations VLBI et GNSS sont toutes deux influencées par la réfraction troposphérique. L'analyse des données a été principalement réalisée avec le logiciel GNSS Bernese. Cependant, ce logiciel complexe a dû être adapté aux tâches spécifiques de la thèse, notamment pour l'introduction des différences d'horloge entre deux télescopes VLBI (liaison temporelle, donnée par le Two-Way Optical Time Transfer (TWOTT) installé à Wettzell) et l'introduction de la liaison troposphérique. Dans l'ensemble, les études approfondies menées par Iván Herrera Pinzón dans le cadre de sa thèse contribuent de manière significative et internationale au sujet de la combinaison et de la co-location des techniques géodésiques spatiales. La CGS exprime sa gratitude à la fois à l'auteur Iván Herrera Pinzón pour sa précieuse contribution et à l'Académie Suisse des Sciences Naturelles (SCNAT) pour la prise en charge des coûts d'impression.

Prof. Dr. M. Rothacher
Institut de Géodésie et Photogrammétrie
ETH Zürich

Prof. Dr. A. Jäggi
ETH Zürich
Président de la CGS

FOREWORD

The International Terrestrial Reference System (ITRS) and its realization, the International Terrestrial Reference Frame (ITRF), are nowadays the metrological basis for all global observing and monitoring of the Earth's system. When considering global change phenomena, especially sea level rise on the order of 2-3 mm/year, an extremely stable and highly accurate realization of the ITRS is of utmost importance. It has been shown that the inaccuracies in the realization of the global terrestrial reference system constitute one of the major factors limiting the reliable estimation of sea level rise. The Global Geodetic Observing System (GGOS) of the International Association of Geodesy (IAG) has, therefore, identified the requirements that overall the ITRF site coordinates should be known to better than 1 mm and the site velocities to better than 0.1 mm/year. Today, the quality of the ITRF itself depends to a large extent on how well and precisely the various space geodetic techniques (GNSS, VLBI, SLR, DORIS) can be tied together at co-location sites. The ITRF2014 realization of the ITRS, e.g., shows discrepancies between the observation technique results and the terrestrially measured local ties of typically 5-40 mm, much too large to achieve the requirements set up by GGOS. These discrepancies are of two-fold origin: a) deficiencies in the local tie measurements and b) considerable technique-specific systematic biases in the individual space geodetic techniques.

The Ph.D. thesis of Iván Herrera Pinzón starts exactly here with the goal to study these discrepancies and their possible origin. For this, he mainly makes use of the special situation at the fundamental station Wettzell, where three VLBI telescopes, two SLR telescopes and several GNSS antennas/receivers are co-located and allow the processing of short intra-technique baselines and the comparison with the local terrestrial measurements for validation. In addition, Iván Herrera Pinzón also studies the rigorous combination of VLBI and GNSS observations during the CONT'17 campaign, a special VLBI campaign, where all available radio telescopes were continuously observing during 15 days. In this combination study, Iván Herrera Pinzón not only includes all common parameters to connect the different space geodetic techniques but also assesses the effect of applying local coordinate ties from terrestrial surveys and the so-called tropospheric ties that are based on the fact that VLBI and GNSS measurements are equally affected by tropospheric refraction. Most of the processing required for this thesis was done with the Bernese GNSS Software, but the complex software package had to be adapted to the specific needs for each of the subtasks of the thesis. The modifications include, among others, the implementation of the clock differences between the VLBI telescopes (clock ties) made available by the Two-Way Optical Time Transfer (TWOTT) established in Wettzell and the implementation of troposphere ties.

In summary, the comprehensive studies conducted by Iván Herrera Pinzón in the course of his dissertation represent an important international contribution to the overall theme of combination and co-location of space geodetic techniques.

The SGC thanks the author for his valuable contribution as well as the Swiss Academy of Sciences (SCNAT) for covering the printing costs of this volume.

Prof. Dr. M. Rothacher
Institute for Geodesy and Photogrammetry
ETH Zürich

Prof. Dr. A. Jäggi
ETH Zürich
President of SGC

ABSTRACT

The modern definition of Geodesy goes beyond the classical task of determining the shape and figure of the Earth and its (external) gravitational field in a three-dimensional time-varying space. Nowadays, Geodesists also deal with the analysis of geodynamical phenomena (Torge, W., 2001). The different space geodetic techniques, Global Navigation Satellite Systems (GNSS), Very Long Baseline Interferometry (VLBI), Satellite Laser Ranging (SLR), and Doppler Orbitography and Radiopositioning Integrated by Satellite (DORIS) contribute to quantify these "Geodetic Earth Observation" tasks. These techniques provide both, in time and space, global and regional observations to measure geodynamical processes. Undoubtedly, the requirements for the appropriate observation of these phenomena are growing. Consequently, the geodetic infrastructure to monitor them requires high accuracy and stability so that the "real" signal in the observations can be separated from the noise and the not-so-important information contained in the measurements. Currently, the International Terrestrial Reference System (ITRS) and its realisation, the International Terrestrial Reference Frame (ITRF), constitute the infrastructure to support this geodetic Earth observing system. The quality of the ITRF relies, to a large extent, on the sufficiency of the combination of the different space geodetic techniques at co-location sites. The predominant threats to establishing a reference frame are the deficiencies in the local tie measurements and technique-specific systematic biases in the individual space geodetic techniques. An alternative to get an insight into these biases is the analysis of co-located instruments of the different techniques. Therefore, the study of co-location strategies constitutes the central element of this work. To improve the understanding of the error sources which affect each technique, we performed a series of intra-technique studies on short baselines, to analyse technique-specific biases, to monitor local ties, and to propose alternative ways to link the different techniques, such as clock and tropospheric ties. Ties among the different techniques are realised by parameters common to more than one technique. Therefore, we assess the performance of various parameters in experiments on GNSS-to-GNSS, SLR-to-SLR, and VLBI-to-VLBI short baselines, where multiple local and environmental effects, such as snow, meteorological data, antenna phase centre variations, and multipath, are investigated. We propose new methodologies and processing strategies to quantify and mitigate these error sources and to achieve a more accurate reference frame. Furthermore, we performed inter-technique experiments including GNSS and VLBI observations, where the task lies in the analysis of biases among the space geodetic techniques and the study of the benefits from a rigorous GNSS-VLBI combination of all common parameter types, including all types of ties available. These experiments contribute to the realisation of a consistent reference frame and constitute a necessary step to improve the realisation of the ITRF.

ZUSAMMENFASSUNG

Die moderne Definition der Geodäsie geht über die klassische Aufgabe hinaus, Form und Gestalt der Erde und ihr (äußeres) Gravitationsfeld in einem dreidimensionalen zeitlich veränderlichen Raum zu bestimmen, und Geodäten beschäftigen sich heute auch mit der Analyse geodynamischer Phänomene (Torge, W., 2001). Die weltraumgeodätischen Techniken, Global Navigation Satellite Systems (GNSS), Very Long Baseline Interferometry (VLBI), Satellite Laser Ranging (SLR) und Doppler Orbitography and Radiopositioning Integrated by Satellite (DORIS) tragen zur Quantifizierung der Aufgaben in der geodätischen Erdbeobachtung bei. Diese Techniken liefern sowohl zeitlich als auch räumlich globale und regionale Beobachtungen zur Messung geodynamischer Prozesse. Zweifellos wachsen die Anforderungen für eine angemessene Beobachtung dieser Phänomene. Folglich erfordert die geodätische Infrastruktur zu ihrer Überwachung eine hohe Genauigkeit und Stabilität, damit sich das "echte" Signal in den Beobachtungen vom Rauschen und von weniger wichtigen Informationen in den Messungen trennen lässt. Derzeit bilden das Internationale Terrestrische Referenzsystem (ITRS) und seine Realisierung, der Internationale Terrestrische Referenzrahmen (ITRF), die Infrastruktur zur Unterstützung dieses geodätischen Erdbeobachtungssystems. Die Qualität des ITRF hängt davon ab, ob die Kombination der verschiedenen weltraumgeodätischen Techniken an Kollokationsstandorten ausreichend ist. Die bislang größte Herausforderung bei der Festlegung eines Referenzrahmens sind Unzulänglichkeiten bei lokalen terrestrischen Messungen ("Local Ties") und technikspezifische systematische Verzerrungen (Biases) bei den einzelnen weltraumgeodätischen Verfahren. Eine Alternative, um Einblick in diese Biases zu erhalten, ist die Analyse von gemeinsam genutzten Instrumenten in den verschiedenen Techniken. Daher bildet die Untersuchung von Co-Location-Strategien das zentrale Element dieser Arbeit. Um das Verständnis für Fehlerquellen zu verbessern, die sich auf jede Technik auswirken, haben wir eine Reihe von Intra-Technik-Studien an kurzen Basislinien durchgeführt, um technikspezifische Biases zu analysieren, "Local Ties" zu überwachen und alternative Wege zur Verknüpfung der verschiedenen Techniken vorzuschlagen, wie zum Beispiel Uhr und troposphärische Ties. Ties zwischen den verschiedenen Techniken werden durch Parameter erzeugt, die mehr als einer Technik gemeinsam sind. Daher haben wir die Leistung verschiedener Parameter in Experimenten an GNSS-zu-GNSS-, SLR-zu-SLR- und VLBI-zu-VLBI-Kurzbasislinien bewertet, bei denen mehrere lokale und umweltbedingte Einflüsse wie Schnee, meteorologische Daten, im Antennenphasenzentrum auftretende Variationen und Multipath untersucht wurden. Wir stellen neue Methoden und Verarbeitungsstrategien vor, um diese Fehlerquellen zu quantifizieren und zu mindern und einen genaueren Referenzrahmen zu erreichen. Darüber hinaus führten wir methodenübergreifende Experimente mit GNSS- und VLBI-Beobachtungen durch, bei denen die Analyse der Biases zwischen den weltraumgeodätischen Techniken und die Untersuchung der Vorteile einer strengen GNSS-VLBI-Kombination aller gängigen Parametertypen, einschließlich aller verfügbaren Ties-Arten, im Vordergrund standen.

Diese Experimente tragen zur Realisierung eines konsistenten Referenzrahmens bei und sind ein notwendiger Schritt zur Verbesserung des ITRF.

CONTENTS

LIST OF FIGURES

LIST OF TABLES

NOTATION

FREQUENTLY USED ACRONYMS

AR	Ambiguity Resolution
BKG	Bundesamt für Kartographie und Geodäsie
C/A	Coarse Acquisition code
CEP	Celestial Ephemeris Pole
CODE	Center for Orbit Determination in Europe
DD	Double-Differences
DORIS	Doppler Orbitography and Radiopositioning Integrated by Satellite
EOP	Earth Orientation Parameter
GAST	Greenwich Apparent Sidereal Time
GFZ	GeoForschungsZentrum Potsdam
GGOS	Global Geodetic Observing System
GLONASS	Globalnaya Navigatsionnaya Sputnikovaya Sistema
GNSS	Global Navigation Satellite System
GPS	Global Positioning
IAU	International Astronomical Union
ICRF	International Celestial Reference Frame
ICRS	International Celestial Reference System
IERS	International Earth Rotation and Reference Systems Service
IGS	International GNSS Service
IVS	International VLBI Service for Geodesy and Astrometry
ILRS	International Laser Ranging Service
ITRF	International Terrestrial Reference Frame
ITRS	International Terrestrial Reference System
IUGG	International Union for Geodesy and Geophysics
JPL	Jet Propulsion Laboratory
LAGEOS	Laser Geodynamics Satellite
LoD	Length of Day
LSA	Least Squares Adjustment
L_3	Ionosphere-Free Linear Combination
MEO	Medium Altitude Orbits
NGS	National Geodetic Service
NNR	No Net Rotation
NNT	No Net Translation

NPT	Normal Point Format
NQo	Normal Equation
PCV	Phase Centre Variation
PPP	Precise Point Positioning
QZSS	Quasi-Zenith Satellite System
RINEX	Receiver Independent Exchange Format
RMS	Root Mean Square
SD	Single-Differences
SI	International System of Units
SINEX	Software Independent Exchange Format
SLR	Satellite Laser Ranging
TT	Terrestrial Time
TWOTT	Two-Way Optical Time-Transfer system
VGOS	VLBI Global Observing System
VLBI	Very Long Baseline Interferometry
WL	Wide-Lane Linear Combination
ZTD	Zenith Total Delay
ZWD	Zenith Wet Delay

1 INTRODUCTION

1.1 MOTIVATION

The International Terrestrial Reference System (ITRS) and its realisation, the International Terrestrial Reference Frame (ITRF), are nowadays the metrological basis for monitoring the Earth system (Rothacher, M. et al., 2009). The ITRF provides the infrastructure for measuring both, in time and space, processes connected to kinematic variations and mass re-distributions in the solid Earth, ocean and atmosphere, which directly affect the well-being of society. The monitoring of these phenomena requires levels of accuracy and stability which allow to separate the signal in the observations from the noise, for an appropriate understanding of their repercussions. Figure 1.1 summarises the precision required for multiple geodetic applications. The observations required to measure this evolving system demand a highly accurate and extremely stable ITRF realisation in which temporal and spatial variations can be accounted for. Typically, the estimation of the ITRF is performed through the combination of

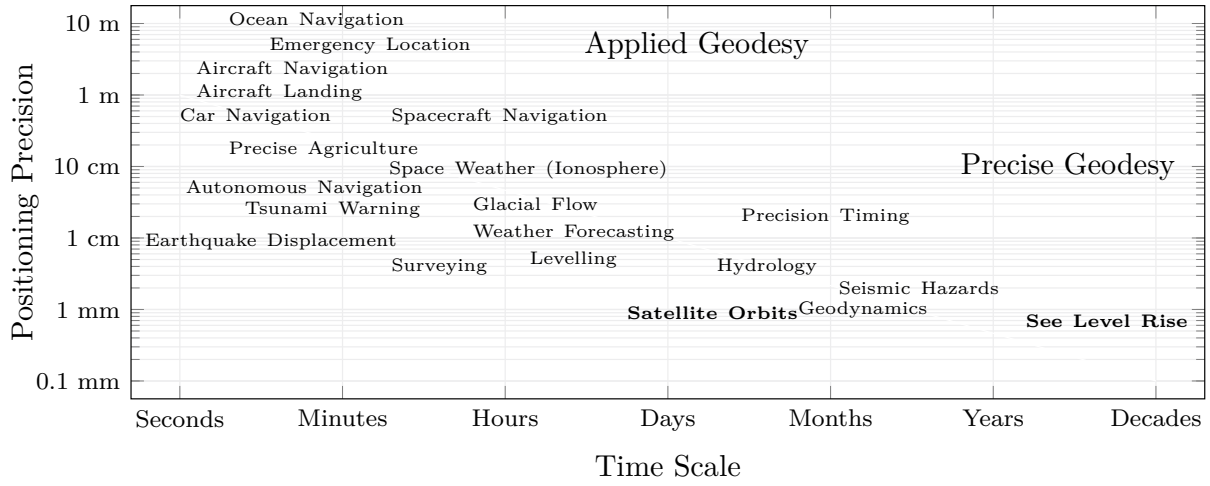

FIGURE 1.1: The wide range of activities which require a highly precise geodetic frame: from ocean navigation, with precision of tens of metres and processes occurring in few minutes, to plate tectonics where millimetre precision is required for changes that are usually noticeable after several months. Two applications stand out: See Level Rising which happens over the course of decades and satellite orbit determination. For both sub-millimetre precision is required. Adapted from Minster, J. B. et al. (2010)

the individual solutions of the four space geodetic techniques: Global Navigation Satellite System (GNSS), Satellite Laser Ranging (SLR), Very Long Baseline Interferometry (VLBI), and Doppler Orbitography and Radiopositioning Integrated by Satellite (DORIS). This combination is complemented with the application of the so-called "Local Ties", terrestrial measurements which provide relative positions among the

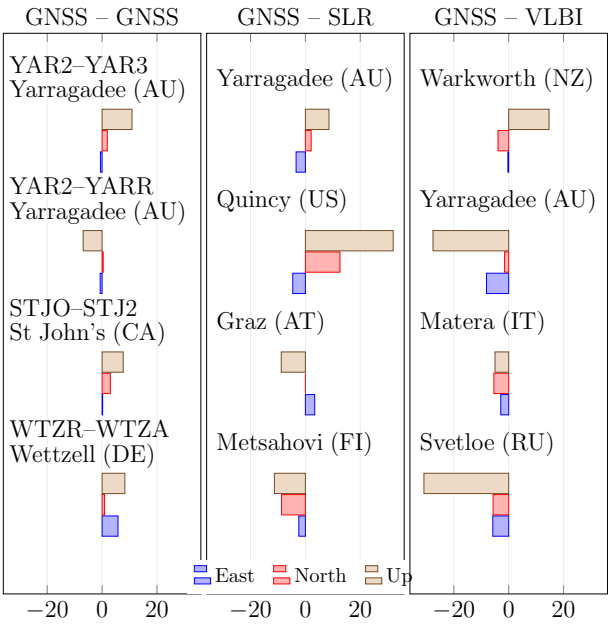

FIGURE 1.2: ITRF2014 tie discrepancies [mm] at selected co-location sites according to Altamimi, Z. et al., 2016.

instrument reference points of each technique at fundamental sites (Abbondanza, C. et al., 2009). The determination and monitoring of the ties to link these techniques constitute a fundamental step and a major challenge for the realisation of the ITRF. However, multiple co-location sites show discrepancies much larger than the requirements of the Global Geodetic Observing System (GGOS): positions $\leq$ 1 mm and velocities $\leq$ 0.1 mm/yr (Rothacher, M. et al., 2009). For instance, based on the tie discrepancies of the ITRF2014, Figure B.1 shows that the differences in east, north and up components for a GNSS-to-GNSS baseline surpass largely the 1 mm requirement at several sites (Altamimi, Z. et al., 2016). This is why, the study of the co-location of space geodetic techniques provides the opportunity to improve the understanding of technique-specific error sources which affect the space geodetic solutions, in order to enhance the combination and accuracy of the geodetic techniques. In this context, this thesis proposes a series of co-location experiments, both intra- and inter-technique, where a detailed assessment of technique-specific biases and the analysis of the discrepancies in the combination of the different geodetic techniques will be performed. Moreover, we conduct investigations on alternative ties among different techniques, namely highly accurate tropospheric ties and clock ties. These experiments are expected to improve the consistency and the realisation of the ITRF by establishing innovative ties and by identifying systematic biases between the existing ones, and therefore will contribute to the integration of space geodetic techniques for the adequate realisation of the next generation of reference frames.

1.2 THESIS OBJECTIVES

The overarching goal of this PhD project is the improvement of existing and generation of alternative co-location strategies for the enhancement of the ties among space

geodetic techniques, to achieve the realisation of a common reference frame able to meet the growing requirements of modern users. The goal of this project is composed of two main tasks:

1. The study of measurements between instruments of the same space geodetic technique, *intra-technique co-location*, to improve the understanding of system-specific error sources. This part of the project aims to collect data from three techniques on very short local baselines (SLR-SLR, VLBI-VLBI and GNSS-GNSS) to test and evaluate new measurement concepts and processing strategies (e.g. SLR single- and double-differences and VLBI observation of GNSS satellites) and to assess error sources for each individual technique. These experiments will be complemented by using an available common clock at the Geodetic Observatory in Wettzell (Germany), which is used to generate a "clock" tie.

2. The study of simultaneous measurements of GNSS and VLBI (*inter-technique co-location*), to investigate systematic biases and local tie accuracy. Moreover, the behaviour of the troposphere at the co-location sites will be analysed in detail, to establish a "tropospheric" ties between GNSS and VLBI stations. These elements constitute a setup that will lead to a significant step in the analysis of technique-specific biases. Using common parameters among the different space geodetic techniques, a rigorous combination at the observation level will be done, achieving highest consistency by using common models and parametrisation.

1.3 GNSS INTRA-TECHNIQUE CO-LOCATION

In the context of this work, and considering that according to the station list of the International GNSS Service (IGS, 2017), approximately 50 sites are currently or have been equipped with two or more GNSS receivers and/or antennas (Figure 1.3), we intend to examine the behaviour of the local GNSS baselines to improve the understanding of the error sources dominating this technique. These sites exhibit multiple differences in their environmental conditions such as station motion (tectonics), troposphere and ionosphere conditions. Moreover, some of these sites have time series of observations spanning up to 15 years, where multiple discontinuities associated to hardware and software changes are presented. As these sites are contributing to the global ITRF solution, local ties connecting the array of stations are provided through highly accurate terrestrial measurements (Sarti, P. et al., 2013), with sufficient accuracy to allow the comparison with the GNSS-derived baselines. Based on these input data, these experiments deal with the generation of GNSS-based coordinate time series, the assessment of the corresponding discrepancies with the available local ties, and the determination of the time-dependent variations in the local GNSS baselines at fundamental sites. To this end, an appropriate parametrisation and processing strategy must be developed to cope with the characteristics and advantages of short GNSS baselines. These experiments are expected to provide detailed information about GNSS-specific error sources and their impact on the ITRF definition. Multiple studies show the challenges and the relevance of GNSS co-locations. The general concepts for the analysis of GNSS local ties have been introduced by Rothacher, M. et al. (2004), with the discussion of elements for an

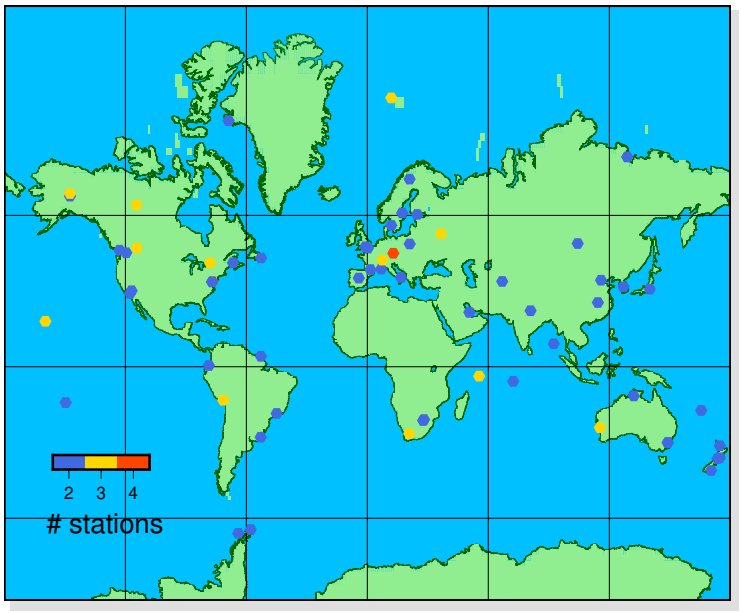

FIGURE 1.3: Potential sites ($\geq$ 2 stations) in the IGS network with time series $>$ 18 years and known local ties. Different local conditions (motion, troposphere, ...), several hardware (receiver, antenna) and software changes, and multiple discontinuities, pose a challenge for the reprocessing of time series of coordinates.

adequate parametrisation and a summary of recommended processing strategies. Their work addresses two fundamental aspects: the monitoring of the local environment to detect anomalies in the time series of coordinates, the so-called *footprint network*, and the assessment of the performance of the hardware in relation to equipment changes, or *antenna array monitoring*. Providing an empirical proof of concept for the latter, this study attained high-quality monitoring of the performance of GNSS arrays and recommended the co-location of GNSS at each ITRF fundamental site. Local effects on co-located GNSS have also been discussed by Steigenberger, P. et al. (2013) with the provision of time series of coordinates for the antenna array at the geodetic observatory in Wettzell (Germany). Motivated by the high discrepancies between local ties and the space geodetic techniques in the realisation of the ITRF2008, their work discusses the performance of GPS-based solutions in relation to terrestrial measurements and the impact of individual receiver antenna calibration. This study found out that discrepancies are mainly caused by GPS and not by the local tie measurements and concluded that near-field effects such as multipath and deficiencies in the antenna calibration are the most probable sources for these frequency-dependent systematic effects. Brockmann, E. et al. (2010) present a study on the benefits of co-located GNSS stations in the Swiss permanent Network. Their work studies the differences of the GNSS-based links and the terrestrial local ties. They found large discrepancies on the height component and conclude that this behaviour depends on the type of antenna due to the high sensitivity of certain antennas with respect to the near-field. The influence of snow on the antenna (leading up to a decimetre change in the height) is also taken into account. Santamaría-Gómez, A. (2013) shows variations in the GNSS baseline length for the two GPS stations at the Yebes Observatory (Spain), with uncertainties related to signal-dependent errors resulting from multipath, antenna calibration and antenna

phase centre migration due to electromagnetic coupling with the station monument. Moreover, the thermal expansion of the buildings at the site is modelled looking for an agreement with the horizontal displacement. Although variations in the baseline length and the time series of temperature at the site display high correlation, the implemented model fails to explain the observed amplitude. A similar approach is shown in Wilkinson, M. et al. (2013) for the stability of the baseline between two GPS receivers at the space geodesy facility in Herstmonceux (UK), showing large variations between GPS-based solutions and the local measurements. All these studies have in common the recommendation of performing a continuous monitoring of GNSS ties at fundamental sites, as a pre-requisite for the improvement of the consistency of the ITRF.

1.4 VLBI INTRA-TECHNIQUE CO-LOCATION

In view of the purpose of this work, the assessment of short VLBI baselines allows to examine local effects and instrument-specific biases inherent to this technique. The study of short baselines in VLBI is of major interest as the intended replacement of legacy antennas by the new VGOS dishes requires an accurate determination of the local baselines. Moreover, the analysis of local baselines allows to investigate instrumental biases as they can be separated from the (nearly) identical environmental influences. For these experiments, the short baseline between the co-located VLBI telescopes at the Geodetic Observatory in Wettzell (Germany) will be studied. This baseline is realised by the legacy 20 m antenna Radio Telescope Wettzell (RTW) and the new 13.2 m diameter TWIN Telescope Wettzell (TTW1) (Figure 1.4). The analysis

FIGURE 1.4: VLBI array at the Wettzell Observatory (Germany). Left: RTW, right: Twin Telescopes. Credits: Jan Kodet

of the local Wettzell baseline benefits, additionally, from a recently installed optical time transferring system. This two-way optical time-transfer system (TWOTT) allows time transfer below 1 ps accuracy between TTW1 and RTW (Kodet, J. et al., 2014). Consequently, these experiments will address the comparison between VLBI-derived local baseline vectors and local clock differences with respect to terrestrial surveys, and will perform the corresponding studies on time transfer, using the TWOTT, to enable the separation of VLBI technique-specific error sources from the local environmental effects, thus providing detailed information about these error sources. The topic of VLBI co-location has gained relevance in recent years, thanks to the installation of new

telescopes at fundamental sites, which made possible the simultaneous observation of targets over short baselines. Plank, L. et al. (2016) address the recent developments for the implementation of strategies of observation with co-located VLBI telescopes, designed to facilitate the observation process while maintaining the high precision of geodetic estimates. These new scheduling modes for the VLBI sessions are validated with data from the sibling telescopes at Hobart (Australia), and are presented as an alternative to obtain local baseline observations for the study of the local tie. Additionally, Schüler, T. et al. (2015) have performed a detailed study of the local baseline between the legacy telescope and the twin telescope in Wettzell (Germany) and its comparison with the local surveyed ties. Their work indicates that local radio frequency interference is one of the most significant problems for short VLBI baselines and they performed experiments at each individual band separately to assess its influence. The compensation for the differences in clock behaviour and multiple reductions and corrections to observations, radio source positions and antenna positions are discussed within their parametrisation. Differences between the VLBI-based baseline and the terrestrial measurements amount from 0.1 to 0.9 mm, indicating a rather satisfactory estimation of the short baseline length. The growing availability of observation for short VLBI baselines must be further exploited to derive insights about the performance of this technique.

1.5 SLR INTRA-TECHNIQUE CO-LOCATION

Two laser telescopes are currently available at the Geodetic Observatory in Wettzell (Germany), the Wettzell Laser Ranging System (WLRS) and the Satellite Observing System Wettzell (SOS-W). These instruments, connected by a local tie derived from terrestrial measurements and sharing a common timing system, provide the opportunity to quantify the magnitude and stability of instrumental biases, evaluate the quality of the local ties and test new observation and processing strategies, namely differencing methods: single- and double-differences. With the use of long time series of data, these experiments address the analysis of the differencing methods on SLR observations. For instance, Figure 1.5 shows a sample of observations collected on the 03.07.2018 (day of year 184), where the potentially simultaneous satellites are tracked by the two telescopes. By forming single-difference observations between the ranges from two stations to one satellite, it is expected that biases related to the satellite orbit and the retro-reflectors will be removed. In addition, by combining two quasi-simultaneous single-differences to two satellites observed by the same two stations (double-difference observation), the station-dependent range biases can be removed. In these experiments, the single- and double-difference results will be compared to the local ties giving additional information about the nature of SLR range biases (**Herrera-Pinzón, I. D.** et al., 2020). An initial idea for a double-difference baseline with co-located SLR observations has been introduced by Svehla, D. et al. (2013) and Svehla, D. (2018). Using real and simulated SLR measurements they discuss the advantages of this strategy and show how common biases can be removed leading to an orbit-free and bias-free estimation of station coordinates, local ties and the precise comparison of tropospheric effects. The developed concept uses quasi-simultaneous observations to two satellites during

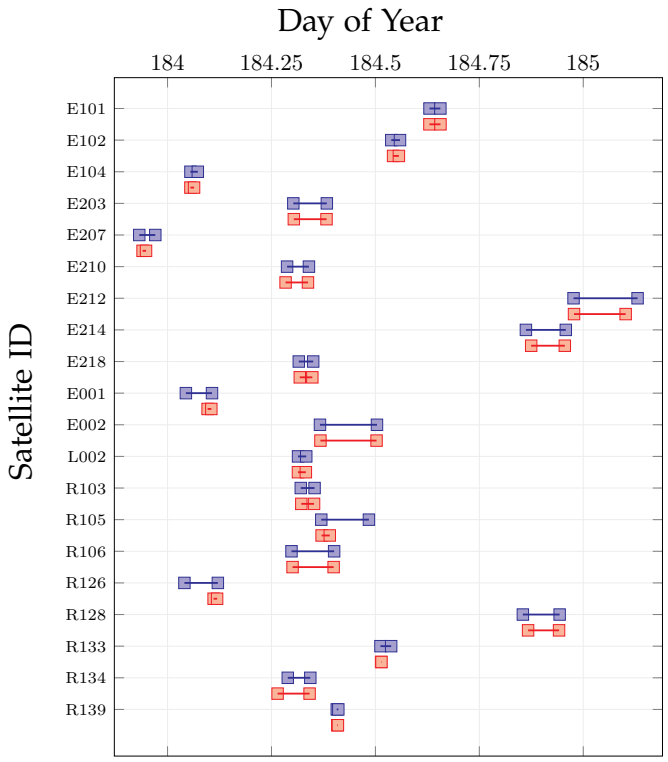

FIGURE 1.5: Potential simultaneous SLR observations at the array of SLR telescopes in Wettzell (Germany). Data corresponds to the 18.07.2018 (day of year 184). The x-axis corresponds to the decimal day of the year, while the y-axis shows the satellite tracked (E for GALILEO and R for GLONASS). The blue and red symbols represent the time intervals with observations from the telescopes WLRS and SOS-W, respectively.

the same tracking session and describes different alternatives for the generation of SLR double-differences based on satellites in different orbits. The discussed methods reveal systematic effects common to both stations at mm-level and claims to achieve station coordinates at similar levels. Moreover, they suggest that the implementation of this approach can be potentially used to estimate accurate local ties by comparing GNSS and SLR double-difference measurements enabling the combination of SLR and GNSS solutions. While this concept is in essence similar to our approach, our strategy uses the advantages of the short baseline, and strives for the utilisation of long time series of observations to demonstrate empirically its potential.

1.6 INTER-TECHNIQUE CO-LOCATION: RIGOROUS COMBINATION

A rigorous combination of space geodetic techniques (Figure 1.6) is fundamental for the generation of highly accurate geodetic and geophysical products (Rothacher, M. et al., 2019). The guiding principle for a rigorous combination lies in the fact that all parameter types common to more than one space geodetic observation technique have to be combined, including their full variance-covariance information as well as the corresponding ties. As both, GNSS and geodetic VLBI are based on microwave frequencies, their physical models and their parameter types (site coordinates and

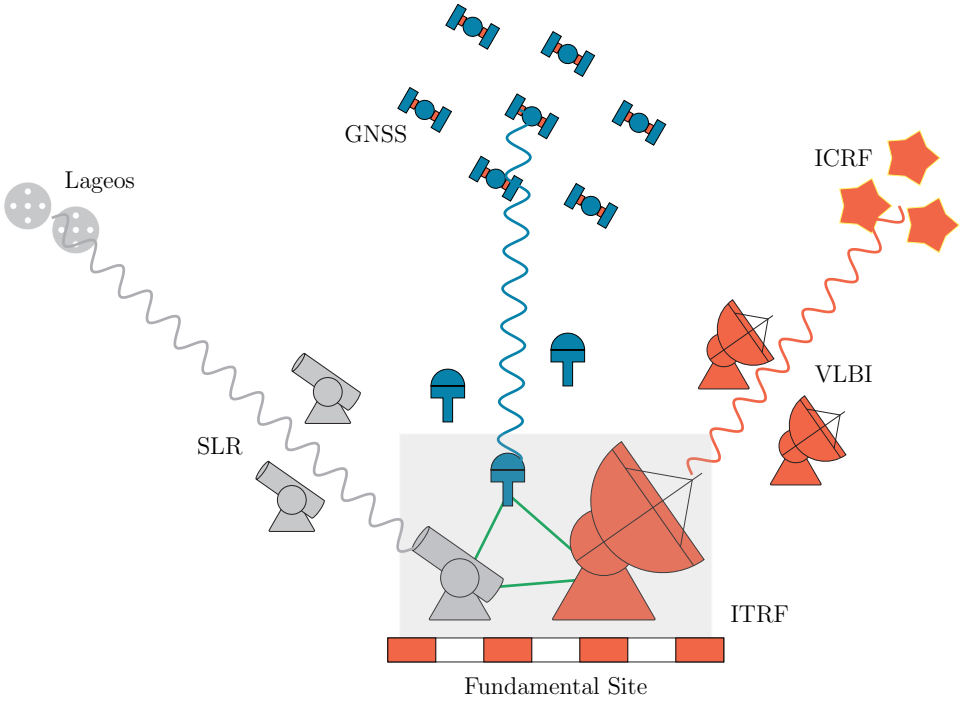

FIGURE 1.6: Concept of Co-Location of Space Geodetic Techniques on the Ground

velocities, troposphere estimates, EOPs and (possibly) clock estimates) are closely related and can be rigorously estimated. With this in mind, these experiments discuss a processing scheme, the challenges and results of a rigorous combination of VLBI and GNSS observations, in order to estimate and densify EOPs, in particular diurnal and sub-diurnal variations for polar motion and UT1-UTC, and to realise an inter-technique tropospheric tie. To achieve a rigorous combination, all parameter types common to more than one space geodetic observation technique should be combined including their full variance-covariance information as well as the corresponding ties. Of particular importance for this analysis are the tropospheric delays, as they can be considered identical for GNSS L-band and VLBI S- and X-band signals. Furthermore, when combining GNSS ground-based observations with measurements of GNSS signals with radio telescopes, the common parameters are the satellite orbits, site coordinates and Earth orientation parameters. Also GNSS and VLBI clock corrections are in common, when the time and frequency distribution is actively compensating for variations. These sets of parameter will be jointly estimated and their impact on the realisation of the ITRF will be studied. In addition, the ionosphere is acting on the same signal frequency and path and therefore will be considered during all the analysis. Special VLBI data sets will be analysed to validate these assumptions and to determine the advantages that the combination of these common parameters at the observation level will bring to the realisation of the ITRF.

1.7 THESIS STRUCTURE

This thesis is organised as follows: Chapter 2 reviews the principles of the space geodetic techniques, as well as the framework and fundamentals for the definition

of global reference frames and the co-location of space geodetic techniques. Some basic concepts are introduced to provide the necessary context to develop the next chapters. Each of the following chapters shows the design, development and results of series of co-location experiments aligned with the objectives of this thesis. In Chapter 3, a reproduction of the paper "Assessment of Local GNSS Baselines at Co-Location Sites" (2018) by **Herrera-Pinzón**, **I. D.** et al., the performance of GNSS-based station coordinates, from the point of view of co-located GNSS instruments, is analysed. We present a tailored processing strategy which delivers millimetre level station coordinates repeatabilities. These results allow the analysis of seasonal effects which affect the quality of the estimated parameters. Moreover, we compare these highly accurate coordinate results with the official local ties at the site, to detect inconsistencies that could propagate into the realisation of a reference frame.

Chapter 4 is an unpublished pre-print which extends the results originally published in the short papers "Co-Location of Space Geodetic Techniques: Studies on Intra-Technique Short Baselines" (2020) by **Herrera-Pinzón**, **I. D.** et al., and "Analysis of the Short VLBI Baseline at the Wettzell Observatory" (2018) by **Herrera-Pinzón**, **I. D.** et al. This work develops a processing strategy for the analysis of short VLBI baselines. We study the performance of VLBI-based station coordinates, tropospheric estimates, and clock offsets, and propose an innovative approach for the realisation of a clock tie between the two VLBI telescopes. This pre-print is presented in-between the actual journal papers to maintain the logic and coherence of the work according to the goals described early in this chapter.

Chapter 5 is a re-print of the work originally published as "Differencing strategies for SLR observations at the Wettzell observatory" (2021) by **Herrera-Pinzón**, **I. D.** et al. proposes a new methodology for the processing of SLR observations based on differencing methods. This unique work is evaluated on a SLR short baseline, where the local ties among the telescopes provide a reference for the validation of the results. This approach shows promising results in terms of repeatabilities of the station coordinates and the mitigation of systematic SLR errors, such as range biases.

Chapter 6, submitted as "Impact of Local- and Tropospheric Ties for the Rigorous Combination of GNSS and VLBI" by **Herrera-Pinzón**, **I. D.** et al., discusses the rigorous combination of VLBI and GNSS observations and the performance of the derived geodetic parameters (e.g. Earth orientation parameters and station coordinates). We develop a processing strategy which performs the combination with the highest consistency level (i.e. at the observation level). Besides the use of an appropriate inter-technique weighting scheme and local ties, we implement an approach for the use of tropospheric ties at co-location sites. This work shows the advantages of the rigorous combination for the estimation of geodetic parameters with respect to single-technique solutions, and demonstrates the need and potential of the use of other type of ties.

Finally, Chapter 7 summarises the main findings of this thesis and provides an outlook with connected topics for future research.

2

THEORETICAL FRAMEWORK

2.1 GENERALITIES OF THE SPACE GEODETIC TECHNIQUES

2.1.1 *Very Long Baseline Interferometry*

The Very Long Baseline Interferometry (VLBI) is an astronomical technique used for astronomy, astrometry, spacecraft navigation, and precise geodesy. Geodetic and astrometric VLBI contributes to the precise determination of station coordinates, the accurate determination of very long distances on the Earth, the motion of the tectonic plates, the orientation of the Earth, and the source coordinates (Heinkelmann, R., 2013). This last fact makes VLBI one of the central contributors to the realisation and maintenance of the reference frames used in geodesy. The core idea of VLBI is the

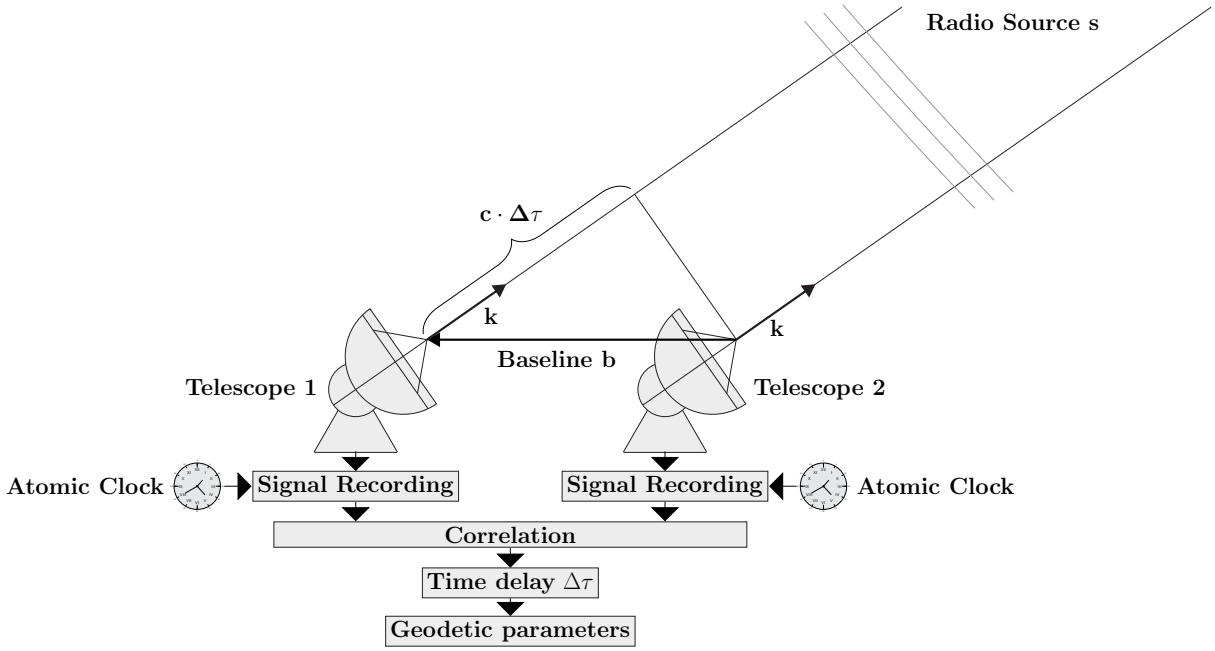

FIGURE 2.1: Basic principle of VLBI, adapted from Rothacher, M. (2017).

simultaneous observation of extra-galactic radio sources by at least two radio telescopes (Figure 2.1). Assuming that the source is located in the distant universe, its emitted wavefront can be consider planar. When the signal of the source **s** arrives at the baseline **b**, it is received first at one telescope and then at the other. The difference between these two arrival times is the so-called "light travel time delay" ($\Delta\tau$) and constitutes the main VLBI observable. $\Delta\tau$ depends on the length of **b** and the orientation of **b** with respect to **s**. This relation reads as (Rothacher, M., 2017; Seitz, M., 2009):

$$\Delta\tau = -\frac{1}{c}\mathbf{b}\cdot\mathbf{k}$$

with

$$\mathbf{k} = \begin{bmatrix} \cos\alpha\cos\delta \\ \sin\alpha\cos\delta \\ \sin\delta \end{bmatrix}, \quad \mathbf{b} = \begin{bmatrix} \mathbf{X}_2 - \mathbf{X}_1 \\ \mathbf{Y}_2 - \mathbf{Y}_1 \\ \mathbf{Z}_2 - \mathbf{Z}_1 \end{bmatrix}$$

where

$\Delta\tau$: Time delay

$\mathbf{b}$: Baseline vector between two telescopes, formed with the Cartesian coordinates $(\mathbf{X}_i, \mathbf{Y}_i, \mathbf{Z}_i)$ of the two telescopes, in the geocentric coordinate system

$\mathbf{k}$: Unit vector in the direction of the radio source, expressed by the equatorial coordinates (declination δ and right ascension α) of the source $\mathbf{s}$

c : Speed of light

VLBI operates between two reference frames as the coordinates of the VLBI telescopes are referred to a terrestrial reference frame, while the coordinates of the sources are given in a celestial reference frame.

Space Segment: Radio Sources

Th space segment of VLBI consists of extra-galactic compact radio sources such as *quasi stellar radio sources* (quasars), active galactic nuclei (AGN), and BL Lacertae objects (Heinkelmann, R., 2013). Quasars are star-like objects that are identified as radio sources, with variable light, large ultraviolet flux of radiation, broad emission lines in the spectra, and located in the distant universe (Kembhavi, A. K. et al., 1999). AGN are X-ray sources characterised by intense energy production, with matter outflow (jets) issuing from the central region (Kembhavi, A. K. et al., 1999). Quasars and AGN are similar objects, but they differ in the geometry of observation. Quasars are radio galaxies where the edge of the dust torus obscures the AGN in the line of sight of the observer (Haas, M. et al., 2003). BL Lacertae objects are AGN characterised by rapid and large-amplitude flux variability and a significant optical polarisation (Padovani, P. et al., 1995). In this type of objects the angle between the line of sight and the direction of the jet is relatively small (Heinkelmann, R., 2013). According to Heinkelmann, R. (2013), for astrometric and geodetic VLBI, a radio source has to meet three characteristics to be useful as a reference object:

- *Brightness*. The source has to be strong enough at frequency bands in which it is observed. Depending on the antenna characteristics, the minimum signal strength is 0.01 Jy[1]. This condition has to be fulfilled to achieve an appropriate signal-to-noise ratio during the correlation process..
- *Compactness*. The spatial extension of the source, specified through the angle diameter of its core, has to be smaller than the intended coordinate precision.
- *Stability*. The source should not exhibit significant proper motion or parallax.

1 Jansky: 1 Jy$= 10^{-26} \cdot W \cdot m^{-2} \cdot Hz^{-1}$

Due to the large distance between the sources and the Earth, these criteria are met by a large number of extra-galactic objects. However, for high-precision applications, the source topology and proper motion have to be considered (Charlot, P. et al., 2020).

Ground Segment: Radio Telescopes

The ground segment of VLBI is composed of fully steerable radio telescopes with a concrete foundation attached to a fixed point which serves as geometric reference (Heinkelmann, R., 2013). Since, the signal flux density of the typical source is in the order of 1 Jy or even lower (Schuh, H. et al., 2013), telescopes with a large reflector diameter are needed. Geodetic and astrometric VLBI use typically the frequencies 8.4 GHz (X-band), 2.3 GHz (S-band) used, 24 GHz (K-band), and 32 GHz (Ka-band). These frequencies correspond to wavelengths of 3.6 cm, 13 cm, 13 mm, and 9 mm, respectively (Charlot, P. et al., 2020). Most of the VLBI telescopes adopt a Cassegrainian layout. The sub-reflector is a hyperboloidal surface, located near to the primary focus (Abbondanza, C. et al., 2010). In this case, the signal first hits the parabolic primary reflector, then it is reflected to the hyperbolic sub-reflector to finally reach the feed horn on the main axis of the system, which filters out all the frequencies outside the desired bands (Rothacher, M., 2017). The telescope reflectors are mounted in different ways. The most common types are the azimuth-elevation mount where the fixed (primary) axis is oriented along the local vertical, the polar mounts with their primary axis oriented parallel to the Earth's rotation axis, and the X/Y mounts with their fixed axes oriented parallel to the local horizontal plane, oriented either north–south or east–west (Nothnagel, A., 2009). The VLBI reference point is an invariant point located at the intersection of the telescope axes. Since this point is usually not directly accessible, it needs to be eccentrically realised through indirect measurements from external reference markers (Heinkelmann, R., 2013).

Correlation and Types of Observables

The correlation process performs the cross-correlation of each pair of signals from two different telescopes. During correlation, the individually recorded signals are shifted in time with respect to each other in such a way that the cross-correlation function is maximised (Heinkelmann, R., 2013). The amplitude of the correlated signals changes depending on the relative phase difference of the two signals. Due to the rotation of the Earth, the phase difference does not change linearly in time. Thus, interference fringes, with slow changing frequencies (fringe rates), are noticed (Rothacher, M., 2017). The result of the correlation process are the phases and amplitudes of these interference fringes determined every 1–2 s in parallel for typically 14 frequency channels (Schuh, H. et al., 2013). The fringe rate $\Phi(\omega_i, t_i)$ for the frequency channel ω_i and time epoch t_i is introduced in a bi-linear least squares adjustment to determine the VLBI observables, namely the phase Φ_0, the phase delay $\Delta\tau_p$, the group delay $\Delta\tau_g$, and the phase-delay rate $\Delta\dot{\tau}_p$, following the relation (Rothacher, M., 2017; Schuh, H. et al., 2013):

$$\Phi(\omega_i, t_i) = \Phi_0(\omega_0, t_0) + \frac{\partial\Phi}{\partial\omega}\Big|_{(\omega_0,t_0)}(\omega - \omega_0) + \frac{\partial\Phi}{\partial t}\Big|_{(\omega_0,t_0)}(t_i - t_0)$$

where

$$\begin{aligned}
\Delta\tau_p &= \frac{\Phi_0}{\omega_0} && \text{Phase delay} \\
\Delta\tau_g &= \frac{\partial\Phi}{\partial\omega}\Big|_{(\omega_0,t_0)} && \text{Group delay} \\
\Delta\dot{\tau}_p &= \frac{1}{\omega_0}\frac{\partial\Phi}{\partial t}\Big|_{(\omega_0,t_0)} && \text{Phase-delay rate}
\end{aligned}$$

In general, only the group delay and the phase-delay rate are used as main VLBI observables (Rothacher, M., 2017). The group delay rate, another possible observable, cannot be measured with the required accuracy to be useful for geodetic or astrometric purposes, and it is only used to resolve group delay ambiguities in a first solution step. The amplitudes are usually not used in geodetic/astrometric VLBI (Schuh, H. et al., 2013).

General Relativistic Model for VLBI Time Delay

The time delay has to be corrected for relativistic effects. The General Theory of Relativity states that a signal is slowed down when propagating through a gravitational field. The general relativistic delay $\delta\Delta\tau_{\text{grav}}$ for the J^{th} body is given by (Petit, G. et al., 2010)

$$\delta\Delta\tau_{\text{grav}_J} = 2\frac{GM_J}{c^3}\ln\left(\frac{\|\mathbf{R_{1_J}}\| + \mathbf{R_{1_J}}\cdot\mathbf{k}}{\|\mathbf{R_{2_J}}\| + \mathbf{R_{2_J}}\cdot\mathbf{k}}\right)$$

with

$\mathbf{R_{i_J}}$: The vector from the J^{th} gravitating body to the i^{th} telescope
$\mathbf{k}$: The unit vector in the direction of the radio source, in the absence of gravitational or aberrational bending
M_J : The mass of the J^{th} gravitating body
G : Gravitational constant
c : Speed of light

The Sun, the Earth and Jupiter must be included, as well as the other planets in the solar system along with the Earth's Moon. At the picosecond level it is possible to simplify the delay due to the Earth as (Rothacher, M., 2017):

$$\delta\Delta\tau_{\text{grav}_E} = 2\frac{GM_E}{c^3}\ln\left(\frac{1+\sin E_1}{1+\sin E_2}\right)$$

where M_E is the rest mass of the Earth, and E_1, E_2 are the elevation angles of the source with respect to each station. The total gravitational delay is the sum over all gravitating bodies including the Earth

$$\delta\Delta\tau_{\text{grav}} = \sum_J \delta\Delta\tau_{\text{grav}_J}$$

The total geocentric vacuum delay in the rational polynomial form is given by (Petit, G. et al., 2010; Rothacher, M., 2017):

$$t_{v_2} - t_{v_1} = \frac{\delta\Delta\tau_{\text{grav}} - \frac{1}{c}\mathbf{b}\cdot\mathbf{k}\left[1 - \frac{2U}{c^2} - \frac{\|\mathbf{v}\|^2}{2c^2} - \frac{\mathbf{v}\cdot\mathbf{v}_2}{c^2}\right] - \frac{\mathbf{v}\cdot\mathbf{v}_2}{c^2}\left(1 + \frac{\mathbf{k}\cdot\mathbf{v}}{2c}\right)}{1 + \frac{\mathbf{k}\cdot(\mathbf{v}+\mathbf{v}_2)}{c}}$$

with

t_{v_i} : Geocentric Coordinate Time (TCG) of arrival of a radio signal at the i^{th} VLBI telescope
$\mathbf{k}$: Unit vector in the direction of the radio source, in the absence of gravitational or aberrational bending
$\mathbf{v}$: Barycentric velocity of the geocentre
$\mathbf{v}_i$: Geocentric velocity of the i^{th} telescope
U : Gravitational potential
c : Speed of light

With this expression for the vacuum delay, the total delay is found by adding the best estimate of the tropospheric propagation delay (Petit, G. et al., 2010)

$$t_2 - t_1 = t_{v_2} - t_{v_1} + (\delta t_{\text{atm}_2} - \delta t_{\text{atm}_1}) + \delta t_{\text{atm}_1}\frac{\mathbf{k}\cdot(\mathbf{v}_2 - \mathbf{v}_1)}{c}$$

VLBI Error Sources

TROPOSPHERIC EFFECT. The non-dispersive delay caused by the troposphere is about 2.3 m at sea level in zenith direction, and usually divided into "hydrostatic" (or dry) and "wet" components (Petit, G. et al., 2010), with the hydrostatic delay being roughly 90% of the total delay (Petit, G. et al., 2010). The tropospheric delay depends on the length of the path through the atmosphere and it is a function of the zenith angle (z) of the source. The delay is often written as the product of the delay in the direction of the zenith and the so-called mapping function $m_{trp}(z)$ as (Rothacher, M., 2017; Schuh, H. et al., 2013)

$$\delta\rho_{trp}(z) = m_{trp}(z)\delta\rho^0_{trp}$$

with $\delta\rho^0_{trp} = \delta\rho_{trp}(z = 0)$. It is common to apply different mapping functions for the dry and the wet part of the atmosphere (Rothacher, M., 2017; Schuh, H. et al., 2013)

$$\delta\rho_{trp}(z) = m_{trp,d}(z)\delta\rho^0_{trp,d} + m_{trp,w}(z)\delta\rho^0_{trp,w}$$

Mapping functions used nowadays include the underlying continued fraction form to all mapping functions of Herring, T. A. (1992), the Vienna Mapping Functions 1 (VMF1) of Böhm, J. et al. (2006b), and the Vienna Mapping Functions 3 (VMF3) of Landskron, D. et al. (2018). In practice, the estimation of accurate a-priori wet

troposphere delay values is not simple, for precise applications a residual delay must be estimated together with other geodetic parameters. The estimation is done with a parametrisation of the tropospheric delay, where the line-of-sight delay D_L is expressed as (Petit, G. et al., 2010):

$$D_L = m_h(e) \cdot D_{hz} + m_w(e) \cdot D_{wz} + m_g(e) \cdot [G_N \cos(a) + G_E \sin(a)]$$

where D_{hz} is the zenith hydrostatic delay, D_{wz} the zenith wet delay, and G_N, G_E the components of horizontal delay gradient. m_h, m_w and m_g are the hydrostatic, wet, and gradient mapping functions, respectively, e is the elevation angle of the observation, and a is the azimuth angle in which the signal is received (Petit, G. et al., 2010). Horizontal tropospheric gradients can exceed 1 mm and their estimation benefits both, GNSS and VLBI (Bar-Sever, Y. E. et al., 1998; Chen, G. et al., 1997).

IONOSPHERIC EFFECT. Since VLBI signals belong to the part of the spectrum corresponding to microwaves, the ionosphere acts as a dispersive medium and its influence on the propagation of the signal is frequency-dependent. Effects of the ionosphere on radio signals are classically accounted for by forming linear combinations of multi-frequency observables, which typically address first order effects. However, for wide-band VLBI observations, higher order dispersive effects induce errors that reach a couple of ps (Petit, G. et al., 2010). In VLBI the first order ionospheric term can cause delays in zenith direction of about 1-15 m for the S-band, and about 4-60 cm for the X-band (Rothacher, M., 2017).

CLOCK BEHAVIOUR. Each clock associated to a telescope runs independently and can only be approximately synchronised, e.g by using GNSS which yields an accuracy of better than 1 μs. Therefore, a clock correction has to be determined for each station but one (as there has to be a reference clock). This correction is typically given in the form of a piece-wise linear representation plus a second-degree polynomial, whose coefficients are estimated simultaneously with all the other geodetic parameters (Rothacher, M., 2017).

ANTENNA DEFORMATION. Antenna deformations occur as a result of thermal variations which affect the light travel time delay. These deformations are typically known as *thermal deformation* and can amount up to several millimetres and can not be neglected (Nothnagel, A., 2009; Wresnik, J. et al., 2007). Additionally, the size, construction material and environment of the telescope can cause a shift in the reference point of the station. This deformation is known as *gravitational deformation*. The path length variation due to gravitational deformation can reach several millimetres (Artz, T. et al., 2014; Bergstrand, S. et al., 2019; Lösler, M. et al., 2019).

2.1.2 *Global Navigation Satellite Systems*

The Global Navigation Satellite Systems (GNSS) were developed to achieve autonomous and instantaneous determination of the position, velocity and time on and near the surface of the Earth, using space vehicles for the transmission of signals carried by

microwaves. The operational GNSS available nowadays are the Global Positioning System (**G**PS), from the US, the Globalnaya Navigatsionnaya Sputnikovaya Sistema (Global Navigation Satellite System, **G**LONASS) from Russia, the European **G**alileo, the Japanese Quasi-Zenith Satellite System (**QZSS**) and the Chinese BeiDou Navigation System.

The GNSS Architecture

SPACE SEGMENT. Composed of the space vehicles, 30 for GPS and Galileo, 24 for GLONASS, placed on nearly circular ($e \approx 0$) Medium Altitude Orbits (**M**EO) with an altitude of ca. 20200 km for GPS, ca. 19000 km for GLONASS, and 23000 km for Galileo, and a period of revolution of 11 hours 58 minutes for GPS, 11 hours 16 minutes for GLONASS, and 14 hours 22 minutes for Galileo. GPS operates in 6 orbital planes, whereas that GLONASS and Galileo do it in three (GSSC, 2022; Petrovski, I. et al., 2012). Table 2.1 summarises the most relevant parameters.

Parameter	GPS	GLONASS	Galileo
Nominal Number of Satellites	24	24	30
Orbital Planes	6	3	3
Internal Orbit Separation	60°	120°	120°
Inclination of the Orbit	55°	64°8′	56°
Orbital Altitude	20180 m	19140 km	23222 km
Period of Revolution	11h 58m	11h 15m	14h 22m

TABLE 2.1: Comparison between the Space Segments of GPS, GLONASS and Galileo according to (GSSC, 2022; Petrovski, I. et al., 2012)

CONTROL SEGMENT. Composed of monitoring stations, master control station and ground control stations, this segment is in charge of monitoring the system status. The monitoring stations track the constellation permanently to determine orbital and clock parameters for each satellite. These data are collected by the master control station to set the status of the satellites, calculate parameters to the orbits, maintain the time system and predict the orbits and satellite parameters.

USER SEGMENT. The user segment comprises the receivers which decode the GNSS signals. Modern GNSS receivers cover a wide range of technological devices, from cellphones to precise GNSS receivers. Standard GNSS stations are able to track multiple satellites and constellations simultaneously in several frequencies with internal data storage and data download for further analysis.

Signal Structure

In the GPS case, signals are transmitted on three radio frequencies in the Ultra High Frequency (UHF) band, usually called L1, L2 and L5, all of them obtained from the *fundamental frequency*, $f_0 = 10.23$ MHz as follows (Borre, K. et al., 2007): $f_{L1} = 154 \cdot f_0 =$

1575.42 MHz, $f_{L2} = 120 \cdot f_0 = 1227.60$ MHz, and $f_{L5} = 115 \cdot f_0 = 1176.45$ MHz. These signals are composed of three parts: the **C**arrier wave f_{L1}, f_{L2} or f_{L5}, the **N**avigation Data containing information about the satellite produced by the Control Segment, and the codes: the coarse acquisition code (C/A), and the precision code (P). The C/A code is only carried on L1 while the P code is carried on both, L1 and L2 (Borre, K. et al., 2007).

Unlike GPS and Galileo, GLONASS uses Frequency-division multiple access (FDMA) rather than CODE-division multiple access (CDMA) for its legacy signals. Originally, the system transmitted the signals in the bands $L1$, 1602.0–1615.5 MHz, and $L2$, 1246.0–1256.5 MHz, at frequencies spaced by 0.5625 MHz at $L1$ and by 0.4375 MHz at $L2$ (Langley, R. B., 2017). This arrangement provided 25 channels, so that each satellite in the full 24-satellite constellation could be assigned a unique frequency. A third band $L3$ (1202.025 MHz) using CDMA is available since 2008 (GSSC, 2022). The Galileo navigation signals are transmitted in the frequency bands E5 (1191.795 MHz), E5a (1176.450 MHz), E5b (1207.140 MHz), E6 (1278.750 MHz), and E1 (1575.420 MHz) (GSC, 2021).

Principles of Satellite Positioning

The simplified form of *Carrier Phase Observation Equation* is given by:

$$L_r^s = \rho_r^s + c\delta_r - c\delta^s + \lambda(\varphi_r - \varphi^s - N_r^s) + O_r^s + \varepsilon_r^s$$

with

$$\rho_r^s = \sqrt{(X^s - x_r)^2 + (Y^s - y_r)^2 + (Z^s - z_r)^2}$$

L_r^s : Carrier phase range between satellite s and receiver r
ρ_r^s : Geometrical range between satellite s and receiver r
δ^s : Satellite clock correction to GPS time for satellite s
δ_r : Receiver clock correction to GPS time for the receiver r
λ : Wavelength (of the carrier wave)
$\varphi^s(\varphi_r)$: Hardware phase biases in cycles generated by the satellite s (resp. receiver r)
N_r^s : Integer ambiguity between satellite s and receiver r
b_r^s : Ambiguity term between satellite s and receiver r
O_r^s : Errors and Biases term for each satellite s and receiver r
ε_r^s : Observation noise between satellite s and receiver r
(X^s, Y^s, Z^s) : Coordinates of satellite s
(x_r, y_r, z_r) : Coordinates of the receiver r
c : Speed of light

GNSS Biases and Error Sources

The path of the signal from the satellite to the receiver is affected by several phenomena, interfering with the proper acquisition of the signal in the receivers causing a degradation on the accuracy and reliability of the desired coordinates.

ACCURACY OF SATELLITE ORBITS. Satellite ephemeris are estimated by using ground stations and their calculation suffers from truncation and mis-modelling errors which affect the accuracy of the final orbits (Montenbruck, O. et al., 2000; Xu, G., 2008). According to the IGS (2017), the accuracy of the GNSS orbits ranges from ca. 2.5 cm (for final orbits with latency of 18 days), to ca. 1 m (for broadcast ephemeris with latency in real time).

ACCURACY AND STABILITY OF SATELLITE CLOCKS. Satellite clocks are normally atomic clocks with high stability, but drifts on the scale of time have to be considered for precise coordinate determination. Nowadays, the accuracy of satellite clocks ranges from ca. 75 ps (RMS of final products), to 5 ns (RMS of broadcast products) (IGS, 2017).

PHASE CENTRE CORRECTIONS. The electrical antenna phase centre has not the same location as the mechanical one and it is dependent on the frequency. The antenna phase centre is a function of the direction of the incoming signal, and it is different for each antenna. With the corrections, the phase observations are reduced to the antenna reference point (ARP), a fixed physical place on an antenna. The phase centre correction is normally divided into two parts, phase centre variation (PCV) and phase centre offset (PCO), which should be used together (Kallio, U. et al., 2019). This correction ranges from few millimetres to several centimetres, depending on the type of antenna, and cannot be ignored in precise applications.

RECEIVER CLOCKS. Receiver clocks are not as stable as the satellite counterparts, mainly due to the fact that they are built with less expensive materials. This receiver time inaccuracy causes range errors that result in position errors. Using relative processing strategies with differenced observations results in the mitigation or cancellation of this error. Typical values for this type of errors are below one millisecond.

AMBIGUITY RESOLUTION. Theoretically speaking, the ambiguity term should be an integer number of cycles (Teunissen, P., 1998). But in fact this is almost never the case: float numbers can also be obtained during the processing of the data, resulting in coordinates with an inferior quality. Many algorithms have been developed to overcome this issue, but all agree that this term has to be included as an additional unknown in the observation equations used to calculate the position of the station. The Lambda Method of (Teunissen, P., 1998) is one of the classical approaches for fixing of the ambiguities to integer numbers.

CYCLE SLIPS During continuous phase lock, the ambiguity remains constant, allowing for cancellation by subtracting two consecutive measurements. However, a temporary loss of phase lock may cause the ambiguity to change, resulting in the

so-called "cycle slip". Cycle slip detection is typically based on the geometry-free linear combination (Kirkko-Jaakkola, M. et al., 2009). If the cycle slip cannot be corrected, a new ambiguity parameter has to be set up.

MULTIPATH EFFECTS. Signal reflections from objects like buildings, water surfaces or trees cause that the ranges gathered by the receiver appear to be larger than they actually are, leading to a misinterpretation of the real position of the station. Alternatives for its mitigation include the modelling based on the signal-to-noise ratio (SNR) (Bilich, A. et al., 2008) and, more recently, machine learning (Hsu, L.-T., 2017).

TROPOSPHERIC DELAY. The troposphere acts as a non-dispersive medium delaying the GNSS signals passing through independently from the frequency. As for the VLBI case, the delay is separated into the hydrostatic and wet components. The hydrostatic part can be accurately computed a priori based on pressure data using the formula of Saastamoinen, J. (1972). Advanced models, based on numerical weather prediction are also available (Böhm, J. et al., 2006b; Landskron, D. et al., 2018). There is no simple method to estimate an accurate a priori value for the wet tropospheric delay, so for precise applications the residual delay must be estimated with the other geodetic quantities of interest (Petit, G. et al., 2010).

IONOSPHERIC DELAY. As for VLBI, the ionosphere acts as a dispersive medium for GNSS signals which affects the signals depending on their frequency. The total influence of the ionosphere can reach several metres in zenith direction and cannot be neglected. In GNSS the first, second and third order ionospheric terms are significant (Petit, G. et al., 2010), where the first order accounts for more than 99% of the total ionospheric delays, with the second and third order terms causing errors of the order of centimetres (Marques, H. A. et al., 2012). For single-frequency observations, additional models based on the total electron content in the atmosphere have to be considered. For multi-frequency observations, the most efficient way to correct the ionospheric effects is combining observations in k different frequencies, which allows to cancel the ionospheric effects up to order $k-1$ (Petit, G. et al., 2010). For instance, in GPS, first order effects of the ionosphere are classically accounted for by the so-call "*ionosphere-free linear combination*" between L1 and L2 observables.

Data Processing Strategies

RELATIVE POSITIONING. In the *Relative Positioning* technique the vector between two receivers is calculated, so differences of coordinates are determined, instead of absolute coordinates, with the conditions that both devices must record data simultaneously observing nearly the same satellite constellation (Petrovski, I. et al., 2012). The *relative positioning* can be used to define the so called *differencing* strategies: a form of range observation with special features in terms of handling errors. The value of such a baseline solution is the fact that it is able to eliminate some of the errors and biases of GNSS (Petrovski, I. et al., 2012). While this is a well-known method in GNSS processing, we reproduce here the main equations, since we will use them in a different context in Chapter 5.

SINGLE DIFFERENCES. The *Single Difference* observations can be achieved in three different ways:

- Having two receivers observing simultaneously the same satellite, the carrier phase observation equation takes the form

$$\Delta^i_{1,2}(t_k) = (\rho^i_2(t_k) - \rho^i_1(t_k)) + c(\delta_2 - \delta_1) + (O^i_2 - O^i_1) + \lambda(b^i_2 - b^i_1) + (\varepsilon^i_2 - \varepsilon^i_1)$$

- Having one receiver observing simultaneously two different satellites, the carrier phase observation equation takes the form

$$\nabla^{i,j}_1(t_k) = (\rho^j_1(t_k) - \rho^i_1(t_k)) + c(\delta^j - \delta^i) + (O^j_1 - O^i_1) + \lambda(b^j_1 - b^i_1) + (\varepsilon^j_1 - \varepsilon^i_1)$$

- Having one receiver observing one satellite in two different epochs, the carrier phase observation equation takes the form

$$\begin{aligned}\delta^i_1(t_{k+1}) - \delta^i_1(t_k) = \left(\rho^i_1(t_{k+1}) - \rho^i_1(t_k)\right) + c\left(\delta_1(t_{k+1}) - \delta_1(t_k) - \delta^i(t_{k+1}) + \delta^i(t_k)\right) \\ + O^i_1(t_{k+1}) - O^i_1(t_k) + \lambda\left(b^i_1(t_{k+1}) - b^i_1(t_k)\right) + \varepsilon^i_1(t_{k+1}) - \varepsilon^i_1(t_k)\end{aligned}$$

DOUBLE DIFFERENCES. Starting with the definition of single differences between two receivers, simultaneous data recorded in two receivers observing two satellites a and b allow to calculate the so-called *Double Differences*, as follows:

$$\begin{aligned}\nabla\Delta L^{a,b}_{1,2} = \Delta L^b_{1,2} - \Delta L^a_{1,2} \;&=\; \left(\rho^b_2 - \rho^b_1 - \rho^a_2 + \rho^a_1\right) + \lambda\left(b^b_2 - b^b_1 - b^a_2 + b^a_1\right) + \\ &\quad \left(O^b_2 - O^b_1 - O^a_2 + O^a_1\right) + \left(\varepsilon^b_2 - \varepsilon^b_1 - \varepsilon^a_2 + \varepsilon^a_1\right)\end{aligned}$$

In this strategy the atmospheric influence is reduced and the clock influence in the data is eliminated. Besides this, when using double differences, the ambiguity term becomes:

$$\begin{aligned}\lambda\left(b^b_2 - b^b_1 - b^a_2 + b^a_1\right) \;&=\; \lambda\left(\varphi_2 - \varphi^b - N^b_2\right) - \lambda\left(\varphi_1 - \varphi^b - N^b_1\right) \\ &\quad -\lambda\left(\varphi_2 - \varphi^a - N^a_2\right) + \lambda\left(\varphi_1 - \varphi^a - N^a_1\right) = -\lambda\nabla\Delta N^{a,b}_{1,2}\end{aligned}$$

Thus, the ambiguity bias $\nabla\Delta N^{a,b}_{1,2}$ is equal to an integer number of cycles. Double differencing carrier phase ambiguities can relatively easily be fixed to integer numbers, so this strategy is one of the most widely used for processing GNSS data.

Linear Combinations of Frequency Observables

In the case of multi-frequency receivers, the elimination of biases and errors from the code and carrier phase equations is not only possible using differenced observation, but also with the so called *linear combination* by forming differences between measurements on the different carrier frequencies at the same epoch with the same station. The general procedure to obtain a linear combination is:

$$L_{LC} = \sum_{i=1}^{n} m_i \cdot L_i$$

Where m_i are the (arbitrary) coefficients of the linear combination. Following this definition an infinite number of linear combinations can be generated, but only a few of them are useful to eliminate error and bias sources and to determine accurately cycles slips and carrier phase ambiguities. Some of the most used linear combinations in the processing of double differenced observations are the so-called *ionosphere-free*, *geometry-free*, and *Melbourne-Wübbenna* linear combinations.

IONOSPHERE-FREE LINEAR COMBINATION For dual-frequency L1, L2 observations, the *ionosphere-free linear combination* is given by

$$L_3 = \frac{f_{L1}^2}{f_{L1}^2 - f_{L2}^2} L1 - \frac{f_{L2}^2}{f_{L1}^2 - f_{L2}^2} L2$$

which removes the first order ionospheric influence of the L1 and L2 carriers. Nevertheless it has the disadvantages that the ambiguity term does not remain as an integer and it has a three times higher noise than the original L1 or L2 observations.

GEOMETRY-FREE LINEAR COMBINATION The difference

$$L_{\mathrm{GF}} = L_1 - L_2$$

is called the *geometry-free linear combination* used to detect cycle slips. It is independent of the observation geometry and particularly useful together with the double differencing strategy, although it is very sensitive to noise and is strongly affected by the fluctuations in the ionosphere.

MELBOURNE-WÜBBENNA LINEAR COMBINATION The linear combination

$$L_{\mathrm{MW}} = \frac{1}{f_{L1} - f_{L2}} \left(f_{L1} \cdot L1 - f_{L2} \cdot L2 \right) - \frac{1}{f_{L1} + f_{L2}} \left(f_{L1} \cdot P1 + f_{L2} \cdot P2 \right)$$

is known as *Melbourne-Wübbenna*, and combines both, carrier phase ($L1$ and $L2$) and code ($P1$ and $P2$) observables. This combination eliminates the effect of the ionosphere, the geometry, the clocks, and the troposphere (Dach, R. et al., 2015).

2.1.3 *Satellite Laser Ranging*

In the basic principle of Satellite Laser Ranging (Figure 2.2) a short laser pulse is generated at the ground station and sent to a satellite with an optical telescope which has a sensitive light detector at its receiving end. The departing pulse triggers an interval counter. The satellite is equipped with retro-reflectors on its surface that reflect the pulse back to the station. At the ground station, the pulse is detected by a sensitive light-detecting device, which stops the interval counter (Combrinck, L., 2010). Based on the time of emission of the original pulse and the time of arrival of the reflected pulse (light travel time), the geometric distance ρ between the satellite and the telescope can be written as

$$\rho = c \cdot \frac{\Delta t}{2}$$

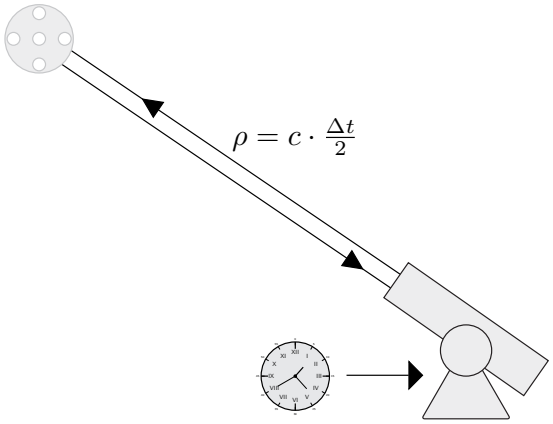

FIGURE 2.2: Simple representation of the Satellite Laser Ranging (SLR) concept.

with Δt the measured light travel time between the station and the satellite in both directions, and c the speed of light. SLR operates in the optical region of the electromagnetic spectrum, so it is less susceptible to biases due to atmospheric refraction. In practice SLR ranges are unaffected by the Earth's ionosphere (Pearlman, M. et al., 2019b). The accurate satellite positions derived from SLR measurements enable the improvement of the gravity field model of the Earth (Bloßfeld, M. et al., 2016), as well as the investigation of other force model effects on satellite orbits. SLR can also be used to estimate EOPs (Moore, T., 1986), and the scale of the measurements allows the determination of the centre of masses of the Earth, as well as the dimensions of the planet and its gravitational constant (Dunn, P., 2003).

Space Segment

The SLR space segment includes satellites equipped with an array of passive, optical corner cubes, capable to compensate for the velocity aberration caused by the moving satellite (Pearlman, M. et al., 2019b). Dedicated SLR satellites are passive spheres, densely covered with corner cubes to present approximately the same high cross section and effective reflection point in all orientations (Paolozzi, A. et al., 2019). Having a passive satellite ensures a long lived target in space, but it has the disadvantage of a return signal strength dependence on the range, limiting most laser ranging systems to satellites at MEO and synchronous altitudes (Pearlman, M. et al., 2019a). Among the older geodetic SLR satellites are Starlette, launched in 1975 by Centre National d'Etudes Spatiales (CNES), and LAGEOS in 1976 by the National Aeronautics and Space Administration (NASA). Recent geodetic satellites include LARES, launched in 2012, and LARES-2, launched in 2022, both by the Italian Space Agency (ASI) (Paolozzi, A. et al., 2019; Pearlman, M. et al., 2019a).

Ground Segment

The typical SLR ground station is composed of (Combrinck, L., 2010):

LASER PULSE GENERATOR, which generates a series of short pulses. Legacy SLR stations use frequency-doubled Neodymium:Yttrium-Aluminium-Granat (Nd:YAG) and

Rubidium (Ruby) lasers, which produced moderate energy (0.4–100 mJ) short duration (35–200 ps) pulses at wavelengths 532–1064 nm, at rates of 10Hz to 2 kHz (Wilkinson, M. et al., 2019).

OPTICAL TELESCOPE, tracking gimbal and control system to point the laser beam at the satellite and collect the signal from the retro-reflectors.

RECEIVING SYSTEM (DETECTOR), sensitive enough to detect the (weak) signal returning from the satellite retro-reflectors.

TIMING EQUIPMENT, which records the times of departure and reception of the laser pulse using an accurate atomic clock. Legacy time interval units had reported a precision of a few ps (Wilkinson, M. et al., 2019). New technologies, such as the New Picosecond Event Timer (NPET), achieve epoch recording with a precision of less than 700 fs (Panek, P. et al., 2010).

METEOROLOGICAL STATION, to record local pressure, temperature, and relative humidity to be input to atmospheric models that provide corrections. Alternatively, observing on two different optical frequencies simultaneously could lead to the estimation of the atmospheric correction (Riepl, S. et al., 2001; Wilkinson, M. et al., 2019).

Preprocessing and Normal Points

Using laser pulse rates of 10 Hz yields 2000 to 3000 range observations for a single satellite pass (Rothacher, M., 2017). This number is larger when considering kHz rates. These highly correlated measurements are compressed in "*normal points*". Using high-precision predictions to generate residuals, fitted residuals are computed and large outliers removed. The fit residuals are subdivided into fixed intervals (bins) with sizes between 5–300 s, depending on the observed satellite. The normal point is then calculated with the use of the mean value of the fit residuals within each bin and its corresponding mean epoch. The report in the normal point data record includes the epoch of the normal point, the normal point range value, the number of observations in each bin, and the RMS of the observations within the bin (ILRS, 2022).

Observation Equation

Based on the general concept, the simplified SLR observation equation reads as:

$$\Delta t_E^S = \frac{2}{c}\left(\rho_E^S + \delta\rho_{\text{atm}} + \delta\rho_{\text{rel}}\right) + \delta\rho_{\text{ecc}}^S + \frac{1}{c}\delta t + \epsilon_E^S$$

with

Δt_E^S : Measured light travel time between the station and the satellite in both directions

ρ_E^S : Geometrical distance between the station and the satellite

$\delta\rho_{\text{atm}}$: Range delay due to the atmosphere refraction

$\delta\rho_{\text{rel}}$: Relativistic range correction
$\delta\rho^S_{\text{ecc}}$: Satellite eccentricities
δt : Signal delay due to the instrumentation
ϵ^S_E : Measurement error
c : Speed of light

The relativistic range correction $\delta\rho_{\text{rel}}$ considers the range delay caused by the gravitational deflection of light in the vicinity of the Earth (Arnold, D. et al., 2019). The satellite eccentricity $\delta\rho^S_{\text{ecc}}$ describes the geometric distance between the centre of mass of the satellite and the reflection point (centre of mass correction, Combrinck, L. (2010)). ϵ^S_E contains satellite- and station-specific systematic errors, in particular orbit offsets, range biases, timing offsets, and calibration issues (Luceri, V. et al., 2019).

Atmospheric Delay Correction

At optical wavelengths the troposphere acts as a dispersive medium (Combrinck, L., 2010). Mendes, V. B. et al. (2004) developed mapping functions for optical wavelengths which improve the modelling of the elevation dependency of the zenith atmospheric delay. Their closed-form expression for the hydrostatic delay is given by:

$$d^z_h = 0.002416579 \cdot \frac{f_h(\lambda)}{f(\varphi, H)} \cdot P_s$$

where d^z_h is the zenith hydrostatic delay in metres and P_s is the surface barometric pressure in hPa. The function $f(\varphi, H)$ is given by the relation

$$f(\varphi, H) = 1 - 0.00266\cos(2\varphi) - 0.00000028 \cdot H$$

where φ is the geodetic latitude of the station and H is the orthometric height of the station in metres. $f_h(\lambda)$ is the dispersion equation for the hydrostatic component:

$$f_h(\lambda) = 10^{-2} \cdot \left[k^*_1 \cdot \frac{k_0 + \sigma^2}{(k_0 - \sigma^2)^2} + k^*_3 \cdot \frac{k_2 + \sigma^2}{(k_2 - \sigma^2)^2}\right] \cdot C_{CO_2}$$

with $k_0 = 238.0185\ \mu m^{-2}$, $k_2 = 57.362\ \mu m^{-2}$, $k^*_1 = 19990.975\ \mu m^{-2}$, and $k^*_3 = 579.55174\ \mu m^{-2}$. σ is the wave number ($\sigma = \lambda - 1$, where λ is the wavelength, in μm), $C_{CO_2} = 1 + 0.534 \times 10^{-6}(x_c - 450)$, and x_c is the carbon dioxide (CO_2) content, in ppm. In the conventional formula, a CO_2 content of 375 ppm should be used, in line with the IAG recommendations, thus $C_{CO_2} = 0.99995995$ should be used (Petit, G. et al., 2010). For the wet component, the relation is given by (Mendes, V. B. et al., 2004)

$$d^z_w = 10^{-4} \times (5.316 \cdot f_w(\lambda) - 3.759 \cdot f_h(\lambda)) \cdot \frac{e_s}{f_s(\varphi, H)}$$

where d^z_w is the zenith wet delay, in metres, and e_s is the surface water vapour pressure, in hPa. $f_w(\lambda)$ is the dispersion formula for the wet component:

$$f_w(\lambda) = 0.003101 \cdot \left(\omega_0 + 3\omega_1\sigma^2 + 5\omega_2\sigma^4 + 7\omega_3\sigma^6\right)$$

where $\omega_0 = 295.235$, $\omega_1 = 2.6422\ \mu m^2$, $\omega_2 = -0.032380\ \mu m^4$, and $\omega_3 = 0.004028\ \mu m^6$.

Relativistic Range Correction

takes into account the range change caused by gravitational bending of the light path (Arnold, D. et al., 2019). When considering only targets in the vicinity of the Earth (e.g. SLR satellites), for an electromagnetic signal is emitted from $\mathbf{x}_1$ at time t_1 and is received at $\mathbf{x}_2$ at time t_2, the time of propagation is given by (Petit, G. et al., 2010)

$$t_2 - t_1 = \frac{\|\mathbf{x}_2(t_2) - \mathbf{x}_1(t_1)\|}{c} + \frac{2GM_E}{c^3} \ln\left(\frac{r_{E_1} + r_{E_2} + \rho}{r_{E_1} + r_{E_2} - \rho}\right)$$

where $r_{E_1} = \|\mathbf{x}_1 - \mathbf{x}_E\|$, $r_{E_2} = \|\mathbf{x}_2 - \mathbf{x}_E\|$, $\rho = \|\mathbf{x}_2 - \mathbf{x}_1\|$, M_E the mass of the Earth, and $\mathbf{x}_E$ the centre of masses of the Earth. Notice that the only body considered in this expression is the Earth, which is a valid simplification of the original model presented in Petit, G. et al. (2010) for near-Earth satellites.

Centre-of-Mass Correction

The geometric distance in the SLR observation equation refers to the distance between the reference point of the telescope reference and the centre of mass of the satellite. However the laser pulses are reflected at the retro-reflectors on the surface of the satellite. The distance needed to compensate for this effect is the so-called "*centre-of-mass (CoM) correction*" (Otsubo, T. et al., 2015). Centre-of-Mass corrections have been determined accurately for spherical geodetic satellites (Neubert, R. et al., 2012; Otsubo, T. et al., 2003; Rodríguez, J. et al., 2019). Neubert, R. et al. (2012) estimate the CoM of spherical satellites as:

$$\begin{aligned} F(x(\phi)) = &\quad \frac{1}{N} \cdot \frac{\eta(\phi)}{R - \dfrac{L \cdot \cos(\phi)}{\sqrt{n^2 - \sin^2(\phi)}}} \\ x(\phi) = &\quad R \cdot \cos(\phi) - L \cdot \sqrt{n^2 - \sin^2(\phi)} \end{aligned}$$

with

$F(x)$: Probability density for the range residual to be inside $(x, x + dx)$ (for an infinitesimal short laser pulse)
x : Distance to the satellite's centre of mass
$\eta(\phi)$: Reflectivity function
ϕ : Angle of incidence
R : radius of the satellite
L : Vertex length of the cube corners
N : Normalising factor
n : Index of refraction

The centre-of-mass correction is given then by:

$$\text{CoM} = \int x \cdot F(x)\, dx$$

Typical values for the CoM are 24.5 cm for LAGEOS satellite and 13.3 cm for the LARES satellite (Neubert, R. et al., 2012).

2.2 GENERALITIES OF REFERENCE SYSTEMS AND FRAMES

International Celestial Reference System

The International Celestial Reference System (ICRS) constitutes the modern basis to describe the motion of the Earth, planetary orbits, and the trajectories of artificial spacecrafts, and the framework for high-accuracy astrometry and geodesy. The ICRF is a quasi-inertial reference system. An inertial reference system implies that the system is either in a state of rest or in a constant linear motion, with respect to another inertial system, and where the Newtonian laws and the dynamic equations of motion are valid, without the need of fictitious forces such as the Coriolis, the centrifugal or the Euler forces (Männel, B., 2016). In fact, the non-rotation property of the ICRS is not a physical characteristic, but it is achieved through mathematical constraints such as the no-net-rotation of the celestial coordinates. The ICRS was adopted by the the International Astronomical Union (IAU) in its 23rd General Assembly in August 1997, following the IAU and the International Union for Geodesy and Geophysics (IUGG) recommendations of 1991 (IAU, 1991). The system complies with the followings characteristics (Arias, E. F. et al., 1995; Arias, E. F. et al., 1990):

- The origin of the ICRS is the barycentre of the solar system and the directions of the axes should be fixed with respect to the quasars (Barycentric Celestial Reference System).
- The ICRS has its principal plane ($\delta = 0$) as close as possible to the mean equator at J2000.0, given through the precession (IAU, 1976) and nutation models Seidelmann, P. K. (1982).
- The origin of the right ascension ($\alpha = 0$, the ascending intersection point between the equatorial and the mean ecliptical planes) in the ICRS should be the dynamical equinox of J2000.0.

International Celestial Reference Frame

The ICRS is materialised by the International Celestial Reference Frame (ICRF) with a pair of equatorial coordinates (declination (δ) and right ascension (α)) of a set of the extra-galactic sources. Since these sources are that far away from the observers, their expected proper motions should be negligibly small, and their positions are known to better than a milliarcsecond (Petit, G. et al., 2010). The latest version of the ICRF is called ICRF3 (Charlot, P. et al., 2020) and it was adopted at the 30th General Assembly of the IAU, and replaced the previous realisation, ICRF2, on January 1st, 2019. The main characteristics of this new frame, taken from Charlot, P. et al. (2020), are described in the following. The ICRF3 is the first multi-frequency celestial reference frame with data acquired by VLBI at the standard geodetic and astrometric radio frequencies

(S/X-band), in addition to higher radio frequencies (K-band and dual-frequency X/Ka-bands). The new frame includes S/X band positions for 4536 sources. Of these, 303 sources, uniformly distributed on the sky, are identified as "defining sources" and are used to define the axes of the frame. Positions at the S/X-band are complemented with positions at the K-band for 824 sources and at the X/Ka-band for 678 sources. In total, ICRF3 comprises 4588 sources, where 600 of these sources have independent positions available at the three frequencies. The coordinates of the sources are given at epoch 2015.0 and must be propagated for observations at other epochs when a higher accuracy is needed, considering the acceleration towards the Galactic centre. The ICRF shows a median positional uncertainty of about 0.1 mas in right ascension and 0.2 mas in declination, with a noise floor of 0.03 mas in the individual source coordinates. A subset of 500 sources is found to have extremely accurate positions, in the range of 0.03–0.06 mas, at the S/X-band (Charlot, P. et al., 2020).

International Terrestrial Reference System

The International Terrestrial Reference System (ITRS) is a spatial reference system co-rotating with the Earth in space. In this system, points on the surface of the Earth have coordinates which have small variations over time, due to, e.g., plate tectonic or tidal deformations. The ITRS is modelled with three orthogonal vectors with a common vertex (origin), forming a right-handed system. The orientation of the ITRS is given by the unit vectors associated to this system, and the length of these vectors is its scale (Petit, G. et al., 2010). The International Earth Rotation and Reference Systems Service (IERS) is in charge of the definition and the realisation of the ITRS. The ITRS is consistent with the resolutions of the IAU and the IUGG (Seitz, M. et al., 2020). According to the IERS, the ITRS is defined as (Petit, G. et al., 2010):

- It is geocentric, its origin being the centre of mass of the whole Earth, including oceans and atmosphere.
- The unit of length is the metre (SI). The scale is consistent with the time coordinate for a geocentric local frame (Temps-coordonnée géocentrique -TCG-), in agreement with IAU and IUGG (1991) resolutions. This is obtained by appropriate relativistic modelling.
- Its orientation was initially given by the Bureau International de l'Heure (BIH) orientation at 1984.0.
- The time evolution of the orientation is ensured by using a no-net-rotation condition with regards to horizontal tectonic motions over the whole Earth.

International Terrestrial Reference Frames

The International Terrestrial Reference Frame (ITRF) is the materialisation of the ITRS. It is defined through the realisation of its origin, orientation and scale, together with their corresponding time evolution. In practice, the ITRF is materialised by a set of fiducial points over the surface of the Earth, with known precise coordinates. To define

the ITRF at a certain epoch, seven parameters (three translations, three rotations, and the scale), together with their time derivatives, are required. The process of selecting these 14 parameters is called "datum definition" (Petit, G. et al., 2010). However, the orientation of the frame cannot be observed by any space geodetic technique, causing that the associated normal equation matrix has a rank deficiency, and it has to be conventionally defined through the use of minimum constrains, so the time evolution of the orientation is defined using a no-net-rotation condition with respect to horizontal tectonic motions over the surface of the Earth (Seitz, M. et al., 2020). In the current realisation of the ITRF, the ITRF2020 (ITRF, 2020), time series of technique-specific solutions for station positions and EOPs are used as input data. These series are provided by the technique centres of the four space geodetic techniques, as well as the local ties at co-location sites, where two or more geodetic techniques are operated. According to ITRF (2020), the ITRF2020 is based on newly reprocessed solutions of the four techniques, featuring:

- The time series of the four techniques were stacked all together, adding local ties and equating station velocities and seasonal signals at co-location sites.
- Annual and semi-annual terms were estimated for stations of the 4 techniques with sufficient time spans.
- Post-Seismic Deformation (PSD) models for stations subject to major earthquakes were determined by fitting GNSS data. The PSD models were then applied to the 3 other technique time series at earthquake co-location sites.

The following list, taken from ITRF, 2020, describes the main steps required for the ITRF2020 combination:

- Apply minimum constraints to the loosely constrained solutions (e.g for the SLR weekly solutions).
- Apply No-Net-Translation and No-Net-Rotation constraints to IVS solutions provided in the form of normal equations.
- Use "*as they are*" the minimal constrained solutions (e.g. GNSS and DORIS weekly solutions).
- Determine PSD parametric models using GNSS data, and then apply them to the remaining techniques at earthquake co-location sites.
- Form per-technique long-term solutions (TRF + EOP), by rigorously stacking the time series, solving for station positions, velocities, EOPs and 7 transformation parameters for each weekly (daily in case of GNSS and session-wise for VLBI) solution with respect to the per-technique cumulative solution. During this iterative stacking process:
  - Annual and semi-annual signals were estimated for stations with sufficient time-spans
  - PSD model corrections were applied to earthquake sites, prior to the construction of the normal equation of the stacking of the time series.

Transformation between ICRS and ITRS

The strategy for the transformation between the inertial and the terrestrial reference frame is the IAU recommended Celestial Intermediate-based transformation approach. This transformation at the time t of observation can be written as (Petit, G. et al., 2010)

$$\mathbf{x}_i(t) = \mathbf{R}_3(-E) \cdot \mathbf{R}_2(-d) \cdot \mathbf{R}_3(E) \cdot \mathbf{R}_3(s) \cdot \mathbf{R}_3(-\mathrm{ERA}) \cdot \mathbf{R}_3(-s') \cdot \mathbf{R}_2(x_{\mathrm{pol}}) \cdot \mathbf{R}_1(y_{\mathrm{pol}}) \cdot \mathbf{x}_e(t)$$

where the parameter t is the terrestrial time from the 1st of January, 2000, at 12 h. This definition is consistent with the IAU 1994 Resolution (IAU, 1994).

The transformation matrix for polar motion, i.e. relating the ITRS and the Terrestrial Intermediate Reference System (TIRS), is given by the terms $\mathbf{R}_3(-s') \cdot \mathbf{R}_2(x_{\mathrm{pol}}) \cdot \mathbf{R}_1(y_{\mathrm{pol}})$ and uses x_{pol} and y_{pol}, the coordinates of the Celestial Intermediate Pole (CIP) in the ITRS at epoch t, and s' named "terrestrial intermediate origin (TIO) locator", which provides the position of the TIO on the equator of the CIP corresponding to the kinematical definition of the "non-rotating" origin (NRO) in the ITRS when the CIP is moving with respect to the ITRS due to polar motion. A good approximation of s' is given by $s = -47\mu as \cdot t$. The use of this quantity was neglected in the classical form, and it is necessary to provide an exact realization of the "instantaneous prime meridian" (TIO meridian) (Petit, G. et al., 2010).

The Celestial Intermediate Origin (CIO) based transformation matrix ($\mathbf{R}_3(-\mathrm{ERA})$) arising from the rotation of the Earth around the axis of the CIP, i.e. relating the TIRS and Celestial Intermediate Reference System (CIRS), uses the Earth Rotation Angle (ERA) between the CIO and the TIO at date t on the equator of the CIP. This provides a rigorous definition of the sidereal rotation of the Earth (Petit, G. et al., 2010).

The CIO based transformation matrix arising from the motion of the CIP in the ICRS $\mathbf{R}_3(-E) \cdot \mathbf{R}_2(-d) \cdot \mathbf{R}_3(E) \cdot \mathbf{R}_3(s)$, uses E and d such that the coordinates of the CIP in the GCRS are:

$$X = \sin d \cos E, \quad Y = \sin d \sin E, \quad Z = \cos d$$

and s the "CIO locator", which provides the position of the CIO on the equator of the CIP corresponding to the kinematical definition of the NRO in the GCRS when the CIP is moving with respect to the GCRS, between the reference epoch and the date t due to precession and nutation (Petit, G. et al., 2010).

An additional classical representation of the transformation between the ITRS into the ICRS, implemented in several software packages such as the Bernese GNSS Software (Dach, R. et al., 2015), is the so-called "equinox-based" approach, which can be written as (Petit, G. et al., 2010; Seitz, M., 2009):

$$\mathbf{x}_i(t) = \mathbf{P}(t) \cdot \mathbf{N}(t) \cdot \mathbf{R}_3(-\Theta) \cdot \mathbf{R}_2(x_{\mathrm{pol}}) \cdot \mathbf{R}_1(y_{\mathrm{pol}}) \cdot \mathbf{x}_e(t)$$

with

t : Epoch of the observation in Terrestrial Time (TT)
$\mathbf{x}_e(t)$: Vector in ITRS at epoch t
$\mathbf{x}_i(t)$: Vector in ICRS at epoch t
$\mathbf{P}(t)$: Precession matrix at epoch t
$\mathbf{N}(t)$: Nutation matrix at epoch t
$\mathbf{R}_i(\alpha)$: Rotation matrix with angle α with respect to axis i
Θ : true sidereal time from Greenwich to epoch t
x_{pol}, y_{pol} : Coordinates of the Celestial Intermediate Pole (CIP) in the ITRS at epoch t

These two representatins can be converted into each other.

No-Net-Translation Condition

A network of station coordinates satisfies the *no-net-translation* (NNT) condition if the weighted sum of the positions, respectively velocities, of the stations relative to a given a-priori reference frame is zero (Seitz, M., 2009). The NNT condition causes that the network experiences neither a shift in the coordinate origin nor a translation in relation to the set of a-priori coordinates. Since the translation of a network can also be viewed as a linear movement of its centre of masses $\Delta\vec{r}_M$, the sum of all corrections of the station position vectors $\Delta\vec{r}_i$ of stations $i = 1, \ldots, n$ must be zero. If additional weights μ_i satisfying $\mu_i > 0$ and $\sum_i^n \mu_i = 1$ are introduced for the station vectors, the NNT condition can be written as (Angermann, D. et al., 2004)

$$\Delta\vec{r}_M = \sum_{i=1}^{n} \mu_i \Delta\vec{r}_i = 0$$

A second condition defines the temporal change of the origin and causes the conservation of speed of the centre of gravity

$$\Delta\vec{v}_M = \sum_{i=1}^{n} \mu_i \Delta\vec{v}_i = 0$$

If the weights μ_i are taken as relative masses, the physical analogue of these equations is the conservation of linear momentum (Angermann, D. et al., 2004; Seitz, M., 2009).

No-Net-Rotation Condition

A network of station coordinates satisfies the *no-net-rotation* (NNR) condition if it does not experience any change in orientation compared to a set of a-priori positions (Altamimi, Z. et al., 2003). For the station position vectors at the reference epoch, this means that the corrections of the station position $\Delta\vec{r}_i$ do not cause the network to rotate. This is (Angermann, D. et al., 2004)

$$\Delta\vec{p} = \sum_{i=1}^{n} \mu_i \vec{r}_i^{\,0} \times \Delta\vec{r}_i = 0$$

If the weights μ_i are taken as relative masses, the physical analogue of these equations is the conservation of angular momentum (Angermann, D. et al., 2004).

2.3 GENERALITIES OF THE COMBINATION OF SPACE GEODETIC TECHNIQUES

Each space geodetic technique has different degrees of sensitivity to different geodetic parameters. Figure 2.3 shows some of the most relevant geodetic parameters which can be the subject of combination. Each individual technique is not capable by itself of estimating the full set of parameters. However, a geodetic parameter type that is common to more than one technique acts as a connection between the techniques. These facts motivate the combination of space geodetic techniques, where the goal is exploiting the positive features of each technique, e.g. the dense network with continuous observation and good geometry of GNSS, the full EOP set of VLBI, and the absolute accuracy, the geocentre estimation, and (possibly) the gravity field from SLR. Moreover,

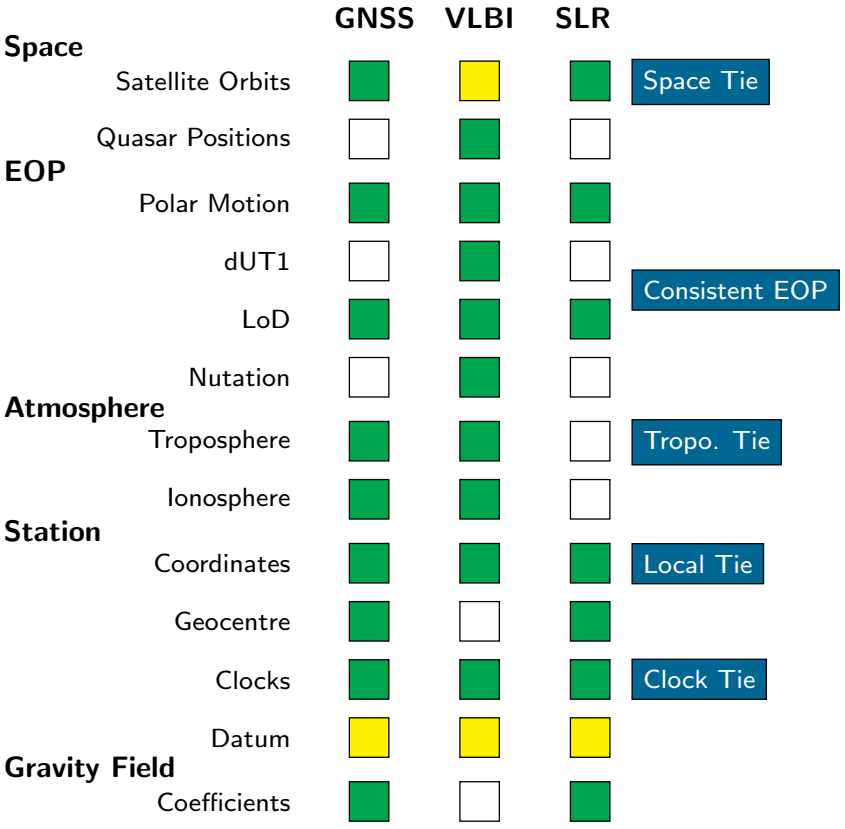

FIGURE 2.3: Geodetic parameters estimated by each space geodetic technique. Green colour indicates that the parameter is fully estimated by the technique, while yellow colour means that the estimation is conditional.

the increased number of observations of the combination is expected to improve the precision of the estimation by reducing the formal errors of the parameters (Seitz, M., 2015). The combination of space geodetic techniques can be performed on three different levels of the least squares adjustment (LSA): at the observation level, at the normal equation level, and at the parameter level. These different approaches can be realised using the linear Gauß-Markov model (Koch, K.-R., 1999).

Gauß-Markov Model

For most geodetic problems the observations are expressed as a function of the unknown parameters, using the so-called Gauß-Markov model. The deterministic part of the Gauß-Markov model is the linearised observation equation (Koch, K.-R., 1999)

$$\mathbf{A}\mathbf{x} = \mathbf{b}$$

with

$$\begin{aligned}\mathbf{b} &: n \times 1 \text{ vector of observations}\\ \mathbf{A} &: n \times u \text{ design matrix}\\ \mathbf{x} &: u \times 1 \text{ vector of unknowns}\end{aligned}$$

For $n > u$ this equation system is not consistent. We obtain a consistent observation system adding the vector of observation errors $\mathbf{v}$ (Koch, K.-R., 1999). Then, the system takes the form

$$\mathbf{A}\mathbf{x} = \mathbf{b} + \mathbf{v}$$

The corresponding variance-covariance matrix of the observations is given by (Koch, K.-R., 1999)

$$\mathbf{C} = \sigma_0^2 \cdot \mathbf{P}^{-1}$$

with σ_0^2 the a-priori variance factor and $\mathbf{P}$ the positive definite weight matrix of observations. The LSA solution for this system is obtained by minimising the squared sum of the residuals (Koch, K.-R., 1999)

$$\sum_{i=1}^{n} \hat{v}_i^2 \rightarrow \min$$

The solution to this system is given by

$$\mathbf{x} = \left(\mathbf{A}^{\mathrm{T}} \cdot \mathbf{P} \cdot \mathbf{A}\right)^{-1} \cdot \mathbf{A}^{\mathrm{T}} \cdot \mathbf{P} \cdot \mathbf{b}$$

With the normal equation matrix

$$\mathbf{N} = \mathbf{A}^{\mathrm{T}} \cdot \mathbf{P} \cdot \mathbf{A}$$

and the right hand side term

$$\mathbf{y} = \mathbf{A}^{\mathrm{T}} \cdot \mathbf{P} \cdot \mathbf{b}$$

So that the system can be written as

$$\mathbf{N} \cdot \hat{\mathbf{x}} = \mathbf{y}$$

To solve this normal equation system, $\mathbf{N}$ needs to be full rank. As mentioned in Section 2.2, this is not the case for the ITRS realisation, where the no-net-rotation condition has to be included to solve for the orientation of the system (Petit, G. et al., 2010). To regularise the normal equation matrix additional pseudo-observations have to be included, so the system becomes (Seitz, M., 2015)

$$\hat{\mathbf{x}} = (\mathbf{N} + \mathbf{D})^{-1}(\mathbf{y} + \mathbf{d})$$

with $\mathbf{D}$ the normal equation system of the pseudo-observations and $\mathbf{d}$ the associated right-hand side vector. The stochastic part of the solution is given by the a-posteriori variance $\hat{\sigma}^2$ as

$$\hat{\sigma}^2 = \frac{\hat{v}^{\mathrm{T}} \cdot \mathbf{P} \cdot v}{n - u}$$

and the corresponding variance-covariance of the estimates (Seitz, M., 2015)

$$\hat{\mathbf{C}}_{\hat{\mathbf{x}}\hat{\mathbf{x}}} = \hat{\sigma}^2 \cdot \left(\mathbf{A}^{\mathrm{T}} \cdot \mathbf{P} \cdot \mathbf{A} \right)^{-1}$$

Combination at the Observation Level

This level of combination is the most rigorous approach. The observations of all the different techniques are jointly processed using the same a-priori models and parametrisation. In this type of combination, pre-processing steps, such as the outlier detection, consider all observation types, which in turn produces a more robust solution (Seitz, M., 2015). The combination at the observation level is formally built as follows: The observation equation system for the technique k, in a combination involving m different techniques, is given by (Seitz, M., 2015)

$$\begin{aligned} \mathbf{A}_k \mathbf{x}_k &= \mathbf{b}_k + \mathbf{v}_k \\ \mathbf{C}_k &= \sigma_0^2 \cdot \mathbf{P}_k^{-1} \end{aligned}$$

with $k = 1, \ldots, m$. Assuming that the different equations contain the same parameters, the same a-priori modelling, and constraints have been considered, each single observation equation can be stacked into the system (Seitz, M., 2015)

$$\begin{bmatrix} \mathbf{A}_1 \\ \mathbf{A}_2 \\ \vdots \\ \mathbf{A}_m \end{bmatrix} \mathbf{x} = \begin{bmatrix} \mathbf{b}_1 \\ \mathbf{b}_2 \\ \vdots \\ \mathbf{b}_m \end{bmatrix} + \begin{bmatrix} \mathbf{v}_1 \\ \mathbf{v}_2 \\ \vdots \\ \mathbf{v}_m \end{bmatrix}$$

with the corresponding stochastic model (Seitz, M., 2015)

$$\mathbf{C} = \sigma_0^2 \begin{bmatrix} \mathbf{P_1}^{-1} & \mathbf{0} & \mathbf{0} \\ \mathbf{0} & \ddots & \mathbf{0} \\ \mathbf{0} & \mathbf{0} & \mathbf{P_m}^{-1} \end{bmatrix}$$

Combination at the Normal Equation Level

This level of combination is an approximation of the combination on observation level, provided that the observation equations are generated using the same a-priori modelling and parametrisation, and that the constraints are applied after the combination of normal equations. The combination on the normal equation level is equivalent to the combination on the observation level, if all common parameters are consistently stacked and the same modelling and parametrisation is used. However, the

pre-processing steps do not consider all observations types simultaneously, so an influence of the outliers is expected in the final solution (Seitz, M., 2015). Formally speaking, the normal equation system for the technique k, in a combination involving m different techniques, is given by (Seitz, M., 2015)

$$\mathbf{N_k} \cdot \hat{\mathbf{x}}_\mathbf{k} = \mathbf{y_k}$$

The normal equations are combined by adding those elements that are related to the same parameters, expanding the size of the parameter space in each normal equation when required.
The combined normal equation system is given by (Seitz, M., 2015)

$$\mathbf{N} = \frac{1}{\sigma_{0_1}^2}\mathbf{N}_1 + \ldots + \frac{1}{\sigma_{0_m}^2}\mathbf{N}_m, \quad \text{with } [\mathbf{N}]_{u\times u}$$
$$\mathbf{y} = \frac{1}{\sigma_{0_1}^2}\mathbf{y}_1 + \ldots + \frac{1}{\sigma_{0_m}^2}\mathbf{y}_m, \quad \text{with } [\mathbf{y}]_{u\times 1}$$

with the condition for the minimisation of the squared sum of the residuals given by (Seitz, M., 2015)

$$\mathbf{b}^\mathrm{T}\mathbf{P}\mathbf{b} = \frac{1}{\sigma_{0_1}^2}\mathbf{b}_1^\mathrm{T}\mathbf{P}_1\mathbf{b}_1 + \ldots + \frac{1}{\sigma_{0_m}^2}\mathbf{b}_m^\mathrm{T}\mathbf{P}_m\mathbf{b}_m$$

Combination at the Parameter Level

In this level of combination, each technique-specific observation equation system has to be solved in advance, using the Gauß-Markov LSA process (Seitz, M., 2015)

$$\mathbf{I}\mathbf{x}_k = \hat{\mathbf{x}} + \mathbf{v}_k$$
$$\hat{\mathbf{C}}_{\hat{\mathbf{x}}_k\hat{\mathbf{x}}_k} = \hat{\sigma}^2 \cdot (\mathbf{N}_k \cdot \mathbf{D}_k)^{-1} = \hat{\sigma}^2 \cdot \mathbf{P}_k^{-1}$$

Then, the estimated parameters are combined in a second LSA considering the full variance-covariance of each adjustment

$$\mathbf{I}\begin{bmatrix}\mathbf{x}_1\\ \mathbf{x}_2\\ \vdots\\ \mathbf{x}_m\end{bmatrix} = \begin{bmatrix}\hat{\mathbf{x}}_1\\ \hat{\mathbf{x}}_2\\ \vdots\\ \hat{\mathbf{x}}_m\end{bmatrix} + \begin{bmatrix}\mathbf{v}_1\\ \mathbf{v}_2\\ \vdots\\ \mathbf{v}_m\end{bmatrix}$$

and the corresponding stochastic model (Seitz, M., 2015)

$$\hat{\mathbf{C}}_{\hat{\mathbf{x}}_k\hat{\mathbf{x}}_k} = \sigma_0^2 \begin{bmatrix}\mathbf{P_1}^{-1} & \mathbf{0} & \mathbf{0}\\ \mathbf{0} & \ddots & \mathbf{0}\\ \mathbf{0} & \mathbf{0} & \mathbf{P_m}^{-1}\end{bmatrix}$$

This approach is the weakest form of combination. This type of combination usually requires additional transformation parameters among the input solutions (to guarantee that the datum definition is done correctly), and usually requires the help of pseudo-observations to compensate for possible rank deficiencies in the combination (Seitz, M., 2015).

Local, Tropospheric and Clock Ties

A co-location site is composed by two or more instruments from one or more space geodetic techniques, separated by a relatively small distance and that have been operating simultaneously during one or more time intervals (Glaser, S. et al., 2019; Ray, J. et al., 2005). Fundamental stations are examples of co-location sites where all four space geodetic techniques are available. Typically, the observations of the different techniques do not refer to a common reference point. To enable the combination of the observations of each technique, either a geometric or a physical relationship among the instruments has to be established. These so-called "ties" can be of the three following types:

LOCAL/TERRESTRIAL TIES. Local ties are the three-dimensional geometric relationship between two instruments obtained with classical surveying techniques. Direction angles, distances, and spirit-levelling measurements are performed between the reference point of the instruments (Ray, J. et al., 2005), which result in station coordinates and their full variance-covariance information. Local ties constitute a central element for the combination of space geodetic techniques, and their precision is one of the major limitations for the realisation of global terrestrial reference frames (Glaser, S. et al., 2018). Considering the GGOS requirements for a reference frame (positions better than 1 mm and velocities better than 0.1 mm/yr (Rothacher, M. et al., 2009), local ties should have a better accuracy. For a local tie to be precise at the 1 mm level, the extension of a co-location site should not exceed 1 km Petit, G. et al., 2010. In practice, local ties are used as additional pseudo-observations in the normal equation system (Altamimi, Z. et al., 2002), and introduced as a baseline differences constrained with their proper formal errors (variance), which is typically based on the deviations of the three components of each tie vector (Petit, G. et al., 2010).

TROPOSPHERIC TIES. For the microwave-based space geodetic techniques, GNSS, VLBI, and DORIS, the influence of the troposphere in the measurements is the same. Then, highly accurate troposphere estimates can be use to relate the stations at co-location sites. A tropospheric tie, i.e. the difference in the tropospheric delay between the reference points of two instruments, can be determined as common parameters. However, differences in troposphere delays among different instruments is expected due to the different reference point location, especially due to the height differences (Heinkelmann, R. et al., 2016; Teke, K. et al., 2011). When the a-priori values of the delays are based on global numerical weather prediction models, such as the European Centre for Medium-Range Weather Forecasts (ECMWF, 2022), the difference between the delays at two stations caused by the height difference is modelled in advance (Wang, J. et al., 2022), and only the delays caused by the residual troposphere should be considered. For instruments separated by short distances, it is expected that the local troposphere behaves in a similar way (Beutler, G. et al., 1987b). Therefore, the delay associated to the relative troposphere, after considering the height difference, is the same.

CLOCK TIES. A timing system based on a physical common clock for all instruments turns time into an additional tie for the detection and identification of intra-technique and inter-technique biases and calibration errors at the station. When a common clock is established between the various measurement systems, the challenge is that all the variable delays have to be completely removed. In the concept of clock ties, clock corrections are set as common parameters in the processing at the observation level, with an expected improvement for the station coordinates and troposphere parameters of the co-located stations. Moreover, the quality of the clock time can be compared with the clock corrections derived and their discrepancies give important clues about remaining un-modelled effects and delays. An example of the realisation of a clock tie is actively compensated two-way optical time and frequency distribution system (TWOTT) (Kodet, J. et al., 2016). This system was installed between the hydrogen maser clocks connected to the VLBI telescopes RTW and TWIN1 at the Wettzell Observatory in Germany (Kodet, J. et al., 2018). The use of this virtual common clock enables the time transfer between the two instrument with a level of accuracy better than 1 ps (Kodet, J. et al., 2014). In the VLBI case, the use of clock ties could be potentially extended to the signal domain, where the time transfer could lead to an improvement in the correlation process and therefore in the quality of the VLBI observables.

3

EXPERIMENTS ON SHORT GNSS BASELINES

Originally published as: ***I. D. Herrera-Pinzón*** *et al. (Sept. 2018a). "Assessment of Local GNSS Baselines at Co-Location Sites". In:* Journal of Geodesy *92.9, pp. 1079–1095.* ISSN: *0949-7714.* DOI: *https://doi.org/10.1007/s00190-017-1108-9*

Paper I

Assessment of Local GNSS Baselines at Co-Location Sites

Iván Herrera-Pinzón and Markus Rothacher
Institute for Geodesy and Photogrammetry
Swiss Federal Institute of Technology in Zurich (ETHZ)

(Author's version. It differs from the published paper only in terms of layout and formatting)

Abstract

As one of the major contributors to the realisation of the International Terrestrial Reference System (ITRS), the Global Navigation Satellite Systems (GNSS) are prone to suffer from irregularities and discontinuities in time series. While often associated with hardware/software changes and the influence of the local environment, these discrepancies constitute a major threat for ITRS realisations. Co-located GNSS at fundamental sites, with two or more available instruments, provide the opportunity to mitigate their influence while improving the accuracy of estimated positions by examining data breaks, local biases, deformations, time-dependent variations and the comparison of GNSS baselines with existing local tie measurements. With the use of co-located GNSS data from a subset sites of the International GNSS Service (IGS) network, this paper discusses a global multi-year analysis with the aim of delivering homogeneous time series of coordinates to analyse system-specific error sources in the local baselines. Results based on the comparison of different GNSS-based solutions with the local survey ties show discrepancies of up to 10 mm despite GNSS coordinate repeatabilities at the sub-mm level. The discrepancies are especially large for the solutions using the ionosphere-free linear combination and estimating tropospheric zenith delays, thus corresponding to the processing strategy used for global solutions. Snow on the antennas causes further problems and seasonal variations of the station coordinates. These demonstrate the need for a permanent high-quality monitoring of the effects present in the short GNSS baselines at fundamental sites.

3.1 INTRODUCTION

The ITRS constitutes the metrological basis for monitoring the Earth system, therefore, the requirements of the Global Geodetic Observing System (GGOS) to reach a reference frame accuracy and stability of 1 mm and 0.1 mm/year, respectively, have to be met (Plag, H.-P. et al., 2009; Rothacher, M. et al., 2009). These requirements demand a comprehensive analysis of technique-specific systematic biases in local measurements, as a pre-requisite for the improvement of ties among the different space geodetic techniques: Global Navigation Satellite System (GNSS), Satellite Laser Ranging (SLR), Very Long Baseline Interferometry (VLBI), and Doppler Orbitography and Radiopositioning Integrated by Satellite (DORIS). For the appropriate combination of space geodetic techniques, terrestrial measurements connecting the reference points of the different techniques are required. Therefore, the quality of the ITRS realisation, the International Terrestrial Reference Frame (ITRF), relies on the accuracy with which these ties between the individual space geodetic techniques are measured at fundamental sites, where the four space geodesy techniques are co-located so that the links among each other can be determined with sub-millimetre accuracy. However, discontinuities and jumps in the time series of coordinates originating from the different space geodetic techniques, associated to hardware changes and environmental effects such as atmospheric conditions and local obstructions, are one of the main threats and error sources for the establishment of the ITRF (Figure 3.1). Table 3.1 shows a sample of such events, responsible for jumps and changes in the behaviour of the time series on three ITRF sites. Thus, intra-technique co-location, where two or more co-located instruments of the same technique are available, constitutes an essential step for analysing individual biases and will result in a better understanding of system-specific error sources in the local baselines at the sites. In particular, for the analysis of biases in GNSS-based

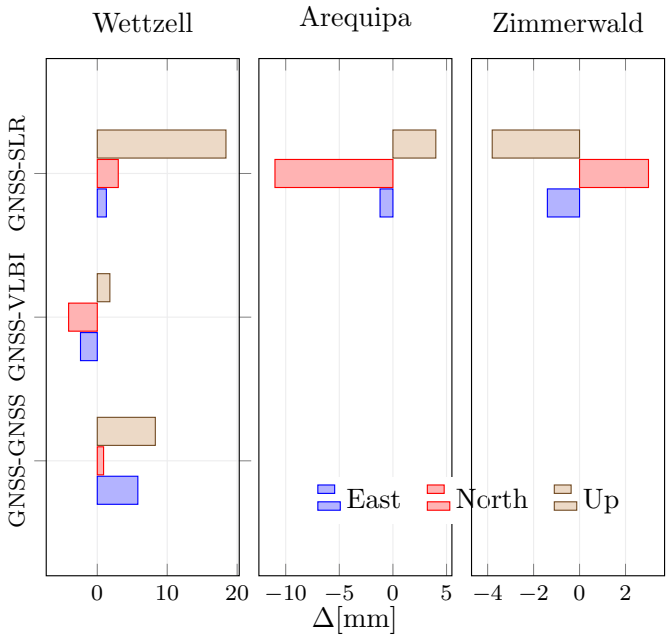

FIGURE 3.1: Selected local ties on the ITRF2014 solution. Frequency-dependent biases, hardware and software changes and GNSS-specific environmental effects, are the cause of discrepancies in the local ties with respect to GNSS-based solutions.

Site	Year	doy	Event
AREQ	1994	088	Antenna change
	1994	160	EQ M8.2, La Paz, Bolivia
	1996	317	EQ M7.7, near coast of central Peru
	1901	174	EQ M8.4, near coast of southern Peru
	2001	188	EQ M7.6, near coast of southern Peru
	2007	227	EQ M8.0, near coast of central Peru
	2014	091	EQ M8.2, 94km NW of Iquique, Chile
IRKM	2011	070	EQ M9.0, near coast of central Japan
YAR2	1997	232	Antenna change
	2002	136	Antenna change
	2012	102	EQ M8.6, west coast northern Sumatra
	2013	171	Antenna change

TABLE 3.1: List of station discontinuities for stations AREQ (Arequipa, Peru), IRKM (Irkutsk, Russia) and YAR2 (Yarragadee, Australia) in the ITRF2014 solution. EQ marks the occurrence of an earthquake with its corresponding magnitude.

solutions, multi-year time series of coordinates at sites of the IGS network (Dow, J. et al., 2009), with two or more co-located receivers, are analysed using short baseline processing methods to determine the adequacy of the local ties. Typically equipped with an array of several GNSS receivers collecting data continuously for several years, the close distance among antennas grants similar tropospheric delays, identical ionospheric conditions, same loading effects and nearly identical station motion due to plate tectonics. For some of these sites, the local baselines are well-known from terrestrial surveys, the relative atmospheric delays can be modelled, and changes in the setup of the antenna array can be monitored and removed. Therefore, the overarching approach of this work includes the following steps: first, the assessment of GPS-specific systematic effects on the positioning, second, the determination of environmental effects at co-location sites, and finally, the mitigation of these effects to achieve a reduction of discontinuities and jumps while connecting the local sites. With an approach based on single-frequency L1 and L2 solutions, and the ionosphere-free linear combination with and without troposphere estimation, the focus lays on the quantification of errors due to hardware and software changes, antenna patterns, environmental effects, local deformations, temperature effects, tilting and other time-dependent variations of the local baselines. The ability to detect these phenomena through this approach is expected to contribute to the improvement of the terrestrial reference frame.

3.2 RELATED WORK

With their work on the local monitoring of fundamental GPS sites, Rothacher, M. et al., 2004 introduced the analysis of GNSS local ties, with the discussion of elements for

an adequate parametrisation and a summary of recommended processing strategies. The developed concept is based on two fundamental aspects: the monitoring of the local environment to detect anomalies in the time series of coordinates, the so-called *f*ootprint network, and the assessment of the performance of the hardware in relation to equipment changes, or *a*ntenna array monitoring. To provide an empirical proof of the scope of the latter, about four years of GPS data collected at five stations at the geodetic observatory in Wettzell (Germany) were used. Different processing strategies, including single frequency L1 and L2 solutions and an ionosphere-free solution with troposphere estimation, this study attained repeatabilities better than 1 mm in all components, granting high-quality monitoring of the performance of the equipment, and concluding with the recommendation of setting up antenna arrays at each ITRF fundamental site.

The topic of GNSS-specific local effects on short baselines has also been discussed by Steigenberger, P. et al., 2013 with the provision of time series of coordinates for the antenna array at the geodetic observatory in Wettzell (Germany). Motivated by the high discrepancies between local ties and the space geodetic techniques in the realisation of the ITRF2008, their work discusses the performance of GPS-based solutions in relation to terrestrial measurements and the impact of individual receiver antenna calibration. This study found out that discrepancies are mainly caused by GPS and not by the local tie measurements. The authors conclude that near-field effects such as multipath and deficiencies in the antenna calibration are the most probable sources for these frequency-dependent systematic effects. By fixing the local ties, the second part of this work shows the estimation of residual maps for the appropriate calibration of antennas. Residual maps are later used for differential corrections, with marginal improvements in the coordinate repeatabilities of the stations, though suggesting their direct implementation in the ITRF solution.

Brockmann, E. et al., 2010 present a study on the benefits of co-located GNSS stations in the Swiss permanent Network. Their work proposes a strategy including L1 and ionosphere-free based solutions, with and without the calculation of troposphere estimates, and the comparison with the terrestrial local ties. With this analysis, they found an agreement on the level of 1-3 mm for the L1-based solutions for all components with the surveyed measurements. However, the ionosphere-free based solutions with troposphere estimates displayed discrepancies on the height component of up to 5 cm. They also conclude that this behaviour depends on the type of antenna due to the high sensitivity of certain antennas with respect to the near-field. A short remark at the end of their work states that the effect of the snow on the antenna has an influence of up to a decimetre on the estimation of the height.

In his study on the relative stability of the two GPS stations at the Yebes Observatory (Spain), Santamaría-Gómez, A., 2013 shows variations in the baseline length up to 1 mm, with uncertainties related to signal-dependent errors resulting from multipath, antenna calibration and antenna phase centre migration due to electromagnetic coupling with the station monument. Moreover, the thermal expansion of the buildings at the site is modelled looking for an agreement with the horizontal displacement.

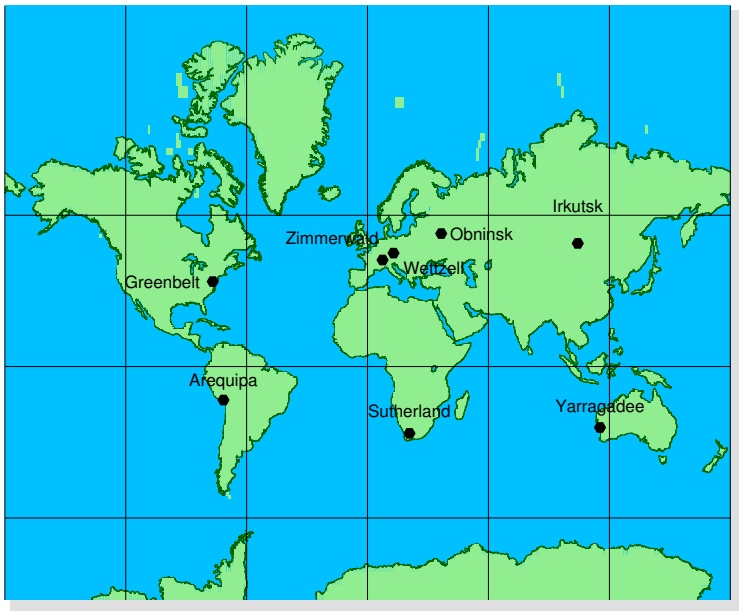

FIGURE 3.2: Global distribution of the selected subset of IGS sites (black polygons), contributing to the ITRF2014 solution, with ≥ 2 co-located GNSS instruments, which will be used in this analysis.

Although variations in the baseline length and the time series of temperature at the site display high correlation, the implemented model fails to explain the observed amplitude. With a similar approach, the results displayed by Wilkinson, M. et al., 2013 on the stability of the baseline between two GPS receivers at the space geodesy facility in Herstmonceux (UK), show repeatabilities worse than 1 mm, demonstrating the challenges to realise an ITRF which fulfils the GGOS requirements mentioned in Plag, H.-P. et al., 2009.

3.3 AVAILABLE DATASET

According to the IGS station list (IGS, 2017) approximately 50 IGS sites are currently or have been equipped with two or more GNSS receivers. For the scope of this paper, a subset of eight sites has been selected, where the potential candidate sites are chosen based on the number of co-located stations (more than two) and the span of their time series (more than two years of continuous data). Figure 3.2 shows the global distribution of the IGS sites with ≥ 2 co-located GNSS instruments used along this study (IGS, 2017). These sites exhibit multiple differences in their environmental conditions such as station motion (tectonics), troposphere and ionosphere conditions. Moreover, some of these sites have time series of observations spanning up to 15 years, where multiple discontinuities associated to hardware and software changes are presented. Table 3.2 summarises the station names and IGS identifiers of the co-located points used, together with their approximate height and the length of the baselines with respect to the corresponding reference station at each sub-network. All relevant GNSS observations have been collected from the IGS official ftp servers (Dow, J. et al., 2009; IGS, 2017), in daily files with a 30 s sampling. While most of the used observations

Site	Station	h[m]	Bsln. Length [m]
Arequipa	AREG	2489.301	15.455
	AREQ⋆	2488.881	–
	AREV⋆	2488.881	0.000
Greenbelt	**GODE**⋆	14.498	–
	GODN	17.864	65.168
	GODS	19.088	141.018
	GODZ⋆	14.498	0.000
Irkutsk	IRKJ	502.040	4.006
	IRKM⋆	502.346	–
	IRKT⋆	502.346	0.000
Obninsk	MOBJ⋆	182.638	12.038
	MOBK⋆	182.638	12.038
	MOBN	182.664	–
Sutherland	SUTH⋆	1799.760	142.142
	SUTM	1797.611	–
	SUTV⋆	1799.760	0.000
Wettzell	WTCO	665.753	61.265
	WTZA	665.914	3.063
	WTZJ	665.927	1.709
	WTZR	666.023	–
	WTZT	665.936	4.087
	WTZZ	665.891	1.598
Yarragadee	**YAR2**	241.276	–
	YAR3	242.432	18.249
	YARR	241.350	3.885
Zimmerwald	ZIM2	956.431	18.768
	ZIMJ	954.286	14.213
	ZIMM	956.332	–
	ZIMZ	953.908	11.570

TABLE 3.2: Summary of co-located stations at the IGS sites. The asterisk (⋆) indicates that the station shares antenna through a signal *splitter*. Names in **bold** indicate the reference station at each small network. WTCO is not part of the IGS network, but a multi-technique ground target for inter-technique co-location purposes located at the Wettzell observatory

come from a single-receiver single-antenna setup, some of the sites also provide data, where multiple receivers are attached to the same antenna by a signal *splitter*. Although the analysis of time series of sites connected by a splitter do not contribute to detect sources of error due to the local environment, their analysis is used to indicate the achievable level of detail of this approach. The record of hardware changes for the used stations is described in Table 3.3. As these sites are contributing to the global ITRF

solution, local ties connecting the array of stations are provided through highly accurate terrestrial measurements (Sarti, P. et al., 2013). Four of the sites in Figure 3.2, Arequipa (Peru), Wettzell (Germany), Yarragadee (Australia) and Zimmerwald (Switzerland), have terrestrial measurements for the array of stations with sufficient accuracy to allow the comparison with the GNSS-derived baselines.According to the log files, the stations in Arequipa have been measured with an accuracy of 1 mm.

Station	Time Interval	Antenna Type	Radome
AREG	01.13 – 12.16	TRM59800.00	NONE
AREQ	02.94 – 08.11	AOAD/M_T	JPLA
AREQ	08.11 – 02.12	AOAD/M_T	NONE
AREQ	02.12 – 12.16	AOAD/M_T	JPLA
AREV	08.09 – 11.10	AOAD/M_T	JPLA
AREV	08.11 – 02.12	AOAD/M_T	NONE
AREV	02.12 – 12.16	AOAD/M_T	JPLA
GODE	04.94 – 07.12	AOAD/M_T	JPLA
GODE	07.12 – 08.12	TRM29659.00	NONE
GODE	08.12 – 12.12	AOAD/M_T	NONE
GODE	12.12 – 01.13	AOAD/M_T	JPLA
GODE	01.13 – 01.13	AOAD/M_T	NONE
GODE	01.13 – 12.16	AOAD/M_T	JPLA
GODN	01.12 – 12.16	TPSCR.G3	SCIS
GODS	01.12 – 12.16	TPSCR.G3	SCIS
GODZ	04.93 – 07.12	AOAD/M_T	JPLA
GODZ	07.12 – 08.12	TRM29659.00	NONE
GODZ	08.12 – 12.12	AOAD/M_T	NONE
GODZ	12.12 – 01.13	AOAD/M_T	JPLA
GODZ	01.13 – 01.13	AOAD/M_T	NONE
GODZ	01.13 – 12.16	AOAD/M_T	JPLA
IRKJ	07.01 – 12.16	JPSREGANT_SD_E	NONE
IRKM	11.04 – 12.16	AOAD/M_T	NONE
IRKT	09.95 – 01.14	AOAD/M_T	NONE
MOBJ	12.05 – 02.07	TPSCR3_GGD	NONE
MOBJ	05.07 – 12.16	JPSREGANT_SD_E1	NONE
MOBK	12.09 – 12.16	JPSREGANT_SD_E1	NONE
MOBN	12.00 – 12.16	ASH701945C_M	SCIS
SUTH	12.97 – 02.02	AOAD/M_T	NONE
SUTH	02.02 – 12.16	ASH701945G_M	NONE
SUTM	03.00 – 05.13	AOAD/M_T	NONE
SUTM	05.13 – 12.16	JAV_RINGANT_G3T	NONE
SUTV	07.09 – 12.16	ASH701945G_M	NONE
WTZA	04.06 – 12.16	ASH700936C_M	SNOW
WTZJ	07.01 – 08.05	JPSREGANT_SD_E2	NONE
WTZJ	08.05 – 12.09	TRM29659.00	NONE
WTZJ	12.09 – 11.10	LEIAR25	LEIT
WTZR	02.95 – 01.09	AOAD/M_T	NONE
WTZR	01.09 – 06.10	LEIAR25	LEIT
WTZR	06.10 – 12.16	LEIAR25.R3	LEIT
WTZT	02.97 – 01.00	TRM22020.00+GP	NONE
WTZT	01.00 – 05.05	TRM29659.00	NONE
WTZZ	10.98 – 06.03	ASH701073.1	SNOW
WTZZ	06.03 – 02.11	TPSCR3_GGD	CONE
WTZZ	02.11 – 12.16	LEIAR25.R3	LEIT
WTCO	07.15 – 12.16	LEIAR25.R4	LEIT
YAR2	06.96 – 08.97	JPLD/M_R	JPLA
YAR2	08.97 – 05.12	AOAD/M_T	JPLA
YAR2	05.12 – 09.12	AOAD/M_T	NONE
YAR2	09.12 – 06.13	AOAD/M_T	JPLA
YAR2	06.13 – 12.16	AOAD/M_T	NONE
YAR3	06.07 – 12.08	LEIAT504	NONE
YAR3	12.08 – 12.16	LEIAR25	NONE
YARR	09.98 – 10.07	ASH701073.1	DOME
YARR	10.07 – 12.16	LEIAT504	NONE
ZIM2	07.11 – 05.09	TRM55971.00	NONE
ZIM2	05.09 – 12.16	TRM59800.00	NONE
ZIMJ	02.99 – 10.12	JPSREGANT_SD_E	NONE
ZIMJ	10.12 – 12.16	JPSREGANT_SD_E1	NONE
ZIMM	07.99 – 12.16	TRM29659.00	NONE
ZIMZ	06.02 – 08.05	ASH701073.1	SNOW

TABLE 3.3: Changes in antennas and radomes for the co-located IGS stations. The format for the time interval is month and year (MM.YY).

Station	Local Tie			Epoch	Station	Local Tie			Epoch
	δE [m]	δN [m]	δU [m]			δE [m]	δN [m]	δU [m]	
AREG	-11.5103	10.3047	0.4180	2013	**YAR2**	–	–	–	1998
AREQ	–	–	–		YAR3	-16.9914	-6.5556	-1.1568	
AREV	0.0000	0.0000	0.0000		YARR	-0.2873	-3.8732	0.0786	
WTCO	-58.9752	16.6138	-0.2710	2004	ZIM2	-18.7604	-0.4260	0.0982	2008
WTZA	-0.4881	3.0217	-0.1125		ZIMJ	-13.2146	4.7910	-2.0455	
WTZJ	1.6780	0.3103	-0.0988		**ZIMM**	–	–	–	
WTZR	–	–	–		ZIM2	-18.7644	-0.4330	0.0970	2014
WTZT	-2.2655	-3.4023	0.0903		ZIMJ	-13.2245	4.7904	-2.0466	
WTZZ	0.4190	-1.5365	0.1313		**ZIMM**	–	–	–	

TABLE 3.4: Available local ties, in topocentric coordinates, for sites Arequipa, Wettzell, Yarragadee and Zimmerwald. Stations in **bold** correspond to the reference for the sub-network and ties are given with respect to them.

The Wettzell site has reported local ties with an accuracy of 1-2 mm (Klügel, T. et al., 2012). At the site Zimmerwald, Ineichen, D. et al., 2015 report the realisation of several measurement campaigns. Those at the epochs 2008 and 2014, with accuracies between 0.9 mm and 1.6 mm, are considered within the scope of this study. The complete list of available local ties with respect to the reference station, is given in Table 3.4.

3.4 PARAMETRISATION AND PROCESSING STRATEGY

The main steps of this work include the generation of GNSS-based coordinate time series, the assessment of the corresponding discrepancies with the available local ties, and the determination of the time-dependent variations in the local GNSS baselines. To this end, an appropriate parametrisation and processing strategy have been developed to cope with the characteristics and advantages of short GNSS baselines. All available observations are processed daily in separate small cluster networks, one per site, using the latest revision of version 5.2 of the Bernese GNSS Software (Dach, R. et al., 2015). As a result of the diversity of the selected sites given in Figure 3.2, not all stations are equipped with GLONASS-capable receivers and therefore only GPS observations are used within this study. Precise GPS orbits and Earth rotation parameters are supplied by the products of the Center for Orbit Determination in Europe (CODE) (Dach, R. et al., 2017). Crustal deformation effects such as ocean and atmospheric tidal loading together with station velocities are considered negligible due to the short distance among stations of the same cluster. The central processing strategy used along this work is based on double-differences of phase observations with ambiguity fixing. Following the clock synchronisation using code observations and the subsequent cycle slip detection and correction and initial outlier removal, ambiguities are fixed separately for L1 and L2 with the Sigma-Dependent Ambiguity Resolution Strategy (Dach, R. et al., 2015). After a final step of outlier exclusion, the approach for the estimation

Type of Solution	Abbreviation
L1-only without troposphere estimation	L1-NT
L2-only without troposphere estimation	L2-NT
Ionosphere-free linear combination without troposphere estimation	L3-NT
L1-only with troposphere estimation	L1-TR
L2-only with troposphere estimation	L2-TR
Ionosphere-free linear combination with troposphere estimation	L3-TR

TABLE 3.5: Naming convention for the investigated solutions described in Section 3.4.

of final coordinates is twofold: first, a group of solutions including an L1-only, an L2-only and an ionosphere-free linear combination (called L3 in the following), are calculated without estimating any tropospheric parameters, since for such small networks with small height differences, differences in tropospheric delays can be modelled ($\Delta h = 10\ m \rightarrow \Delta\varrho_{trp} = 3\ mm$) (Beutler, G. et al., 1987b; Dilßner, F. et al., 2008; Santerre, R. et al., 1990). In a second stage, L1-, L2-, and L3-solutions are calculated, with the estimation of troposphere parameters (except for the reference station) as piece-wise linear functions with a parameter spacing of 2 h using the dry and wet Global Mapping Function (GMF), with a priori delays computed based on the Global Pressure Temperature model (GPT) (Böhm, J. et al., 2006a; Dach, R. et al., 2015). Hereafter the naming convention of Table 3.5 will be used to refer to these solutions. While the solutions without troposphere estimation are expected to provide cleaner time series, the solutions with troposphere estimation, specially the L3 linear combination, are much closer to the approach used for the realisation of the ITRF. At each cluster network, the ITRF2014 coordinates and velocities of the station with the least discontinuities and enclosing the time span of the remaining stations, are fixed. For the rest of stations composing the cluster, baselines connecting them to the reference station are built (STAR strategy in (Dach, R. et al., 2015)). Observations are leveraged with a weight of $sin^2 e$ depending on the elevation e, and an elevation cut-off angle of 3° is used. The results of the daily processing are stored as normal equations for the posterior generation of multi-year solutions. Before determining the repeatabilities for each solution at a site, an additional step to find outliers and discontinuities in the time series has been implemented. The detection of such anomalies allows to obtain highly accurate multi–year solutions and clean coordinate time series, with the additional advantage of the estimation of periodic signals in the series (Dach, R. et al., 2015). These time series are the input for the final step of repeatability calculations, used to determine the level of agreement of the estimated coordinates. At the last step of the analysis, the east, north and height components of the calculated baselines are compared with the local ties, if available.

3.4.1 *Reprocessing Results and Discontinuities*

With the processing strategies of Section 3.4, daily station coordinates for the six different types of solutions at the eight individual cluster networks have been estimated. The SIGMA method for ambiguity resolution delivers a success rate of solved ambiguities above 99 % for each sub-network, and time series of coordinate differences, with respect to an unique combined solution, are calculated. While the RMS of the residuals are better than 2 mm for the horizontal component and 4 mm for the vertical component, these time series suffer from the effect of jumps due to hardware changes and site-specific environmental factors. In general, sites in the southern hemisphere display smaller uncertainties, without strong periodic gradients, in contrast to stations in the northern hemisphere, visibly more affected by seasonal effects such as periods of snow at the different sites. The topic of periodic signals is further discussed in Section 3.4.3, for those sites with large seasonal variations. Figure 3.3 shows the height component of these residuals for station WTZZ (Wettzell, Germany), for the six processing strategies, where values are within ± 3 mm. Single-frequency-based solutions deliver the smallest values, while breaks and jumps are more noticeable in the linear combinations. Discontinuities associated to hardware changes reported in Table 3.3 are detected in all the solutions (vertical lines in Figure 3.3), with larger magnitudes for both L3 solutions. Other discontinuities, as well as outliers, not reported as hardware changes are detected for each type of solution. Table 3.6 shows a sample of events with

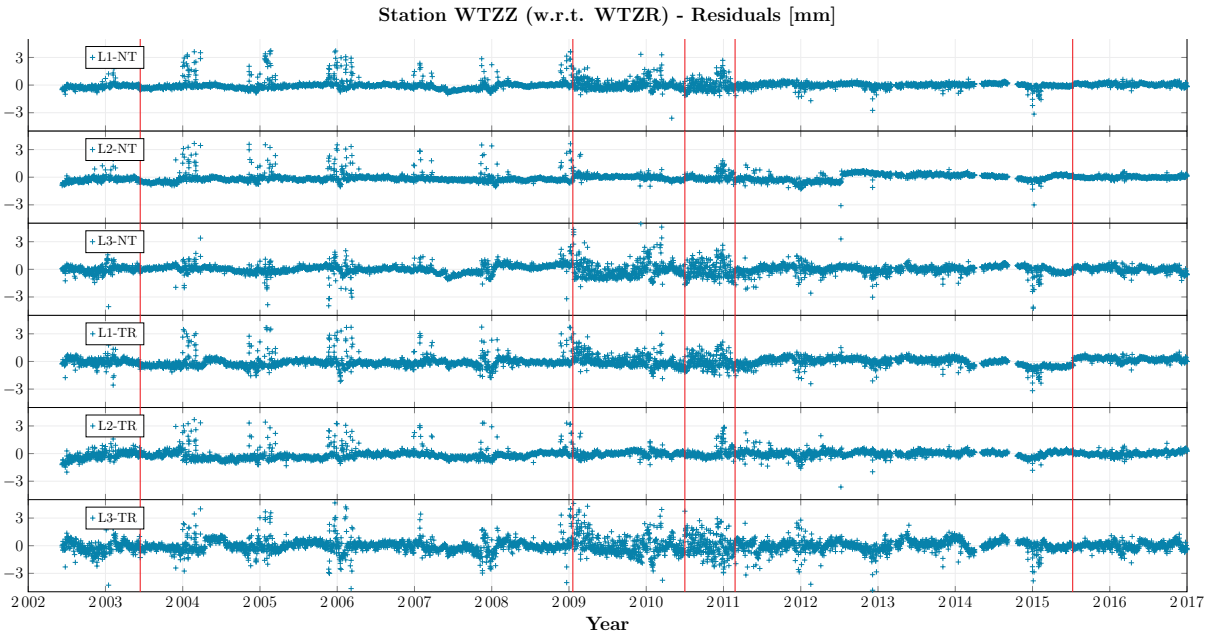

FIGURE 3.3: Residuals of the height component of station WTZZ with respect to WTZR (Wettzell, Germany). Vertical solid lines indicate changes in hardware.

a magnitude larger than 1.5 mm for the L3-TR solution for station WTZZ. Larger values of noise in years 2009 and 2010 are observed, especially in the L1 and L3 solutions. These increased residuals result as a consequence of changes on both antenna and receivers on the station, and suggest a greater sensitivity of some antennas to the environmental conditions. Several large jumps (outliers) with amplitudes up to 4 mm

are detected with this approach. Some of these outliers can be associated to the periods of snow at the site, which in general covers the months of December, January and February. Images from a webcam located close to the array of antennas confirm the presence of snow on the antennas in some of these cases (Figure 3.4). However, within this work, these images were not used consistently to eliminate outliers but only as an auxiliary source for the identification of particular events.

Date	Size of Jump [mm]	Remark
2003-06-11	3.1	Antenna change
2005-02-16	1.6	Periods of snow
2010-06-30	2.9	Antenna change
2011-02-22	1.8	Antenna change
2015-07-13	2.9	Antenna change

TABLE 3.6: Discontinuities and outliers at station WTZZ. Height component of the L3-TR solution. Only significant events with more than 1.5 mm of amplitude are displayed.

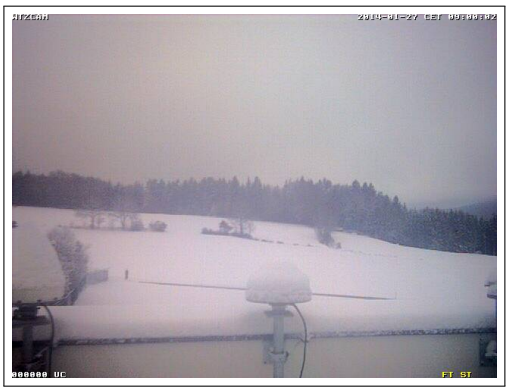

FIGURE 3.4: Snow on the Wettzell Site for date 12.12.2012. Outliers up to 3 mm are visible during the months of December and January. Credits: Wettzell Observatory.

In contrast, as an example of the behaviour of stations in the southern hemisphere, coordinate residuals for site AREG (Arequipa, Peru) show small variability (Figure 3.5a) throughout the interval of calculation, with values for the three components within ± 1 mm for the six investigated solutions. Despite this behaviour, two characteristic anomalies in the time series are detected: relatively large noise values at the first quarter of 2015, and a jump in the series of approximately 1 mm at first quarter of 2016, preceded by a ramp that is observable in the L2 and L3 solutions. These small amplitude variations cannot be clearly associated to hardware changes, and they are a probable indications for changes in the environmental conditions at the site. The last example shows the time series for a so-called *zero-baseline*, composed by two stations attached to the same antenna through a signal splitter. Figure 3.5b displays the residuals for the height component of a *zero-baseline*: station GODZ (Greenbelt, USA). The behaviour of the residuals, with values within ± 0.2 mm, results from the elimination of adverse effects, such as multipath and antenna phase patterns. Although breaks and jumps are visually detectable, their magnitude amounts to less than 0.1 mm, and therefore,

cannot be clearly associated to hardware (receiver) changes nor to environmental conditions. Results for this type of baselines indicate the resolution attained, and provide empirical thresholds for the levels of noise achievable with this approach. Comparable results to those observed for these three stations are obtained after the

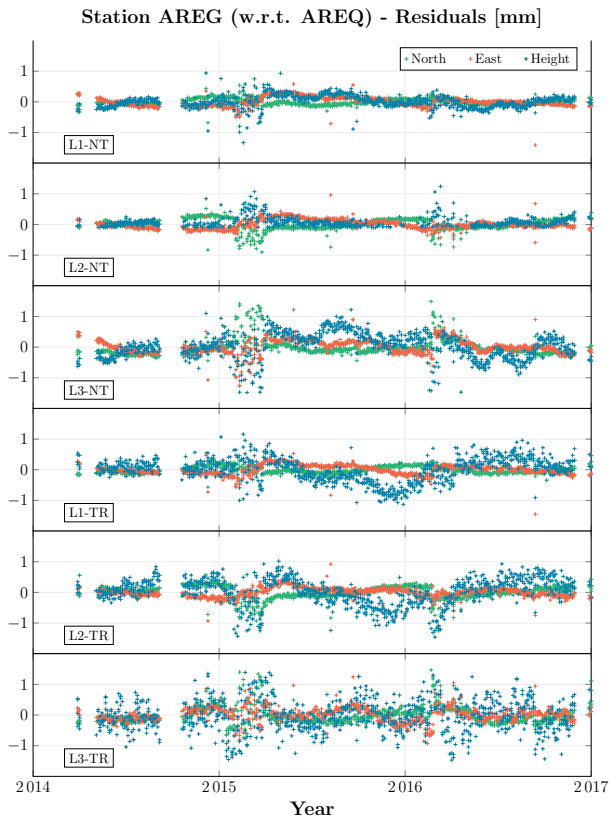

(a) Residuals of the height component of station AREG (Arequipa, Peru).

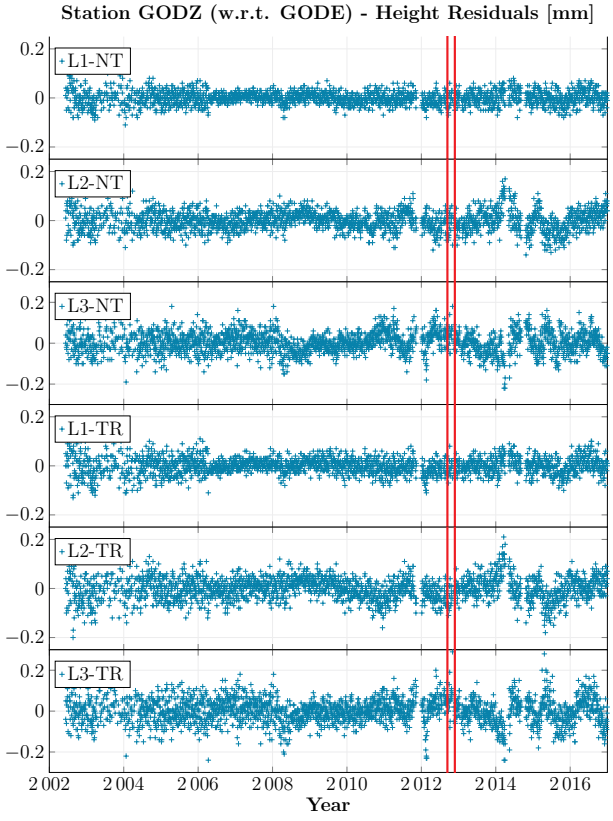

(b) Residuals of height component of station GODZ (Greenbelt, USA). GODZ and GODE (reference) share the same antenna. Solid lines indicate changes in hardware.

FIGURE 3.5: Residuals of height component, stations AREQ and GODZ.

processing of the remaining sub-networks, with a similar performance regarding the identification of discontinuities and periodic signals. Significant jumps in the time series of coordinate residuals are removed by establishing a new set of reference solutions after the occurrence of each of these events, for the posterior analysis and determination of repeatabilities, whereas the effect of the periodic signals remains present in these series.

3.4.2 *Station Repeatabilities*

To assess the quality of the estimated station coordinates, results from the daily processing (X_i^r) were compared with respect to those of the multi-year solution (X_m^r), to compute the repeatabilities σ_r:

$$\sigma_r = \sqrt{\frac{1}{p-1}\sum_{i=1}^{p}(X_i^r - X_m^r)^2} \qquad r \in \{n, e, h\} \tag{3.1}$$

where a new combined reference solution X_m^2 is calculated after each of the breaks determined in Section 3.4.1. The results of this step are summarised in Table 3.7, with the values for all the stations in Table 3.2, except for those that serve as reference for the sub-networks. In general, the different processing approaches deliver clean time series with repeatabilities better than 1 mm in 60 % of the investigated solutions, and exceeding 2 mm in only 16 % of the cases. Single-frequency L1-NT and L2-NT show comparably small results, with 70 % of solutions below 1 mm. Visibly much noisier, L3-NT solutions meet the requirements of solutions below 1 mm in about 53 % of the cases. In contrast, solutions with troposphere estimates are considerably worse, with the worst results for the L3-TR solution, where less than 38 % of the solutions are able to cope with the 1 mm threshold. Few outliers (repeatabilities $\geq$ 3 mm) are detected, with two specific sites (Irkutsk and Obninsk) showing the worst values, especially for the height component. This behaviour will be examined in more detail in the following section. The best values for this indicator are displayed by the stations in the southern hemisphere, while stations in the northern hemisphere show dissimilar results.The process to benchmark these uncertainties and determine tolerable differences is twofold. First, to test the hypothesis whether the increase in noise level in the L3 solutions is mainly due to forming the linear combination, the expected noise in the L3 solution is calculated, based on the noise present in the L1 and L2 solutions. Assuming uncorrelated measurements on the two frequencies, theoretical uncertainties for the linear combination can be calculated as

$$\begin{aligned} \sigma_{L3} &= \sqrt{\kappa_1^2\sigma_{L1}^2 + \kappa_2^2\sigma_{L2}^2} \\ \kappa_i &= (-1)^{i+1}\frac{f_i^2}{f_1^2 - f_2^2},\ i \in \{1, 2\} \end{aligned} \tag{3.2}$$

where f_1 and f_2 are the GPS L1 and L2 fundamental frequencies. In particular, if $\sigma_{L1} \approx \sigma_{L2}$, then $\sigma_{L3} \approx 3\sigma_{L1}$. Forming a similar expression based on the coordinate repeatabilities (s_{Li}) of Table 3.7, namely:

$$s_{L3} = \sqrt{\kappa_1^2 s_{L1}^2 + \kappa_2^2 s_{L2}^2} \tag{3.3}$$

these repeatability values can be compared with the corresponding σ_{L3} of the L3-NT and L3-TR solutions, for the horizontal and the vertical component separately. Results indicate a high level of agreement between σ_{L3} and s_{L3} with ratios $\frac{s_{L3}}{\sigma_{L3}} \approx 1.2$, and about 95 % of the results satisfying $\|\sigma_{L3} - s_{L3}\| \leq 1$ mm, with few high values for

	East						North						Up					
	NT			TR			NT			TR			NT			TR		
Station	L_1	L_2	L_3	L_1	L_2	L_3	L_1	L_2	L_3	L_1	L_2	L_3	L_1	L_2	L_3	L_1	L_2	L_3
AREG	0.11	0.13	0.30	0.19	0.26	0.26	0.10	0.12	0.29	0.29	0.21	0.52	0.16	0.21	0.40	0.81	0.45	0.97
AREV	0.04	0.04	0.07	0.03	0.10	0.14	0.04	0.04	0.07	0.07	0.11	0.17	0.06	0.07	0.15	0.13	0.14	0.21
GODN	0.95	0.30	0.40	0.84	0.33	0.45	0.53	0.53	0.73	0.56	0.51	0.74	0.91	0.64	1.62	1.25	0.83	3.26
GODS	0.84	0.31	0.40	0.76	0.33	0.49	0.37	0.36	0.61	0.41	0.35	0.65	0.87	0.59	1.68	1.28	0.77	3.33
GODZ	0.52	0.06	0.20	0.54	0.13	0.17	0.15	0.15	0.09	0.21	0.12	0.09	0.28	0.17	0.13	0.18	0.19	0.20
IRKJ	0.99	0.96	2.24	0.91	0.79	2.44	1.03	1.70	2.18	0.76	0.57	2.14	**3.10**	**3.35**	**3.44**	**3.50**	**2.53**	**4.71**
MOBJ	1.24	1.40	1.55	1.77	1.13	2.10	1.83	2.00	1.99	2.05	2.81	2.28	**5.69**	**4.03**	**9.37**	**6.69**	**4.25**	**9.76**
MOBK	1.19	1.18	1.48	1.24	1.00	2.02	1.87	1.76	1.92	1.59	2.32	2.06	**5.52**	**3.06**	**9.26**	**6.72**	**4.10**	**9.63**
SUTH	1.05	0.80	1.00	1.03	0.81	0.98	0.52	0.50	0.41	0.49	0.47	0.44	0.54	0.49	0.59	0.51	0.48	0.90
SUTV	0.76	0.73	0.75	0.75	0.74	0.73	0.51	0.54	0.45	0.51	0.51	0.46	0.50	0.52	0.58	0.50	0.51	0.79
WTCO	0.42	0.53	0.50	2.00	2.01	2.23	0.29	0.21	0.28	0.82	0.54	1.36	0.32	0.27	0.63	1.27	0.77	1.36
WTZA	0.35	0.58	0.49	1.23	1.25	1.37	0.41	0.54	0.53	0.64	1.82	0.60	0.90	0.50	1.78	2.50	0.74	2.57
WTZJ	0.77	1.03	1.15	1.72	1.97	2.47	1.07	0.87	1.82	1.46	1.66	2.84	1.20	1.75	1.81	2.63	2.34	**3.22**
WTZT	0.54	0.49	1.47	1.42	1.63	1.73	0.60	0.50	1.20	1.29	1.43	1.62	0.73	1.09	1.20	2.62	1.44	**3.19**
WTZZ	0.46	0.51	0.47	1.32	1.91	2.16	0.53	0.33	0.56	1.07	1.20	1.46	0.88	1.09	1.89	1.56	1.20	2.10
YAR3	0.19	0.18	0.39	0.21	0.21	1.19	0.10	0.19	0.29	0.12	0.20	1.15	0.49	0.33	1.11	0.90	1.17	1.67
YARR	0.29	0.20	0.62	0.19	0.14	1.00	0.20	0.22	0.66	0.34	0.15	1.04	0.92	0.41	2.04	1.00	1.06	1.74
ZIM2	0.44	0.29	0.92	0.43	0.31	0.96	0.59	0.33	0.88	0.64	0.36	0.95	0.57	0.89	1.47	0.97	0.74	2.36
ZIMJ	1.15	1.34	1.34	1.25	1.21	1.35	1.29	1.46	1.32	1.32	1.29	1.32	1.10	1.16	1.98	1.48	1.43	2.89
ZIMZ	0.95	0.70	2.34	0.92	0.74	2.22	1.22	1.03	1.99	1.33	1.06	2.20	1.37	1.45	1.83	1.68	1.71	2.51

TABLE 3.7: Station coordinate repeatabilities, in mm. **NT** indicates that the solution does not include the estimation of the relative troposphere, while the solutions under **TR** include this type of estimate.

the height component. From this analysis, uncertainties for stations at Irkutsk and Obninsk show the largest deviations, especially in the height component, whereas their horizontal components perform within tolerable boundaries. The unfavourable results for these two stations are further discussed in Section 3.4.3. Finally, ratios $\kappa = \frac{s^{TR}}{s^{NT}}$ between solutions with and without troposphere estimation are calculated and compared with the corresponding ratio of the formal errors of the height estimates. The variation of these values is used to detect possible anomalies and inconsistencies among solutions coming from the estimation of tropospheric parameters, and it is considered only for the height component. However, results of this step show a high variability among solutions with values ranging between 0.47 and 2.66, an average $\kappa = 1.6$, and a relatively large standard deviation of 0.85. The strong deviations of many of the baseline repeatabilities and the expectations derived from formal errors allow to conclude that for large values of κ, significant systematic effects must be present in the solutions.

3.4.3 *Seasonal Signals*

High uncertainties detected in the repeatabilities of the stations at sites Irkutsk and Obninsk (Russia), especially for the height component, motivate an additional analysis of these networks. In particular, for station IRKJ (Irkutsk), Figure 3.6a shows the coordinate residuals for the height component stacked over 11 years. The image on the top corresponds to the L1-NT solution, the image in the middle to the L3-TR solution, while the bottom image is derived from the coordinate residuals provided by the Jet Propulsion Laboratory, forming the difference between stations IRKJ and IRKM. This solution is generated using Precise Point Positioning (PPP) with the ionosphere-free linear combination including the estimation of tropospheric parameters. Therefore, it corresponds to the L3-TR solution (JPL, 2017). The two solutions L1-NT and L3-TR were chosen due to the high variability with respect to each other, demonstrated in Section 3.4.2, so that the two extreme cases are taken into account. Time series in the two upper images of Figure 3.6a are evidently driven by the presence of periodic signals. Large differences, up to 12 mm for L1-NT and 20 mm for L3-TR, with high levels of noise are observed between the months of November and March most certainly caused by snow on the antennas. To provide an additional proof of the presence of these periodic signals in the coordinate residuals, the data was fitted with a curve based on a Fourier series with two harmonic terms. The functional model used for the fitting is based on the following relation

$$S(t) = a_0 + \sum_{k=1}^{2} \left[a_k \cos(k\,\omega\,t) + b_k \sin(k\,\omega\,t) \right], \tag{3.4}$$

where a_0 models an intercept term in the data, ω is the frequency of the signal, and a_k, b_k, with $k \in \{1,\ 2\}$, are the harmonic coefficients of the series. The estimated parameters $A_k = \sqrt{a_k^2 + b_k^2}$ (amplitude) and $\phi_k = \arctan \frac{b_k}{a_k}$ (phase) for the time series are displayed in Table 3.8, together with the corresponding RMS of the fitting process. Data corresponding to the months of December, January and February were not

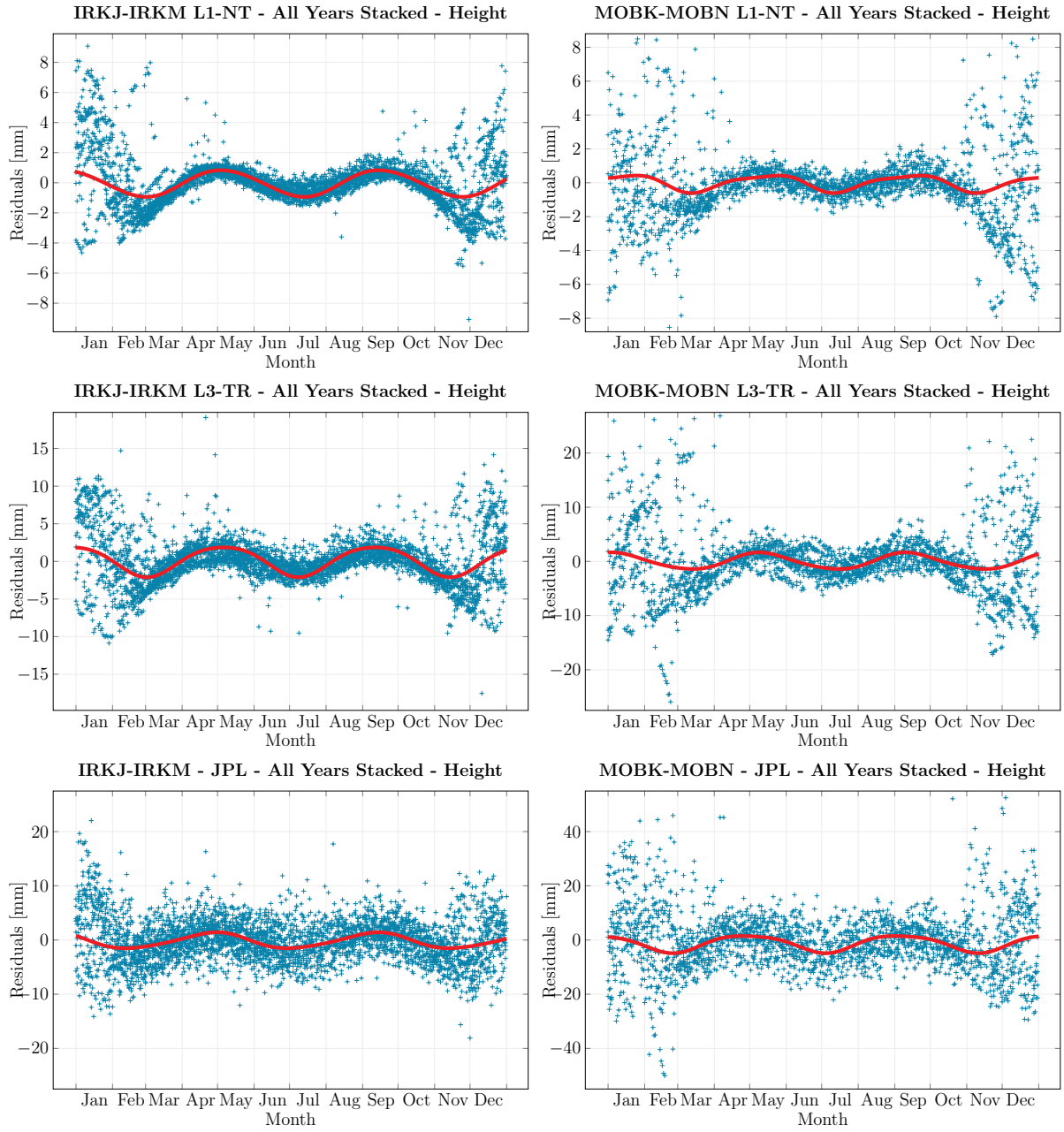

(a) Time series of height residuals for station IRKJ with respect to IRKM (Irkutsk - Russia). Daily values are stacked for 11 years. Top: L1-NT solution. Middle: L3-TR solution. Bottom: JPL-derived. Solid curves represent the fitted Fourier series.

(b) Time series of height residuals for station MOBK with respect to MOBN (Obninsk - Russia). Daily values are stacked over 7 years. Top: L1-NT solution. Middle: L3-TR solution. Bottom: JPL-derived. Solid curves represent the fitted Fourier series.

FIGURE 3.6: Seasonal signals in the time series of the Russian co-location sites.

considered during this fitting process, since they exhibit large levels of noise. In the three cases, the small RMS values confirm the goodness of the fitting. Of particular interest is the estimated primary period T of the signal, with similar values for the three series, that amounts approximately to 4.5 months. The Fourier series are additionally displayed in Figure 3.6a, as solid curves superposed to the data, where an agreement

between the L1-NT and the L3-TR residuals and the estimated Fourier series is clearly noticed. Comparing the JPL-based solution with the L3-TR solution (Figure 3.6a), it can be observed that the former shows practically the same local behaviour of the two stations IRKJ and IRKM. Therefore, it is evident that the global solutions of the IGS are also affected by these local effects and that they are not an artefact of the processing of the short baselines. The noise level in the global solutions (JPL) is, however, much larger and contains many more effects that are common to both stations and therefore such local signals cannot be detected easily in global results. Local analyses are much more precise and allow the detection and quantification of such effects to improve the knowledge about global, regional and local signals. Moreover, the same type of analysis was performed for the stations MOBJ and MOBK

	Station IRKJ							Station MOBK						
	a_0	A_1	A_2	ϕ_1	ϕ_2	T	rms	a_0	A_1	A_2	ϕ_1	ϕ_2	T	rms
L1-NT	-0.03	0.88	0.05	-22.0	-162.7	4.5	0.8	-0.00	0.49	0.13	42.8	-128.4	4.1	1.5
L3-TR	0.11	1.98	0.24	-8.4	160.1	4.3	2.9	0.02	1.51	0.17	19.9	-2.8	4.1	4.2
JPL	-0.14	1.43	0.19	-53.2	-50.0	4.6	3.3	-1.17	3.15	0.57	-27.9	139.5	4.3	8.2

TABLE 3.8: Parameters of the Fourier series and RMS of the fitting process, for the periodic signals of Figures 3.6a and 3.6b. The period of the signal (T) is given in months, and the phase (ϕ_i) in degrees.

(Obninsk, Russia), where comparable periodic signals are observed in the time series of residuals for the height component. Figure 3.6b shows the yearly stacked height residuals for the L1-NT and L3-TR solutions, in comparison to the JPL-derived solution, for station MOBK. Differences of up to -16 mm for the L1-NT solution and 30 mm for the L3-TR solution are observed between the months of November and March, and the characteristic depletion during July remains present. The corresponding Fourier series were determined using the functional model of Equation (3.4), once more with two harmonic terms, and the estimated parameters and RMS of the fitting process are summarised in Table 3.8. Higher RMS values are obtained, larger than those of station IRKJ. This is a consequence of the high scatter of the original data. The estimated primary period T exhibits also a larger variation, but the different solutions deliver comparable values, with which an effective period of approximately 4.1 months can be verified. Figure 3.6b shows additionally these Fourier series (solid curves). Results obtained with the Fourier series for coordinate residuals at both stations, suggest the presence of a signal with a period of approximately 4 months. The reason for these time variations between IRKJ and IRKM, and between MOBK and MOBN are not known at present. Particularly strange is the noticeable similarity between the seasonal variations at Irkutsk and Obninsk. No reason for this fact has been found yet.

3.4.4 *Local Ties Comparison*

The local terrestrial measurements described in Table 3.4 are used to examine the deviations of the GPS-based baselines from these local ties. At the first investigated

site, Arequipa, the baseline is realised using the surveyed local ties of station AREG with respect to station AREQ, with a local system centred at station AREQ. The reprocessing of AREG delivered one set of coordinates, as no discontinuities were found. Figure 3.7 shows the difference of the GPS baseline with respect to the surveyed local ties. Solutions without troposphere estimation deliver smaller differences with respect to the local ties than the corresponding solutions with troposphere estimation. The largest discrepancies are obtained for the L3 solutions with values above 2 mm for the height component, while the single-frequency solutions exhibit, as expected, the best results. It is encouraging to see that L1-NT and L2-NT solutions deviate by less than 1 mm from the local tie values. A bias above 2 mm is observed in the height component for most of the solutions, and reaches the maximum for L3-TR with 4.5 mm. It is worth mentioning that, even with an agreement between the L1-NT and the L2-NT solutions and the terrestrial local ties at the sub-millimetre level, the L3 solutions deviate by up to 4 mm. These results support the fact that the small systematic errors in the L1 and L2 solutions are unfortunately heavily amplified in L3. In contrast, the processing of the stations at site Wettzell show that most of the

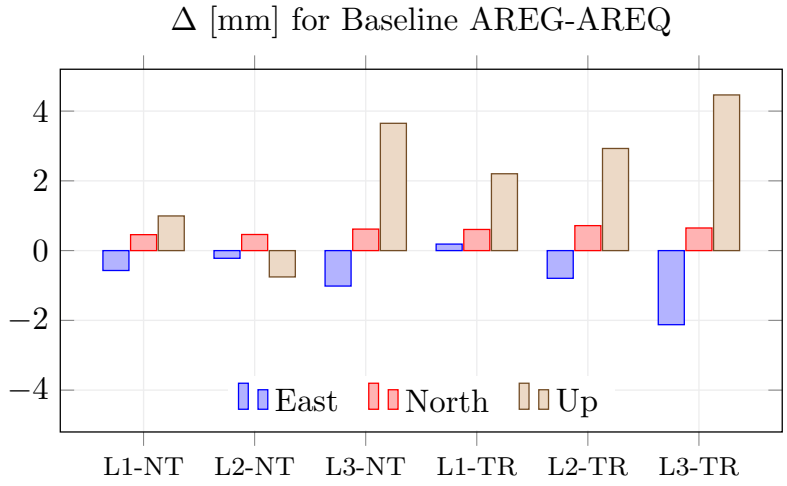

FIGURE 3.7: Differences between GPS solutions and surveyed terrestrial measurements. Baseline AREG-AREQ, Arequipa, Peru.

stations have multiple solutions due to the discontinuities detected in each time series. Table 3.9 shows the periods for which these solutions are valid. These intervals are in accordance with changes in hardware at the site. Differences for the height component between the surveyed local ties and the GPS solutions of those stations with multiple solutions are displayed in Figure 3.8a. In most of the cases these differences exceed the 1 mm, with some solutions reaching the centimetre level. In general, single-frequency solutions without troposphere estimates show a better agreement. Most of the worst agreements in the height component are seen in the ionosphere-free linear combination, specially in those with troposphere estimation. It is again noticeable that even with acceptable single-frequency solutions, there is a large amplification of the differences in the ionosphere-free solutions. Moreover, Figure 3.8b shows the differences between the last GPS solution of Table 3.9 and the local ties for all components and stations of the site Wettzell. Deviations from the local ties of more than 1 mm are observed for all the stations, with the worst performance in the height component. Station WTCO shows

Station	Sol. #	Epoch	Station	Sol. #	Epoch
WTCO	1	07.2015 – 12.2016		1	03.1999 – 01.2000
WTZA	1	04.2006 – 12.2016		2	01.2000 – 11.2000
	1	07.2001 – 08.2005	WTZT	3	11.2000 – 12.2001
	2	08.2005 – 01.2009		4	12.2001 – 08.2002
WTZJ	3	01.2009 – 12.2009		5	08.2002 – 05.2005
	4	12.2009 – 07.2010		1	06.2002 – 06.2003
	5	07.2010 – 11.2010		2	06.2003 – 01.2009
			WTZZ	3	01.2009 – 07.2010
				4	07.2010 – 02.2011
				5	02.2011 – 12.2016

TABLE 3.9: Interval of validity for the solutions in site Wettzell. The different solutions are associated to discontinuities on the time series of each station. The format for the epoch is MM.YYYY

consistently large deviations for all solutions, in all components, with 8.5 mm for the height component in the L3-TR solution. For the remaining stations in Wettzell, despite the fact that the local ties are expected to be close to the 1 mm level, large significant deviations are observed, even with respect to the L1-NT and L2-NT solutions. While the higher agreement with respect to the local ties is reached by these two solutions, once more the L3 solutions show a large amplification of the errors, for both horizontal and vertical components. The ITRF2014 solution of (Altamimi, Z. et al., 2016) reports discrepancies with respect to the local ties of 5.8, 0.9 and 8.3 mm for the east, north and up components of the baseline WTZR-WTZA. These results agree very nicely with those obtained with the approach for the L3-TR solution: 3.8, 0.2 and 11.2 mm, respectively. Similarly, the same work reports discrepancies for the baseline WTZR-WTZZ of 0.5, 1.4 and -1.3 mm, for east, north and height components. The L3-TR solution within this work shows comparable results: 0.1, 0.4 and 1.9 mm, respectively. While these two approaches cannot be directly compared, this fact suggests that the L3-TR solution is comparable – to a certain extend – with a global solution[1]. The reprocessing of the Yarragadee site has delivered only one set of coordinates for each station, despite the changes in antenna seen in Table 3.3. This solution was used to calculate a GPS-based baseline with respect to station YAR2. The differences of these baselines with respect to the terrestrial measurements, in a system centred in YAR2, are shown in Figure 3.9. Both stations show a similar behaviour, with small differences in the horizontal components while the height component exceeds the 1 mm level. Once again, both single-frequency solutions show smaller differences than those of the ionosphere-free solutions. These differences reach the centimetre level for station YARR. The discrepancies of the ITRF2014 in (Altamimi, Z. et al., 2016) for baseline YAR2-YARR are -0.6, -0.5 and -8.9 mm, for east, north and up components, whereas those obtained with the L3-TR approach are 0.6, -0.5, and 11.8 mm, respectively. Reported discrepancies for baseline YAR2-YAR3 of -0.6, 1.9, 10.9 mm, in east, north

1 These differences are available as supplementary material of the definition of the ITRF2014 as "Tie Residuals". These data were accessed at the ITRF website: itrf.ign.fr/ITRF_solutions/2014

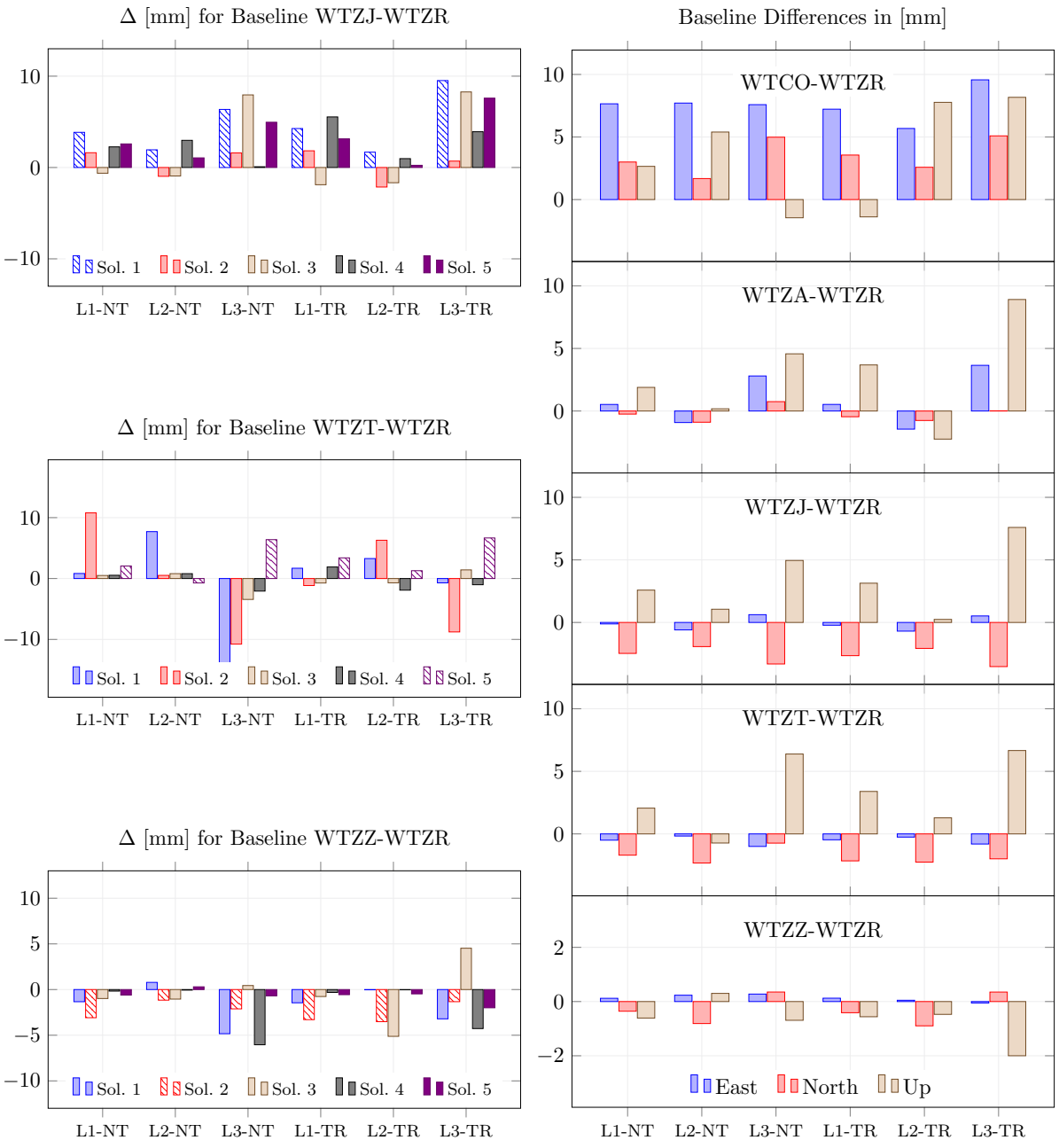

(a) Height differences of GPS-based baselines w.r.t. the local ties for the multiple solutions of Table 3.9 at site Wettzell. Patterns indicate that the solution corresponds to the epoch of the local tie.

(b) Differences between the last GPS solution of Table 3.9 and surveyed terrestrial measurements, with respect to WTZR. Site Wettzell, Germany. Note the different values for the *y*-axis in the WTZZ station.

FIGURE 3.8: Results of the reprocessing and the comparison to the local ties at the co-location site Wettzell (Germany).

and up components, which are in slightly better agreement with those derived from the L3-TR solution: 0.5, −1.9 and 5.7 mm, respectively. At the last site with available local ties, Zimmerwald, multiple GPS-based solutions are provided for both stations. The validity intervals for these solutions are summarised in Table 3.10. The two sets of available local ties displayed in Table 3.4 are compared to the multiple GPS-derived

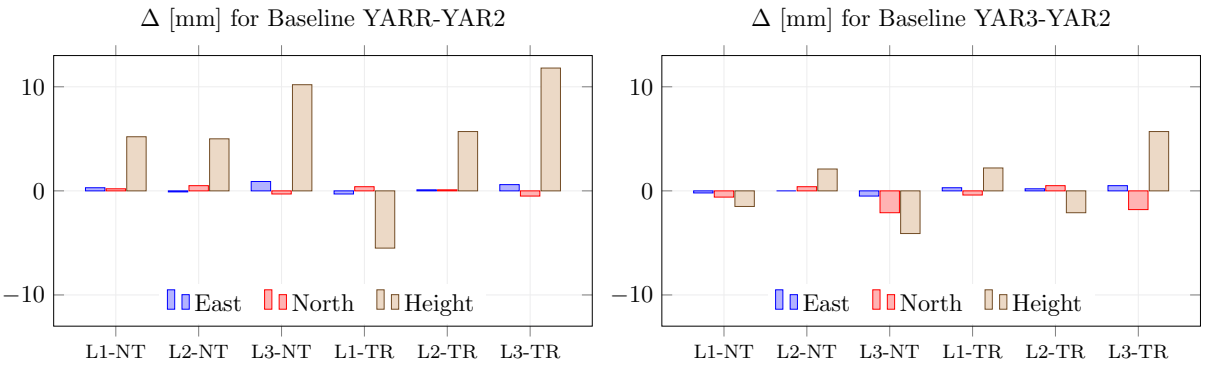

FIGURE 3.9: Differences between GPS-based baselines and surveyed terrestrial measurements, with respect to YAR2. Site Yarragadee, Australia.

baselines. Deviations were computed with respect to station ZIMM in a local system centred in station ZIMM. Figure 3.10 shows the results of this comparison regarding the local ties for the epoch 2008. Both stations show distinctive biases in the horizontal components. Deviations in the baseline including station ZIM2 show a systematic bias for the east component of 3.3 mm $\pm$ 1.3 mm, and of -5.6 mm $\pm$ -1.7 mm for the north component. Differences ranging from -10.9 mm up to 10.8 mm are observed in the height component, where no systematic bias is found. The third set of solutions,

Station	Sol. #	Epoch	Station	Sol. #	Epoch
ZIM2	1	11.2007 – 05.2009	ZIMJ	1	06.2002 – 10.2012
	2	05.2009 – 10.2013		2	10.2012 – 10.2013
	3	10.2013 – 12.2016		3	10.2013 – 12.2016

TABLE 3.10: Interval of validity for the solutions on site Zimmerwald. The different solutions are associated to discontinuities on the time series of each station. The format for the epoch is MM.YYYY.

corresponding to the change after October 2013, displays consistently the largest deviations for the six investigated processing strategies. This is a probable indication of an environmental factor changing the baseline length. For the baseline including station ZIMJ, deviations show mean biases in the east component of 7.7 mm $\pm$ 1.6 mm, and in the north component of -5.3 mm $\pm$ 2.4 mm. There is neither evidence of a bias in the height component, nor an indication, which of the three solutions has the worst performance. On the other hand, Figure 3.11 shows the deviations of the multiple GPS-based baselines with respect to the local ties for the epoch 2014. For the baseline including station ZIM2 a noticeable change of the biases is observed. The east components show an improvement with an average value of -1.4 mm $\pm$ 0.3 mm, while the north component remains heavily biased with an average value of -13.1 mm $\pm$ 0.9 mm. The height component does not display any noticeable bias. However, the third set of solutions, corresponding to the epoch October 2013, has the best agreement with the height component of the local tie. This suggests that the new local ties are in closer agreement with the GPS-based solutions. The baseline including station ZIMJ remains biased to a lesser extent. The east components show an average value of

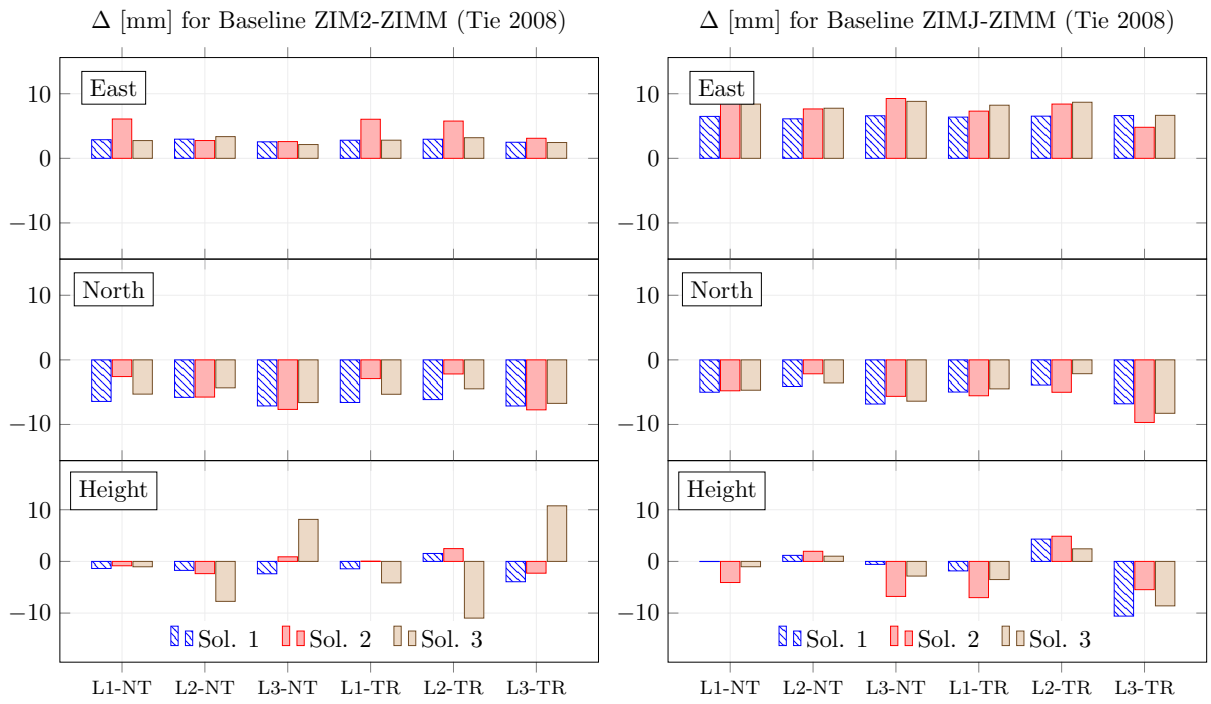

FIGURE 3.10: Differences between GPS solutions and surveyed terrestrial measurements at epoch 2008. Baseline ZIM2-ZIMM. Site Zimmerwald, Switzerland. Patterns indicate that the solution corresponds to the epoch of the local tie.

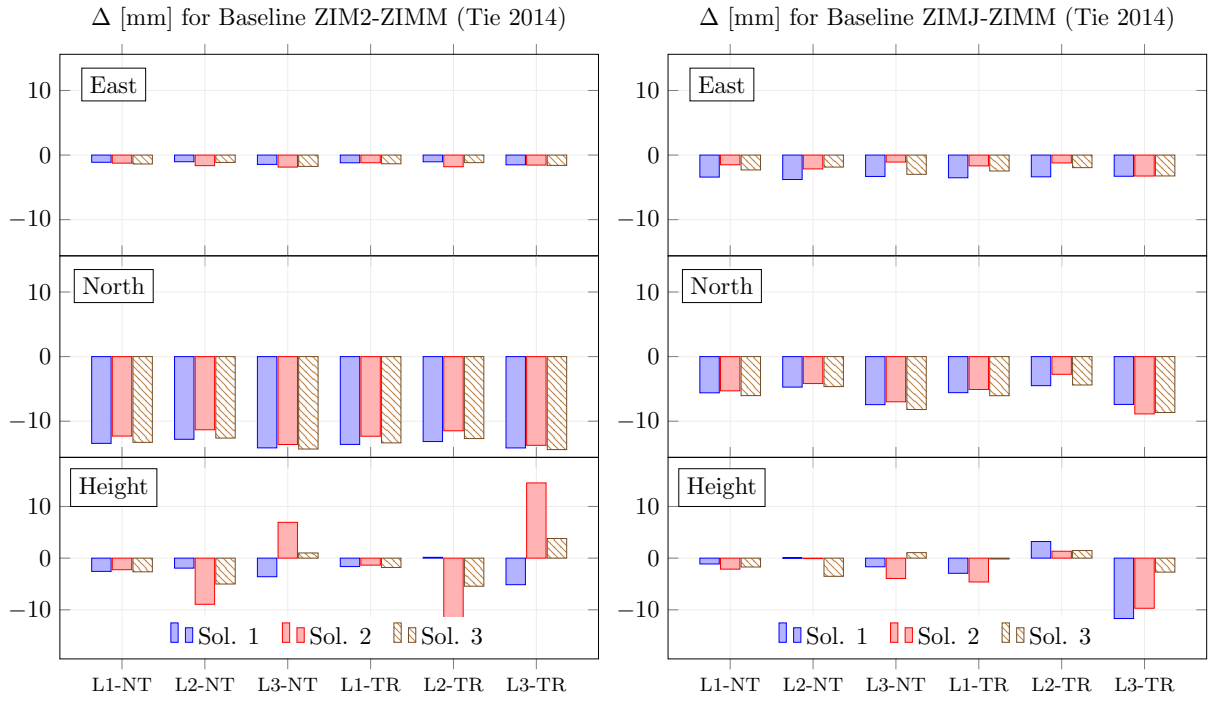

FIGURE 3.11: Differences between GPS solutions and surveyed terrestrial measurements at epoch 2014. Baseline ZIMJ-ZIMM. Site Zimmerwald, Switzerland. Patterns indicate that the solution corresponds to the epoch of the local tie.

-2.5 mm $\pm$ 1.1 mm, while the north component has an average of -5.9 mm $\pm$ 1.8 mm. Again, the height component remains unbiased with a tendency to favour the third

solution (epoch October 2013). (Ineichen, D. et al., 2015) have reported the installation of a crane at the site Zimmerwald for the construction of a new building in 2013 causing a subsidence of the ground. This type of local deformations of the ground can affect both the horizontal and vertical component of the stations and are most probably the cause for the observed differences. In general, regarding the height component, differences exceed the 1 mm threshold reaching the centimetre level in some cases. The characteristic behaviour of single-frequency based solutions performing better than those based on the L3 linear combination is observed. Height deviations confirm that solutions with troposphere estimates deliver the worst performance between processing strategies, demonstrating that an extremely accurate calibration of the sites and antennas is required to reduce these effects that will be present in the global solutions.

3.5 CONCLUSIONS AND OUTLOOK

The different processing strategies used in this study attain homogeneous results in terms of repeatabilities, with a marginally better performance for the sites in the southern hemisphere, where periodic signals associated with seasonal environmental conditions, most importantly the periods of snow, do not affect the estimation of positions. In particular, as expected, the parametrisation to derive solutions without troposphere estimation deliver the best performance of residuals in time series of coordinates, with values around 1 mm for each component for the majority of the sites. However, the use of different frequencies leads to results that differ from each other by several millimetres, with a clear amplification of the errors in the L3 ionosphere-free linear combination with respect to the single-frequency solutions. The large frequency-dependent differences among solutions stress the fact that differences are mainly originating from GNSS-related errors, such as those described by (Steigenberger, P. et al., 2013) associated with the calibration of the phase centre variation of the antenna and multipath. Furthermore, the level of detail achieved with the single-frequency based strategy tailored for short baselines enables the differentiation of seasonal phenomena with amplitudes of few millimetres, revealing discontinuities and periodic signals with high resolution, as seen for both Russian sites. Examples such as the baselines at Irkutsk and Obninsk demonstrate the presence of local effects that will also show up in the global solutions, in this case those provided by JPL, and that could be detected and quantified accurately by the analysis of the local co-located antennas. The puzzling fact that the local baselines at Irkutsk and Obninsk show a rather similar behaviour should be analysed further, as well as the causes of these variations. The study of the deviations of GNSS-based solutions from the local ties at the investigated sites shows differences exceeding largely the precision of both techniques. Since differences of this order of magnitude can be seen among the different processing strategies, the source of these deviations is most likely to come from GNSS-related errors. Nevertheless, the existence of large deviations with the same magnitude and tendency in the site Zimmerwald suggests the possibility of disturbances originating from the local environment, in particular, construction activities near the station, with an influence not only on the height components but also on the horizontal position of the antenna. The lack of local

ties for the remaining locations listed in Table 3.2 prevents an extension of this analysis. Further studies are required to quantify the influence of the deviations between the GNSS-based solutions and the local ties on a global scale. These should make use of multi-GNSS data, including GLONASS and Galileo, for a comprehensive modelling of system specific errors. At this point, a precise antenna pattern calibration for the additional systems (especially Galileo) is a prerequisite to achieve sub-millimetre accuracy. Next steps for this analysis are the simulation of a global solution including the co-located stations used here for the assessment of local baselines, and applying the deviations with respect to both, the cluster-network solutions and the local ties, could contribute to quantify the impact of these errors on the reference frame. Additionally, it should be considered whether the differences between the local L1-NT solutions and the L3-TR solutions could be used to calibrate the systematic effects in the global L3 solutions.

ACKNOWLEDGEMENTS This work has been developed within the project "Co-location of Space Geodetic Techniques on Ground and in Space" in the frame of the DFG funded research unit on Reference Systems, and funded by the Swiss National Foundation (SNF). The authors would like to thank the IGS (Dow, J. et al., 2009) for providing the GPS observations. We would like to acknowledge the dedicated efforts of the operators of the GNSS sites used within this work. An special thanks to the GO-Wettzell, for the provision of the data of station WTCO.

4

EXPERIMENTS ON SHORT VLBI BASELINES

ABSTRACT

This work discusses the analysis of the short baseline between two co-located VLBI telescopes at the Geodetic Observatory in Wettzell (Germany). Geodetic VLBI sessions between July 2015 and January 2016 are processed using the VLBI capabilities of the Bernese GNSS Software to estimate station coordinates, troposphere zenith delays and clock parameters, applying two strategies: global VLBI solutions and baseline solutions. Results show a sub-millimetre agreement of the VLBI-derived baseline and the local ties. Zenith tropospheric delays compared to a co-located GNSS station show an agreement better than 10 mm, when considering the height differences between the telescopes. The quality of clock corrections is further assessed, where the differences between the VLBI-based clock estimates and a Two-Way Optical Time Transfer (TWOTT) system are in acceptable agreement, with values below 50 ps. These results indicate that the proposed processing strategies represent a valuable tool for the continuous monitoring of systematic effects and the local ties at the site.

4.1 INTRODUCTION

Within the overarching goal of the VLBI Geodetic Observing System (VGOS) (Petrachenko, W. T. et al., 2012), new radio telescopes with increased observation capabilities have been realised, built as twin telescopes or placed close to legacy antennas. In consequence, the assessment of short VLBI baselines, with baseline lengths of less than a few hundred metres, has become possible. These intra-technique experiments contribute to identify local effects and instrument-specific biases, as they can be separated from -nearly- identical influences, such as tropospheric delays, Earth rotation, quasar coordinates and source structures, and constitute a pre-requisite to improve the realisation of the terrestrial reference frame. Additionally, these studies are expected to help with the intended replacement of legacy antennas by the new VGOS dishes, where an accurate determination of the local baselines is required. The determination of station coordinates at fundamental sites, with positions better than 1 mm (Plag, H.-P. et al., 2009), requires an appropriate parametrisation allowing the identification of antenna-related errors, such as the thermal deformation and the gravitational sag due to the weight of the structure (Kallio, U. et al., 2012).Plank, L. et al. (2016) have already explored strategies of observation using co-located VLBI telescopes, with the goal to facilitate the observation process while maintaining the high precision required for the estimation of geodetic parameters. The new scheduling modes for VLBI sessions, validated with data from the sibling telescopes at Hobart (Australia), are presented as an alternative to obtain local baseline observations for the study of the local ties. In this chapter we discuss an alternative approach for the estimation of parameters for

the short VLBI baseline in Wettzell (Germany), established between the legacy 20 m Radio Telescope Wettzell (RTW) and the new TWIN Telescope Wettzell (TTW1) with a diameter of 13.2 m (Figure 1.4). Schüler, T. et al. (2015) already performed an analysis of the local baselines among the array of telescopes at Wettzell and their comparison with a local surveyed ties. Their work shows satisfactory X-band group delays and an 1-2 mm agreement between the derived baseline length and terrestrial surveys. The S-band group delays however, influenced by local radio signals, were reported to be 10 times less precise. These differences reveal the presence of a bias of about 1 mm. The authors attribute this systematic effect to the mismodelling of the thermal expansion of the telescope structure, and to the gravitational deformation of the antenna structure. In addition to this, Halsig, S. et al. (2019) present results on the performance for VLBI observations on short baselines, focusing on the analysis of the atmospheric refraction. Sessions with a large number of observations per baseline were used in this study, where relative differences in zenith wet delays were on the order of 1-3 mm. The stability of the observing system was assessed by using the two-way optical time transfer method for the clock correction parameters, where the agreement is on the level of 20-30 ps. Our approach uses a custom-made processing strategy to work out the advantages and disadvantages of short baselines. Differences between VLBI- and GNSS-based tropospheric zenith delays, with respect to a co-located GNSS station at the site, are also evaluated to investigate the behaviour of absolute and relative atmospheric delays. The analysis of the local Wettzell baseline benefits, additionally, from recently installed optical two way time transfer system. More details on the activities towards the modernisation of the time dissemination system at the Wettzell Observatory can be found in Kodet, J. et al. (2018). Part of this activities were focused on the development of the time comparison system which was used as an independent "clock tie", an additional link between the space geodetic techniques. This tie is realised by an actively stabilised two-way optical time and frequency distribution system (TWOTT), using a two way measurement approach, which compares two time distribution nodes at the observatory (Kodet, J. et al., 2016; Panek, P. et al., 2013). It provides a unique method, which compares time difference between the two radio-telescope without degradation of timing properties by the link between the two TWOTT terminals. Since this system does not distribute timing signals and just compares two nodes, it can be used only in post-processing. It provides the time comparison between the two telescopes which can be eventually used in analyses as an additional information. Therefore this system provides a virtual common clock between TTW1 and RTW. Within this work, the comparison between the VLBI derived local baseline length and between the local clock differences and the terrestrial surveys and TWOTT is used to separate VLBI technique-specific error sources and environmental effects, and provides an alternative to monitor the behaviour of the local baseline.

4.2 VLBI CAPABILITIES IN THE BERNESE GNSS SOFTWARE

A VLBI processing chain has been already implemented in a BSW v4.3 project version (Schmid, R., 2009). However, since these capabilities were never included into the official releases, within the project "Co-location of Geodetic Space Techniques

on Ground and in Space" the processing chain has been re-implemented into BSW v5.2 project version. The BSW VLBI processing strategy is based on VLBI observations provided in NGS card files. First, these files are converted into baseline-wise BSW single-difference observation files. Correction values for transmission delays and ionospheric delays are considered. The resulting single-differences are subsequently processed in a tailored version of GPSEST (Dach, R. et al., 2015). In contrast to dedicated VLBI packages, the BSW implementation uses a piece-wise linear representation for the receiver clock, without estimating linear and quadratic polynomials. Since the implementation is ongoing, several features need to be improved. Among others, it is not possible to estimate source positions in the current version, and BSW quality check functionalities have to be improved. To validate these implemented capabilities, the

Solution	Software	N	E	U
ETH (Männel, B., 2016)	BSW	4.5	3.3	10.0
Hobiger, T. et al. (2015)	c5++	6.0	7.3	13.0
Soja, B. et al. (2015)	VieVs	3.3	2.3	7.5
Schmid, R. (2009)	BSW	3.6	3.5	10.0

TABLE 4.1: CONT14 station coordinate repeatabilities, in mm. The results for Schmid, R. (2009) are obtained after processing with the BSW v4.3 VLBI implementation

VLBI CONT14 sessions are processed. Additional details on the parametrisation and obtained results can be found in Männel, B. (2016). Table 4.1 shows the derived mean station coordinate repeatabilities averaged over all 17 participating stations, including the results found in the literature. A sufficient agreement and a mean precision level of around 1 cm is found. Considering other indicators, large residuals are found compared to those derived by dedicated VLBI packages. Differences in troposphere zenith delays with respect to co-located GNSS stations are small, in the order of few millimetres, and derived Earth rotation parameters differ by less than 0.5 mas and 0.2 ms from the IERS C04 series.

4.3 DATABASE AND PROCESSING STRATEGY

Geodetic VLBI observations extracted from IVS campaigns sessions are processed using the VLBI version of the BSW version described in Section 4.2. Initially, the database used corresponded to 57 VLBI sessions of the IVS campaign, which contain the baseline RTW–TWIN1 Behrend, D., 2013. These geodetic sessions were carried out between July 2015 and June 2016. However, due to interference in cross-correlation caused by the presence of the pCal system in both radio telescopes, it was recommended to deselect the local Wettzell baseline after January 26th, 2016. Therefore, the cross correlation of the short baseline was available only for 21 out of the 57 sessions. Moreover, to profit from the clock tie provided by the TWOTT, we selected 12 VLBI sessions, trying to maximise the occurrence of the RTW (WETTZELL) and TTW1 (WETTZ13N) baseline. These selected sessions contain data of several other stations (Figure 4.1), that are considered within a global network solution as a benchmark for the short baseline.

The complete list of the R1 and R4 sessions used is shown in Table 4.2. The data

FIGURE 4.1: VLBI sites used within the GLO approach.

analysis is performed with three different processing strategies. The first approach consists of a *global solution* (GLO), where all VLBI observations were used. The datum for the station coordinates was defined by minimum constraints conditions (no-net-rotation and no-net translation) with respect to the ITRF2014 (Altamimi, Z. et al., 2016). Earth rotation parameters were modelled as piece-wise linear functions for 24 h intervals. 13 zenith wet tropospheric delays (every two hours) were mapped with the wet VMF (Böhm, J. et al., 2006b), and two gradients (east-west and north-south) were mapped with Chen, G. et al., 1997, for each station and session. For a comprehensive analysis of the clock behaviour, receiver clock offsets were estimated in intervals of 30 minutes, 1, 2, 6, 12, 24 and 48 hours for each session and for each station, except for WETTZELL. The second processing approach corresponds to a *short baseline solution*

Year: **2015**

DoY	281	286	295	299	309	323
MJD	57303	57308	57317	57321	57331	57345
ID	R4708	R1709	R4710	R1711	R4712	R4714

DoY	327	337	341	351	355	363
MJD	57349	57359	57363	57373	57377	57385
ID	R1715	R4716	R1717	R4718	R1719	R4720

TABLE 4.2: List of geodetic VLBI sessions used in this work, containing the (successfully correlated) baseline RTW (WETTZELL) and TTW1 (WETTZ13N). The rows indicate the Day of Year, Modified Julian Date and Session ID.

(BAS), where only the WETTZELL-WETTZ13N baseline observations were used. The datum for the station coordinates was realised by constraining the coordinates of the station WETTZELL to 1 mm. Earth rotation parameters were not estimated, and receiver clock offsets were estimated for WETTZ13N, with the same intervals as in the GLO approach. The main feature of this approach is that the troposphere wet delays between the two stations were not estimated, due to the assumption that for such a small distance and height difference, differences in tropospheric delays can be modelled. Thus, only the hydrostatic part of the troposphere is considered. The third and final approach corresponds again to a *short baseline solution* (BA2), where only the WETTZELL-WETTZ13N baseline observations were used. Earth rotation parameters were not estimated and the datum and receiver clock offsets were defined in the same way as for the BAS solution. In contrast to the BAS solution, 13 zenith tropospheric delays were set up and mapped with wet VMF for WETTZ13N for each session. A summary of these processing strategies, together with additional parameters used, can be found in Table 4.3.

To complement the analysis, external products were used to compare the estimated station coordinates, the zenith tropospheric delays and the receiver clock offsets. First, tropospheric parameters estimated for each approach are compared with those of the co-located GNSS station WTZR from the IGS network (Dow, J. et al., 2009). These tropospheric delays were supplied by the Centre for Orbit Determination in Europe (CODE) (Dach, R. et al., 2017). Table 4.4 lists the ellipsoidal heights for the reference point of each telescope in relation to the station WTZR. Additionally, the length of the baseline between the two telescopes derived from terrestrial measurements, taken from (Schüler, T. et al., 2015), is mentioned. Furthermore, Table 4.4 also displays the tropospheric ties between WETTZELL and WTRZ, according to Teke, K. et al., 2011.

Additionally, data from the TWOTT system is used to assess the stability of the VLBI-based clock estimation. The TWOTT system has been installed between the hydrogen maser clocks connected to the VLBI telescopes RTW and TTW1. This allows for the exchange of timing signals with an accuracy better than 1 ps using standard optical telecommunication transceivers (Kodet, J. et al., 2016). Within the scope of this work, TWOTT clock synchronisation values between September 2015 and January 2016 were used. Figure 4.2 shows a sample of these data, and the residuals of the TWOTT data with respect to a linear fitting, for sessions R4708 and R4712. In session R4708, residuals with respect to a linear interpolation are in the range of ± 15 ns and indicate a high frequency stability, whereas the residuals of session R4712 show a different, namely quadratic, behaviour. The (straight) blue lines in Figure 4.2 depict the original TWOTT data after the removal of the daily offset, and therefore is labelled as δTWOTT. Notice that the units of these data are ns (left label). The green marks represent the difference of the δTWOTT data with respect to a daily linear fit using the same data. Also notice that the units of these data are ps (right label). The top plot shows that the clock behaviour can be achieved with much higher resolution and a small level of noise when using the TWOTT data. The quadratic trend, observed in bottom plot was caused by a failure of temperature stabilisation inside H-Maser.

Modelling and a-priori information	
Troposphere	6-hourly ECMWF-based hydrostatic troposphere delays mapped with VMF
Solid Earth tides	IERS 2010 conventions (Petit, G. et al., 2010)
Permanent tide	Conventional tide free
Ocean tide model	FES2004 (Lyard, F. et al., 2006)
Ocean loading	Tidal: FES2004 (Lyard, F. et al., 2006), computed with the free ocean tide loading provider Non-tidal: 6-hourly GRACE AOD1B atmospheric and oceanic de-aliasing product
Global solution (GLO)	
Observations	All VLBI observations
Coordinates	NNT/NNR w.r.t. ITRF2014
Earth rotation	Pole coordinates and UT1 for 24 h intervals, piece-wise linear
Troposphere	13 zenith wet delays (VMF), two gradients (Chen, G. et al., 1997) for every station and session
Receiver clock	Clock offsets for every station and session, except for WETTZELL, each 30 min., 1, 2, 6, 12, 24 and 48 h.
Baseline A (BAS) solution	
Observations	WETTZELL-WETTZ13N baseline observations
Coordinates	WETTZELL constrained to 1 mm
Earth rotation	not estimated
Troposphere	not estimated
Receiver clock	Clock offsets for every station and session, except for WETTZELL, each 30 min., 1, 2, 6, 12, 24 and 48 h.
Baseline B (BA2) solution	
Observations	WETTZELL-WETTZ13N baseline observations
Coordinates	WETTZELL constrained to 1 mm
Earth rotation	not estimated
Troposphere	13 zenith wet delays (VMF) for WETTZELL in every session
Receiver clock	Clock offsets for every station and session, except for WETTZELL, each 30 min., 1, 2, 6, 12, 24 and 48 h.

TABLE 4.3: Summary of the parameterisation and main processing strategies used for the VLBI analysis.

Station	Height [m]	Baseline
WETTZELL	669.117	123.3070 m ± 0.7 mm
WETTZ13N	672.549	
WTZR (GNSS)	666.013	

Tropospheric Tie WETTZELL-WTZR [mm]		
ZTD	ZHD	ZWD
-0.9	-0.8	-0.1

TABLE 4.4: Characteristics of the local VLBI baseline. Top: ITRF2014 heights for the VLBI telescopes and baseline vector (local tie). The height of the co-located GNSS station WTZR is also included. Bottom: Tropospheric tie in Wettzell, according to Teke, K. et al., 2011.

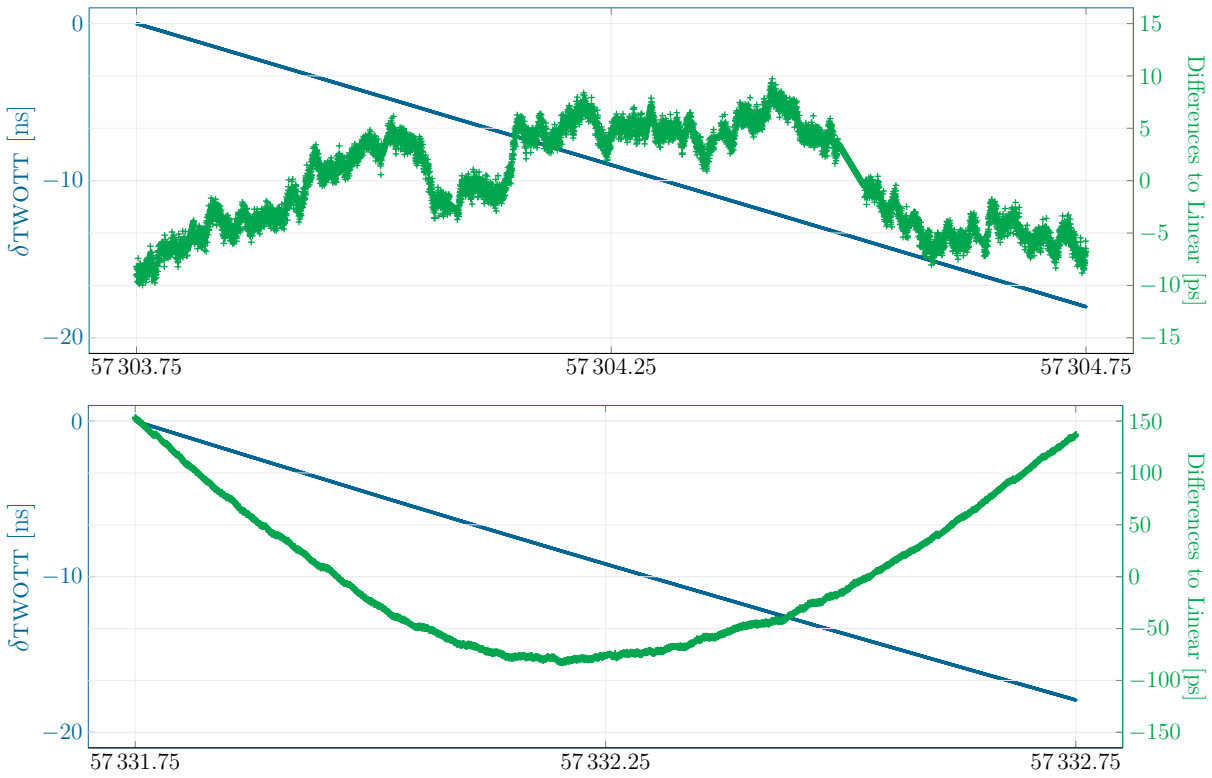

FIGURE 4.2: Behaviour of the TWOTT data, for sessions R4708 (top) and R4712 (bottom)

4.4 RESULTS AND DISCUSSION

4.4.1 *Residuals of the Least Squares Adjustment*

Residuals of the least squares adjustment were analysed to evaluate the goodness of the parameter estimation, as well as to detect outliers in each session. The time series of the standard deviations of the residuals, in picoseconds, are displayed in Figure 4.3, for the global solution and the two local baseline solutions, in relation to the different intervals considered for the estimation of the clock offset. Figure 4.3 shows the role of the clock parametrisation in the behaviour of the residuals, particularly for the GLO solution. Considering the GLO solution, the smallest residuals are consistently found in the solution which uses an interval of 30 min for the clock estimation, as the increased number of estimated parameters tend to reduce the standard deviation of the residuals, even when not improving the results. Variations of up to 50 ps can be observed among the extreme cases, 30 min. and 48 h intervals, for example at sessions R4710 and R1717. These differences are not so pronounced for the short baseline solutions, where the different parametrisations show comparable results. The two short baseline solutions, BAS and BA2, display rather homogeneous time series of standard deviations. This highlights the presence of an outlier session, R4712, corresponding to *doy* 309 of 2015. This atypical behaviour is also noticed in the TWOTT data of this day (cf. bottom of Figure 4.2). Table 4.5 summarises these time series with the mean value over time of the standard deviation, after the removal of the session R4712. In particular, the local baseline solutions display an average standard deviation of 20.85 ps for BAS and 18.31 ps for BA2, which implies a residual noise of 6 mm, and with a maximum difference between sessions of 5.42 ps for BAS and 3.96 ps for BA2, so that the maximum difference found for the noise of the residuals of the different solutions is ca. 1 mm. The much smaller standard deviations for BAS and BA2 show that systematic unmodelled effects can be reduced by a factor of about four. It is to be expected that this leads to similar improvements in the estimated parameters, especially more precise baseline coordinates and a better assessment of remaining systematic effects.

Clock Interval [h]	0.5	1	2	6	12	24	48
GLO	60.45	65.50	72.91	77.74	83.81	86.93	92.45
BAS	17.70	19.12	20.05	21.32	22.20	22.44	23.12
BA2	15.66	17.17	18.11	18.86	19.32	19.42	19.62

TABLE 4.5: Mean value [ps] over time of the standard deviations of Figure 4.3, for the different intervals of clock parametrisation

4.4.2 *Performance of Clock Estimates*

Before analysing the local tie performance in the positioning domain, the simultaneous VLBI observations are analysed and the estimated local clock corrections for the station WETTZ13N are compared to assess their delay stability. The parametrisation

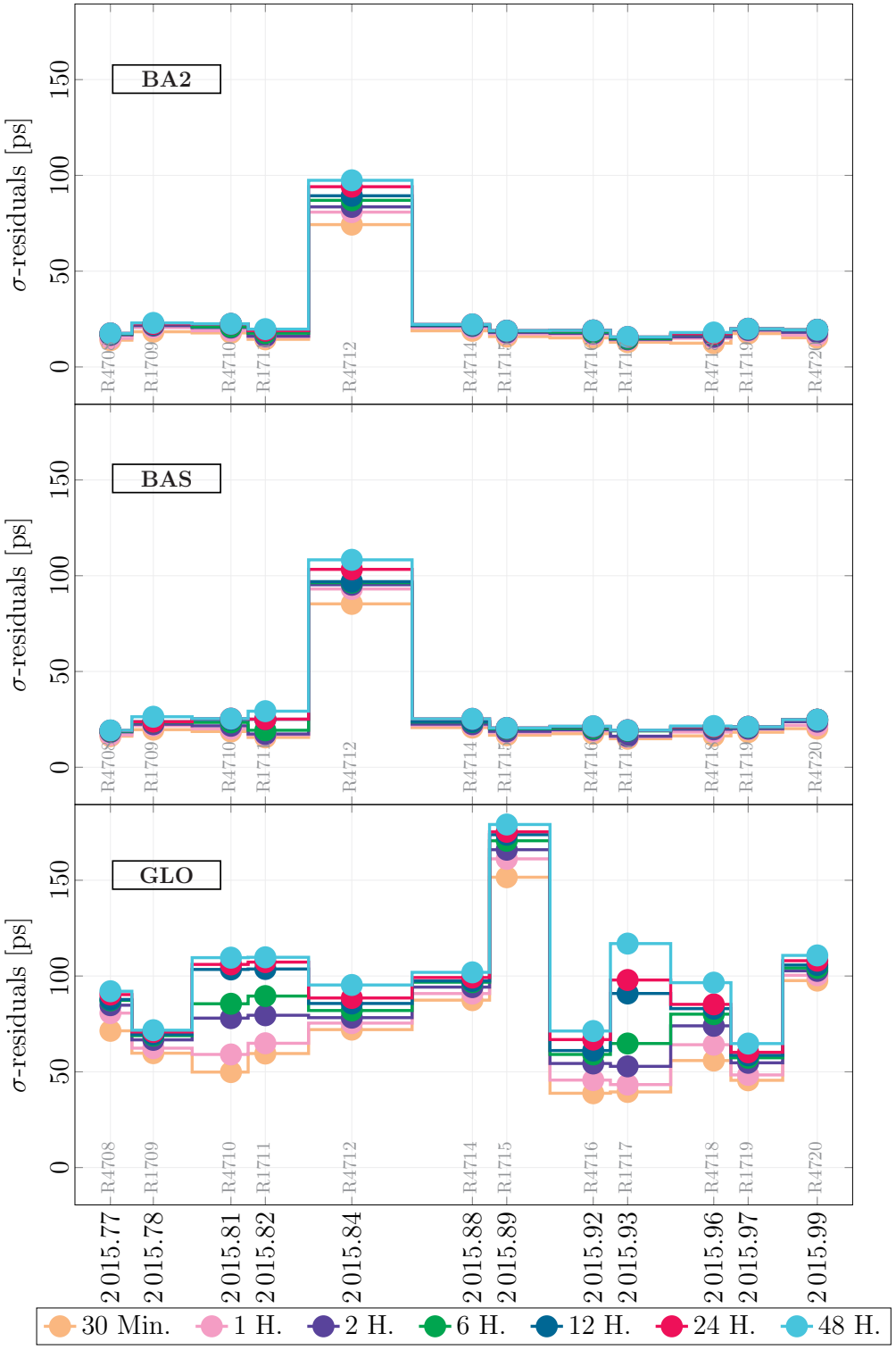

FIGURE 4.3: Standard deviation of the residuals of the least squares estimation of parameters (per session), in ps, for the processing approaches of Table 4.3, including a comprehensive analysis of the clock behaviour, receiver clock offsets were estimated in intervals of 30 minutes, 1, 2, 6, 12, 24 and 48 hours for each session and for each station, except for WETTZELL. Top: Global solution (GLO), middle: Baseline A (BAS) solution, and bottom: Baseline B (BA2) solution. Each coloured line represents a different interval for the estimation of the clock offsets.

proposed to calculate the clock corrections consists of several offsets per session with a linear behaviour between these estimates. The change in the temporal resolution of the parameters is supposed to find the optimal number of parameters to accurately describe the session clock behaviour during one session. The differences in the values of the clocks estimates for each interval and the mean for the session is calculated. These results are shown in Figure 4.4, where an overall high level of agreement is seen in both local baseline solutions (in red) displaying consistently small differences, within ± 30 ps, with the exception of session R4712, where the quadratic behaviour of the clock is only captured when using an interval for the estimation of the clock of 30 minutes. The differences between the clock estimates for the local baseline solutions and the global solution, are generally within ± 50 ps, however growing large for session R4720. As for the residuals performance, the optimal parametrisation, with the smallest mean differences, is found when using an interval of 6 h.

In addition, the deviations of these VLBI clock estimates with respect to a daily linear fit are calculated and used to characterise the clock behaviour. Moreover, the detrended TWOTT data is used to assess their behaviour. As instrumental delays are usually constant during one session, a session-wise mean bias between TWOTT and VLBI was subtracted from the VLBI results. Then, the session differences of the estimated value were averaged and their variability was calculated. Figure 4.5 shows this comparison, for each approach, when considering a time resolution for the VLBI clock estimation of 6 h. The blue marks represent the differences of the TWOTT data with respect to a linear fit, considering the entire time interval. The red marks indicate the differences of the VLBI estimates w.r.t a daily linear fit. Both blue and red marks can be seen as residuals of the data to their corresponding linear fit, therefore they are labelled as "Residuals" (left label). The units of these two sets of data are ns. Finally, the green marks show the differences between the TWOTT-VLBI "residuals" to linear fit. Notice that the units for these "double" differences (TWOTT-VLBI minus linear fit) is ps (right label). These differences between TWOTT and VLBI-based clock estimates range from -65 to 48 ps for the global solution, and have a slightly better performance for the local solutions: from -38 to 45 ps for BAS, and -54 to 50 ps for BA2.

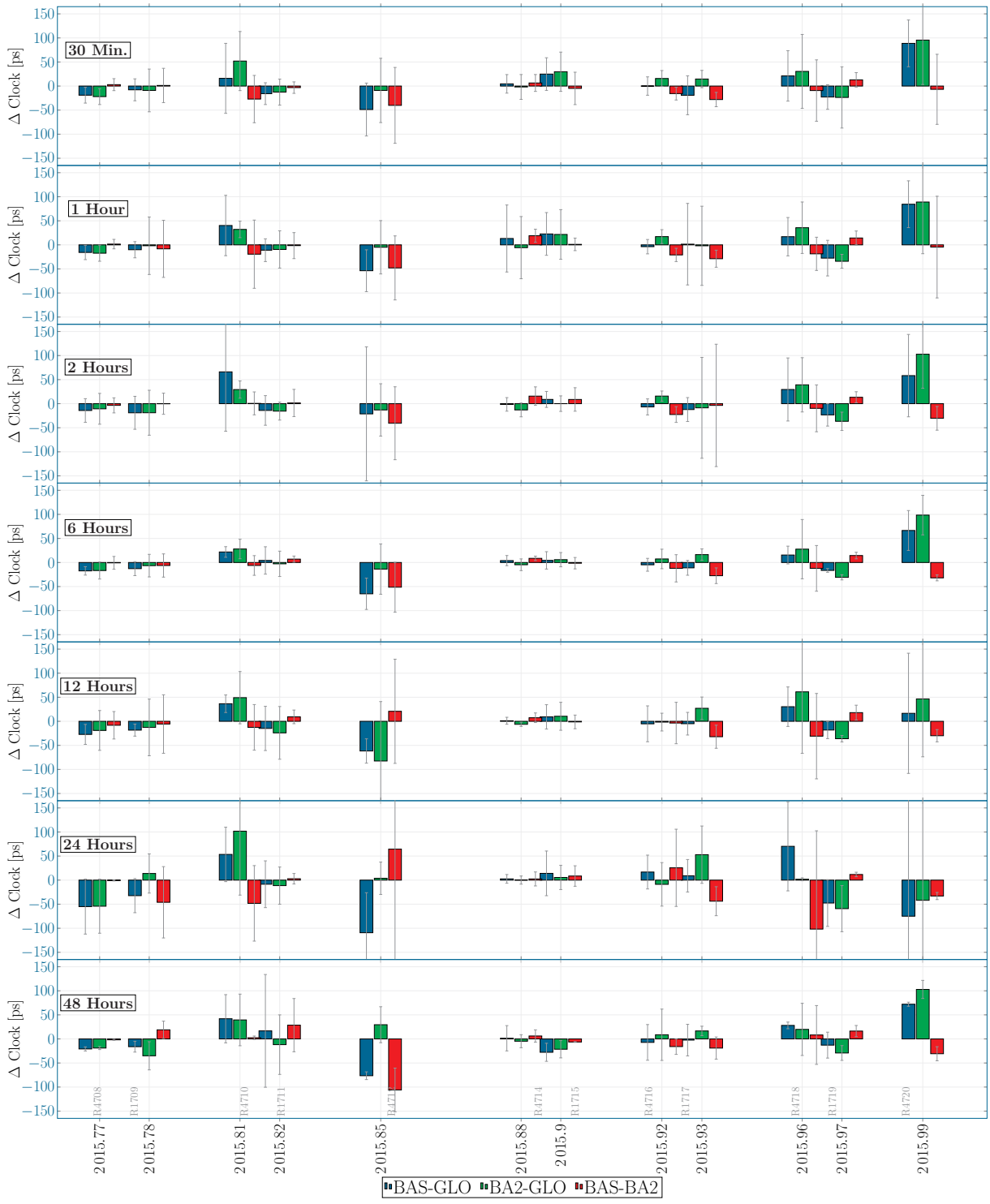

FIGURE 4.4: Mean session differences for the clock estimates of the WETTZ13N telescope, for the three different solution types.

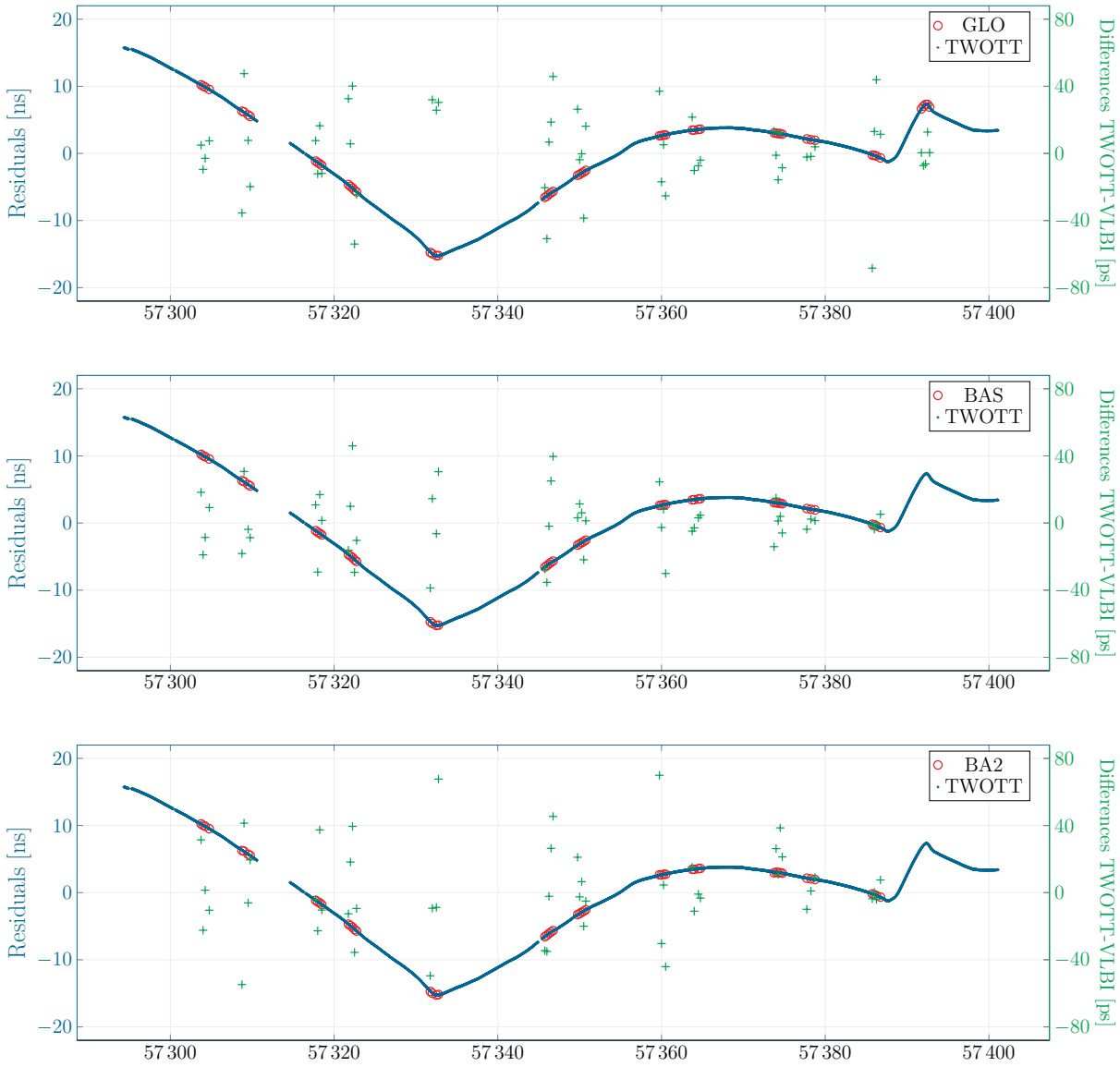

FIGURE 4.5: Differences between the VLBI clock and the TWOTT data, for each approach when considering a time resolution for the VLBI clock estimation of 6 h, with respect to the mean Julian date.

4.4.3 *Performance of Differential Tropospheric Zenith Total Delays*

As mentioned in Section 4.3, the relative troposphere parameters were set up exclusively for the solution type BA2. 13 differential zenith tropospheric delays were estimated and mapped with the wet VMF for the station WETTZ13N for each session. In a similar fashion to the residuals of Section 4.4, the different intervals for the parametrisation of the clock estimates were tested. Thus, six time series of session-wise tropospheric wet delays were obtained. The mean ZWD values obtained over one session, and the corresponding daily standard deviation, are displayed in Figure 4.6, where all the values have been corrected to account for the height difference between the two telescopes.

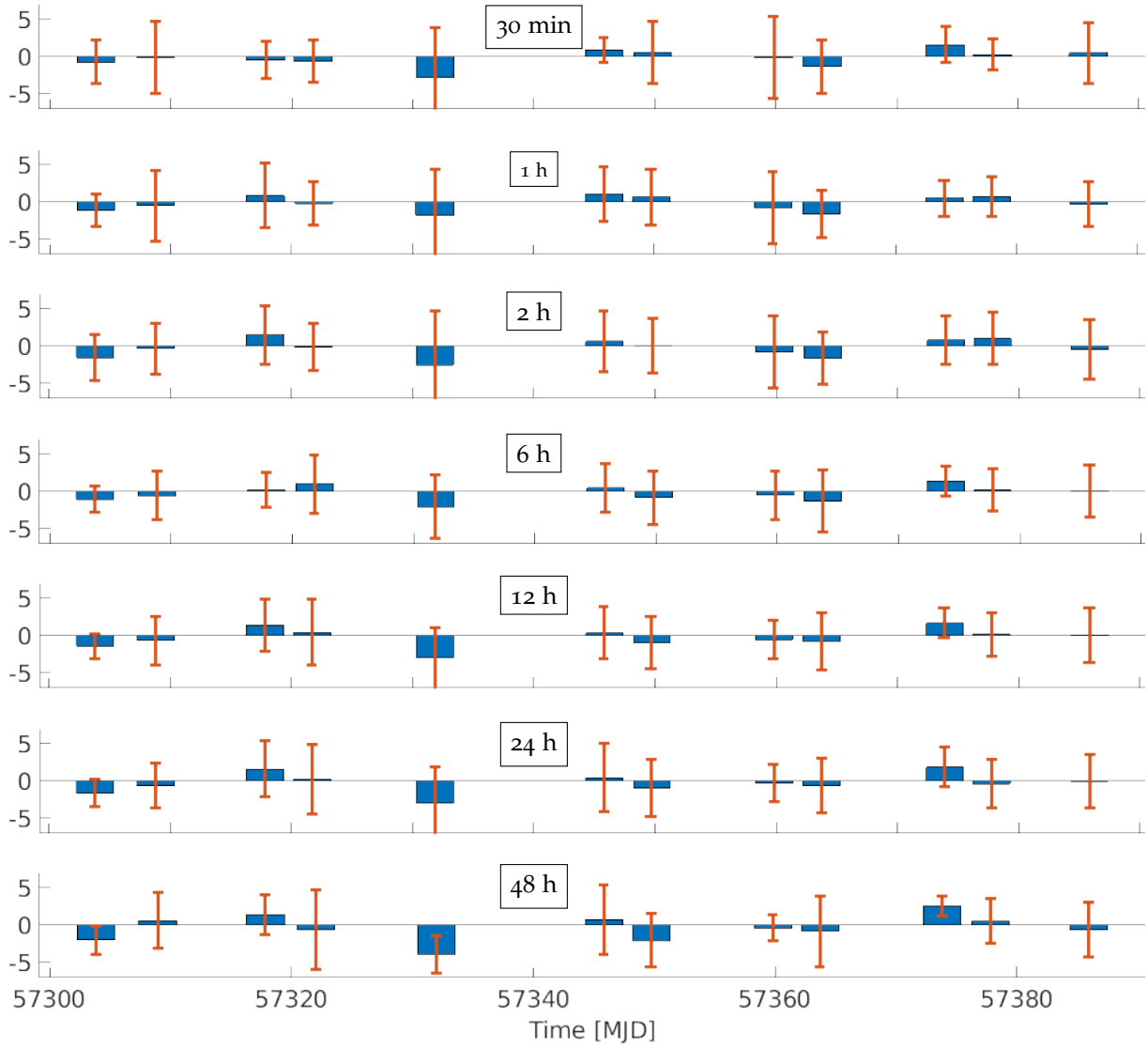

FIGURE 4.6: Mean zenith wet delays and standard deviations (in mm) over each session for WETTZ13N relative to WETTZELL, for the different parametrisations of the clock (time resolution), in the BA2 approach.

All mean δZWD values range within -3.9 mm and 2.6 mm, with an average scatter of 3.5 mm. Both the minimum mean value and the largest scatter are found in session R4712 (MJD 57331). This session shows consistently large δZWD values, a behaviour also seen in the residuals of Figure 4.3. The behaviour of the mean δZWD is affected by the change in the clock interval, with variations at in the sub-mm level, where the mean values of the δZWD range from -0.16 mm to -0.36 mm for the clock parametrisation using 2 h and 48 h, respectively. This indicates that systematic effects in height are smaller than about 1.5 mm, as a tropospheric error of 1 mm will lead to an error in height of about 4 mm (Beutler, G. et al., 1987b). The solutions with a clock parametrisation of 6 h show the smallest values of standard deviations (3.18 mm), which indicates again the suitability of this interval for the clock parameters. Moreover, to complement the analysis of the troposphere, the daily average differences of the troposphere delays between the VLBI-based estimation and the CODE products for the GNSS station WTZR (Dach, R. et al. (2017)) were calculated. Figure 4.7 shows the session mean differences for the global solution GLO for WETTZELL in red and for WETTZ13N in green, where the ZTD have been corrected for the height difference between the reference points of the telescopes and the GNSS antenna. Once more, the mean values of the time series for both groups of differences, show a mm to sub-mm agreement with respect to the GNSS station WTZR, after considering the height difference of the antennas. Table 4.6 shows a summary of these values for all the investigated solutions. The sub-mm differences for parametrisations lower than six hours support the selection of the intervals of clock estimation.

	Clock Interval [h]	0.5	1	2	6	12	24	48
WETTZELL-WTZR	Mean [mm]	-0.3	-0.6	-0.9	-1.0	-1.6	-1.8	-1.7
WETTZ13N-WTZR	Mean [mm]	-0.5	-0.6	-0.9	-1.0	-1.5	-1.6	-1.7

TABLE 4.6: Mean zenith tropospheric differences between VLBI and GNSS (in mm), for different intervals of the clock parametrisation (corrected for height differences).

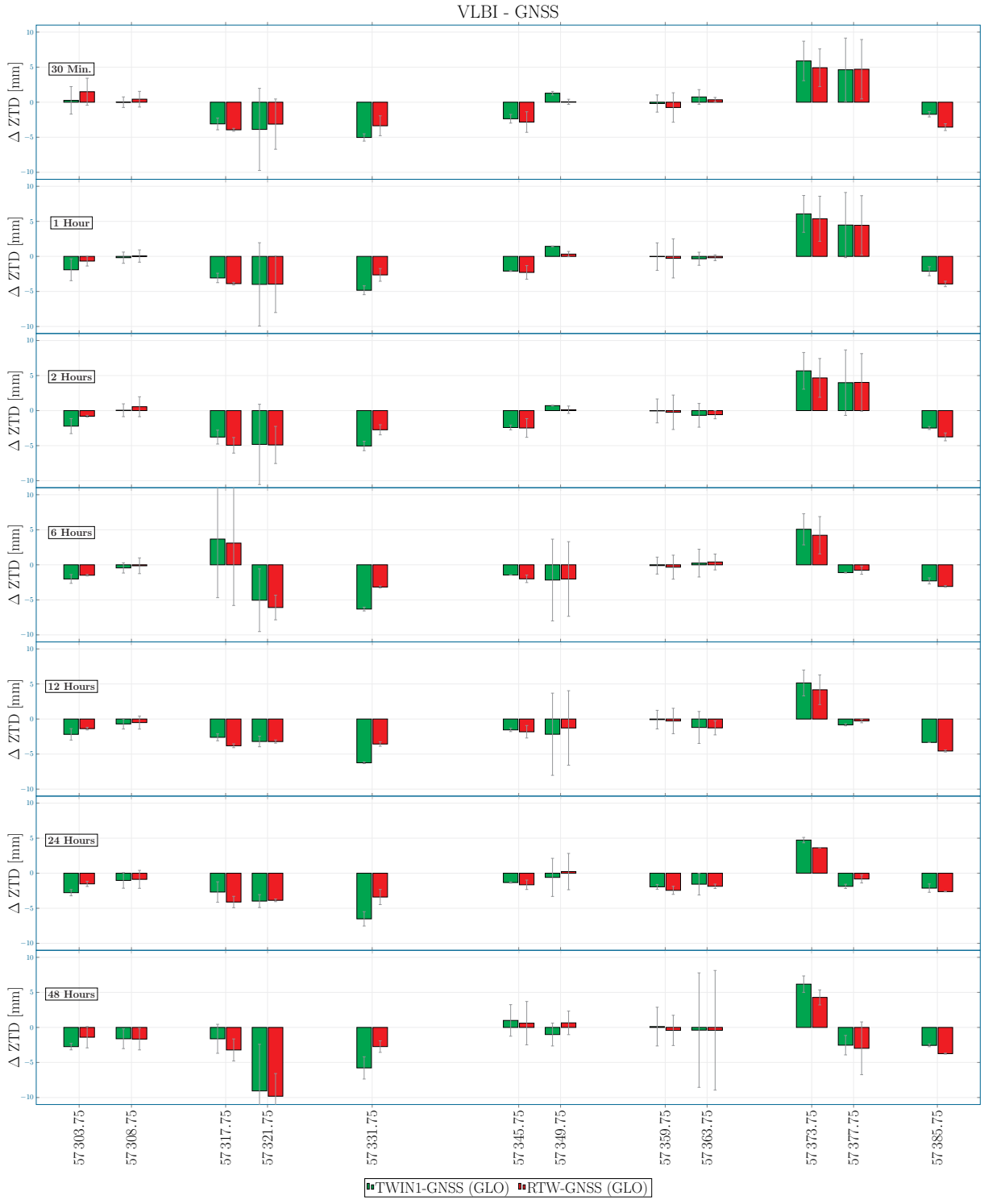

FIGURE 4.7: Tropospheric zenith total delay difference WETTZELL-WTZR (Red) and WETTZ13N-WTZR (Green), from the GLO solution for the different parametrisations of the clock estimates, with respect to the mean Julian date (x-axis). The ZTD have been corrected to account for the height difference among stations.

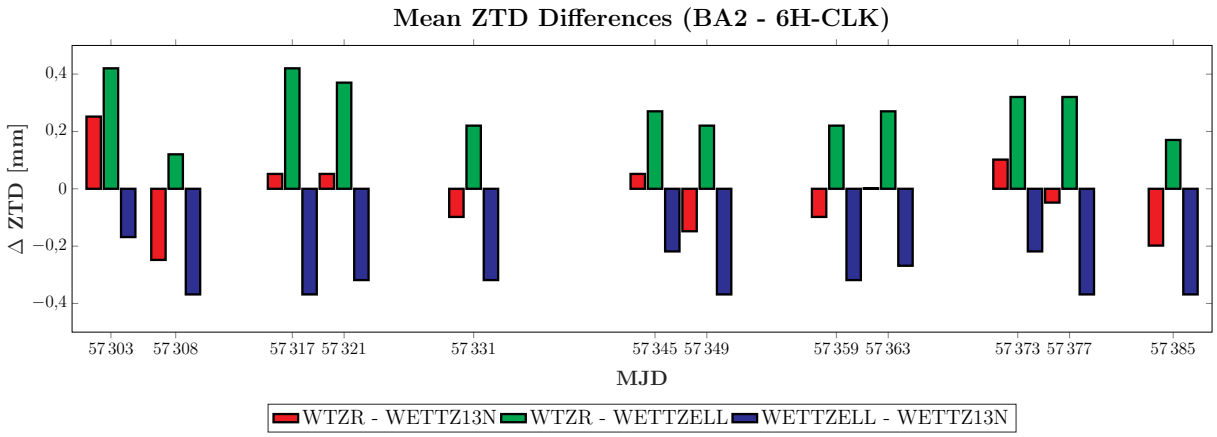

FIGURE 4.8: Mean ZTD difference between VLBI and GNSS (corrected for height differences).

4.4.4 *Station Coordinate Behaviour and Comparison to Local Ties*

The estimation of station coordinates is performed per session and solution and, since for the short baseline solutions the datum was fixed using station WETTZELL, the resulting daily 3D Cartesian coordinates of station WETTZ13N are compared with the "ground truth" coordinates, provided by the ITRF2014 solution. Figure 4.9 shows these differences for the solutions with intervals for the estimation of the clock offset of 30 min. As expected, the global solution displays the largest differences, of up to 20 mm, whereas the short baseline solutions show a mm to sub-mm agreement for the three components. Table 4.7 summarises these average differences, per component, together with their standard deviations. Both local baseline solutions exhibit a similar average performance, the main difference being their standard deviations, with the smaller scatter found for the BAS solutions. Regarding the selection of the interval for the estimation of the clock offsets, the three solutions (GLO, BAS and BA2) show the best agreement when selecting intervals of 6 h or 12 h. Additionally, with the coordinate estimates per session, the baseline WETTZELL-WETTZ13N is calculated and compared to the terrestrial measurements of Table 4.4. These time series of differences are displayed in Figure 4.10. The comparison of the VLBI-derived baseline length with the local ties shows a much better agreement. The differences for the GLO solutions range from -13.6 mm to 8.4 mm, whereas the performance for the baseline solutions is much better, ranging from -3.0 mm to 5.7 mm for the BAS solution, and from -3.9 mm to 2.6 mm for the BA2 solution. Session R4712 delivers the largest differences, especially for the GLO solutions. Despite the mm-level minimum and maximum values of the time series, the mean values show satisfactory results. The three solutions (BAS, BA2 and GLO), show a sub-mm agreement between the VLBI-derived baseline and the local tie. The best results for the BA2-based differences are obtained with an interval for the clock estimates of 6 h with a mean value of -0.0 ± 1.7 mm. The best results for the BAS-based differences is obtained with an interval for the clock estimates of 12 h with a mean difference of 0.1 ± 1.8 mm. Likewise, the GLO-based differences reach the best value with an interval for the clock estimates of 12 h, with a mean value of -0.3 ± 4.3 mm. In general terms, all the investigated solutions show an agreement on the sub-mm level, albeit a large variability along the time series for

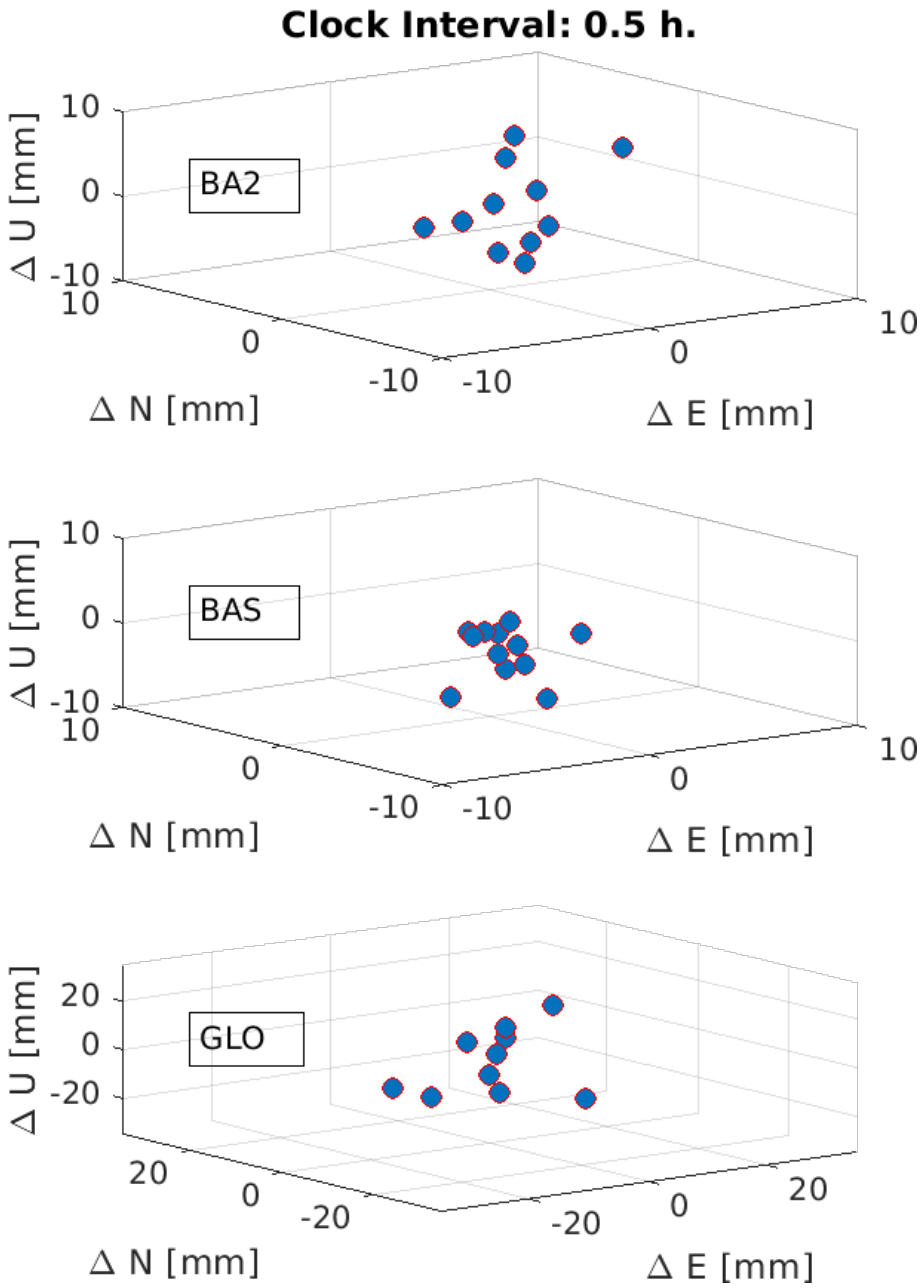

FIGURE 4.9: Differences with respect to the ITRF2014 solution, for the station WETTZ13N in ENU components, for the three different approaches, with clock estimates each 30 min. Notice the different scale of the axes for the bottom plots (height component).

the global approach. The complete list of average values and standard deviations of the time series is summarised in Table 4.8. The time series obtained do not provide evidence of the occurrence of a particular bias in the estimation of the VLBI-derived baseline, at least with a resolution on the mm-level, so the influence of the thermal and gravitational deformation of the antennas mentioned by Schüler, T. et al. (2015) could not be observed. The influence of these factors is most likely to be present in the height component, and therefore cannot be determined from the analysis of the baseline.

Type, Clk. Interval [h]		$\overline{E}$	$\overline{N}$	$\overline{U}$	σ_E	σ_N	σ_U
BA2	0.5	-0.3	-0.7	1.0	3.6	4.5	4.5
	1	-0.5	-0.3	1.3	3.1	4.8	4.9
	2	-0.3	0.1	2.0	2.6	4.7	4.8
	6	0.0	0.1	1.5	1.7	5.1	5.2
	12	0.3	-0.0	0.9	1.6	4.8	4.9
	24	0.5	-0.1	1.8	1.6	5.1	5.6
	48	0.6	-0.0	1.0	2.2	7.5	7.9
BAS	0.5	0.3	-0.5	-2.2	1.4	2.2	2.3
	1	0.3	-0.3	-2.0	1.3	2.1	2.2
	2	0.3	-0.1	-2.0	1.3	1.8	1.9
	6	0.5	-0.1	-2.1	1.1	2.0	2.1
	12	0.5	-0.0	-2.3	1.2	2.0	2.1
	24	0.8	-0.0	-2.0	1.5	2.1	2.1
	48	0.9	0.2	-2.2	2.0	2.0	2.1
GLO	0.5	0.1	-0.8	-1.8	3.9	5.0	5.5
	1	0.1	-0.8	-2.2	3.7	4.7	5.1
	2	0.1	-1.1	-3.0	3.3	4.7	5.1
	6	-0.2	-0.9	-2.5	2.6	4.3	4.7
	12	-0.4	-0.5	-2.2	2.4	4.0	4.3
	24	-0.3	-0.0	-2.1	2.2	4.6	5.1
	48	-0.7	0.0	-2.4	2.7	7.8	8.6

TABLE 4.7: Mean differences and standard deviations (in mm), with respect to the ITRF2014 solution, for the geocentric Cartesian coordinates of station WETTZ13N, expresed in a local coordinate frame (ENU).

	BA2 [mm]		BAS [mm]		GLO [mm]	
Clk. Int. [h]	$\overline{\Delta}$	σ	$\overline{\Delta}$	σ	$\overline{\Delta}$	σ
0.5	0.6	1.9	0.5	1.6	-0.6	4.7
1	0.3	2.0	0.3	1.3	-0.6	4.9
2	-0.1	1.9	0.1	1.2	-1.0	4.7
6	-0.0	1.7	0.2	1.7	-0.7	4.4
12	0.1	1.7	0.1	1.8	-0.3	4.3
24	0.2	1.6	0.1	2.0	-0.5	4.1
48	0.1	1.8	-0.1	1.4	-0.5	4.4

TABLE 4.8: Differences in baseline length between the investigated solutions and the local ties. The $\overline{\Delta}$ indicates the average value of the baseline length differences and σ their corresponding standard deviation of the time series which includes all the processed VLBI sessions, in relation to the different clock intervals used.

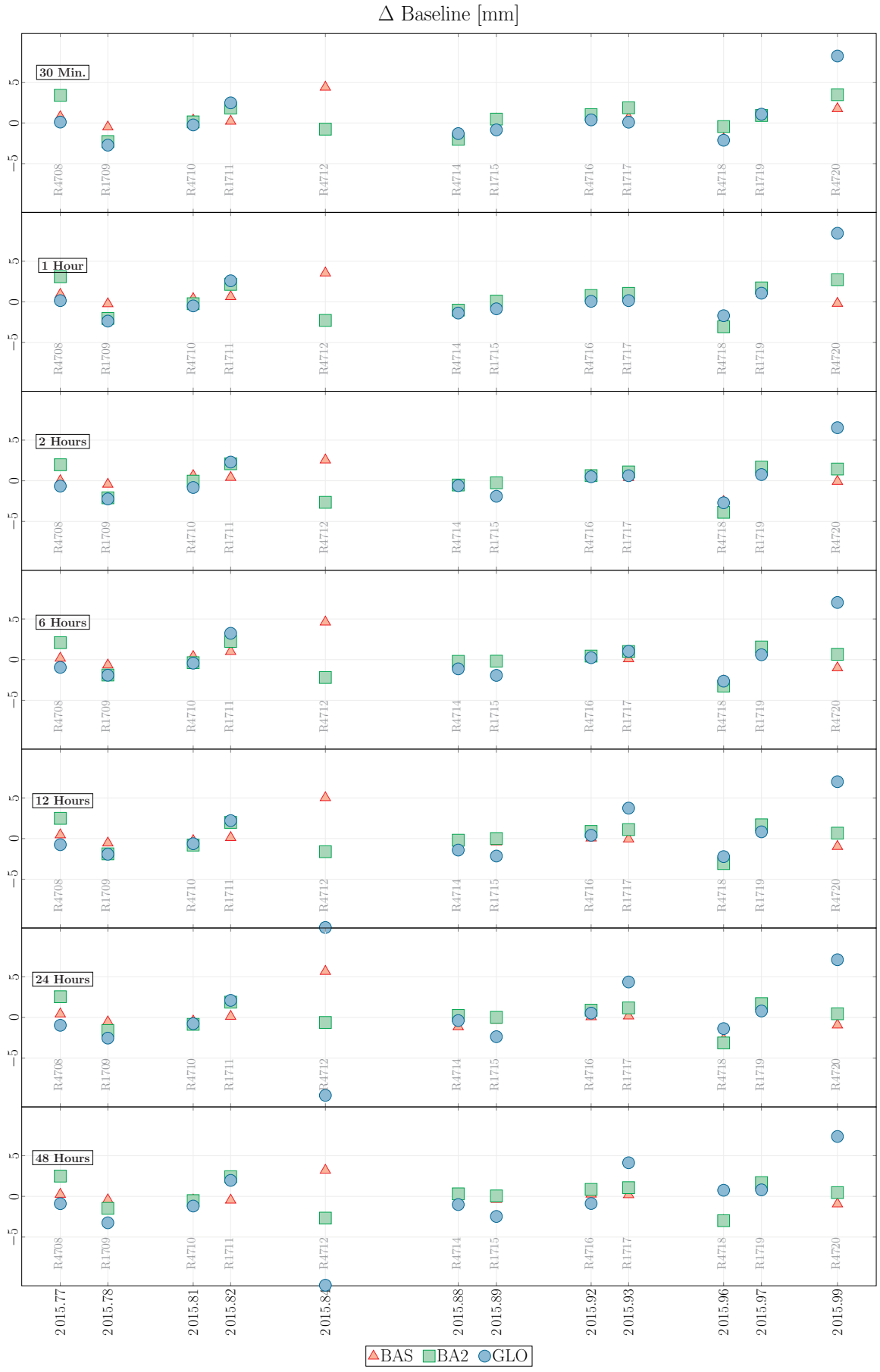

FIGURE 4.10: Difference between the local tie and the VLBI-derived baseline length (in mm), for the three different solution types.

4.4.5 *Comparison of VLBI Clock Estimates and TWOTT-Based Solutions*

It is the ultimate goal of the TWOTT to distribute time at the fundamental station and make the estimation of clock corrections unnecessary, apart from one clock offset per session. To test whether the TWOTT data can replace the clock estimation, the TWOTT time series of clock corrections was introduced into the VLBI analysis. As TWOTT and VLBI clock corrections differ by a large offset, a mean clock offset was removed for each session. The resulting values were used as clock corrections in a solution, where only coordinates were estimated. In addition to the linear trend, possible biases due to un-calibrated instrumental delays offsets absorbed in the VLBI estimates have to be eliminated. These station- and session-specific delays are absorbed by the estimated receiver clock and distort the estimated clock differences by tens of nanoseconds. Furthermore, the comparison of each coordinate solution with respect to the local tie was studied.

Figure 4.11 shows the time series of the local tie comparison, when using TWOTT clock corrections for both local baseline solutions. While most of the session solutions are nearly identical, the overall performance of the time series shows promising results: with a mean value of 0.0 ± 1.6 mm for the BAS solution, and -0.2 ± 1.7 mm for the BA2 solution. Thus, the use of the TWOTT data contributes to achieve a sub-mm agreement for the baseline solution with respect to the local tie, accounting for the clock behaviour during the session without introducing new parameters in the estimation. This shows the potential of its use for the attainment of stronger solutions, in the sense that they require less parameters to estimate, while keeping a comparable level of precision.

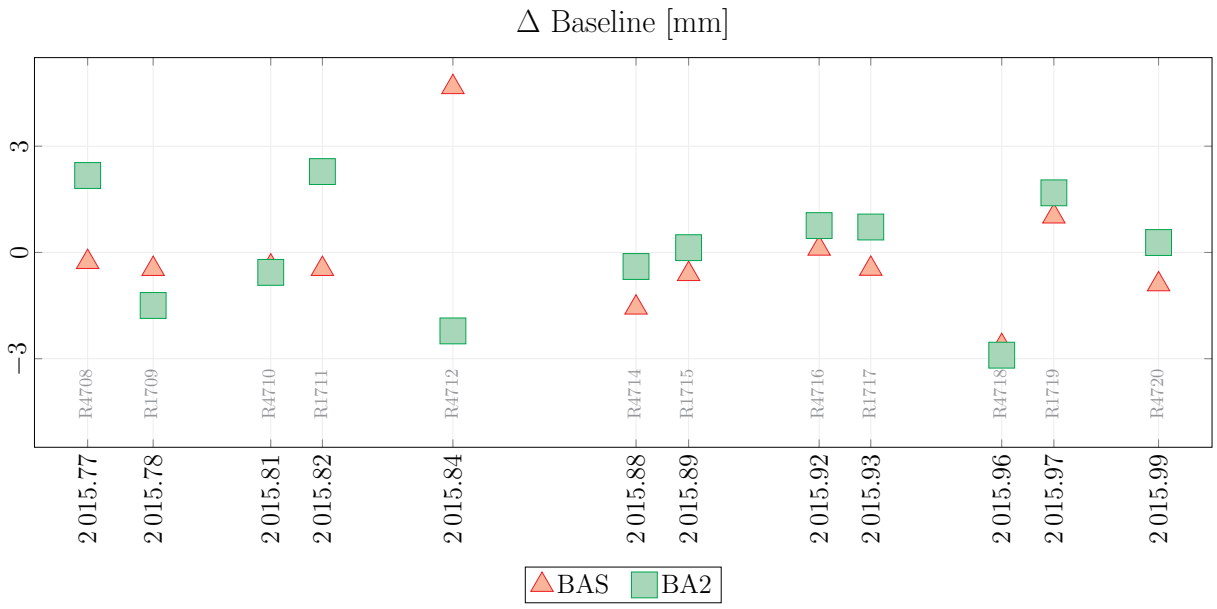

FIGURE 4.11: Difference between the local tie and the TWOTT-based baseline length (in mm), for the local baseline approaches BAS and BA2.

4.5 CONCLUSIONS AND OUTLOOK

This work presents investigations on the determination of geodetic parameters using the short VLBI baseline between the RTW and the TWIN1 telescopes, at the Wettzell Observatory, where several processing approaches in terms of local troposphere and clock parametrisation were tested. The coordinates obtained for these solutions were subsequently compared with the local tie (baseline length and components) at the site, obtaining a sub-mm agreement of the estimated baseline with the terrestrial measurements, with mm-level standard deviations. Moreover, the estimated troposphere parameters (zenith wet delays) were also calculated and validated with respect to the troposphere tie at the site, where a mm-level agreement (after considering the height difference between the telescopes) was found. Besides the multiple time intervals for the parametrisation of the clock offset, an additional analysis of the clock behaviour for the short VLBI baseline was performed, where the TWOTT data is used to replace the clock estimation. Comparable results for the clock modelling in terms of drift are obtained, with a significant improvement of the RMS. The use of TWOTT to replace the clock estimation yields comparable results in terms of station coordinates, and their comparison with the local tie, to those obtained from the pure VLBI estimation. Moreover, for sessions with an atypical clock behaviour (quadratic rather than linear), the use of TWOTT improves the consistency of the solutions. These multiple studies serve as a tool to show the potential of the clock modelling using the TWOTT data, to reach the goals of accuracy and stability of GGOS. Future work will focus on the use of the local time transfer system, to improve the estimation of other geodetic parameters, such as Earth Orientation Parameters.

ACKNOWLEDGEMENTS Special thanks to Dr. Jan Kodet and Prof. Dr. Ulrich Schreiber, at the Geodetic Observatory Wettzell, and to Dr. Benjamin Männel, at the GeoForschungZentrum Potsdam, for their support in the realisation of this work.

5

EXPERIMENTS ON SHORT SLR BASELINES

Originally published as: ***I. D. Herrera-Pinzón*** *et al. (Dec. 2021). "Differencing strategies for SLR observations at the Wettzell observatory". In:* Journal of Geodesy *96.4.* ISSN*: 1432-1394.* DOI*:*
https://doi.org/10.1007/s00190-021-01588-4

Paper IV

Differencing Strategies for SLR Observations at the Wettzell Observatory

Iván Herrera-Pinzón[1], Markus Rothacher[1] and Stefan Riepl[2]
[1] Institute for Geodesy and Photogrammetry, ETH Zurich. Switzerland
[2] Federal Agency for Cartography and Geodesy, Wettzell Observatory. Germany

(Author's version. It differs from the published paper only in terms of layout and formatting)

Abstract

The precise estimation of geodetic parameters using single- and double-differenced SLR observations is investigated. While the differencing of observables is a standard approach for the GNSS processing, double differences of simultaneous SLR observations are practically impossible to obtain due to the SLR basic principle of observing one satellite at a time. Despite this, the availability of co-located SLR telescopes and the use of the alternative concept of *quasi-simultaneity* allow the forming of SLR differences under certain assumptions, thus enabling the use of these processing strategies. These differences are in principle almost free of both, satellite- and station-specific error sources, and are shown to be a valuable tool to obtain relative coordinates and range biases, and to validate local ties. Tested with the two co-located SLR telescopes at the Geodetic Observatory Wettzell (Germany) using SLR observations to GLONASS and LAGEOS, the developed differencing approach shows that it is possible to obtain single- and double-difference residuals at the millimetre level, and that it is possible to estimate parameters, such as range biases at the stations and the local baseline vector with a precision at the millimetre level and an accuracy comparable to traditional terrestrial survey methods. The presented SLR differences constitute a valuable alternative for the monitoring of the local baselines and the estimation of geodetic parameters.

5.1 INTRODUCTION

Satellite Laser Ranging (SLR) is one of the four main geodetic techniques involved in the realisation of the International Terrestrial Reference Frame (ITRF). In particular, SLR contributes to the determination of the scale and the origin of the frame, but it is also involved in the determination of the gravity field of the Earth, and it is widely used for the validation of satellite orbits. In the operating principle of SLR, at an SLR ground station, a short laser pulse is generated and sent with an optical telescope to a single satellite. The satellite has retro-reflectors attached to its surface, that reflect the laser pulse back to the ground station. With the telescope at the ground station the reflected pulse is then detected and analysed. Based on the time of emission of the original pulse and the time of reception of the reflected pulse, the light travel time, the range between the satellite and the telescope can be computed. Core stations of the International Laser Ranging Service (ILRS) (Pearlman, M. et al., 2019b) are able to provided normal point measurements with a millimetre-level precision (Luceri, V. et al., 2019). Thus, observations to SLR-dedicated satellite missions, such as LAGEOS or Etalon, and more recently to Global Navigation Satellite Systems (GNSS) satellites, turn SLR into a reliable and accurate technique for the determination of geodetic and geophysical parameters. However, systematic errors at the station level together with mismodellings of the centre of masses of the satellites, threaten the accuracy of these range observations. To this end, the ILRS performs the continuous monitoring of systematic error sources at the station level, for an enhancement of the realisation of the ITRF, searching for improving the agreement between the scale provided by SLR and the remaining geodetic techniques (Luceri, V. et al., 2019). Systematic time biases in range observations (which amount to few μs) degrade the accuracy of the estimated satellite orbits, affecting the station coordinates by several millimetres, and have to be removed, for instance with the time synchronisation of stations using time transfer by laser links to satellites (Exertier, P. et al., 2017).

At the Geodetic Observatory Wettzell, two SLR telescopes, increasing the observation capabilities, have been operating for quite some time. In consequence, an ideal setup for the assessment and testing of the differencing approach has become available on a very short SLR baseline. The two co-located SLR telescopes, connected by a local tie, controlled by a common timing system and affected by (almost) the same atmospheric effects, allow the study of the size and stability of instrumental biases, the quality of the local tie, and a detailed investigation of new processing strategies. Forming double-differences is a standard approach in GNSS processing (Hofmann-Wellenhof, B. et al., 2008). The advantage of forming single- or double-differences is the elimination (or strong reduction) of satellite- (differences between stations) and station-specific (differences between satellites) error sources and the high accuracy achieved for short baselines, as well as an adequate approach to reduce the number of parameters (especially clock corrections) during the estimation procedure. Applying these methods to SLR observations results in a tool to assess existing satellite- and station-specific biases in SLR, and to estimate accurate relative coordinates between neighbouring telescopes, an important approach to validate local ties. However, it is very difficult to obtain simultaneous SLR observations in practice. While two SLR telescopes can

in principle observe the same satellite simultaneously, when given the same schedule for the observation and under optimal weather conditions, simultaneous SLR observations from one telescope to two satellites are not feasible in practice. Therefore simultaneous double-differences cannot be formed, and therefore, we have to resort to *quasi-simultaneous* observations.

The idea of *quasi-simultaneity* was first introduced in Pavlis, E., 1985 as a tool to avoid the propagation of orbital errors, implicitly included in the range observations, into the estimated parameters. To achieve simultaneous SLR observations, the ranges of two stations were interpolated using cubic splines. Based on a large set of observations to the LAGEOS satellites, as well as multiple simulations, his thorough analysis showed that the use of differenced ranges mitigates orbital errors and achieves the estimation of baseline lengths with centimetre-level accuracy, even under the presence of satellite orbit errors on the metre level. Additionally, the quality of this method was demonstrated to be related to the geometry of the network and the observed satellites, with the best results obtained from passes parallel to the baseline direction. Similarly, Dedes, G. C. et al., 1989 used the idea of quasi-simultaneous observations from pairs of stations to obtain simultaneous range differences for the estimation of baselines independently of orbital errors. Their work used SLR observations to LAGEOS satellites, and the quasi-simultaneity is achieved through the interpolation of the observed laser ranges with Chebychev polynomials, and a careful procedure for the elimination of outlier observations. They concluded that, given enough observations, it is possible to estimate baselines up to 1000 km with centimetre-level accuracy. A concept for double-differences of SLR obsrvations was later explored by Svehla, D., 2018 with the baseline between the telescopes GRZL at Graz (Austria) and HERL at Herstmonceux (UK), and observing only two Galileo satellites. This approach forms SLR normal points at common epochs for both satellites, using first order polynomials fitted to the normal points of the GRZL station, so that its SLR normal points are interpolated to epochs of the normal points of the HERL station, separately for each satellite and tracking pass. By fixing the IGS orbits, his study shows that the formed double-differences allow the estimation of relative coordinates for the baseline GRZL-HERL at the level of 1-8 mm.

In contrast, our approach for building differences uses the advantage of a very short SLR baseline, with a custom-made quasi-simultaneity strategy to build single- and double-differences based on the linearised observation equations derived for the original ranges, without the need to interpolate either the normal points nor the original ranges. We only require a continuous representation of the satellite orbits, i.e., dynamic orbits. Additionally we try to maximise the number of observations by focusing on more than two satellites simultaneously, including SLR observations to both, GNSS and LEO satellites. From this perspective, this paper discusses the applicability and potential of the differencing approaches, namely single- and double-differences, for the estimation of geodetic parameters with SLR observations. These differences, together with the original ranges (zero-differences), are used to get estimates of both, satellite- and station-specific error sources, so that systematic effects common to both stations can be identified at millimetre-level. This approach, therefore, may potentially improve

the processing of classical SLR observations of GNSS and LEO satellites and the estimation of accurate local ties. The rest of the paper is structured as follows: Section 5.2 outlines the concept of quasi-simultaneity, which constitutes the basis of our work. The available data set and the processing strategy used for the estimation of parameters are described in Section 5.3. Before summarising the paper in Section 5.5, Section 5.4 discusses the results derived from the short SLR baseline in Wettzell regarding station coordinates and range biases, and the comparison of the derived baseline vector with the terrestrial local tie.

5.2 IDEA AND FORMALISM

5.2.1 *Concept of Quasi-Simultaneity*

The fundamental tool to build single and double differences of SLR observations is the concept of *quasi-simultaneous* observations. Two observations are considered quasi-simultaneous if they lie within a specified time window. This is, range i from telescope 1 to satellite k observed at time t_i ($\rho_1^k(t_i)$) and range j from telescope 2 to satellite l at time t_j ($\rho_2^l(t_j)$) are considered quasi-simultaneous if $\|(t_j - t_i)\| \leq \delta_t$, where δ_t is the so-called quasi-simultaneity, a fixed value. If t_j and t_i satisfy this condition, they are considered *quasi-simultaneous epochs*. Figure B.7 shows the concept of quasi-simultaneity for an SLR baseline, where the time epochs for the observations from telescope 2 with respect to telescope 1 are t_1 and t_2 for satellite 1 and 2, respectively. Using this idea, three types of differences can be built, namely

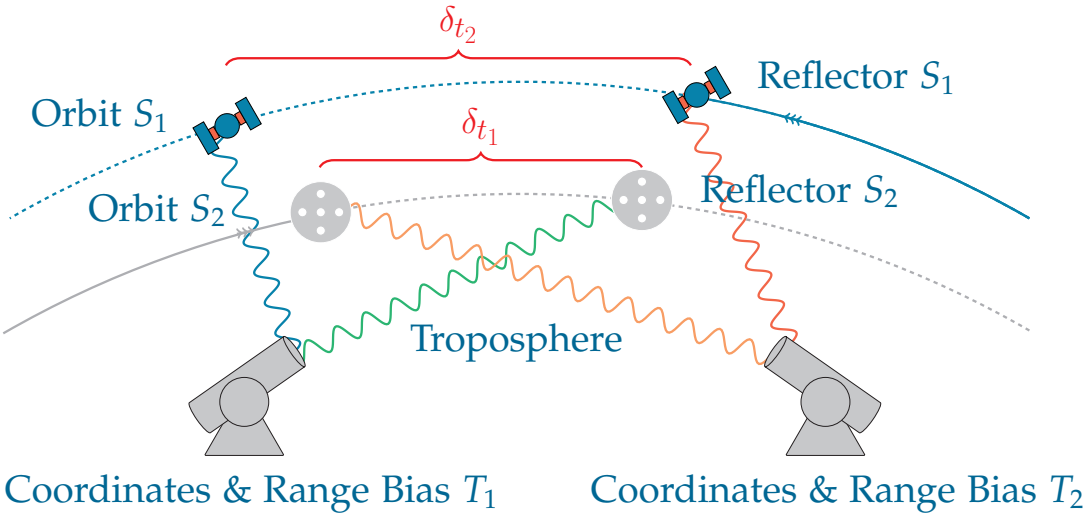

FIGURE 5.1: Concept of quasi-simultaneity for the differencing of SLR observations, together with the error sources targeted with these approaches. Two satellites (S_1 and S_2) in different orbits are observed. The quasi-simultaneity of the observations to satellite S_1 is given by δ_{t_1}, while the quasi-simultaneity of the observations to satellite S_2 is given by δ_{t_2}.

1. Single-differences from two telescopes to the same satellite:

$$SD_{1,2}^l(t_i, t_j) = \rho_2^l(t_j) - \rho_1^l(t_i), \quad \text{for} \quad \|(t_j - t_i)\| \leq \delta_t$$

By observing the same satellite from two telescopes at quasi-simultaneous epochs, orbit and retro-reflector errors are strongly reduced. For the short baseline in Wettzell the tropospheric delays are eliminated as well (apart from the effect of the height difference between the telescopes).

2. Single-differences from one telescope to two satellites:

$$SD_m^{k,l}(t_i, t_j) = \rho_m^l(t_j) - \rho_m^k(t_i), \quad \text{for} \quad \|(t_j - t_i)\| \leq \delta_t, \quad m = 1, 2$$

This definition includes the special case of observing the same satellite at two different epochs, as long as the quasi-simultaneity condition is met:

$$SD_m^k(t_i, t_j) = \rho_m^k(t_j) - \rho_m^k(t_i), \quad \text{for} \quad \|(t_j - t_i)\| \leq \delta_t, \quad m = 1, 2$$

If observations are made from one telescope to two satellites at quasi-simultaneous epochs, the influence of instrumental biases caused by the station setup are practically eliminated.

3. Double-differences:

$$DD_{1,2}^{k,l}(t_{i_1}, t_{j_1}, t_{i_2}, t_{j_2}) = \left(\rho_2^l(t_{j_1}) - \rho_1^l(t_{i_1})\right) - \left(\rho_2^k(t_{j_2}) - \rho_1^k(t_{i_2})\right),$$

for $\|(t_{j_1} - t_{i_1})\| \leq \delta_{t_1}$ and $\|(t_{j_2} - t_{i_2})\| \leq \delta_{t_2}$. Similarly to the single differences from one telescope to two satellites, building double differences with the concept of quasi-simultaneous observations allows the special case of having double differences to the same satellite ($k = l$) at different epochs. Double-differences are expected to eliminate both, satellite-specific (orbits and retro-reflectors) and station-specific (instrumental biases) errors.

5.2.2 *Single-Difference Observation Equation from two Telescopes to one Satellite*

From a practical perspective, the SLR ranges are processed as in a usual SLR processing to obtain the so-called *zero-difference* linearised observation equations. These zero-difference linearised observation equations are later differenced to obtain the single- and double-difference systems of linear equations. The use of zero-difference ensures that the original ranges are processed at the exact epoch, which in turn avoids the necessity to interpolate the two ranges to a common epoch. Formally, given an observation from the telescope m to the satellite k at time t_i, $\rho_m^k(t_i)$, the simplified SLR observation equation reads as

$$\rho_m^k(t_i) = \mathrm{P}_m^k + \delta\rho_{m,atm}^k + \delta\rho_{m,rel}^k + \delta\rho_{m,sys} + \delta\rho_{sys}^k + \varepsilon_m^k$$

with P_m^k the geometrical distance between the satellite and the station at the observation time t_i, $\delta\rho_{m,atm}^k$ the delay (refraction) in the troposphere, $\delta\rho_{m,rel}^k$ the relativistic correction, $\delta\rho_{m,sys}$ delays in the laser system (among others a range bias B_m), $\delta\rho_{sys}^k$ the retroreflector correction and ε_m^k the measurement error. Using standard models to account for the troposphere, such as Mendes, V. B. et al., 2004, applying the relativistic correction,

and using precise orbits for the satellites, the linearized zero-difference observation equations are given by

$$\mathbf{A}_m^{ZD}\,\boldsymbol{\Delta x} - \mathbf{b}_m^{ZD} = \mathbf{v}_m^{ZD}$$

where $\boldsymbol{\Delta x} = (x_m, y_m, z_m, B_m)^T$ is the vector of the unknown parameters containing geocentric coordinates and range biases, $\mathbf{A}_m^{ZD}$ contains the partials of the observation equation with respect to the unknowns

$$\left(\frac{\partial \rho_m^k(t_i)}{\partial x_k(t_i)}, \quad \frac{\partial \rho_m^k(t_i)}{\partial y_k(t_i)}, \quad \frac{\partial \rho_m^k(t_i)}{\partial z_k(t_i)}, \quad \frac{\partial \rho_m^k(t_i)}{\partial B_k(z_i)}\right)$$

and each element of the reduced observation vector (observed–computed) $\mathbf{b}_m^{ZD} = [b_m^k(t_i)]$ is given by

$$b_m^k(t_i) = \rho_m^k(t_i) - \rho_{0_m}^{\,k}(t_i)$$

with $\rho_{0_m}^{\,k}(t_i)$ the result of the a-priori values applied in the observation equation. When n_1 and n_2 observations are available for telescope 1 and 2, respectively, the system of linear equations is given by

$$\mathbf{A_m^{ZD}} = \begin{bmatrix} \frac{\partial \rho_m^1(t_1)}{\partial x_1(t_1)} & \frac{\partial \rho_m^1(t_1)}{\partial y_1(t_1)} & \frac{\partial \rho_m^1(t_1)}{\partial z_1(t_1)} & \frac{\partial \rho_m^1(t_1)}{\partial B_1(t_1)} \\ \frac{\partial \rho_m^2(t_2)}{\partial x_2(t_2)} & \frac{\partial \rho_m^2(t_2)}{\partial y_2(t_2)} & \frac{\partial \rho_m^2(t_2)}{\partial z_2(t_2)} & \frac{\partial \rho_m^2(t_2)}{\partial B_2(t_2)} \\ \vdots & \vdots & \vdots & \vdots \\ \frac{\partial \rho_m^k(t_i)}{\partial x_{n_m}(t_i)}, & \frac{\partial \rho_m^k(t_i)}{\partial y_{n_m}(t_i)}, & \frac{\partial \rho_m^k(t_i)}{\partial z_{n_m}(t_i)}, & \frac{\partial \rho_m^{S_k}(t_i)}{\partial B_{n_m}(t_i)} \end{bmatrix}_{n_m \times 4}, \quad \mathbf{b_m^{ZD}} = \begin{bmatrix} b_m^1(t_1) \\ b_m^2(t_2) \\ \vdots \\ b_m^k(t_i) \end{bmatrix}_{n_m \times 1}$$

with the index $m = 1, 2$ for each telescope. In order to build the single-difference linear equation system from two telescopes to one satellite, we adapt the approach of Beutler, G. et al., 1987a; Beutler, G. et al., 1986 to the SLR case using all the available observations at the two telescopes $[\mathbf{b_1^{ZD}}, \mathbf{b_2^{ZD}}]^T$ which satisfy the quasi-simultaneity condition $\|t_i - t_j\| \leq \delta_t$, and define the single-difference operator $\mathbf{C_{sd}}$ as

$$\mathbf{C_{sd}} = \begin{bmatrix} 1 & 0 & 0 & \cdots & -1 & 0 & 0 & 0 \\ 1 & 0 & 0 & \cdots & 0 & -1 & 0 & 0 \\ 1 & 0 & 0 & \cdots & 0 & 0 & -1 & 0 \\ 0 & 1 & 0 & \cdots & 0 & 0 & -1 & 0 \\ \vdots & \vdots & \vdots & \vdots & \vdots & \vdots & \cdots & \vdots \\ 0 & 0 & 1 & \cdots & 0 & 0 & 0 & -1 \end{bmatrix}$$

where C_{sd} is a matrix with n_m rows and $2n_m$ columns. The single-difference system is obtained as

$$\mathbf{b_{1,2}^{SD}} = \mathbf{C_{sd}} \cdot \begin{bmatrix} \mathbf{b_1^{ZD}} \\ \mathbf{b_2^{ZD}} \end{bmatrix}$$

At this point, the assumption of co-located telescopes, separated by a short baseline, comes into play. For short SLR baselines, quasi-simultaneous observations from two

telescopes observe the satellite in (approximately) the same relative position, provided that δ_t is small enough to account for the dynamics of the orbit. Under this assumption of having the same relative geometry for the two telescopes, the partials of the two telescopes become (nearly) identical, this is $\mathbf{A_1^{ZD}} = \mathbf{A_2^{ZD}}$. Thus, to build the single-difference matrix of partials $\mathbf{A_{1,2}^{SD}}$, only the partials of the first telescope are used. With the help of the single-difference operator, $\mathbf{A_{1,2}^{SD}}$ is calculated as

$$\mathbf{A_{1,2}^{SD}} = \mathbf{C_{sd}} \cdot \begin{bmatrix} \mathbf{A_1^{ZD}} \\ \mathbf{0} \end{bmatrix}$$

Where the zero in the lower part of the matrix represents a matrix with the same dimensions as $\mathbf{A_2^{ZD}}$ and whose elements are zero. The $\mathbf{C_{sd}}$ operator is a function of the number of satellites and the number of epochs at which they are observed, which is ultimately defined by the quasi-simultaneity δ_t used. To take into account the correlations of the single differences, we introduce the weight matrix $\mathbf{P_{sd}}$ (Beutler, G. et al., 1987a; Beutler, G. et al., 1986)

$$\mathbf{P_{sd}} = \left(\mathbf{C_{sd}} \cdot \mathbf{C_{sd}}^T \right)^{-1}$$

The solution of the least squares adjustment (LSA) for the single-differences, using the matrices $\mathbf{A_{1,2}^{SD}}$, $\mathbf{P_{sd}}$ and $\mathbf{b_m^{SD}}$, provides three relative coordinates ($\Delta X = X_2 - X_1$, $\Delta Y = Y_2 - Y_1, \Delta Z = Z_2 - Z_1$) and the relative range biases ΔB. The quasi-simultaneity δ_t and, ultimately, the single-differenced linearised equations system are strongly conditioned by the quality and the dynamics of the satellite orbits. For GNSS and LEO satellites this value should not be larger than 2 h, after which it is no longer possible to ensure that satellite positions have a similar error. A detailed analysis of the optimal threshold for the quasi-simultaniety is discussed in Section 5.3.4. With this assumption in mind, single-differences of two telescopes to one satellite constitute a tool for the estimation of relative coordinates and range biases differences, while mitigating errors associated to the orbits of the satellites.

5.2.3 *Double-Difference Observation Equations*

Similarly to the single-difference case of Section 5.2.2, we build the double-difference observation equation system using all the available observations at the two telescopes $[\mathbf{b_1^{ZD}}, \mathbf{b_2^{ZD}}]^T$ which satisfy the quasi-simultaneity conditions $\|t_i - t_j\| \leq \delta_t$ and $\|t_k - t_l\| \leq \delta_t$, and define the double-difference operator $\mathbf{C_{dd}}$ as

$$\mathbf{C_{dd}} = \begin{bmatrix} 1 & -1 & 0 & 0 & -1 & 1 & \cdots & 0 & 0 & 0 & 0 \\ 1 & 0 & -1 & 0 & -1 & 1 & \cdots & 0 & 0 & 0 & 0 \\ 1 & 0 & 0 & -1 & -1 & 1 & \cdots & 0 & 0 & 0 & 0 \\ \vdots & \vdots & \vdots & \vdots & \vdots & \vdots & \cdots & \vdots & \vdots & \vdots & \vdots \\ 0 & 0 & 0 & 0 & 0 & 0 & \cdots & 1 & -1 & -1 & 1 \end{bmatrix}$$

so that the double-difference system is obtained with

$$\mathbf{b}_{1,2}^{\mathbf{DD}} = \mathbf{C_{dd}} \cdot \begin{bmatrix} \mathbf{b}_1^{\mathbf{ZD}} \\ \mathbf{b}_2^{\mathbf{ZD}} \end{bmatrix} \quad \text{and} \quad \mathbf{A}_{1,2}^{\mathbf{DD}} = \mathbf{C_{dd}} \cdot \begin{bmatrix} \mathbf{A}_1^{\mathbf{ZD}} \\ \mathbf{0} \end{bmatrix}$$

Where the zero in the lower part of the matrix represents a matrix with the same dimensions as $\mathbf{A}_2^{\mathbf{ZD}}$, and whose elements are zero. Notice that this system of linearised equations does not contain the instrumental biases any longer, as they are reduced by the differencing at the same telescope. Similarly to Section 5.2.2, to take into account the correlations between the double-differences, the weight matrix $\mathbf{P_{dd}}$

$$\mathbf{P_{dd}} = \left(\mathbf{C_{dd}} \cdot \mathbf{C_{dd}}^T\right)^{-1}$$

is introduced. The solution of the least squares adjustment for the double-differences, using the matrices $\mathbf{A}_{1,2}^{\mathbf{DD}}$, $\mathbf{P_{dd}}$ and $\mathbf{b}_{\mathbf{m}}^{\mathbf{DD}}$, provides only the three relative coordinates $(\Delta X,\ \Delta Y, \Delta Z)$. To facilitate the understanding of the construction of the single- and double-difference systems of linear equations, Appendix 5.6 shows an example of the technical procedure to build these systems, based on real data.

5.3 AVAILABLE DATA AND PARAMETERISATION

5.3.1 *The Co-located SLR Telescopes at the Wettzell Observatory*

The SLR short baseline at the Geodetic Observatory Wettzell is realised by the Wettzell Laser Ranging System (WLRS) and the Satellite Observing System Wettzell (SOS-W), two optical telescopes operating at the wavelengths 532.1 nm and 1064 nm for WLRS and 849.8 nm for SOS-W. While WLRS has been contributing for more than 30 years to the realisation of the ITRF, SOS-W was placed in operation in early 2016 to cope with the need to track more satellites and distribute the workload. The horizontal distance between systems is ca. 58 m, and the difference in height is about 2.3 m (Figure 5.2). The local tie vector between the two telescopes has been determined by

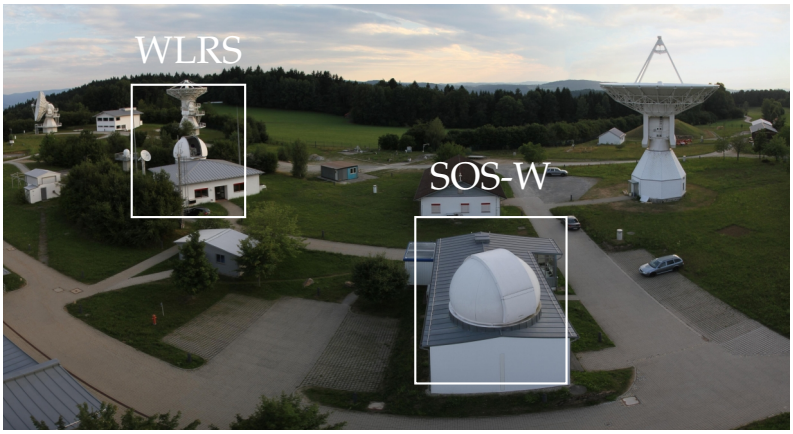

FIGURE 5.2: SLR system at the Geodetic Observatory Wettzell (Source: Technical University Munich).

terrestrial measurements and is continuously compared to the SLR-derived solutions. Moreover, an external calibration target for the SLR systems is available, providing sub-mm accuracy for the definition of the SLR reference points. More details about the operation and the performance of the two systems as well as the characteristics of the local surveys can be found in Riepl, S. et al., 2019. The ITRF2014 coordinates and velocities of the station WLRS from Altamimi, Z. et al., 2016 and the local tie to connect WLRS to SOS-W from Riepl, S. et al., 2019 are given in Table 5.1. Notice that the coordinates of SOS-W are calculated from the ITRF2014 coordinates of WLRS by applying the local tie. More details on the methodology and accuracy of the classical approach for the calculation of the local ties in Wettzell as well as novel approaches for their determination can be found in Klügel, T. et al., 2012; Kodet, J. et al., 2018.

ITRF2014

	X [m]	Y [m]	Z [m]	V_X [m/y]	V_Y [m/y]	V_Z [m/y]
WLRS	4075576.6506	931785.6790	4801583.6984	-0.0157	0.0171	0.0110
SOS-W	4075530.9984	931781.9262	4801619.9971			

Local Tie

ΔX [m]	ΔY [m]	ΔZ [m]
45.6522	3.7528	-36.2987

TABLE 5.1: Coordinates (epoch 2010.0) and velocities of the WLRS system at Wettzell according to Altamimi, Z. et al., 2016. Local tie between WLRS and SOS-W according to Riepl, S. et al., 2019

5.3.2 *SLR Normal Points and Meteorological Data*

The SLR processing using the differencing strategy is based on SLR observations provided as normal point (npt) files. For the scope of this work, we restrict our study to only LAGEOS and GLONASS observations, and we analyse the behaviour of the SLR differences using the available ILRS data (Pearlman, M. et al., 2019b) in the 2-year time interval from 01.01.2018 to 31.12.2019. Selecting those days where WLRS and SOW-S tracked the same satellites, yielded 402 potential sessions with data, from which 172 and 255 sessions contain sufficient GLONASS and LAGEOS data, respectively, to obtain differences. The npt files are converted into range observation files and processed using a dedicated project version of the Bernese GNSS Software (BSW) v5.2 (Dach, R. et al., 2015). In addition, the meteorological data in the npt files is used to calculate corrections for the range observations associated with the influence of the troposphere, using the standard model of Mendes, V. B. et al., 2004. One of the main features of the short SLR baseline is the behaviour of the relative troposphere, where for such a small distance and small height change, meteorological data is expected to vary marginally between the two stations. Analogously to GNSS, this guarantees that the dry part of the relative tropospheric delays can be calculated with the use of standard models (Beutler, G. et al., 1987b; Dilßner, F. et al., 2008; Saastamoinen, J., 1972). To test this assumption, the daily values of atmospheric pressure for the two

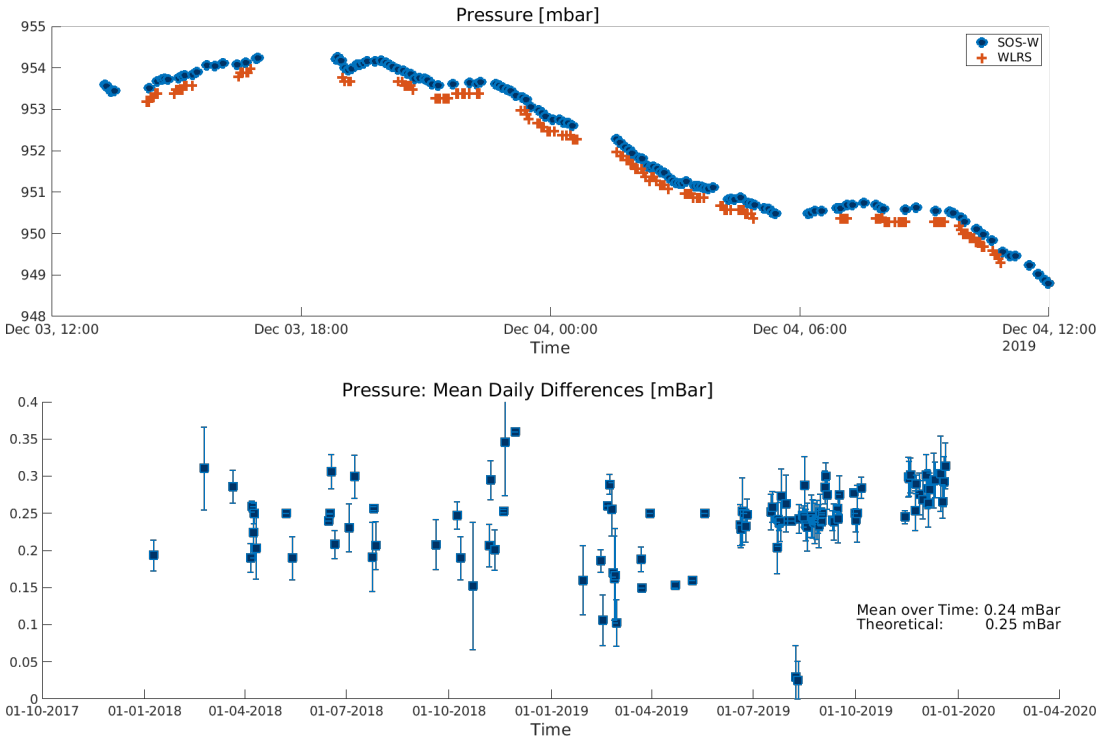

FIGURE 5.3: Top: Atmospheric pressure for the two telescopes (WLRS and SOS-W), for days 03.-04.12.2019. Bottom: Mean daily difference (WLRS minus SOS-W) for the linearly interpolated values at common epochs, and their daily standard deviations. The theoretical difference according to Saastamoinen, J., 1972 is given next to the average over the time series

telescopes were interpolated to common epochs, using the nearest neighbour method, and subsequently subtracted, to obtain a daily mean interpolated difference. Figure 5.3 (top) shows the behaviour of the atmospheric pressure for 03.-04.12.2019 (days of year -DoY- 337 and 338), and the daily mean differences at common interpolated points (bottom), for the 2-year interval. These estimated differences reach 0.26 mbar for the days 03.-04.12.2009, and have an average value of 0.24 mbar over the two investigated years. Additionally, using the height difference between the stations, based on the local tie, a "theoretical" pressure difference was calculated using the simplified model of Saastamoinen, J., 1972 ($P = 1013.25(1 - 0.0000226(h - h_0))^{5.225}$). This theoretical difference amounts to 0.25 mbar. The difference between the daily mean and the theoretical value amounts to less than 0.01 mbar, which in turn corresponds to a negligible differential hydrostatic delay in zenith direction (Beutler, G. et al., 1987b). These results support the assumption of a similar troposphere influence on both ends of the short baseline, and they make sure that we do not introduce errors into the baseline results by using erroneous meteorological data.

5.3.3 *Processing Strategies: Zero-Test and Baseline Estimation*

The data analysis is performed with two types of processing strategies. In the first approach, the so-called *zero-test*, coordinates of the stations are derived from the

ITRF2014 coordinates and velocities, together with the local tie, and are kept fixed for each processed day. Earth rotation parameters, pole coordinates and satellite orbits are assumed fixed and supplied by the products of the Centre for Orbit Determination in Europe (CODE) (Dach, R. et al., 2017), for GNSS, and the ILRS orbits (Pearlman, M. et al., 2019b), for LAGEOS. The meteorological data provided in the npt files are used to correct the ranges for the delays induced by the troposphere, with the help of the empirical model of Mendes, V. B. et al., 2004. Finally, the range biases were not introduced. With this in mind, each station-satellite range is processed individually at each observation epoch. Under these assumptions, namely fixed station coordinates, orbits and Earth orientation parameters, and fixed troposphere parameters, the zero-test processing of a single station-satellite range does not estimate any geodetic parameters, but it is used to obtain the residual of the measurements with respect to the observation model, which in turn serves as a tool to evaluate the quality and noise of the raw observations. The residuals of the two telescopes, called *zero-difference* residuals, are then subtracted considering the concept of quasi-simultaneity of Section 5.2.1, to build single- and double-differenced residuals. On the other hand, for the *baseline* estimation, Earth rotation parameters, pole coordinates and satellite orbits are once more assumed fixed and supplied by the products (CODE & ILRS), and the meteorological data provided in the npt files are used in the Mendes, V. B. et al., 2004 model, and again, no range biases were used during the process. In contrast to the zero-test, for the baseline estimation, the station coordinates are assumed as unknown and calculated with a weighted least squares adjustment. Once more, each station-satellite range is processed individually, and daily station coordinates of both stations are estimated. This process delivers the zero-differenced linearised equation system $\mathbf{A}^{\mathbf{ZD}}_{\mathbf{T_m}}$ and its corresponding zero-differenced reduced observation vector $\mathbf{b}^{\mathbf{ZD}}_{\mathbf{T_m}}$, $m = 1, 2$, for each telescope and each processed day. These linearised equations and reduced observation vectors are then subtracted, using the quasi-simultaneity concept described in Section 5.2.2, to obtain the single- and double-difference linearised equation systems and the single- and double-difference reduced observation vectors, which constitute the main element for our estimation of geodetic parameters. Figure 5.4 shows a summary description of our two main processing strategies. Aside from these two differencing strategies, "standard" SLR solutions are calculated. Within these solutions coordinates and range biases per constellation are determined to benchmark the results of the differencing methods. Their daily normal equations are stored and combined to obtain parameters with the same validity as those obtained with the differencing approaches.

5.3.4 *Selection of the Threshold for the Quasi-Simultaneity*

As mentioned before, the threshold for the quasi-simultaneity δ_t is conditioned by the quality and the dynamics of the satellite orbits. To determine the impact of this limit on the double-differences, we designed a test using satellite orbit solutions from two different processing centres, reflecting the orbital errors to be expected, to form single- and double-differences. The solutions involved are COM (Center for Orbit Determination in Europe -CODE-) and GFZ (GeoForschungsZentrum Potsdam) for the GLONASS satellites, and ILRSA (International Laser Ranging Service) and BKG

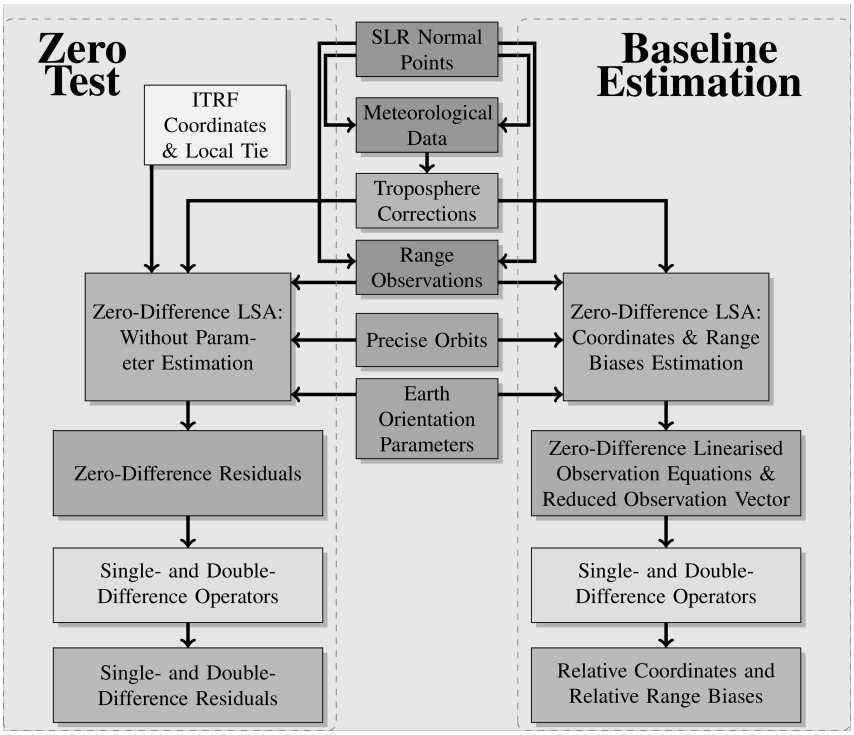

FIGURE 5.4: Summary of the investigated processing approaches. While the zero-test does not perform the estimation of any parameters, thus delivering only zero-difference residuals wrt. the observation model, the baseline estimation performs the calculation of station coordinates, providing the zero-difference linearised equations and reduced observation vectors.

(Bundesamt für Kartographie und Geodäsie) for the LAGEOS satellites. To simulate the effect of the orbital errors on the double-difference observations, we form the double-differences of the two orbits according to Figure 5.5 and the formula

$$\vec{r}_{DD}(\delta_t = t_2 - t_1) = \Delta\vec{r}_2 - \Delta\vec{r}_1 = \left(\vec{r}_{orb_2}(t_2) - \vec{r}_{orb_1}(t_2)\right) - \left(\vec{r}_{orb_2}(t_1) - \vec{r}_{orb_1}(t_1)\right)$$

Thereby $\delta_t = t_2 - t_1$ denotes the quasi-simultaneity value of the double-difference orbit errors. Using values of 1 s, 2 s,..., for the quasi-simultaneity we can compute the RMS of the radial orbit error double-differences as a function of δ_t. This procedure is done individually for each satellite, and we use "equal" instead of "smaller than" for the quasi-simultaneity. Of special interest is the radial component of the orbit, as it is closely related to the SLR ranges. As we perform the differences with *exactly* certain time step ($QS = \delta_t$), instead of less than or equal to ($QS \leq \delta_t$), the number of differences decreases when increasing the lapse for the difference. From each of these groups of differences (with quasi-simultaneity 1 s, 2 s, ...) we take the RMS and use it as a metric for our analysis.

Figure 5.6 shows these RMS values, for the radial component, in relation to the quasi-simultaneity, where the top plot shows the RMS values at each quasi-simultaneity for satellite GLONASS 13, and the bottom plot for satellite LAGEOS 2. In both cases the quasi-simultaneity was truncated at about the revolution period of each satellite:

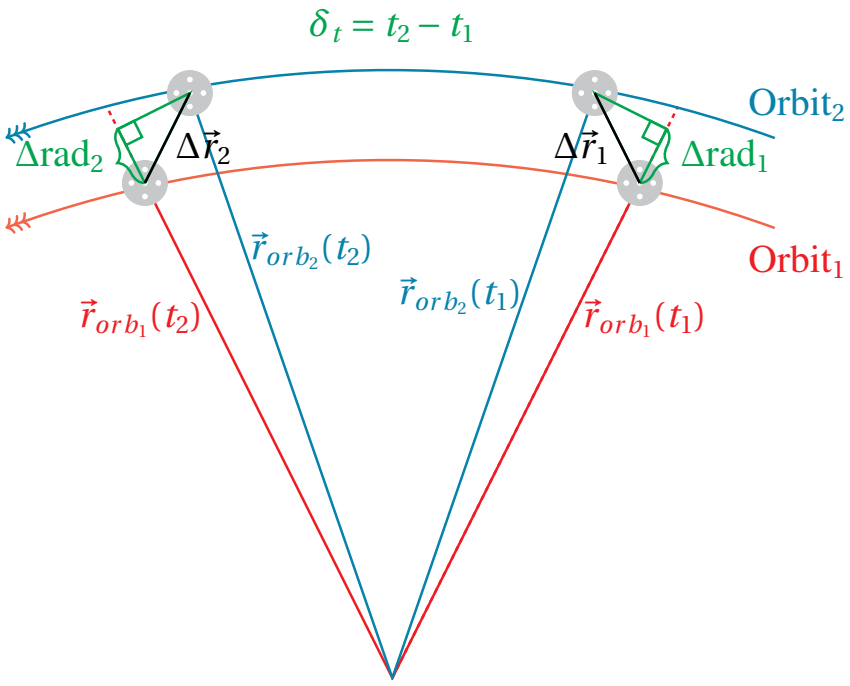

FIGURE 5.5: Concept for the determination of the best quasi-simultaneity threshold. Using only one satellite, two different orbit solutions (from different processing centres) are compared. First, perfectly simultaneous single-differences between orbit solutions are formed ($\Delta\vec{r}_1$ and $\Delta\vec{r}_2$, with their corresponding radial components Δrad_1 and Δrad_2). Then, double-differences with all possible time steps are built, and the RMS value of the double-differences at a certain time step is calculated.

223 min for LAGEOS 2 and 11 h 15 min for GLONASS 13. As expected, the RMS increases with the quasi-simultaneity. Moreover, it is evident that if all differences smaller or equal to a certain quasi-simultaneity were considered, the RMS values would grow in a similar way. It is also visible that a threshold for the quasi-simultaneity of 0.5 h ensures a relatively small RMS value. In this way we guarantee that possible errors of the orbits are not propagating into the differences.

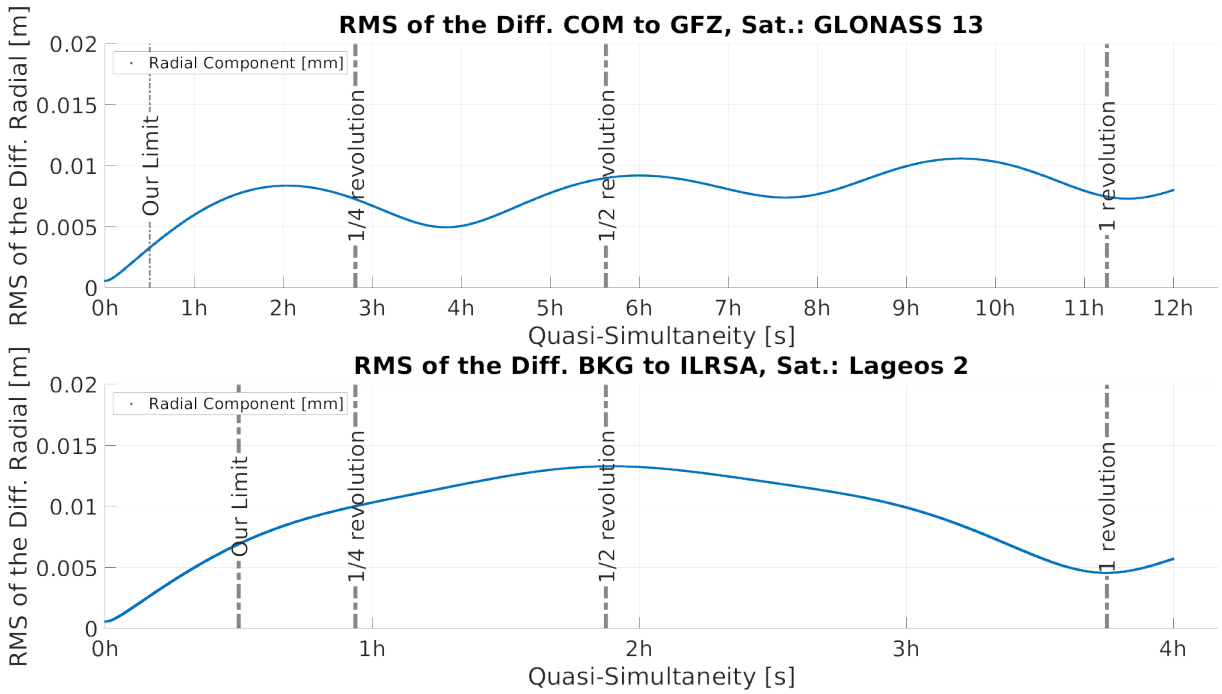

FIGURE 5.6: RMS of the double-differences to a single satellite, in relation to the quasi-simultaneity, for the radial component. Top: Satellite GLONASS 13. Bottom: Satellite LAGEOS 2. These differences have been built using two different orbital products. Moreover, the bins for the RMS calculation are considered with quasi-simultaneity $QS = d_t$ instead of $QS \leq d_t$

5.4 RESULTS

5.4.1 *Analysis of the Residuals from the Zero-Test*

With the Zero-Test strategy described in Section 5.3.3, the SLR data corresponding to the two telescopes in the time interval between 01.01.2018 and 31.12.2019 was processed in daily sessions, using the BSW software. Figure 5.7 shows the behaviour of the GLONASS and LAGEOS residuals as a function of the azimuth and elevation angle, for two of these days, namely 07.03.2018 (2018, DoY 184) and 03.12.2019 (2019, DoY 337), displayed by telescope. These residuals represent the level of noise of the observations plus orbit errors and possible instrumental biases. A summary of the statistics of these residuals is shown in Table 5.2. Aside from the difference in the number of observations and the presence of few outliers, the residuals of both days are among nominal values for the SLR technique, between -10 cm and 10 cm. However, there is a large contrast between the mean values obtained for the data set on the left wrt. the data set on the right in Table 5.2, mainly caused by the range bias of the station.

To further investigate the presence of instrumental biases associated with the stations, the single-difference of the zero-difference residuals is built. For this, we considered a quasi-simultaneity of 2 h, and built the differences from two telescopes to one satellite. For the 03.07.2018, 513 single-difference residuals are formed, from which

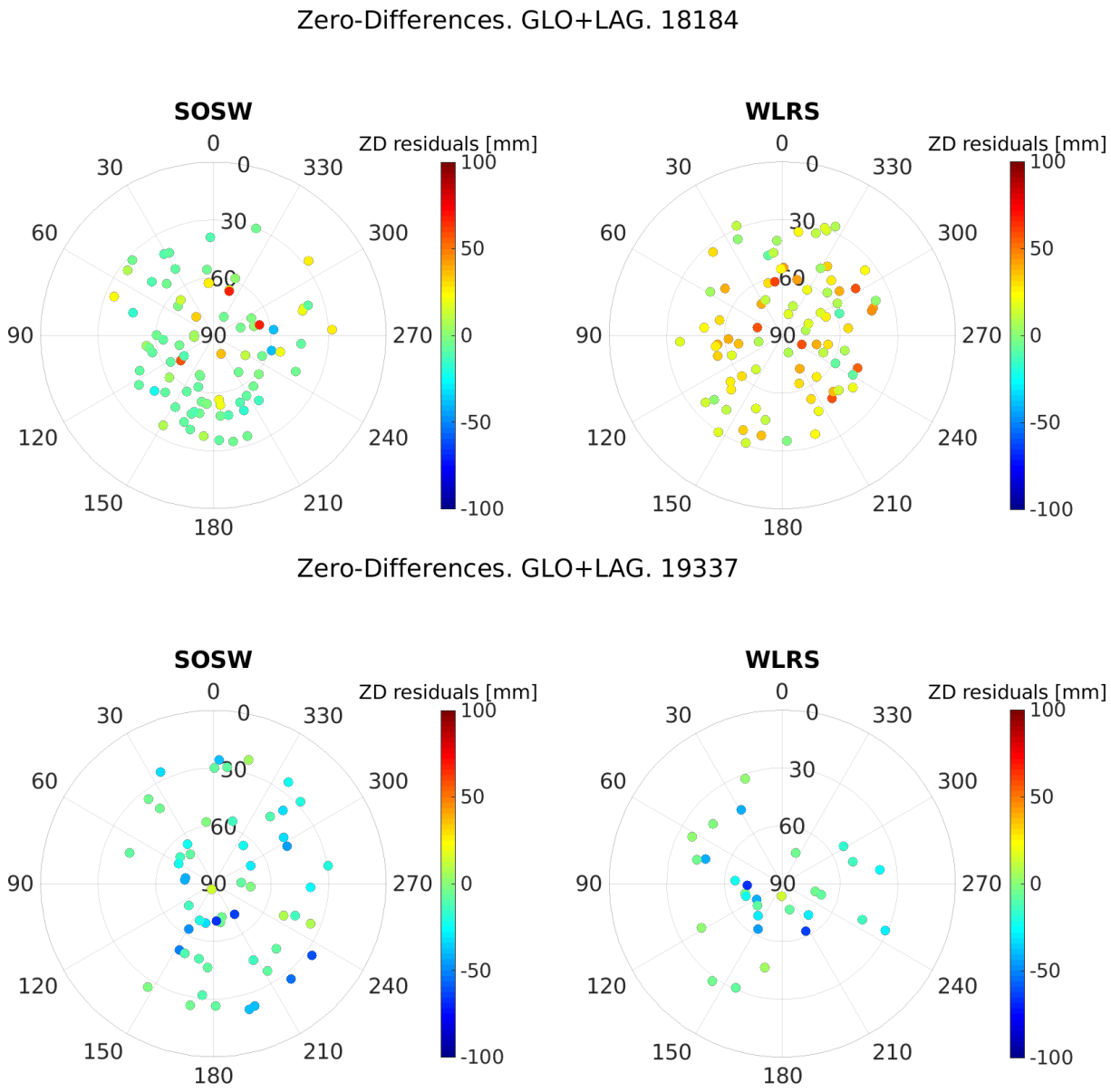

FIGURE 5.7: Skyplots of the zero-difference residuals of the Zero-Test, separately for each telescope. Top: 03.07.2018 (DoY 184, 2018). Bottom: 03.12.2019 (DoY 337, 2019)

		Data from 03.07.2018	
		Mean [mm]	Std [mm]
SOS-W	GLO	1.5	11.7
	LAG	6.9	2.6
WLRS	GLO	21.6	9.7
	LAG	7.8	6.0

		Data from 03.12.2019	
		Mean [mm]	Std [mm]
SOS-W	GLO	-11.1	7.0
	LAG	-12.3	7.9
WLRS	GLO	-14.9	11.4
	LAG	-8.4	7.9

TABLE 5.2: Summary statistics of the zero-difference residuals of the Zero-Test, separately for each telescope. Left: 03.07.2018 (DoY 184, 2018). Right: 03.12.2019 (DoY 337, 2019)

276 correspond to differences to GLONASS satellites, and the remaining 237 are to LAGEOS. The same procedure produced 200 single-difference residuals for day 03.12.2019 with 98 differences for GLONASS and 102 for LAGEOS. These difference residuals are displayed in Figure 5.8. As the range bias for the WLRS station was not applied during the processing, the single-difference residuals of day 03.07.2018 show a distinctive bias with a mean of −30.2 mm and −16.8 mm for GLONASS and LAGEOS, respectively. However, the difference residuals of the second data set are almost unbiased, with mean bias values of 0.5 mm and -3.4 mm for GLONASS and LAGEOS, respectively.

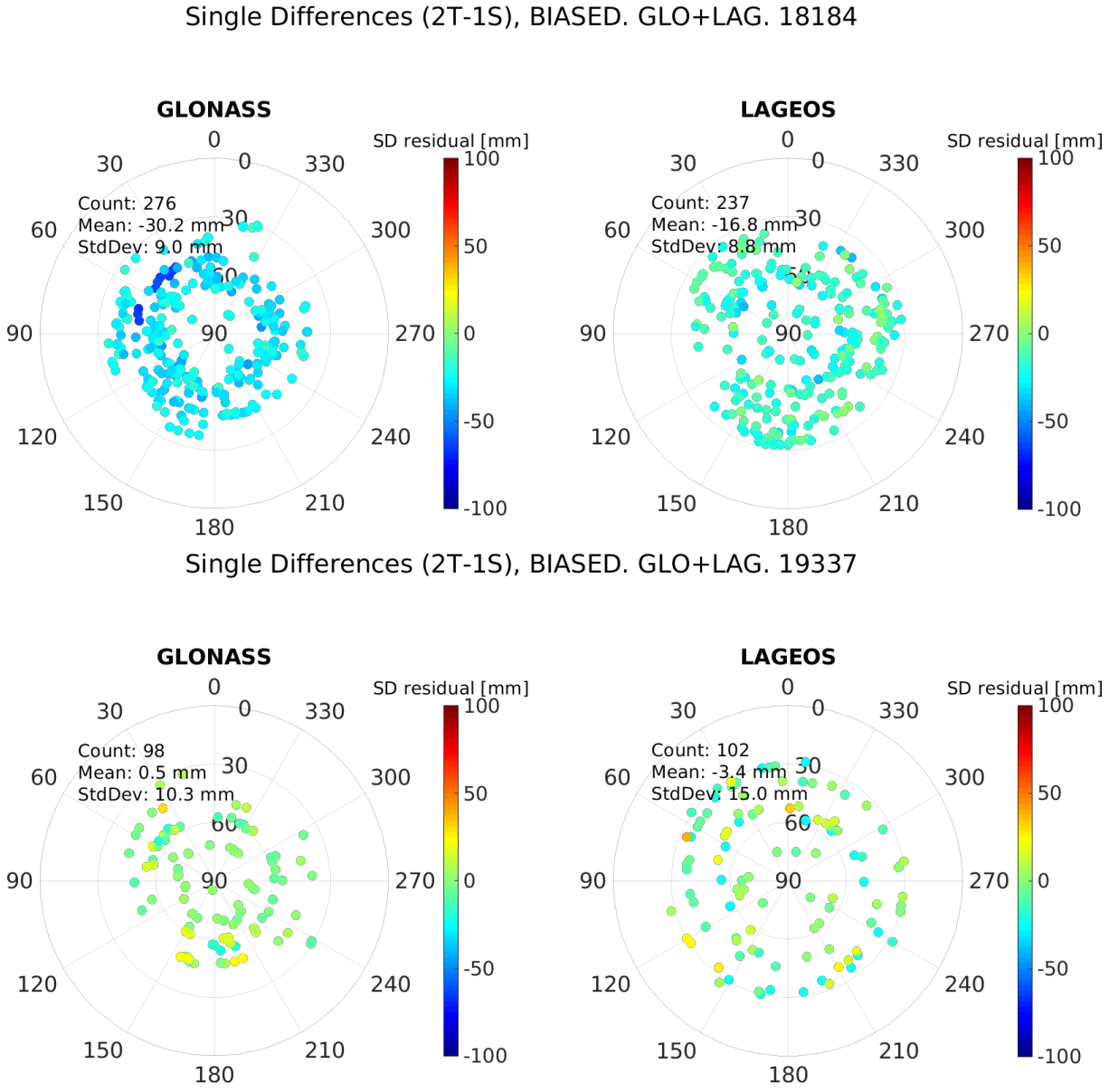

FIGURE 5.8: Skyplots of the single-difference residuals of the Zero-Test, using a quasi-simultaneity of 2 h, separately for each constellation. Top: 03.07.2018 (DoY 184, 2018). Bottom: 03.12.2019 (DoY 337, 2019)

To determine the behaviour of the instrumental bias and establish the time of possible bias changes, the time series of single-difference residuals is analysed. As seen in

Figure 5.8, when using a quasi-simultaneity of 2 h, it is possible to build multiple single-differences per day. In light of the results of section 5.3.4, where a threshold of quasi-simultaneity of 0.5 h was found as the best option to minimise errors from the orbits, we consider as unique "representative" for each day the differences with quasi-simultaneity $\leq$ 0.5 h. These daily values are displayed in the top plots of Figures 5.9 and 5.10, where the mean single-difference residuals, together with the daily standard deviation are displayed. While the standard deviation of the daily mean difference residuals is considerably larger for the GLONASS satellites than for LAGEOS, both time series display a distinctive break ca. 01.06.2019, confirming the results seen in Figure 5.8.

Therefore, we calculated the weighted mean value of these daily results imposing a break on DoY 156 of 2019, and the corresponding error for the mean is calculated. The middle plots of Figures 5.9 and 5.10, show these mean values over the entire time series, where the vertical black line indicates the date of the break imposed for the calculation. Notice that the imposed break ensures the calculation of different values for the instrumental biases, 23.19 mm and 5.03 mm for GLONASS, and 12.56 mm and 0.98 mm for LAGEOS, with sub-mm errors for these mean values. If these instrumental biases are removed, the (unbiased) time series show a zero-mean behaviour (bottom plots of Figures 5.9 and 5.10). These results demonstrate that the use of SLR single-differences can be a useful tool for the accurate estimation of instrumental biases.

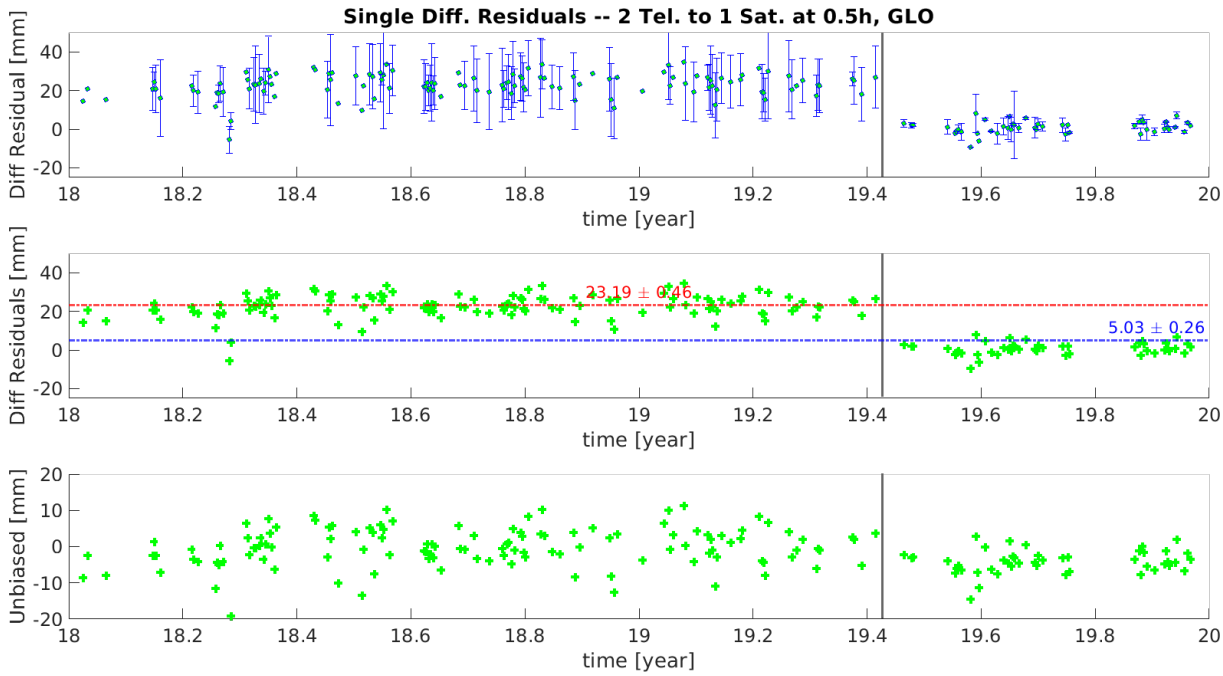

FIGURE 5.9: Time series of the daily mean single-difference residuals of the Zero-Test, at quasi-simultaneity of 0.5 h, for the GLONASS satellites. Top: Mean daily single-difference at quasi-simultaneity 0.5 h, with its corresponding daily standard deviation. Middle: Mean daily single-difference at quasi-simultaneity 0.5 h, averaged over the two years to obtain the (relative) range biases. Bottom: Unbiased time series of daily mean single-differences, after removing the range biases.

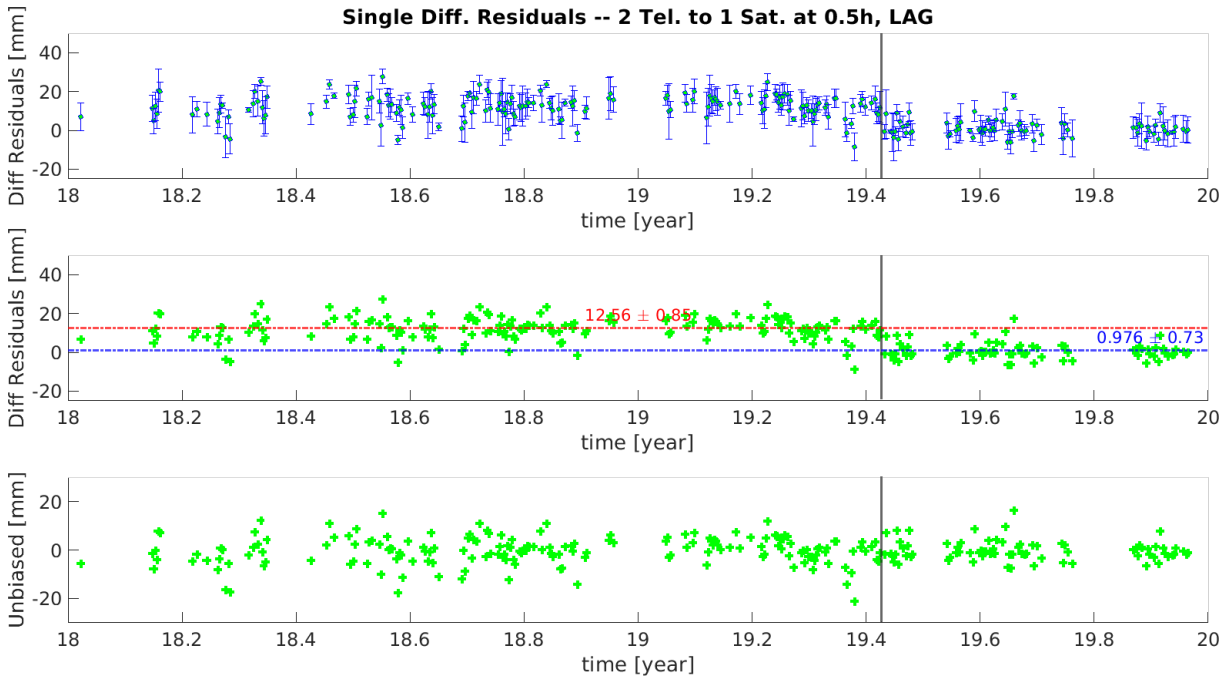

FIGURE 5.10: Time series of mean single-difference residuals of the Zero-Test, at quasi-simultaneity of 0.5 h, for the LAGEOS satellites. Top: Mean daily single-difference at quasi-simultaneity 0.5 h, with its corresponding daily standard deviation. Middle: Mean daily single-difference at quasi-simultaneity 0.5 h, averaged over the two years to obtain the (relative) range biases. Bottom: Unbiased time series of daily mean single-differences, after removing the range biases.

When now forming the double-difference residuals, the effects of these instrumental biases, and possible errors in the orbits of the satellites, are eliminated or mitigated. Figure 5.11 shows the double-difference residuals of days 03.07.2018 and 03.12.2019 allowing a quasi-simultaneity of 2 h. In these figures, the x-axis indicates the quasi-simultaneity allowed to build the single-differenced residuals from the SOS-W telescope to two satellites, while the y-axis shows the quasi-simultaneity allowed to build the single-differences from the WLRS telescope to two satellites. Finally, the colour bar indicates the value of the residuals. With this approach we built 4596 and 3374 double-differences, for day 03.07.2018 and 03.12.2019, respectively. These residuals are no longer biased, with mean values of 5.1 mm for the former, and 3.3 mm for the latter day. These small mean daily values, together with mm-level standard deviations, are an indication that SLR double-difference observations are potential candidates for the estimation of geodetic parameters.

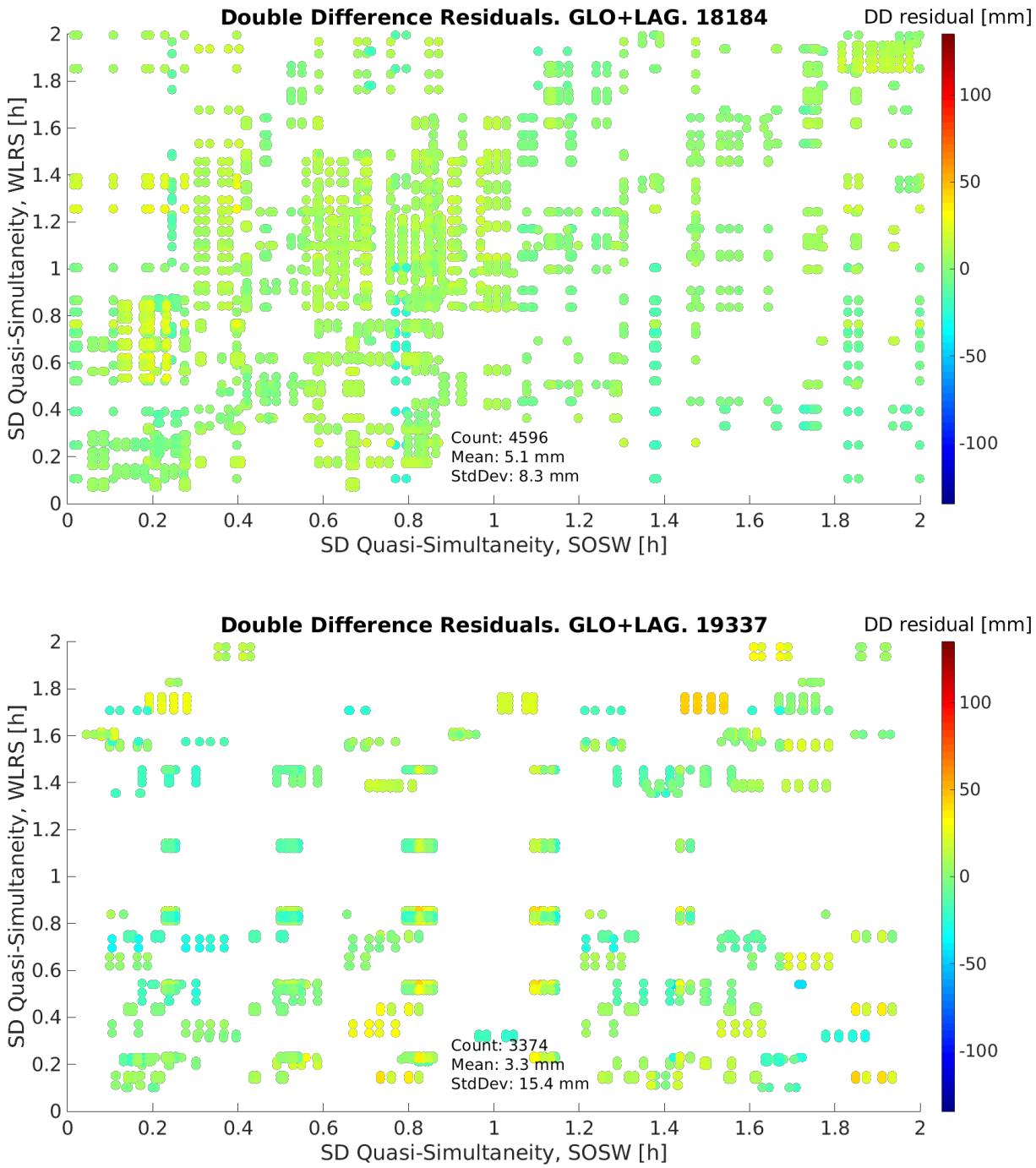

FIGURE 5.11: Double-difference residuals of the Zero-Test, as a function of the quasi-simultaneity up to 2 h, for both, the WLRS and SOS-W telescope. Top: 03.07.2018 (DoY 184, 2018). Bottom: 03.12.2019 (DoY 337, 2019)

5.4.2 *Baseline Estimation based on Single-Differences*

The first step of the baseline estimation process performs the determination of coordinates and instrumental biases based on single differences from two telescopes to one satellite, for each day individually. All the linearised equations satisfying the quasi-simultaneity condition $\|t_i - t_j\| \leq \delta_t$ with $\delta_t = 0.5$ hours, are stacked, as de-

scribed in Section 5.2.2, and a weighted least squares adjustment is used to derive the corresponding 5 parameters, three relative coordinates ($\Delta X,\ \Delta Y, \Delta Z$) and two range biases, one for GLONASS and one for LAGEOS. For instance, the behaviour of the aggregated instrumental bias at the day 03.07.2018, shows the trade-off between a larger quasi-simultaneity value and the orbital errors, a crucial point at this stage of the estimation. While large values of quasi-simultaneity guarantee a larger number of observations, which in turn favour the estimation process and improve the formal errors, the errors caused by the orbits (intrinsic to our method) grow larger. Due to the large amount of data available on day 03.07.2018 (Figure 5.12), the values at quasi-simultaneity 0.5 h, 21.9 ± 2.3 mm for GLONASS and 14.8 ± 2.1 for LAGEOS, are in agreement with the preliminary values observed for the same day in Section 5.4.1, during the entire session. Similarly, the difference of the estimates for the east, north and up (ENU) components of the baseline with respect to the local tie, show that the daily estimated values are in a close agreement with the local tie, with mean differences per component of $[4.7,\ 4.5,\ -10.1] \pm [1.2,\ 0.9,\ 2.9]$ mm, for east, north and up, respectively.

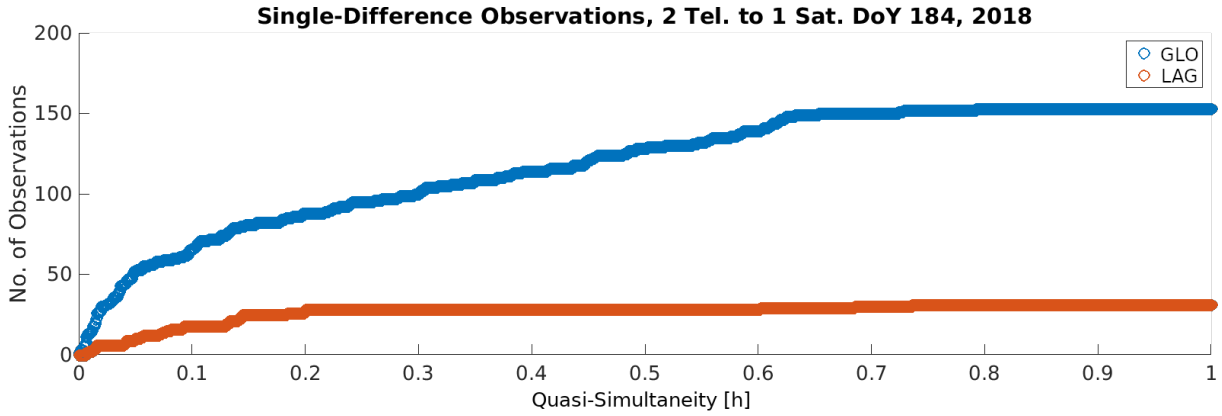

FIGURE 5.12: Available single-difference observations, as a function of the quasi-simultaneity up to 1 h, separately for each constellation, for the day 03.07.2018 (DoY 184, 2018)

As a compromise between the number of observations and the influence of the orbital errors, we have selected those values obtained for a quasi-simultaneity of 0.5 h for each day's weighted least squares estimation. With this, we form the time series of daily estimates, three coordinate components and two biases (GLONASS and LAGEOS), over the period of the two years of interest. Figure 5.13 shows these time series, with the time (year) of observation in the x-axis. This daily estimation additionally shows the need to differentiate between the instrumental biases before and after the observed break at day 01.06.2019.

These results support the results of Section 5.4.1 regarding the changes in the instrumental biases, and the need for a break in the data during the estimation process. For the coordinate estimates, the differences between the ENU estimates and the local ties are displayed. This daily analysis also facilitates the assessment of the performance

of the differencing strategies regarding the number of formed differences and possible outliers.

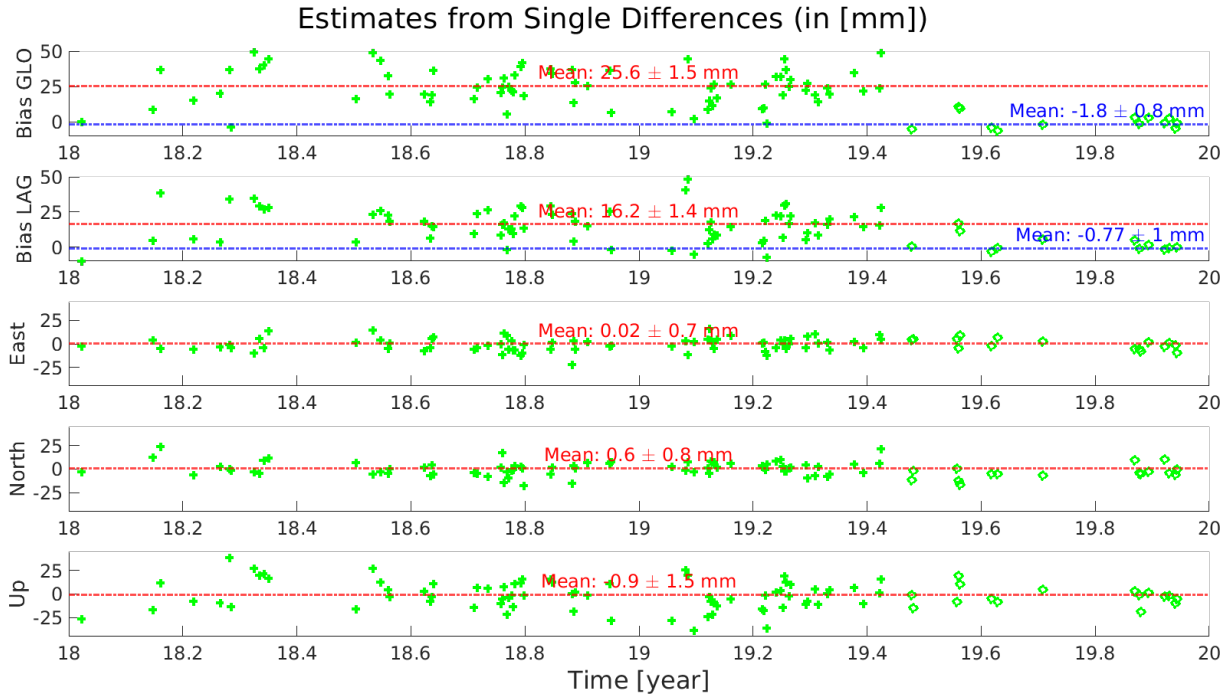

FIGURE 5.13: Time series of daily estimated parameters using single differences, when selecting as representative of each day the values obtained with a quasi-simultaneity of 0.5 h. The ENU fields correspond to the differences of the estimated values wrt. the local ties.

Despite the high level of agreement between the daily estimates and the local tie, for a more rigorous and accurate solution, a complete (unified) weighted least squares solution is preferred. This least squares solution is computed by stacking all the daily linearised equations with quasi-simultaneity $\leq$ 0.5 h over the two years, and producing a unique weighted least squares solution. When considering this approach with the available data, three cases are possible (Table 5.3):

1. Estimation of five parameters, three coordinates and two range biases, where jump in the biases is not considered
2. Estimation of ten parameters, three coordinates and two range biases before and the same 5 parameters after the observed bias jump
3. Estimation of seven parameters, three coordinates and four range biases. These four biases correspond to two biases for GLONASS and two for LAGEOS, when considering the bias jump in the observation time series

Figure 5.14 shows the residuals of the weighted least squares adjustment for these three cases. The time series with respect to the day of observation, shows an evident break for the residuals when estimating only five parameters (plot on the top-left), while the cases where breaks in the instrumental biases were considered, show unbiased

Case	Jan. 2018 – Jun 2019	Jul 2019 – Dec. 2019
5 Parameteres	3 Relative Coordinates 2 Relative Range Biases	
10 Parameters	3 Relative Coordinates 2 Relative Range Biases	3 Relative Coordinates 2 Relative Range Biases
7 Parameters	3 Relative Coordinates 2 Relative Range Biases	2 Relative Range Biases

TABLE 5.3: Timeline of the validity of the parameters estimated with the three rigorous LSA, based on single-difference observations

zero-mean residuals in time. The right plot of Figure 5.14 also shows that for larger values of quasi-simultaneity the residuals of the estimation begin to slowly increase, justifying the selection of a relatively small quasi-simultaneity value of 0.5 h.

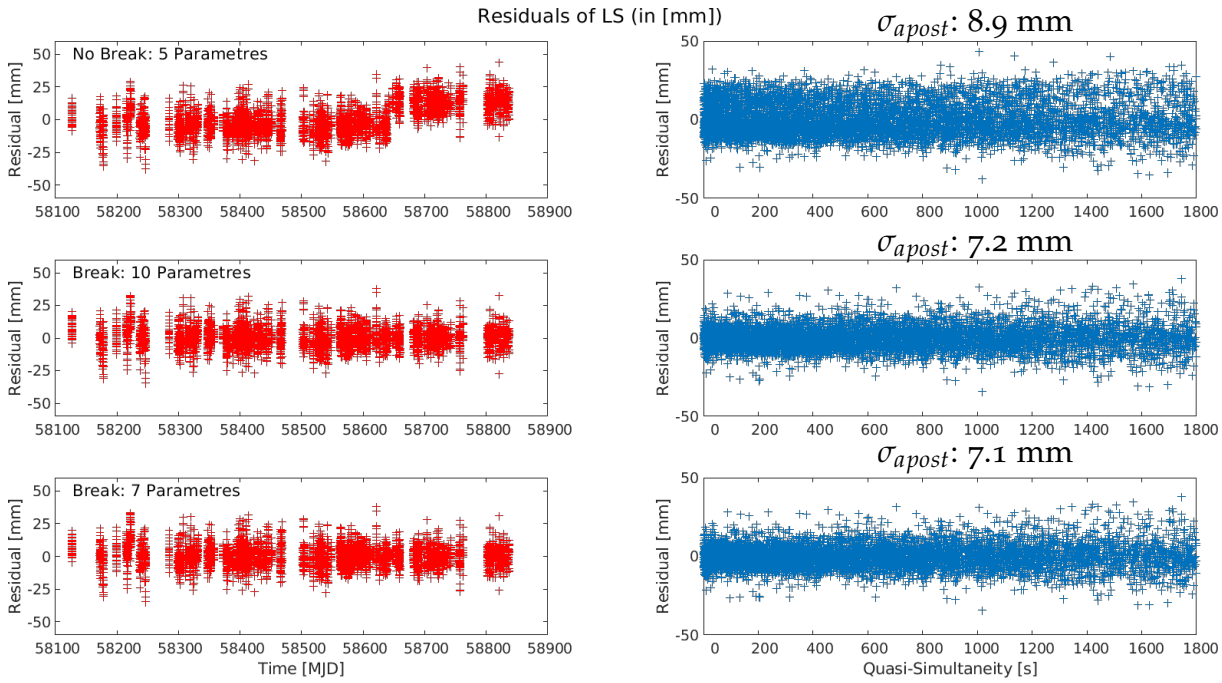

FIGURE 5.14: Residuals of the unified weighted least squares adjustment, for the single differences case. Left: Time series with respect to the day of observation (mean Julian date), Right: Residuals in relation to their quasi-simultaneity and their σ-aposteriori $\left(\frac{v^T P v}{n-u}\right)$.

Table 5.4 summarises the estimated values, together with the formal errors, of these three cases. As done before, the ENU estimates were subtracted from the local tie, so the values depict the difference of the SLR estimates with respect to the terrestrial measurements. While all the coordinate estimates are in a millimetre to sub-millimetre agreement with the local ties, there is an improvement in the formal errors for those solutions considering a break for the instrumental biases in the data. A tendency of lower values of the formal errors in the north component is seen in the three

	Without break (5 Param.)		With break (10 Param.)		With break (7 Param.)	
	Estimate	Formal Error	Estimate	Formal Error	Estimate	Formal Error
E [mm]	1.1	1.0	0.4	0.6	0.2	0.7
			-0.5	0.3		
N [mm]	0.6	1.0	1.6	0.5	0.8	0.6
			-1.8	0.3		
U [mm]	-0.7	1.1	-1.9	0.6	-2.1	0.7
			-2.0	0.4		
Bias GLO [mm]	20.8	0.9	24.3	0.5	24.0	0.5
			0.1	0.2	0.4	0.2
Bias LAG [mm]	11.6	1.5	14.9	0.8	14.8	0.8
			-1.3	0.5	-1.3	0.5

TABLE 5.4: Differences of the ENU estimates wrt. the local tie and formal errors of the rigorous two-year (unified) weighted least squares adjustment, based on single differences from two telescopes to one satellite. All values in millimetres

approaches, as a result of the south-north orientation of the baseline. As in the case of the GNSS-based solutions, the formal errors of the up component show the largest values. When comparing the values for the estimates of the instrumental biases, we see a clear difference between the approach with only five parameters and the remaining two cases. Looking at the solutions considering breaks for the range biases, we see that the biases for the GLONASS satellites change from 24.3 mm to 0.1 mm and 24.0 mm to 0.4 mm, for the 10 and 7 parameters solutions, respectively. These changes are statistically significant, when considering the formal errors of these values: 0.49 mm and 0.23 mm for the 10 parameters, and 0.50 mm and 0.23 mm for the 7 parameters. Similarly, with the formal errors found for the range biases, the change in the range biases is statistically significant and cannot be ignored. These results support the preference for the solution including a break for the estimation of the instrumental biases. As the coordinates of the stations are not expected to change due to the change in the bias, the solution with 7 parameters, where the components of the baseline vector are estimated once, is preferred. The correlations among the estimates for this approach are shown in the left part of Figure 5.16. The small correlations ($\|\rho\| \leq .25$) among the coordinate components, zero correlation among the biases, and the expected large correlations between the height component and the range biases, support this selection.

5.4.3 *Baseline Estimation Based on Double-Differences*

Although the estimated coordinates based on single differences from Section 5.4.2 show a millimetre agreement with the local tie, with relatively low formal errors, possible temporal variations of the instrumental biases are still present in the adjustment, and may have an impact on the final solution. To avoid these issues with the determination of instrumental biases and to reduce and mitigate the influence of other error sources, a double-difference weighted least squares estimation has been performed. Moreover,

as discussed in Section 5.3.2, due to the short distance between the two telescopes, the influence of the troposphere on the SLR signal is expected to be the same (apart from the height difference).

Therefore, with the use of double-difference observations, the tropospheric delay affecting the original observations is mitigated or strongly reduced. To perform the estimation process, we used the idea of Section 5.2.3 to select the daily linearised equations which satisfy the quasi-simultaneity condition $\delta_t \leq 0.5$ h. This set of linearised equations is free of the influence of the troposphere, instrumental biases, and with a reduced influence of orbital errors. Instead of performing a daily estimation of parameters and then a calculation of the corresponding mean, we stack the linearised equations for one rigorous 2-year (unified) weighted least squares adjustment, where the only unknowns are the components of the baseline between the telescopes.

Figure 5.15 shows the behaviour and distribution of the residuals of this weighted least squares adjustment, where the absence of any systematic influence of the instrumental biases is noticed. Moreover, for relatively short periods of quasi-simultaneity ($\leq$ 600 s) the majority of the residuals of the double-differences are between -10 mm and 10 mm. As for the single-difference case, we calculate the differences between the resulting coordinates and the local tie. The ENU components of this difference amount to East : 0.7 ± 0.2 mm, North : -0.9 ± 0.2 mm, Up : -0.6 ± 0.2 mm. Furthermore, the correlations among these estimates (right part of Figure 5.16) show small values. The high level of agreement with the local tie and favourable correlations among the estimates, support the use of SLR double-differences for the estimation of the local short baseline.

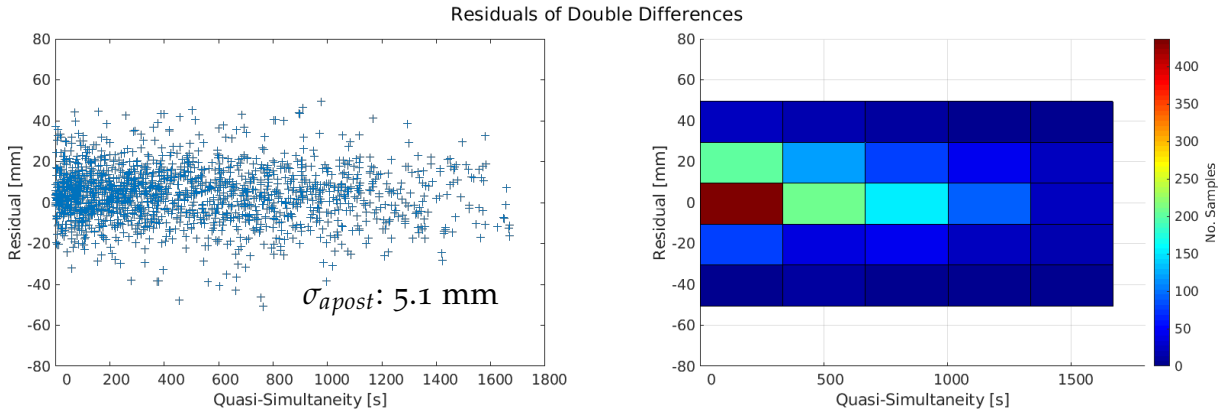

FIGURE 5.15: Residuals of the rigorous weighted LSA, for the double-differences case. Left: Residuals in relation to their quasi-simultaneity, with their σ-aposteriori. Right: Histogram of residuals in relation to their quasi-simultaneity.

5.5 CONCLUSIONS

The single- and double-differences of SLR observations for the short baseline in Wettzell have been investigated, and a novel approach to build differences of SLR observations

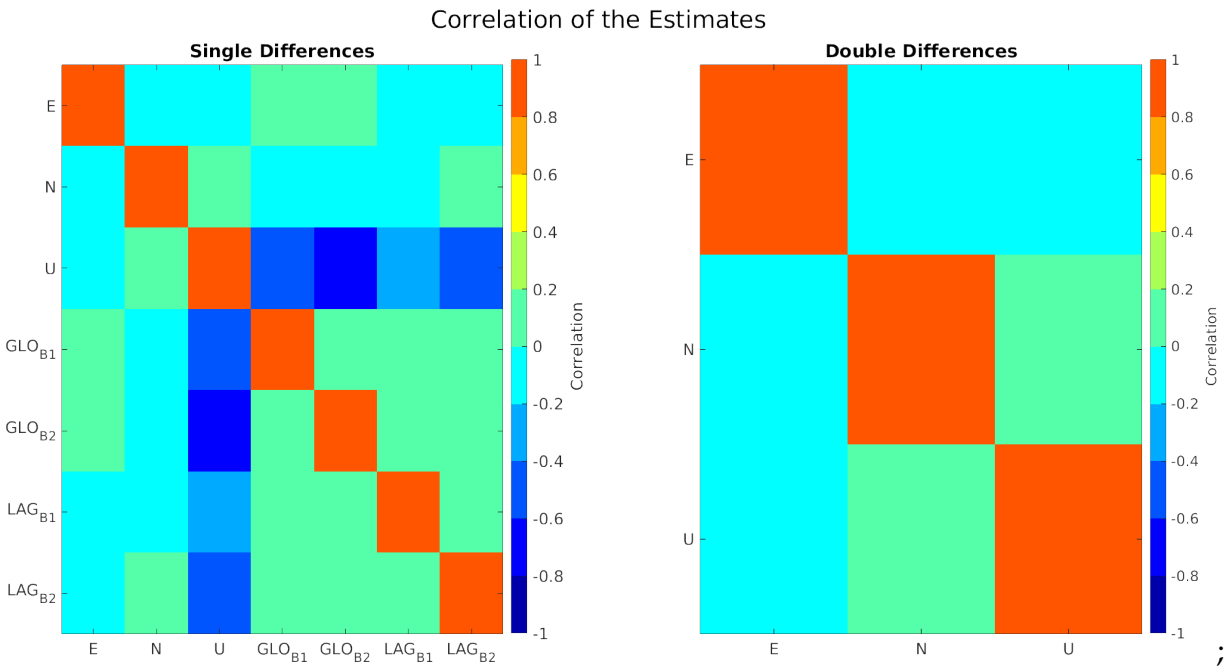

FIGURE 5.16: Correlations between estimated parameters for two of the investigated approaches. Left: Based on single-differences with 7 parameters. Right: Based on double-differences.

has been developed, based on the concept of quasi-Simultaneity. These differences are built with the linearised equations of the zero-difference processing. Therefore, the interpolation of the SLR ranges is no longer required, and systematic errors common to the baseline can be targeted. The experiments over two years of SLR observations with the co-located telescopes in Wettzell, showed the advantages of the proposed method, namely the estimation of relative coordinates, suitable for the validation of local ties, and the estimation/elimination of instrumental range biases. Table 5.5 summarises the estimated values obtained using all the investigated methods, in addition to the "standard" results obtain for the same time interval (Bernese Zero Estimates). In particular, the single-difference rigorous solution with 7 estimates shows a much higher level of agreement with respect to the local ties, especially in the up component, with a difference of -2.1 mm against the 10.5 mm of the standard zero-difference solution. Furthermore, the formal errors of the ENU components for the single-difference method are significantly better than those of the zero-differences. While there is no benchmark for the values of the range biases, the analysis of the formal errors of the single-differences in relation to the standard method of the zero-differences, shows a much higher performance of the former, with a sub-mm level for the errors. However, in contrast to the zero-difference approach, the single-difference strategy is only able to provide range bias differences between the stations. Nevertheless, to avoid the estimation of range biases, the double-differences were studied. With the elimination of these biases, the estimation of relative coordinates, and therefore the validation of the local ties, is performed clearly more accurately. We found that the agreement of the relative coordinates and the local tie is within 1 mm for each of the ENU components, with corresponding formal errors in the sub-mm domain. Moreover, with a σ_{apost} of 5.1 mm of the double-difference solution, against 7.1 mm for the solution based

on single-differences, the double-difference approach shows an additional and more effective reduction of systematic biases. The main improvement is observed in height component, which corresponds to the expectations, as the error sources mitigated with our approach (range biases, orbit errors, troposphere) are influencing the height the most. These characteristics support the usability of the proposed differencing methods for the estimation of geodetic parameters with a high degree of accuracy and their usability for the validation of local ties. Future activities will include the study of longer baselines, where we expect that the principle still works, however with a less pronounced reduction of orbit and tropospheric errors.

ACKNOWLEDGEMENTS This work has been developed within the project "Co-location of Space Geodetic Techniques on Ground and in Space" in the frame of the DFG funded research unit on reference systems, and funded by the Swiss National Foundation (SNF, 200021E-160421). Additionally, the authors would like to thank the team at the GO-Wettzell, in particular to Dr. Jan Kodet for providing the initial SLR data. The authors would like to thank the IERS, CODE and CDDIS for providing the necessary orbital products and reference coordinates required for the realisation of this work.

AUTHOR CONTRIBUTION STATEMENT I.H.P. and M.R. design the study and developed the methodology. S.R provided inputs to refine the analysis. I.H.P developed the processing tools and analysed the data with the help of M.R. I.H.P wrote the manuscript with support of M.R. and S.R, and all authors read and approved the final manuscript.

DATA AVAILABILITY STATEMENT The SLR datasets used for this study are available from ftp://edc.dgfi.tum.de/pub/slr/data. The GNSS orbits used can be found at ftp.aiub.unibe.ch/CODE_MGEX/CODE/ and the LAGEOS orbits can be found at ftp://edc.dgfi.tum.de/slr/products/orbits/. The datasets generated during this study are available from the corresponding author on reasonable request.

	Differencing Approaches																	
	Bernese Zero Estimation (Difference of Estimates)				Fixed to Local Tie		Single Differences 2 Telescopes - 1 Satellite								Double Differences			
	5 Estimates (No Break)		10 Estimates		7 Estimates (4 Biases)		Only Biases (4 Par.)		Mean of Daily Estimates (5 Par.)		5 Estimates (No Break)		10 Estimates		7 Estimates (4 Biases)		3 Estimates (No Biases)	
	Val.	σ	Val.	σ	Val.	σ	Val.	σ	Val.	σ	Val.	σ	Val.	σ	Val.	σ	Val.	σ
E [mm]	0.4	0.9	0.3	1.0	0.2	0.7			-0.5	0.6	1.1	1.0	0.4	0.6	0.2	0.7	0.7	0.2
			0.2	1.9									-0.5	0.3				
N [mm]	-0.5	1.7	1.5	2.0	-0.1	1.3			0.1	0.9	0.6	1.0	1.6	0.5	0.8	0.6	-0.9	0.2
			-5.0	3.6									-1.8	0.3				
U [mm]	10.2	2.2	8.0	3.6	10.5	1.7			-0.5	1.4	-0.7	1.1	-1.9	0.6	-2.1	0.7	-0.6	0.2
			-17.3	4.6									-2.0	0.4				
GLO_b (mm)	37.3	1.9	39.6	2.2	41.2	1.5	23.1	0.5	25.6	1.5	20.8	0.9	24.3	0.5	24.0	0.5		
			22.2	4.0	18.2	1.7	5.3	0.3	-1.8	0.8			0.1	0.2	0.4	0.2		
LAG_b (mm)	19.4	1.8	21.5	2.1	23.0	1.4	12.6	0.9	16.2	1.4	11.6	1.5	14.9	0.8	14.8	0.8		
			14.3	3.8	9.6	1.6	1.0	0.7	-0.7	1.0			-1.3	0.5	-1.3	0.5		
	Stacking of linearised equations ("Rigorous 2-years LSA")																	

TABLE 5.5: Estimated ENU coordinate difference w.r.t the local ties, and instrumental biases with the different strategies discussed in this paper. The left column shows the value for the estimated parameter, and the right column the corresponding formal error.

5.6 APPENDIX: SINGLE- AND DOUBLE-DIFFERENCE SYSTEMS OF LINEAR EQUATIONS

Table 5.6 shows a sample of observations collected at the two telescopes in Wettzell for DoY 184, 2018. Considering a quasi-simultaneity condition of $\delta_t \leq 1\ h$, the single

Telescope	Sat.	MJD	$\mathbf{A_m^{ZD}}$			$\mathbf{b^{ZD}}$
SOS-W	952	58302.14577	-0.9341	0.3497	-0.0714	0.0285
SOS-W	104	58302.12057	-0.9269	-0.3715	-0.0532	0.0061
SOS-W	952	58302.14662	-0.9400	0.3216	-0.1137	0.0075
SOS-W	119	58302.29856	-0.7634	-0.6091	-0.2149	0.0093
SOS-W	109	58302.29092	-0.3450	0.1958	-0.9179	0.0053
WLRS	952	58302.16049	-0.6007	-0.3553	-0.7162	-0.0080
WLRS	104	58302.11941	-0.9258	-0.3715	-0.0702	-0.0216
WLRS	952	58302.16049	-0.6007	-0.3553	-0.7162	-0.0080
WLRS	119	58302.30681	-0.7328	-0.5934	-0.3330	-0.0289
WLRS	109	58302.27069	-0.3365	0.4532	-0.8255	-0.0348

TABLE 5.6: Linearised observation equations obtained when processing the raw SLR ranges (zero-differences) for telescopes SOS-W and WLRS

differences are built with the help of the $\mathbf{C_{sd}}$ operator

$$\mathbf{C_{sd}} = \left(\begin{array}{ccccc|ccccc} 952 & 104 & 952 & 119 & 109 & 952 & 104 & 952 & 119 & 109 \\ 1 & 0 & 0 & 0 & 0 & -1 & 0 & 0 & 0 & 0 \\ 0 & 1 & 0 & 0 & 0 & 0 & -1 & 0 & 0 & 0 \\ 0 & 0 & 1 & 0 & 0 & 0 & 0 & -1 & 0 & 0 \\ 0 & 0 & 0 & 1 & 0 & 0 & 0 & 0 & -1 & 0 \\ 0 & 0 & 0 & 0 & 1 & 0 & 0 & 0 & 0 & -1 \end{array}\right)$$

Similarly, the double differences are built using the $\mathbf{C_{dd}}$ operator

$$\mathbf{C_{dd}} = \left(\begin{array}{ccccc|ccccc} 952 & 104 & 952 & 119 & 109 & 952 & 104 & 952 & 119 & 109 \\ 1 & -1 & 0 & 0 & 0 & -1 & 1 & 0 & 0 & 0 \\ 0 & -1 & 1 & 0 & 0 & 0 & 1 & -1 & 0 & 0 \\ 0 & 0 & 0 & 1 & -1 & 0 & 0 & 0 & -1 & 1 \end{array}\right)$$

Thus, the single- and double-differenced linear equation systems are given by

$$\mathbf{b_{1,2}^{SD}} = \mathbf{C_{sd}} \cdot \mathbf{b_1^{ZD}} \quad \text{and} \quad \mathbf{A_{1,2}^{SD}} = \mathbf{C_{sd}} \cdot \begin{bmatrix} \mathbf{A_1^{ZD}} \\ \mathbf{0_{5\times 3}} \end{bmatrix}$$

$$\mathbf{b_{1,2}^{DD}} = \mathbf{C_{dd}} \cdot \mathbf{b_1^{ZD}} \quad \text{and} \quad \mathbf{A_{1,2}^{DD}} = \mathbf{C_{dd}} \cdot \begin{bmatrix} \mathbf{A_1^{ZD}} \\ \mathbf{0_{5\times 3}} \end{bmatrix}$$

6

RIGOROUS COMBINATION OF GNSS AND VLBI

Based on: ***I. D. Herrera-Pinzón*** *et al. (2023). "Impact of Local- and Tropospheric Ties for the Rigorous Combination of GNSS and VLBI". In:* Proceedings of the IAG International Symposium on Reference Frames for Applications in Geosciences (REFAG 2022). DOI: *https://doi.org/10.1007/1345_2023_195*

Paper V

On the Impact of Local- and Tropospheric Ties for the Rigorous Combination of GNSS and VLBI

Iván Herrera-Pinzón and Markus Rothacher
Institute for Geodesy and Photogrammetry, ETH Zurich

(Author's version. It differs from the submitted paper in terms of layout and formatting)

Abstract

In this contribution, we study the impact of the use of tropospheric ties between VLBI and GNSS observations at co-location sites during the CONT17 campaign. In our approach, we perform the rigorous estimation of all parameter types common to these techniques, namely: station coordinates, troposphere zenith delays and gradients, and the full set of Earth Orientation Parameters (EOPs) and their rates, including their full variance-covariance information. The core element of our processing scheme is the combination of observations via local and tropospheric ties, which are essential especially for the height estimates. By using and evaluating different weighting schemes, to obtain a unique set of consistent parameters, we analyse coordinate repeatabilities and the behaviour of the EOPs, to discuss the impact of the accuracy and weighting of the local and troposphere ties on the estimation of geodetic parameters. We discuss the challenges and results of this rigorous inter-technique combination of VLBI and GNSS observations, and provide evidence of the need of such an approach.

6.1 RIGOROUS COMBINATION OF SPACE GEODETIC TECHNIQUES

Earth Orientation Parameters (EOPs) are heterogeneously determined in the current realisation of the International Terrestrial Reference Frame (ITRF). Polar motion (x-pole and y-pole) is estimated based on the combination of the four space geodetic techniques, whereas their rates are only based on two techniques, Global Navigation Satellite Systems (GNSS) and Very Long Baseline Interferometry (VLBI). Moreover, the Earth's phase of rotation (UT1-UTC) and Length of Day (LoD) are taken solely from the VLBI solution. In addition, the combination of troposphere parameters from VLBI and GNSS through the use of tropospheric ties at fundamental sites is not implemented in ITRF's combination strategy. Hence, a rigorous combination of all parameter types common to all techniques, with consistent EOPs and with appropriate inter-technique tropospheric ties, is still a challenge. A consistent estimation of the TRF, capable of exploiting the advantages of the dense GNSS network with continuous observation and excellent geometry, and the full set of EOP delivered by VLBI, is required to achieve higher precision levels following the GGOS requirements of Rothacher, M. et al., 2009.

The need for a consistent, rigorous combination of space geodetic techniques has been identified for a long time as a fundamental task for the generation of highly accurate geodetic and geophysical products, including terrestrial and celestial reference frames (Rothacher, M. et al., 2019), and has been the topic of discussion in multiple works over the last two decades. A complete definition of the standards, models and parametrisation required for the consistent processing of the different space geodetic techniques is presented by (Rothacher, M. et al., 2010), within the scope of the GGOS Germany initiative (GGOS-D). Their work discusses the important aspects of a rigorous combination of space geodetic techniques, and emphasises the need for the computation of consistent time series of the parameters relevant to the different techniques, extending the parameter space to link geometry, Earth rotation, and gravity field. In their comprehensive work, Coulot, D. et al. (2007) carry out an early attempt of combining GPS, VLBI, SLR and DORIS data on the observation level. With data over the span of one year (2002), their work strives to perform the combination by estimating parameters simultaneously, while making use of all their correlation information. In her PhD thesis, Thaller, D. (2008) performs a combination of VLBI, GPS, and SLR normal equations, during the CONT02 campaign, in order to estimate station coordinates, EOPs, and troposphere parameters. Her approach aims for the homogenisation of the normal equations, through the use of identical a priori models in the estimation of the parameters common to the three techniques. Her approach performs the combination at the normal equation level, with all common parameter types included, where the improvement of the combined solution regarding the individual technique solution is noticeable. In particular, she accomplished a successful estimation of UT1-UTC and LOD, and the stabilisation of the determination of the height component of the coordinates thanks to the common estimation of troposphere zenith delays and gradients. More recently Diamantidis, P.-K. et al. (2021) perform a combination at the observation level of VLBI and GNSS data during the CONT17 campaign, using a unified piece of software based on a batch least squares estimator. Their work reports an improvement in the coordinate repeatabilities, polar motion, and UT1-UTC of 25 %, 20 % and 30 %,

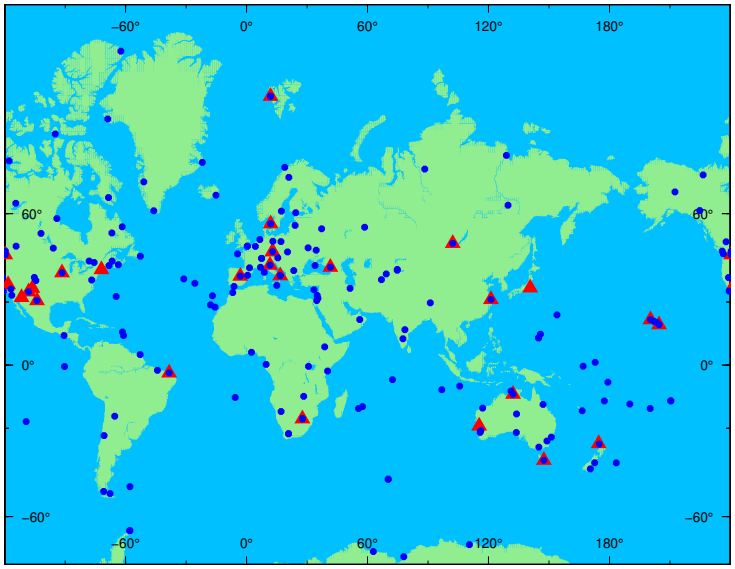

FIGURE 6.1: Global distribution of used stations. The red triangles show the VLBI antennas of the two legacy networks of the CONT17 campaign, whereas the blue circles show the GNSS antennas selected from the IGS network.

respectively, with respect to the single technique solutions. In a similar fashion, Wang, J. et al. (2022) use the data of the CONT05–CONT17 campaigns, aiming for the integrated processing of VLBI and GNSS data, to achieve a combination at the observation level. The main characteristic of their approach is the use of the tropospheric ties among VLBI and GNSS co-located stations, where residual ZWD and gradients for VLBI and GNSS were estimated. As their work uses different tropospheric tie setups, the improvement of the coordinate repeatabilites ranges between 12 % and 28 %, while for EOPs it goes from 2 % up to 18 %.

6.2 DATASET AND PROCESSING STRATEGY

The test scenario to validate our strategy is the data of the Continuous VLBI Campaign 2017 (CONT17). CONT17 was a campaign of continuous VLBI sessions, carried out between November 28th, 2017, and December 12th, 2017. CONT17 was composed of three independent networks observed: two legacy S/X networks with 14 stations each, and one VGOS broadband network consisting of six stations (Behrend, D. et al., 2020). For the scope of this work, we only use the two legacy networks. The geodetic VLBI data of this campaign was extracted from the corresponding NGS cards. Since we use only the legacy networks, the processing of the data was performed using the S/X part of the source catalogue of the 3rd realisation of the International Celestial Reference Frame (ICRF3) of Charlot, P. et al. (2020). To complement the VLBI observations, we selected about 180 GNSS stations of the IGS network (Dow, J. et al., 2009), covering the same time interval. For the selection of the GNSS stations, we made sure that there was at least a GNSS receiver co-located with each VLBI telescope. Figure 6.1 shows the global distribution of the VLBI and GNSS stations involved in this work. As mentioned in Section 6.1, the integrated processing of the different techniques at the observation level provides the most rigorous and consistent solution, especially, when

all the possible ties are considered. To guarantee the consistency of the combination, it is better perform it with a single piece of software, which should be able to process all the techniques with state-of-the-art models and homogeneous parametrisation. To handle the process of the VLBI and GNSS data at the observation level, we use a modified version of the Bernese GNSS Software v5.2 (Dach, R. et al., 2015), capable of processing VLBI data. This so-called Bernese v5.2 – VLBI Version, inherits all the GNSS & SLR capabilities of the original version: Pre-processing, outlier detection, residual screening, time-series analysis, daily and session processing, generation of normal equations, and more. The main advantages of this development are:

- The use of an identical parametrisation for all the techniques (e.g. piece-wise linear estimates, offset-drift estimates, interpolation methods, ...).
- The use of identical modelling for all techniques (e.g loading, troposphere, ...), with identical handling of parameter constraints.
- Appropriate datum definition (No-Net-Rotation (NNR), No-Net-Translation (NNT), No-Scale, fixed coordinates, ...).
- The implementation of local and tropospheric ties.

Table 6.1 shows a summary of the modelling and a-priori information used for the rigorous combination of VLBI and GNSS data. For the combination of the data, we estimate the common parameters with daily resolution: daily station coordinates using the NNR–NNT condition, and daily EOPs: polar motion, UT1-UTC, LOD, and celestial pole offsets, and their corresponding rates of change. Zenith tropospheric delays are estimated with 1-hour resolution and tropospheric gradients every 24 hours. We estimate VLBI clock offsets piece-wise linearly with intervals of 3 hours. Additionally, we calculate geocentre coordinates and GNSS orbits. Finally, for the 15-day rigorous combination, we additionally use the available terrestrial ties and our approach for tropospheric ties.

6.3 REALISATION OF TROPOSPHERIC TIES

For the modelling of the troposphere, we use as a-priori values for the zenith hydrostatic delays and mapping function, the data of the Vienna Mapping Function 1 (VMF1) of Böhm, J. et al. (2006b). The use of this type of modelling ensures that the zenith total delay (ZTD) difference between GNSS and VLBI at co-located stations caused by the height difference is modelled in advance. The residual wet delays are then estimated as one-hourly piece-wise-linear functions and the topospheric gradients with daily resolution. Figure 6.2 shows the results of the troposphere estimates at two co-location sites, Wettzell (Germany) and Fort Davis (USA). Figure 6.2a shows the differences of the modelled zenith hydrostatic delay (ZHD) and the estimated ZWD for the baseline WETTZELL–WTZR. The modelled ΔZHD amounts to -0.8 mm (top plot), which has been reported by other works (c.f. Teke, K. et al. (2011)), and it is expected considering the height difference of the stations. The estimated ΔZWD (bottom plot) has a mean value of -1.4 mm, with a standard deviation of 2.2 mm, and

Modelling and a-priori information	
Troposphere	6-hourly ECMWF-based hydrostatic troposphere delays mapped with VMF
	Piecewise linear functions, with VMF mapping function, for non-hydrostatic troposphere
Solid Earth tides	IERS 2010 conventions
Permanent tide	Conventional tide free
Ocean tide model	FES2004
Ocean loading	Tidal: FES2004
	Non-tidal: 6-hourly GRACE AOD1B atmospheric and oceanic de-aliasing product
Source catalogue	ICRF3
Observations	GNSS: RINEX
	VLBI: NGS cards
Processing approach	GNSS: Double differences with ambiguity resolution
	VLBI: Baselines
Datum definition	NNT-NNR
Earth rotation	Piecewise linear functions
Receiver clock	VLBI: Piecewise linear functions
Satellite orbits	Dynamic modelling
Antenna	VLBI: Axis offset. No thermal deformation
	GNSS: phase centre variations (PCV)
Weighting Scheme	Based on repeatabilities

TABLE 6.1: Modelling and a-priori information used for the rigorous combination of VLBI and GNSS data.

an overall RMS of 2.5 mm. These results are in agreement with the results of Teke, K. et al. (2013), which show that the bias of ZTD between GNSS and VLBI ranges between -4 and 4 mm. Similarly, Figure 6.2b show the modelled ΔZHD and the estimated ΔZWD for the baseline FD-VLBA–MDO1. We observed that the mean ΔZHD has a significantly large value, 91.7 mm, mostly due to the large height difference between the stations (ca. 398 m). The statistics associated with the ΔZWD also have an inferior performance: 7.4 mm for the mean, 4.6 mm of standard deviation, and RMS of 8.7 mm. This clearly shows that the height difference at the co-location site Fort Davis is too large to apply a tropospheric tie and the ZWD parameters for MDO1 and FD-VLBI cannot be stacked. At the remaining co-location sites, we observed that the ΔZWD is not correlated to the height difference, and has ZWD mean values within $\pm$5 mm (excluding FD-VLBI–MDO1). These mean differences can be seen in Figure 6.3. We define the tropospheric tie as the difference in the tropospheric delay between the reference points of the VLBI and the GNSS antennas. Since the a-priori values of these delays are based on state-of-the-art global numerical weather prediction models, the difference between the delays at two stations caused by the height difference is modelled in advance (Wang, J. et al., 2022) and only the delays caused by the residual

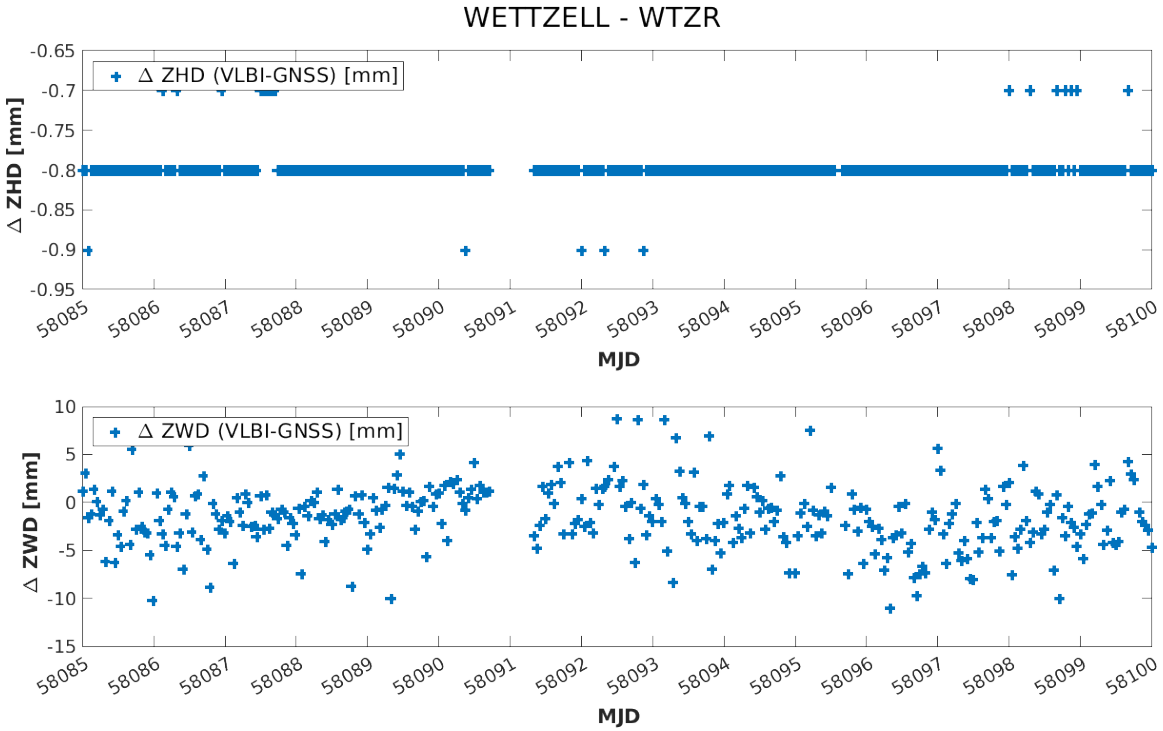

(a) Zenith tropospheric delay differences, baseline WETTZELL–WTZR.

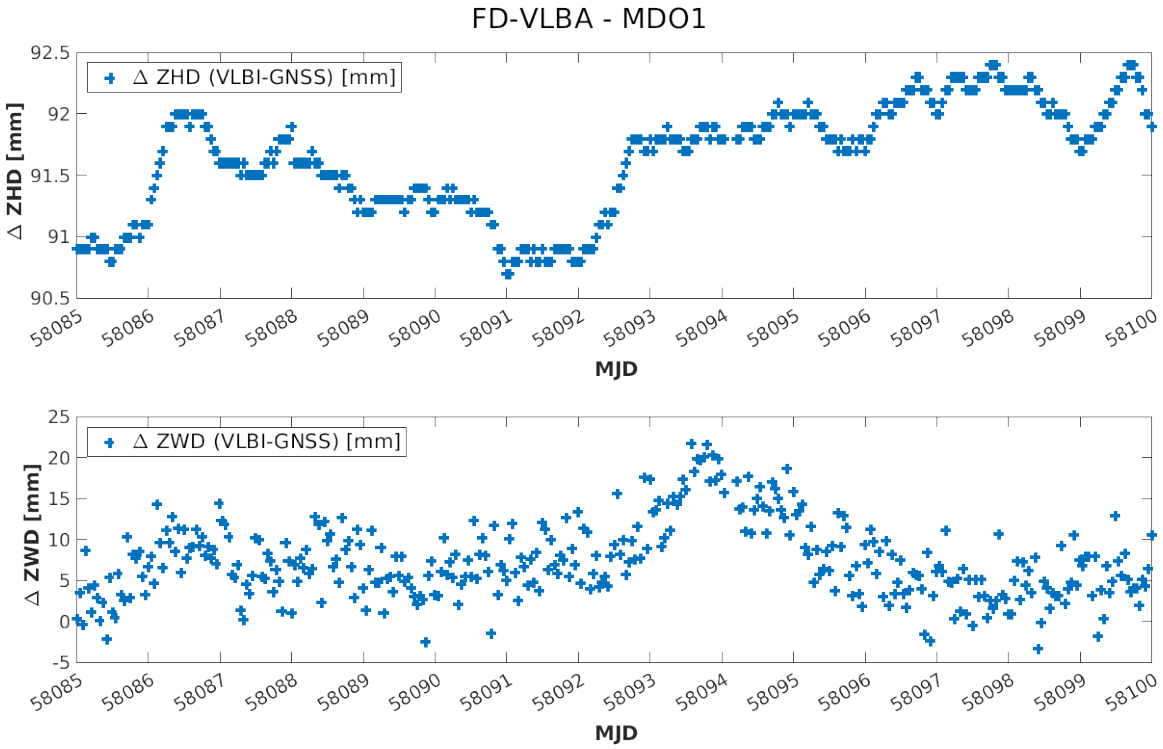

(b) Zenith tropospheric delay differences, baseline FD-VLBA–MDO1.

FIGURE 6.2: ZHD and ZWD differences at co-location sites FD-VLBA–MDO1 & WETTZELL–WTZR.

troposphere should be considered. Moreover, the mean differences shown in Figure 6.3 are not taken into account in the tropospheric ties, but are interpreted as resulting

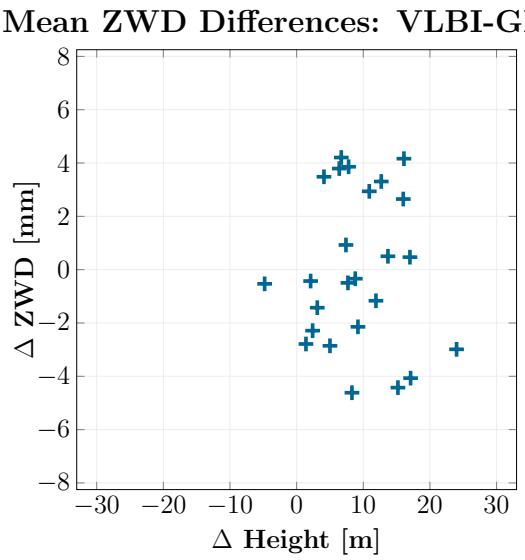

FIGURE 6.3: Summary of the mean zenith wet delay differences for co-located sites, regarding the height difference in the baseline.

from small systematic-effects that are not due to the troposphere or troposphere delays modelling.

6.4 DETERMINATION OF THE OPTIMAL WEIGHTING OF THE COMBINATION

An important aspect of the combination is the weighting of each technique, as the quality of the individual techniques varies considerably. Figure 6.4, shows the a posteriori σ of the observations resulting from the estimation process for each type of technique. The large contrast in the formal errors of each solution supports the need for an adequate inter-technique weighting. Our approach follows the idea of Thaller, D. (2008), using coordinate repeatabilities as the base of the weights, since they are directly part of the terrestrial reference frame. First, the quadratic mean repeatability of the station coordinates for all co-located stations over the 15 days of the CONT17 campaign, as an indicator of the quality of the observations (and the solution) is calculated:

$$r^2 = \frac{r_e^2 + r_n^2 + r_u^2}{3}$$

With this, a relative weighting among techniques i and j is computed:

$$w_{rep_{ij}} = \frac{r_i^2}{r_j^2}$$

Then, the sum of the main-diagonal elements of the normal equation matrix is calculated:

$$\overline{N} = \frac{1}{n_{crd}} \sum_{i=1}^{n_{crd}} N_{ii}$$

where the parameter n_{crd} refers to the number of diagonal elements of the normal equation. Since the weight is based on repeatabilities, only coordinates are considered.

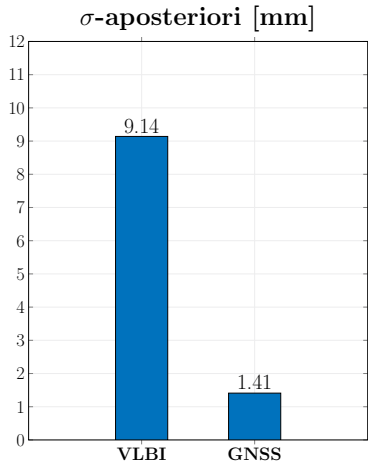

FIGURE 6.4: A posteriori σ of the observations resulting from the estimation process for each type of solution. A large difference in the quality of the results delivered by each technique motivates the use of inter-technique weighting.

Moreover, only the coordinates of the co-location sites are used. Finally, the $\overline{N}$ values of each technique are combined with the weight of the corresponding parameter in the solution, to obtain the weighting a technique j with respect to the technique i:

$$w_{ij} = \frac{\overline{N}_i}{\overline{N}_j} \cdot w_{rep_{ij}}$$

Table 6.2 shows the results of the calculation of the optimal inter-technique weight. For the data of the CONT17 campaign, an optimal weight for the VLBI NEQs of 0.276 was determined.

Indicator			
RMS Rep. VLBI	3.54	3.11	8.07
RMS Rep. GNSS	2.57	2.71	6.16
r^2_{VLBI}		29.10	
r^2_{GNSS}		17.27	
$w_{rep_{ij}}$		1.69	
$\overline{N}$ VLBI		2238.22	
$\overline{N}$ GNSS		1040.80	
Weight factor		0.276	

TABLE 6.2: Results of the calculation of the optimal inter-technique weight for the data of the CONT17 campaign. Repeatabilities are given for east, north and up components, respectively, in millimetres.

6.5 VALIDATION OF THE OPTIMAL WEIGHTING OF THE COMBINATION

To test the adequacy of the weight determined in Section 6.4, we study the performance of the repeatabilities of the combined solution, for typical cases of inter-technique

weights, taking as reference the GNSS solution and using the parametrisation of Section 6.2. This is, in all the cases the GNSS solution has a weight of 1, while we vary the weight of the VLBI solution. A large number of cases was investigated, but four specific cases give the essence of the behaviour. These are: (1) 100^{-2}, meaning that the GNSS observations will have a considerably larger contribution to the final solution. (2) 0.276, the "optimal weight" of Section 6.4. (3) 1, meaning that both techniques are equally weighted. (4) 100^{2}, meaning that the VLBI observations will have a considerably larger contribution to the final solution. Figure 6.5 shows an example of the repeatabilities for two co-location sites, Pietown and Brewster (USA). For these two cases, the repeatabilities of the solution with the optimal weight show a marginally better performance, especially when it comes to the height component when compared to the solution with equal weights. From these two examples, it is also noticeable that the solutions with larger weights for either VLBI or GNSS underperform when compared to the solution with optimal weights.

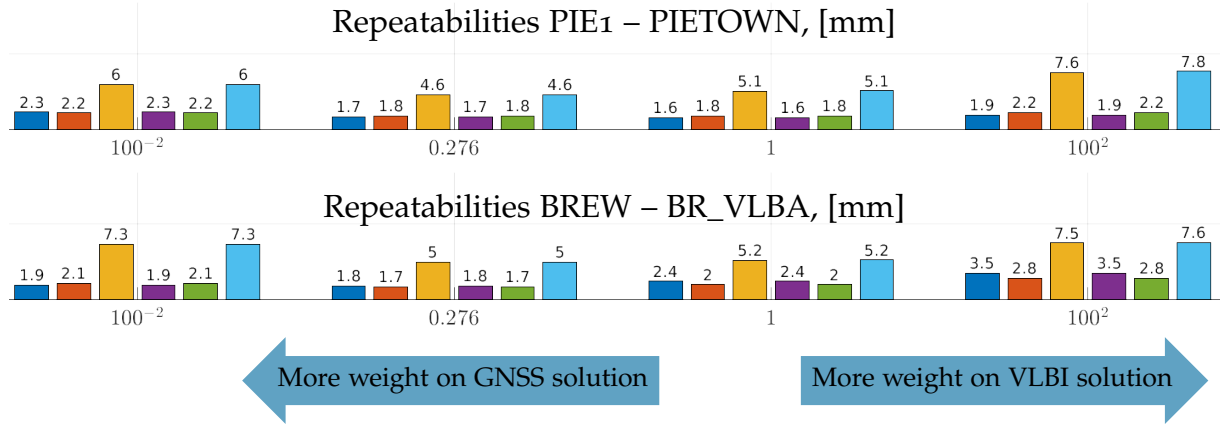

FIGURE 6.5: Example of the repeatabilities of the combined solution, for different inter-technique weights. All values in mm. The first three values (blue, red and yellow colours) are the repeatabilities for the GNSS station, while the remaining three (purple, green and cyan colours) correspond to the VLBI station.

Moreover, Figure 6.6 displays the RMS of the coordinate repeatabilities for the combined solutions over the 15 days of the CONT17 campaign, when using different inter-technique weights, using exclusively the stations at co-location sites. While the repeatabilities of the horizontal components remain almost unchanged, there is an improvement in the height component when analysing all stations together (top plot of Figure 6.6). The differences are more noticeable when looking at the stations separated by technique, especially for the GNSS case, where the height component of the solution with the optimal weight outperforms all the other solutions by more than 10 %. Since the optimal inter-technique weight is based on the coordinate repeatabilites, it is fair to assume that its influence is not so evident in the remaining parameters. However, we looked into the performance of a subset of the EOPs, to test whether the improvement remains. Figure 6.7 shows the RMS of the differences in the estimated polar motion, UT1-UTC, and LoD, with respect to the IERS C04 series, for each inter-technique weight. As for the repeatabilities case, we observed that the solution with the optimal weight shows a marginal improvement concerning the solution with equal weights,

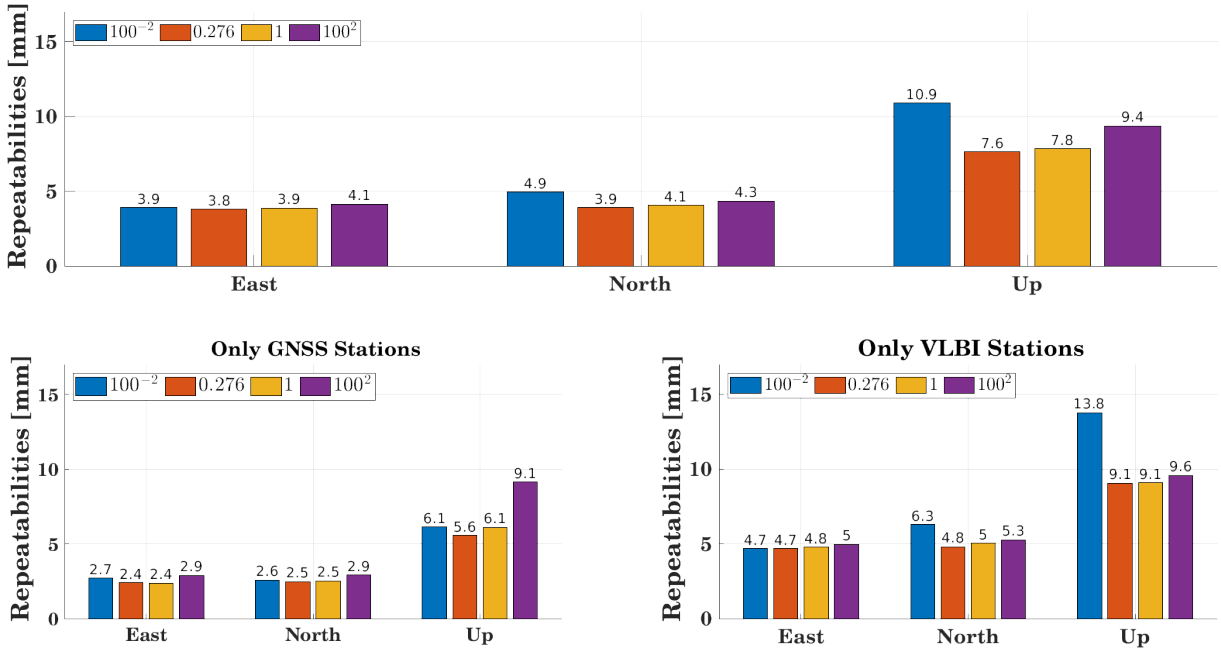

FIGURE 6.6: RMS of the repeatabilities of the combined solution over the 15 days of the CONT17 campaign, for different inter-technique weights. The RMS value was calculated using all the co-located stations. All values in mm.

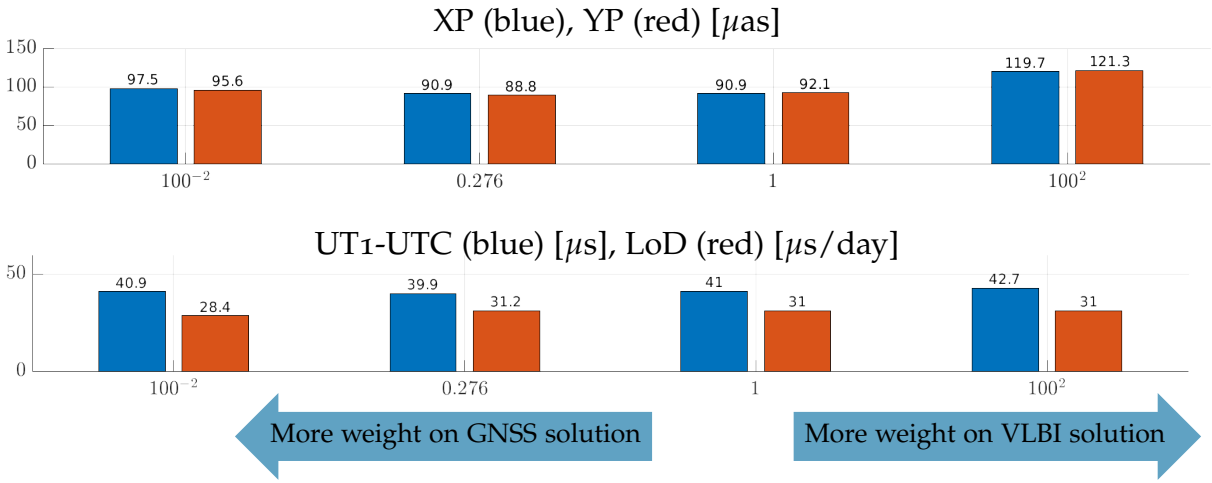

FIGURE 6.7: RMS of the differences of the estimated EOPs wrt. IERS C04 series, for each inter-technique weight. Top: RMS of Polar Motion [μas]. Bottom: UT1-UTC [μs] and LoD [μs/day].

and outperforms the solutions with large weights for either VLBI or GNSS. These results support the selection of the optimal inter-technique weight (0.276) of Section 6.4.

6.6 REALISATION OF THE LOCAL TIES

A central element in the combination of space geodetic techniques is the use of local ties (Sarti, P. et al., 2013), and in particular, the quality with which they are determined. To realise the local ties, we use the ITRF2014 coordinates of the GNSS stations and

add the local ties to get VLBI coordinates. Then, we apply relative constraints to fix the vector between the co-located VLBI and GNSS stations. This ensures that the coordinates are consistent with the local tie values. To investigate their quality, we use as relative constraints the formal errors of the coordinates contained in the SINEX files of the local ties of the ITRF2014 solution, from the IERS website. These formal errors (σ_{snx}) are the starting point for the remaining test solutions. We calculate combined solutions with relative constraints of $10^{1}\sigma_{snx}$, $10^{-1}\sigma_{snx}$ and $10^{-2}\sigma_{snx}$, and analyse the coordinate repeatabilities. Figure 6.8 shows an example of these repeatabilities for the sites Brewster (USA) and Fortaleza (Brasil). It is expected that a strong local tie causes the

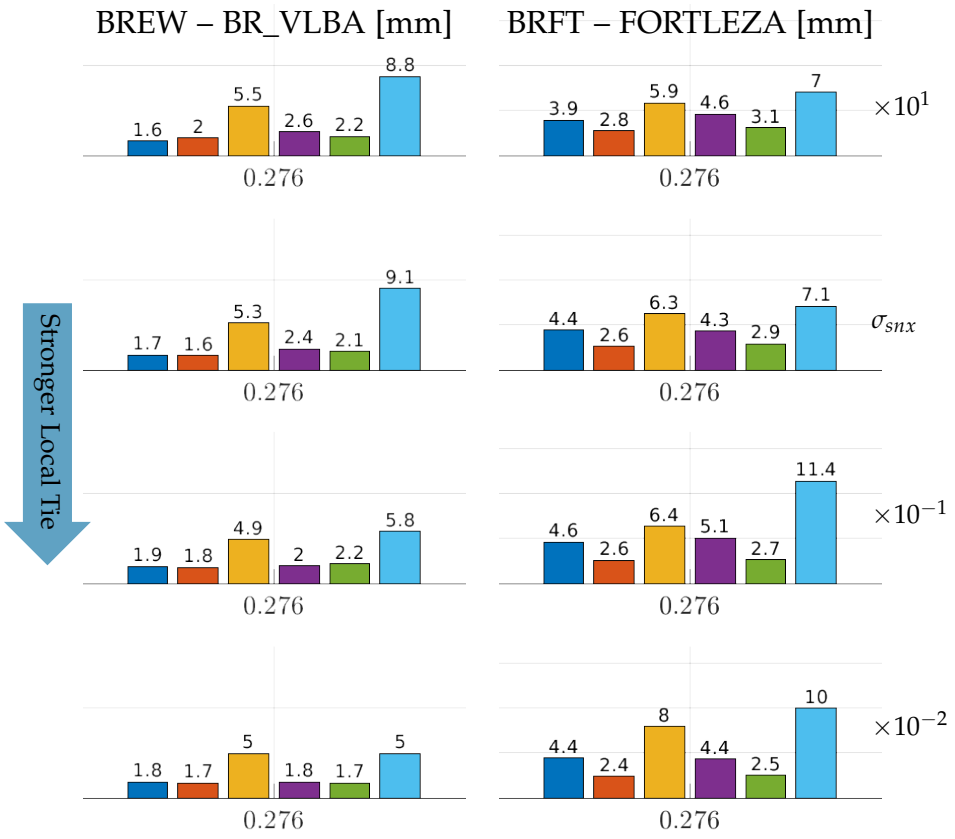

FIGURE 6.8: Coordinate repeatabilities of the combined solution, regarding the type of constraint used for the local tie. For the combination, the optimal inter-technique weight of Section 6.5 was used. All values in mm. The first three values (blue, red and yellow colours) are the repeatabilities for the GNSS station, while the remaining three (purple, green and cyan colours) correspond to the VLBI station.

repeatabilities of the two stations to converge to the same value. We observed that the quality of the local ties varies among the co-location sites, and that different co-location sites have different responses to the relative constraint used. The two co-location sites shown in Figure 6.8 represent these behaviours. For the baseline BR_VLBA–BREW, the original relative constraints (σ_{snx}) end up in different repeatabilities, especially for the up component. Similarly to the case when using a softer relative constraint. However, when using stronger versions of σ_{snx}, the repeatabilities of the two stations converge to the same (low) values. In contrast, the co-location baseline FORTLEZA–BRFT shows larger differences in the repeatabilities of the vertical component, when using stronger

values for σ_{snx} and do not converge to the same numbers for both co-location sites, indicating strong inconsistencies between the two techniques. In this case, a softer version of the local ties delivers the best results for this co-location site. Based on this analysis, we select the optimal set of local tie constraints, for each baseline at the co-location sites, so that it minimises the repeatabilities of the two stations, while trying to get them to converge to the same value. Figure 6.9 shows two additional baselines at co-location sites, where the advantage of using an individual level of relative constraints for each baseline is shown. For the two co-location sites, Fort Davis (USA) and ZELENCHK (Russia), the repeatabilities of the height component of the VLBI and GNSS stations are largely reduced, when proper local tie constraints are applied, and their corresponding values show a larger degree of convergence. Finally,

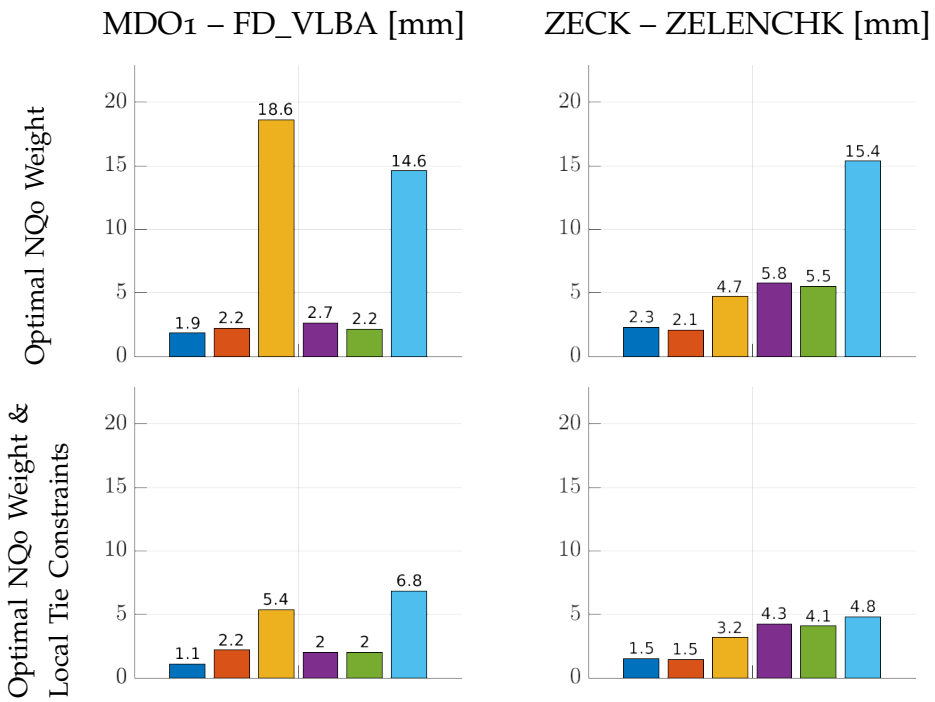

FIGURE 6.9: Improvement in the coordinate repeatabilities of several stations in the combined solution, when using an appropriate constraint for the local tie. All values in mm. The first three values (blue, red and yellow colours) are the repeatabilities for the GNSS station, while the remaining three (purple, green and cyan colours) correspond to the VLBI station.

we calculate the RMS of the coordinate repeatabilities when using these appropriate constraints for the local ties, and display them in Figure 6.10. The benefits of the solution with optimal relative constraints are noticeable. The repeatabilities improve by 18 %, 13 %, and 14 %, for the east, north, and height components, respectively (top plot of Figure 6.10). When looking only at the GNSS stations, the improvements are 12 % for the horizontal, and 11 % for the vertical component. The largest improvement can be seen in the repeatabilities of the VLBI stations, with 21 % 12 %, and 17 %, for the east, north and height component, respectively (bottom plots of Figure 6.10). Table 6.3 show the constraints selected for each co-located site in the solution with optimal weights and optimal local tie constraints.

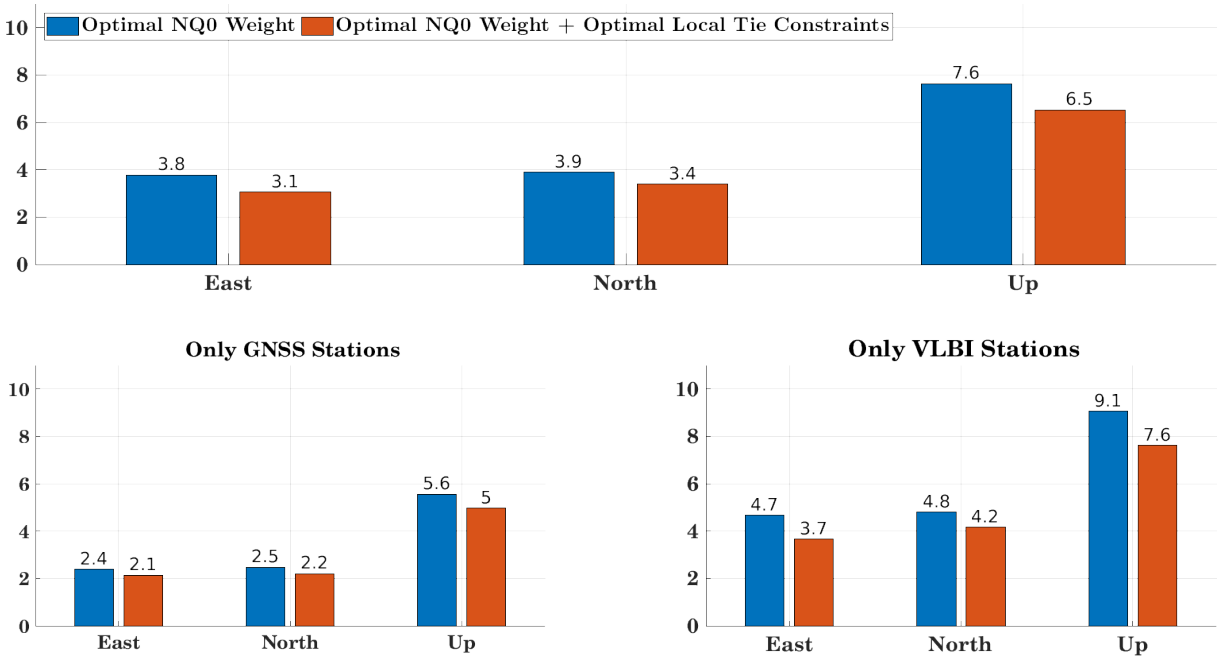

FIGURE 6.10: RMS of the repeatabilities of the combined solution over the 15 days of the CONT17 campaign using appropriate constraint for local ties. All values in mm.

6.7 DIFFERENCES OF EARTH ORIENTATION PARAMETERS TO IGS SOLUTION

To assess the improvement in the EOPs we use the IGS final solutions as reference for the comparison, and the two 15-days rigorous combined solutions of Sections 6.5 and 6.6 are analysed. The RMS of the differences of the daily EOP estimates regarding the IGS solution are displayed in Figure 6.11. Both solutions agree with the IGS solution at approximately the same level for the LoD and polar motion rate parameters. However, there is a large improvement in both polar motion components: 36 % and 42 % for the X and Y components, respectively. It should be mentioned that there is a difficulty to find a solution that can be used as ground truth for a comparison, as the rigorously combined solution is expected to be better than any other solution.

Site	Type	Site	Type	Site	Type
Badary (RU)	$\times 10^{1}$	Matera (IT)	$\times 10^{-2}$	Wettzell (DE)	$\times 10^{1}$
Fortaleza (BR)	$\times 10^{-2}$	Mauna Kea (US)	$\times 10^{-2}$	Yarragadee (AU)	$\times 10^{-2}$
Ft. Davis (US)*	$\times 10^{1}$	Medicina (IT)	$\times 10^{-2}$	Pie Town (US)	$\times 10^{-2}$
Hartebeesthoek (ZA)	$\times 10^{-2}$	North Liberty (US)	$\times 10^{1}$	Yebes (ES)	$\times 10^{-2}$
Hobart (AU)	$\times 10^{-2}$	Ny Alesund (NO)	$\times 10^{-2}$	Zelenchukskaya (RU)	$\times 10^{0}$
Katherine (AU)	$\times 10^{1}$	Onsala (SE)	$\times 10^{0}$		
Kokee Park (US)	$\times 10^{0}$	Seshan (CN)	$\times 10^{0}$		

TABLE 6.3: Type of constraint for the local tie at each co-location site. The constraint is given in multiples of the formal errors (σ_{snx}) of the coordinates contained in the SINEX files of the local ties, according to the IERS. At the Ft. Davis site, no tropospheric ties were used. Country codes in parenthesis according to ISO_3166-2.

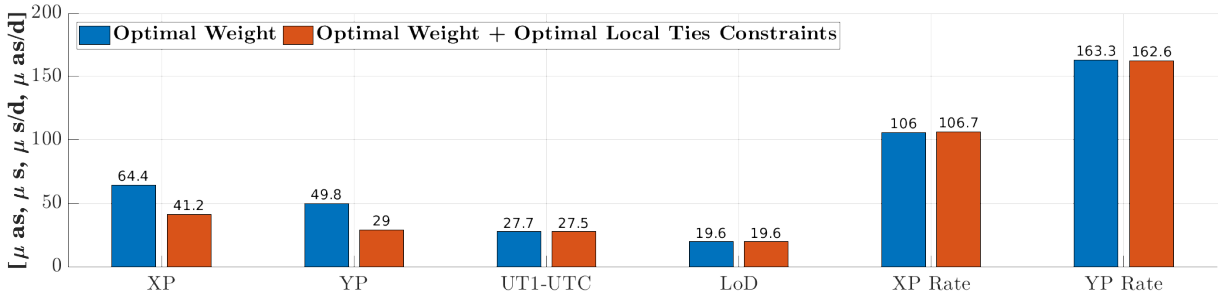

FIGURE 6.11: RMS of differences of the daily estimated EOP, in the combined solutions, regarding the IGS solution. Notice the different units (left-hand side of the plot) for each type of parameter.

6.8 COMPARISON OF THE RIGOROUS SOLUTION TO THE SINGLE TECHNIQUE SOLUTIONS

The final step in the study of the rigorous combination is the comparison of the relevant parameters to the single-technique solutions. Moreover, as an additional reference for comparison, we include a rigorous combination where only local ties were used. We start with the analysis of the RMS for the coordinate repeatabilities. While the combined results of both techniques may show a decrease in the performance of the rigorous solution with respect to the GNSS solution (top plot of Figure 6.12) when separating the repeatabilities per technique, the benefits of the combined solution are more evident. The improvement in the repeatabilities of the GNSS stations in the rigorous solution regarding the GNSS-only solution are 22 %, 24 %, and 19 %, for east, north and height, respectively. Similarly, the improvement regarding the VLBI-only solution amount to 2 % and 14 % for the north and height component, respectively. We also observed an improvement in the coordinate repeatabilities when comparing the rigorous solution with local and tropospheric ties with the rigorous solution with only local ties, with the height component of the former improving the performance by 11 % (only GNSS stations), 7 % (only VLBI stations), and 6 % (all stations included). Additionally, the RMS of the difference of the EOPs regarding the IGS final solution is investigated, and displayed in Figure 6.13. Once again, the rigorous solution outperforms the single-technique solutions in the polar motion estimates, with an improvement of 35 % and 9 % regarding the GNSS-only solution, for the X and Y components, respectively, and 25 % and 19 % regarding the VLBI-only solution, for the X and Y components, respectively. The three solutions agree with the IGS solution at approximately the same level for the UT1-UTC, with the rigorous solution helping to improve the results in the LoD estimate: 48 % and 10 %, regarding the GNSS-only and VLBI-only solutions, respectively. The rate of change of polar motion shows a favourable tendency towards the rigorous solution: 20 % and 2 % for the rate of the X and Y component, respectively, regarding the GNSS-only solution, and 9 % and 20 % for the rate of the X and Y component, respectively, regarding the VLBI-only solution. The comparison of the rigorous solution with local and tropospheric ties with the rigorous solution with only local ties showed that both approaches yield similar

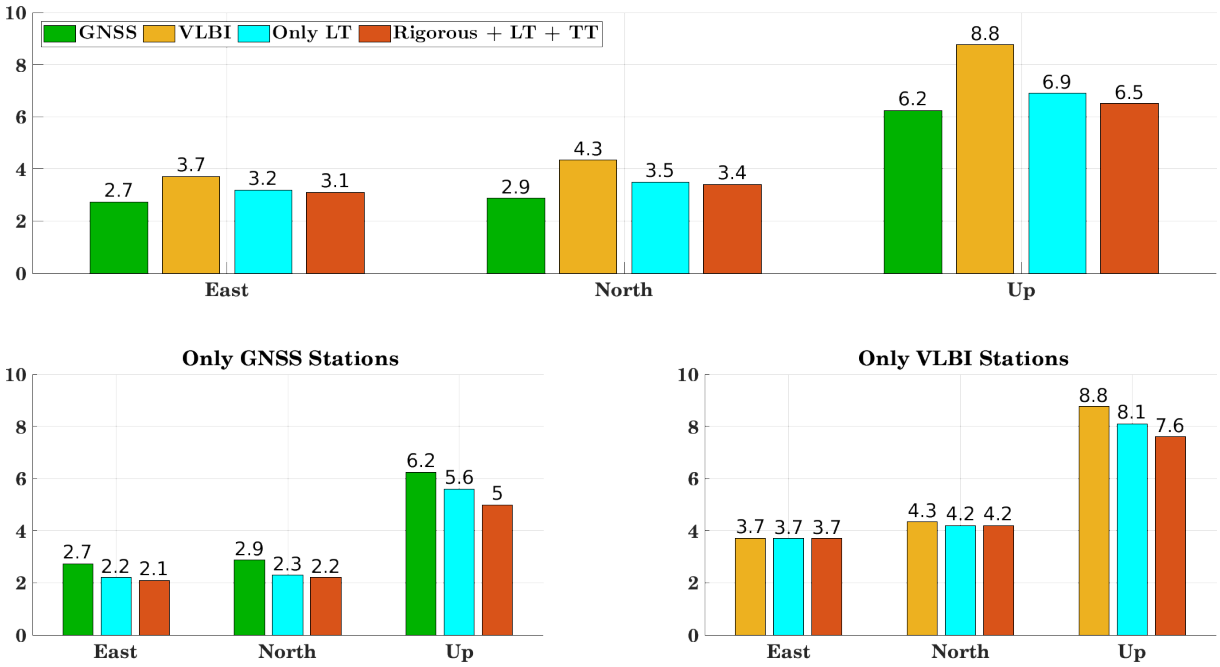

FIGURE 6.12: RMS of coordinate repeatabilities for the individual technique solutions, and the combined solutions. All values in mm.

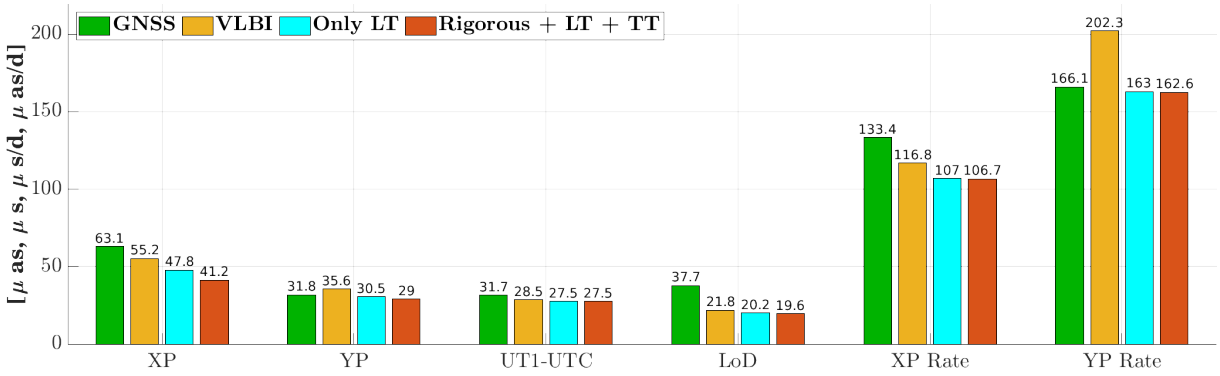

FIGURE 6.13: RMS of daily EOP differences to IGS for the individual technique solutions, and the combined solutions. Notice the different units on the left side for each parameter.

results regarding the LoD estimation, with an improvement of the polar motion on the former solution of 14 % and 5 %, for the X and Y components, respectively.

6.9 ESTIMATION OF SUB-DAILY EOPS

To study the high-frequency EOP variations, we calculated polar motion and UT1-UTC with an hourly resolution, and from the estimated time series we subtracted the interpolated values of the IGS final series. While the interpolation of the IGS reference should not constitute an issue when it comes to the polar motion estimates, it could become problematic for the comparison of the UT1-UTC results (instead of UT1-UTC, UT1R-UTC has to be interpolated). Despite these issues, the RMS of the differences is in the order 125 and 130 μas, for the X and Y components of the polar motion, respectively,

and 25 μs and 29 μas/day for the UT1-UTC and the LoD differences, respectively. These results are well in agreement with those of other works (e.g Rothacher, M. et al. (2001)). We then calculated the Fourier spectra for the remaining polar motion ($XP - i \times YP$) and for UT1-UTC differences. These spectra can be seen in Figure 6.14. Although

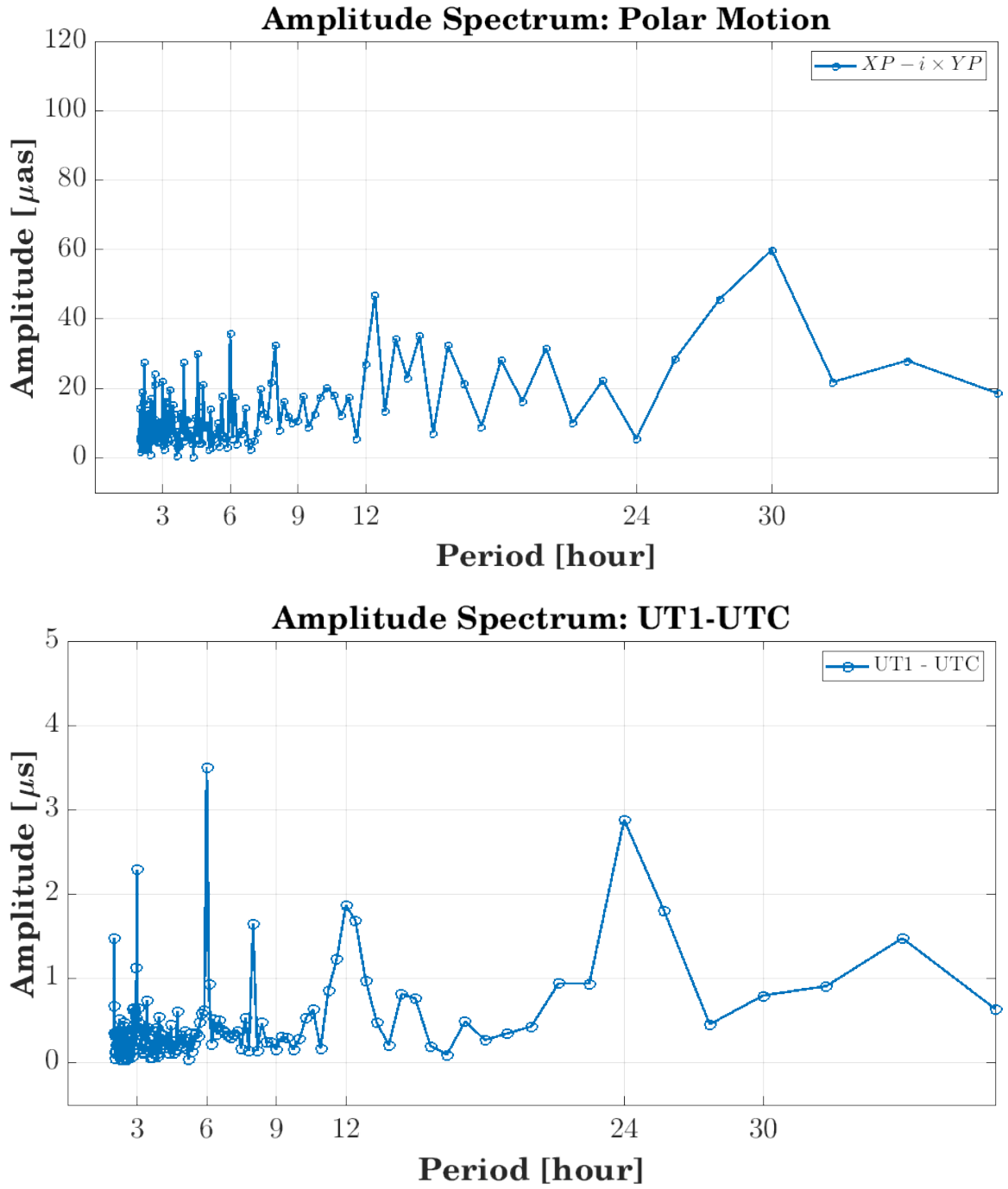

FIGURE 6.14: Fourier spectra of the sub-daily difference of the EOPs regarding the IGS final series. Top: polar motion ($XP - i \times YP$). Bottom: UT1-UTC

we did not expect to see any significant variation, we observe peaks of considerable magnitude in the polar motion at the 6 h, 12 h, and 30 h, and in the UT1-UTC spectra at 6 h, 12 h, and 24 h. Similar frequency peaks have been found in Nilsson, T. et al. (2019), for a VLBI-only solution, where he attributes the cause of these peaks to systematic

errors associated to the VLBI solution, e.g. related to the observed radio sources, as the same radio source is scheduled to be observed by the same stations at about the same time every day, producing errors with a period of ca. 1 day. Moreover, station-related errors may also contribute to these sub-diurnal variations.

6.10 SUMMARY AND OUTLOOK

A rigorously combined solution for the estimation of geodetic parameters including GNSS and VLBI data has been achieved. This solution, based on the data of the CONT17 campaign plus GNSS/IGS data, profits from the use of local ties with appropriate constraints, tropospheric ties at co-location sites, as well as from a tailored inter-technique weighting scheme based on the repeatabilities of the station coordinates. The combined solution was processed in a single state-of-the-art software, Bernese v5.2 – VLBI Version, where not only the a priori modelling and the parametrisation for both techniques was the same, but also was the variance-covariance of all the estimates, and the constraints for all the parameters used throughout the estimation process. The combined solution with local and troposphere ties generally improves the precision of all the estimated geodetic parameters. In particular, the repeatabilities of the station coordinates are improved by 22 %, 24 %, and 19 %, for east, north, and height, respectively, compared to the GNSS-only solution, and by 2 % and 14 % for the north and height component, respectively, compared to the VLBI-only solution. Additionally, the EOPs estimates are also improved, with the rigorous solution outperforming the single-technique solutions in the polar motion estimates, by 35 % and 9 % compared to the GNSS-only solution, for the X and Y components, respectively, and 25 % and 19 % compared to the VLBI-only solution, for the X and Y components, respectively. The rigorous combination contributes to the stabilisation of the UT1-UTC, with the improvement of the LoD, showing an gain of 48 % and 10 %, compared to the GNSS-only and VLBI-only solutions, respectively. While there is an improvement with the use of tropospheric ties, further studies are required to improve the agreement among the VLBI and GNSS tropospheric estimates, which is currently at the level of 1–5 mm. Future activities will include an approach using variance component estimation for the weighting, the study of additional parameters in the combination (such as geocentre), additional studies compared to the combination of intensive VLBI sessions with GNSS for the estimation of UT1-UTC, and the rigorous triple combination with SLR observations.

ACKNOWLEDGEMENTS This work has been developed within the project "Co-location of Space Geodetic Techniques on Ground and in Space" in the frame of the DFG funded research unit on reference systems, and funded by the Swiss National Foundation (SNF, 200021E-160421). Additionally, the authors would like to thank the IERS, CODE, IVS and CDDIS for providing the necessary reference coordinates, orbital products, VLBI data, and GNSS data required for the realisation of this work.

7

CONCLUSIONS AND FUTURE WORK

7.1 CONCLUSIONS

The overarching goal of this thesis was the study of alternative strategies for the co-location of space geodetic techniques, to improve the understanding of technique-specific error sources, and to contribute to their mitigation by providing insights into systematic technique-related errors, leading to a better agreement with the local ties at fundamental sites. These studies constitute a necessary step to improve the realisation of the ITRF and to fulfil the GGOS goals in terms of accuracy and stability. The experiments presented in this thesis contribute to two fundamental aspects of the combination of space geodetic techniques:

- The detailed analysis of biases of individual instruments on short baselines, with emphasis on the many environmental effects common to all instruments, through intra-technique co-location (GNSS–GNSS, VLBI–VLBI and SLR-SLR). This includes the definition of alternative and innovative processing strategies, such as the differencing approaches for SLR observations, and the use of time transfer data as the realisation of a clock tie for processing VLBI short baselines.

- The homogeneous processing of the different techniques, with state-of-the-art models, same a priori modelling, identical parametrisation, and equivalent use of constraints, in a single piece of software. Through an integrated process at the observation level, this work achieves a rigorous, consistent combination of GNSS and VLBI data, which profits from using accurate local and tropospheric ties.

Through the use of several GNSS processing strategies, this work showed the magnitude of the impact of environmental conditions, such as periods of snow, in the estimation of station coordinates. The single-frequency-based strategies for short baselines developed in this work were able to differentiate seasonal phenomena with amplitudes of a few millimetres, showing discontinuities and periodic signals with high resolution. These demonstrate the presence of local effects that propagate into the global solutions that could be accurately measured by the analysis of the local co-located GNSS stations. The different approaches for the parametrisation of the troposphere explored in this work showed that it is possible to achieve sub-mm coordinate repeatabilities, e.g. using single-frequency-based solutions, modelling in advance the ZTD difference between stations caused by the height difference, and neglecting the residual wet delays. In contrast, this work showed that multi-frequency-based solutions, such as the ionospheric-free linear combination, suffer from the amplification of errors, and that these large frequency-dependent differences mainly originate from GNSS-related errors, such as the phase centre variation of the antenna and multipath. Moreover, this analysis showed that the differences between GNSS-based solutions and the local ties are beyond the precision of both techniques.

This work also showed the feasibility of the estimation of geodetic parameters for short VLBI baselines, using the short VLBI baseline between the RTW and the TWIN1 telescopes, at the Wettzell Observatory in Germany. Similarly to the analysis of GNSS short baselines, this thesis developed several processing strategies to analyse the data in this setup, where the relative behaviour of the local troposphere and the receiver clock offset estimates were analysed in multiple ways. A common element of these solutions was the sub-mm agreement of the estimated baseline length with the local ties. All solutions displayed mm-level formal errors, with a small favourable tendency towards the solutions with neglected residual wet tropospheric delays among the telescopes. When available, the estimated troposphere parameters were compared to the troposphere tie at the site, and a mm-level agreement was found. One of the main highlights of this analysis was the use of a clock tie, in the form of the TWOTT data, to replace the clock estimation. These experiments showed a sub-mm agreement between the estimated baseline length and the local tie, improving the RMS and the consistency of the solutions. This unique clock tie showed that the time distribution at the fundamental site Wettzell was possible and that the estimation of clock corrections can be made unnecessary, provided that a clock offset per session is calculated. This strategy removes the strong correlation between clock and height estimates and thus improves the precision of the height estimates.

This work also proposed an innovative differencing strategy for the estimation of geodetic parameters using SLR data, developing the concept of quasi-simultaneous SLR observations. Single- and double-differences of SLR observations for the short SLR baseline between the WLRS and SOS-W telescopes at the Wettzell Observatory, were calculated. The analysis of about two years of data showed that systematic errors common to both ends of the baseline can be estimated or eliminated. The single-difference-based solution showed a mm-level agreement with the local tie, with the additional feature of an estimation of a differential range bias among the two stations, with mm-level formal errors. Moreover, this work showed that the estimation of range biases can be avoided by using the double-difference processing strategy. This approach resulted in more accurate station coordinates, where the agreement with the local tie was in the sub-millimetre domain, as well as for the corresponding formal errors. While the estimation of additional parameters still remains under investigation (for instance for SLR-derived geocentre coordinates, and residual corrections for the centre-of-mass of the satellite), this work showed, for the first time, realistic results that support the potential of differencing strategies for SLR towards geodetic applications.

Finally, this work develop a processing strategy for the rigorous combination of VLBI and GNSS at the observation level. The main aspects of this solution are the use of local ties with appropriate constraints, the use of tropospheric ties at co-location sites, an appropriate inter-technique weighting scheme to integrate observations, and the use of the full variance-covariance information of all the estimates. Using the CONT17 campaign data and the IGS network, this thesis showed that a rigorous solution with these characteristics improves the precision of all the estimated geodetic parameters. Repeatabilities of the station coordinates are improved significantly com-

pared to the single-technique solutions. The improvement was even more evident in the up-component, where the tropospheric tie plays a fundamental role helping to stabilise the performance of the height estimates of the stations. Other geodetic parameters also improved with the combination. The EOPs estimated with the rigorous solution outperforming the single-technique solutions in terms of polar motion estimates, while a stabilisation of the UT1-UTC was accomplished, thanks to the improvement of the LoD estimates.

Some remaining questions still need to be addressed. The intra-technique processing strategies on short baselines proved to be a robust tool for determining station coordinates, receiver clock offsets (VLBI case), and range biases (SLR case). In the case of SLR, it would be interesting to analyse if these strategies can be applied to longer baselines, and that single- or double-differences will give access to the full set of parameters like geocentre, EOPs, satellite orbits, ..., for a global network of baselines. Additionally, a more detailed analysis of the remaining parameters in the combined solution is necessary. More experiments using the TWOTT data as a source for a clock tie are also required. Further studies on the performance of satellite orbits, source coordinates, and geocentre coordinates would be helpful. Future trials could implement a more sophisticated inter-technique weighting scheme based on variance-component estimation. To this end, these future activities need to consider additional VLBI data, e.g., previous VLBI CONT campaigns and possibly some VLBI intensive sessions. The next logical step after this work is the rigorous triple combination of space geodetic techniques: GNSS–VLBI–SLR. The software developments achieved in this work already prepared the ground for this task. Proving the advantages of this approach will require the analysis of more data sets and simulations.

7.2 PERSPECTIVES AND FUTURE WORK

Co-Location in Space on Board of GNSS Satellites

SLR Observations of GNSS satellites is an standard practice which provides co-location in space for these two techniques (Thaller, D. et al., 2011). However, VLBI (and DORIS) are still missing. VLBI observations of GNSS satellites in the L-band (G-VLBI) provide direct access to co-location in space, while connecting the terrestrial and inertial frames. This type of observations is expected to complement the use of local ties at co-location sites on the ground and improve the consistency on the realisation of the ITRF. Several test have been carried out to implement VLBI capabilities to observe GNSS satellites. Tornatore, V. et al. (2014a) and Tornatore, V. et al. (2014b) achieved the first satisfactory VLBI observations of GLONASS satellites, with an experiment using the telescopes in Medicina (Italy) and Onsala (Sweden). In Kodet, J. et al. (2014), a receiver unit able to observe the L1 frequency of GNSS satellites using the radio telescope in Wettzell (Germany), has been developed. With these hardware modifications Haas, R. et al. (2014) have demonstrated the generation of the first set of delay observables suitable for geodetic applications. Plank, L. et al. (2017) have carried out a successful set of single-frequency VLBI observations to GNSS at the Australian sites Ceduna and Hobart

(Figure 7.1). The measurement process, including the planning of the observations, the correlation of the data and the calculation of time delay observables, is expected to be implemented automatically for further experiments. Their work reports some observation and correlation problems, and some lack of information such as the phase centre offsets for the observed satellites. Additional refinements in their parametrisation are required. However, the comparison of the observed and the modelled delays in this study shows promising results, and constitute the first completely successful observation of GNSS satellites with VLBI telescopes for geodetic applications. For an

FIGURE 7.1: VLBI Baseline CEDUNA-HOBART26.

initial evaluation of the accuracy in terms of the noise of the G-VLBI observations from the CEDUNA-HOBART26 baseline, we have created a processing chain for the analysis of the data of Plank, L. et al. (2017), using the Bernese v52 – VLBI version. The observations used in our small test were collected on May 10th, 2016, between 17:24 h and 22:08 h. As a result of this measurement campaign, five GNSS satellites were observed, and 629 observations (delays) were finally obtained. Figure 7.2 shows the time series of delays available from this campaign. An initial strategy for the quality assessment was done by comparing the observed delay with the modelled one (observed minus computed, o-c). Satellite orbits and Earth orientation parameters were provide by the Centre for Orbit Determination in Europe (CODE) (Dach, R. et al., 2017), and the station coordinates and antenna types/offsets were fixed to the values of Table 7.1. With these parameters, we found residuals within ca. 3 m or 10 ns, which suggests deficiencies in the modelling (Table 7.2). The skyplot of residuals (Figure 7.3b), which uses the mean elevation angle, shows that satellite G02 and G24 have the largest residuals for low elevation angles. This is an obvious consequence of the inappropriate atmospheric modelling in our processing approach. No ionosphere corrections were applied during this initial test. Tropospheric hydrostatic delays were calculated for both stations, but the wet delays were not estimated. While additional work has to be performed to improve this processing strategy, for instance by introducing

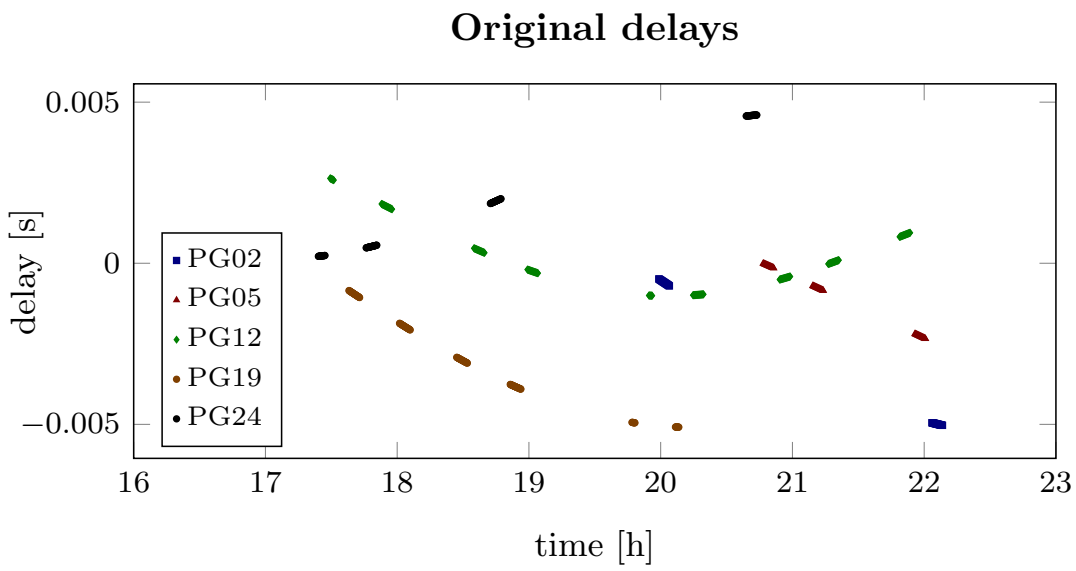

FIGURE 7.2: Time series of original G-VLBI single-frequency observations (VLBI delays).

	HOBART26	CEDUNA
X $[m]$	-3950236.8559	-3753442.7457
Y $[m]$	2522347.5744	3912709.7530
Z $[m]$	-4311562.4144	-3348067.6095
V_X $[m/yr]$	-0.0383	-0.0417
V_Y $[m/yr]$	0.0083	0.0027
V_Z $[m/yr]$	0.0414	0.0499
Axis Offset [m]	8.1912	0
Telescope Mount	X-YE	–

TABLE 7.1: Parameters of the VLBI baseline CEDUNA-HOBART26.

# of obs.	629
A post. σ [m]	1.0855
Maximum residual [m]	2.945
Minimum residual [m]	-2.986
Mean Residual [m]	0.176

TABLE 7.2: Summary of the residual delays (o-c), for the G-VLBI single-frequency observations from the CEDUNA-HOBART26 baseline.

ionospheric corrections from co-located GNSS observations using the geometry-free linear combination as done by Männel, B. et al. (2016a), these initial results show the potential of this new set of observations. Complementary, the realisation of a space tie, with the use of dedicated satellite missions, has been presented by many different studies as the tool for the enhancement of the definition of the ITRF. Three

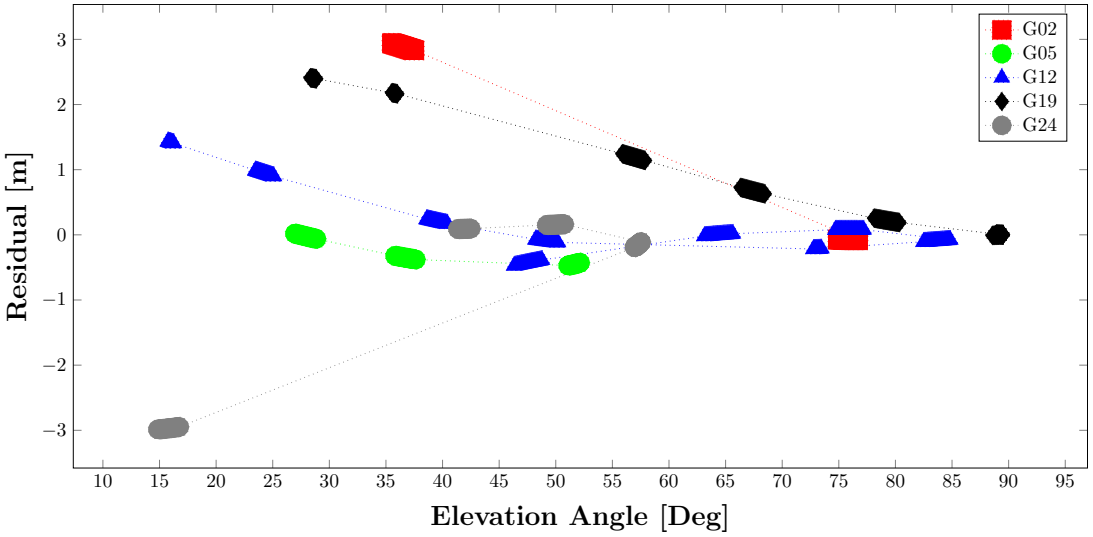

(a) Residuals in relation to elevation angle.

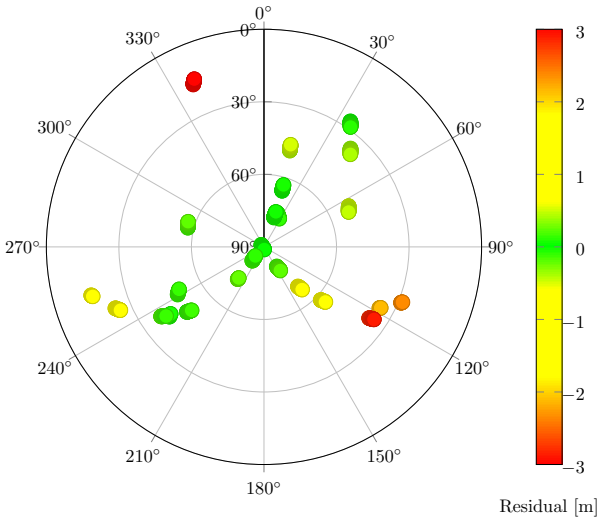

(b) Sky-plot of residuals.

FIGURE 7.3: Performance of the residual delays (o-c), for the single-frequency G-VLBI observations from the CEDUNA-HOBART26 baseline.

missions, GRASP: Geodetic Reference Antenna in Space in Nerem, R. et al. (2011), E-GRIP: The Einstein Gravitational Red-Shift Probe in Männel, B. et al. (2016b) and E-GRASP/Eratosthenes European Geodetic Reference Antenna in Space/European Reference Antenna of Space Geodetic Techniques Enhancing Earth Science of Biancale, R. et al., 2017, have been proposed to improve the consistency of the combination of space geodetic techniques through the triple co-location (GNSS, SLR and VLBI) in space. This satellite mission, as its proposed predecessors, is expected to enable the realisation of an ITRF with the accuracy and stability specified by the Global Geodetic Observing System (GGOS) (Plag, H.-P. et al., 2009). While these two missions are still to be approved, the mission APOD: Atmospheric density detection and Precise Orbit Determination in Tang, G. et al. (2016) was started with its scientific goals and, albeit

problems with the on-board GNSS receivers, it was briefly observed by SLR and VLBI telescopes.

Combination of VLBI Intensives and GNSS Data for the Estimation of UT1-UTC

The difference between Universal Time (UT1) and Coordinated Universal Time (UTC) is commonly estimated using observations from the so-called VLBI *intensives*: dedicated 1-hour, single baseline sessions. Here, the main condition for an accurate estimation of UT1-UTC is an adequate geometry between the telescopes, which requires typically a long east–west extension of the baseline (Schartner, M. et al., 2021). A complete description of the performance of the VLBI Intensive observing programs INT2 and INT3 during the last five years, has been performed in Schartner, M. et al., 2022, with a great level of detail, where the characteristics, differences and quality levels of the results of several analysis centres have been addressed. As a proof of concept, our small experiment uses ten intensive sessions of the VLBI Global Observing System (VGOS) telescopes MACGO12M (Fort Davis, USA) and WETTZ13S (Wettzell, Germany), carried out between 18.01.2022 and 29.03.2022. Similarly to the discussion of Chapter 6, we aim for a rigorous combination of VLBI and GNSS data, focusing on the estimation of UT1-UTC and the corresponding VLBI zenith wet delays. To this end, the VLBI part of the processing includes fixing the station coordinates to the ITRF2020 solution of the IERS. Additionally, zenith tropospheric delays are estimated each 15 minutes, without performing the estimation of troposphere gradients. Clock offsets are calculated with the same resolution (15 min.) using as reference the station WETTZ13S. Finally, one UT1-UTC parameter is estimated per session. On the other hand, the GNSS part of the solution includes ca. 180 GNSS stations, with GPS and GLONASS observations, for which we estimate daily coordinates, using the NNR–NNT conditions. Daily EOP parameters are estimated in the form of pole motion, UT1-UTC, LoD, celestial pole offsets, and their corresponding rates. The troposphere parametrisation of the GNSS solutions includes ZWD with 1 h resolution and gradients each 24 h. This combined solution realises the tropospheric ties with the use of the IGS stations MDO1 and WTZR, co-located with the VLBI stations MACGO12M and WETTZ13S, respectively. The remaining parameters and the processing strategy follows the same approach of a rigorous combination described in Chapter 6, except that equal inter-technique weights are used. Figure 7.4 shows the results of this process regarding the estimation of UT1-UTC. We investigated two approaches: a pure VLBI solution (Bernese) and a rigorous solution with local and tropospheric ties (Bernese+TT), and compared their results with the IVS solution and the C04 series. The RMS of the differences of both approaches has a similar performance in both solution, with the solution with tropospheric ties being closer to the IVS estimates, and the pure VLBI solution closer to the C04 final solution. This good agreement is further supported with an improvement in the formal error of the solutions. While the formal errors of the VLBI solution are at the same level as the IVS solution, we found out that the formal error of the combination with tropospheric ties is considerably reduced. This reduction is a consequence of the combined use of the GNSS which increases the number of observations drastically. It is to be expected, however, that the formal errors from

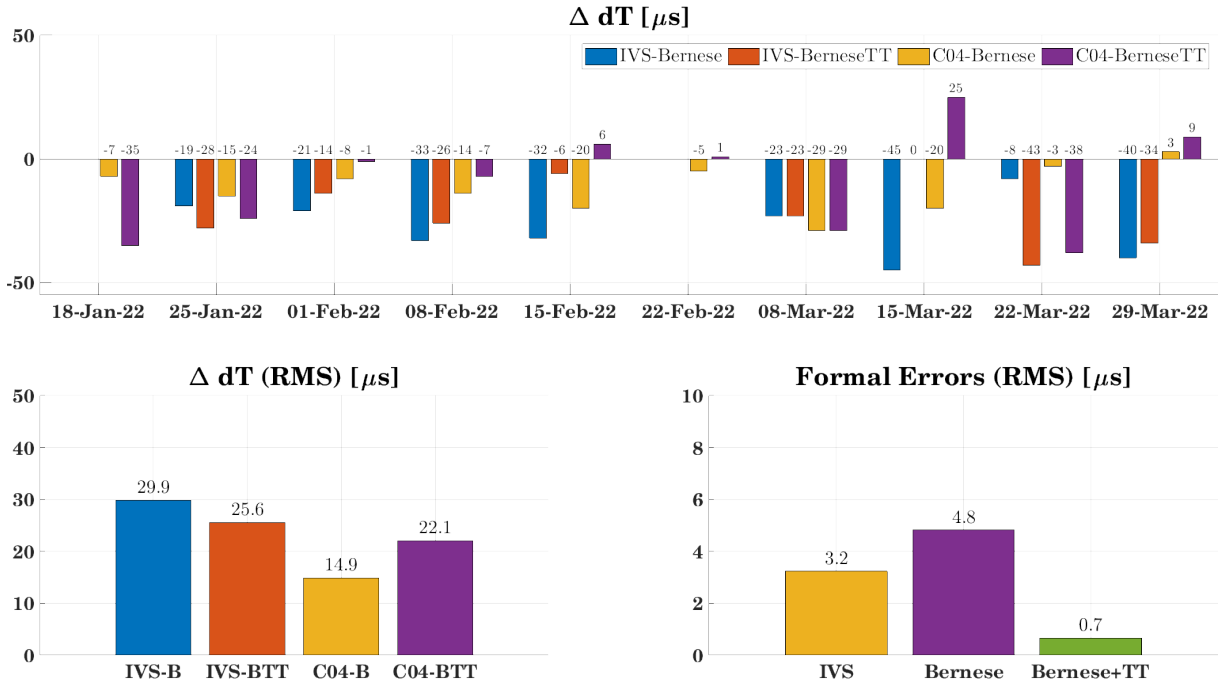

FIGURE 7.4: Differences of UT1-UTC estimates in the rigorous combination of VLBI Intensives and GNSS. These plots display the time series of UT1-UTC differences to the IVS solution and the C04 final solutions, for a pure VLBI solution (Bernese, B) and a rigorous solution with tropospheric ties (Bernese+TT, BTT).

GNSS are too optimistic, so that this issue needs to be further investigated. Moreover, the time resolution of the estimated troposphere parameters of each technique is not consistent. Thus, a refined parametrisation is required.

A

APPENDIX: PAPER II

Originally published as: ***I. D. Herrera-Pinzón*** *et al. (2018b). "Analysis of the Short VLBI Baseline at the Wettzell Observatory". In:* Proceedings of the 10th IVS General Meeting (2018). *Kartverket, S.49.* URL: *https://ivscc.gsfc.nasa.gov/publications/gm2018/*

Paper II

Analysis of the Short VLBI Baseline at the Wettzell Observatory

Iván Herrera-Pinzón[1], Markus Rothacher[1], Jan Kodet[2], and Ulrich Schreiber[2]
[1] Institute for Geodesy and Photogrammetry, ETH Zurich. Switzerland
[2] Federal Agency for Cartography and Geodesy, Wettzell Observatory. Germany

(Author's version. It differs from the published paper only in terms of layout and formatting)

Abstract

Within this work, we present results on the assessment of the short baseline between the co-located VLBI telescopes at the Geodetic Observatory in Wettzell (Germany). VLBI sessions between July 2015 and June 2016 are processed using the VLBI capabilities of the Bernese GNSS Software, to estimate geodetic parameters. Through the use of several parametrisation approaches, this analysis shows a sub-millimetre agreement of the VLBI-derived baselines with the terrestrial measurements (local ties).

INTRODUCTION

The analysis of short VLBI baselines, with baseline lengths of less of a few hundred metres, contributes to identify local effects and instrument-specific biases, as they can be much better separated from (nearly) identical environmental influences, and constitutes a pre-requisite to improve the realisation of the International Terrestrial Reference Frame (ITRF) and to fulfil the GGOS goals in terms of accuracy and stability (Plag, H.-P. et al., 2009). In particular, these intra-technique experiments are expected to provide insights into systematic technique-related errors, leading to better agreement with the local ties at the fundamental sites. For this purpose, the estimation of geodetic parameters (station coordinates, zenith tropospheric delays, clock offsets and Earth orientation parameters) was performed for the short VLBI baseline at the Fundamental station Wettzell in Germany, realised by the legacy 20 m dish Radio Telescope Wettzell (RTW) and the new 13.2 m diameter TWIN Telescope Wettzell (TTW1). A tailored parametrisation was developed, to work out the advantages and disadvantages of short baselines. Then, the main task was to compare these derived parameters with terrestrial surveys (for the coordinates) to study the performance of the VLBI solutions.

METHODS

The database used corresponds to 57 VLBI sessions of the IVS campaign, which contain the baseline RTW–TWIN1 (Behrend, D., 2013). These geodetic sessions were carried out between July 2015 and June 2016. Each session contains a subset of the stations of the global network. However, due to interference in the phaseCal system, it was recommended to deselect the local Wettzell baseline after January 26th, 2016. Therefore, the short baseline is available only for 21 out of the 57 sessions.

The VLBI data have been taken from the NGS cards. Cable delays have been applied to the data, when available. It is worth to notice that the cable delays for station TTW1 are not present, so only those for the RTW could be applied. The NGS files were converted into baseline single difference files and processed in a tailored version of the Bernese GNSS Software v5.2 (Dach, R. et al., 2015; Schmid, R., 2009). For the parametrisation, 4 different approaches have been designed, where the modelling of the dry atmosphere, the solid Earth tides and ocean loading, are common for all these solutions. The first approach (**GLO**) is a global solution, where all VLBI observations are used. The datum for the station coordinates is defined by a minimum constraint condition, i.e. with NNR and NNT conditions w.r.t. ITRF2008. Earth rotation parameters, for 24 h intervals, are modelled as a linear function. Zenith wet delays are estimated as a piece-wise linear function with 2 h intervals, using the wet VMF model for mapping (Böhm, J. et al., 2006b). Receiver clock offsets are estimated are parametrised as a linear polynomial during the session, for each station except for WETTZELL.

The second processing approach (**BAS**) is a short baseline solution, where only the RTW–TTW1 (WETTZELL–WETTZ13N) baseline observations are used. The datum for the station coordinates is given by constraining the coordinates of WETTZELL. Earth rotation parameters are not estimated, and receiver clock offsets are calculated each 24 hours for WETTZ13N, for each session. The main feature of this approach is that the troposphere wet delays between the two stations are not estimated, on the assumption that for such a small distance and small height difference, differences in tropospheric delays can be modelled (**Herrera-Pinzón, I. D.** et al., 2018a). The third approach is a baseline solution (**BA2**), where only the WETTZELL-WETTZ13N baseline observations are used. Earth rotation parameters are not estimated and the datum and receiver clock offsets are defined in the same way as for the **BAS** solution. In contrast to the **BAS** solution, zenith wet tropospheric delays are estimated piece-wise linearly with a time resolution of 2 h and mapped with the wet VMF model for WETTZELL. Finally, to bridge the outage of data in 2016, a fourth processing chain (**BA3**) uses the station NYALES20, in Ny-Alesund (Svalbard, Norway) with a baseline to Wettzell of ca. 3300 km, to connect the two Wettzell telescopes. The datum for this solution is given by constraining the coordinates of the station NYALES20, while Earth rotation parameters are not estimated and receiver clock offsets are defined as in the **BA2** solution. Zenith wet tropospheric delays are set up as for the **GLO** solution.

RESULTS

Least Squares Residuals

To evaluate the quality of the estimation, the standard deviation of the residuals per session is provided. This step of the analysis is used to identify significant outliers. Session R1703 for the BA3 solution, and sessions R4712, R4716, and R4718 for the BAS and BA2 solution, display an anomalous behaviour (Figure A.1).For the remaining

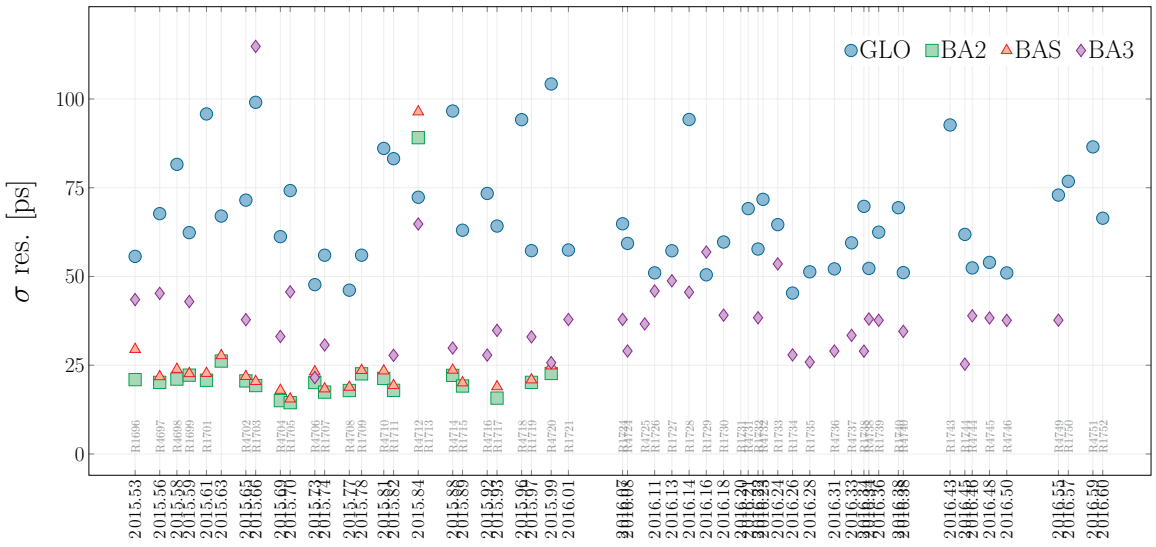

FIGURE A.1: Standard deviation of residuals per session [ps].

sections of this work, these sessions are not considered for the statistical analysis of the results. The appropriate handling and down-weighing of the problematic observations is left for future work. After removing these sessions, the standard deviations of the residuals are 66.17 ps for GLO, 37.27 ps for BA3, 21.85 ps for BAS and 19.90 for the BAS solution. The standard deviations obtained for the local baseline solutions (BAS and BA2) ensure homogeneous and precise solutions.

Clock Offsets WETTZ13N–WETTZELL

The parametrisation used to calculate the clock corrections, consists of two offsets per session with a linear behaviour between these estimates. These two parameters may not accurately describe the session clock behaviour during one session. To increase the time resolution and the statistical significance of the analysis of the clock behaviour, a local baseline solution without the estimation of any parameters has been done, where coordinates are given by the local ties and troposphere delays by models. In this way, the residuals of this estimation are equivalent to the clock corrections, plus the observation noise.

Figure A.2 shows the behaviour for these residuals (straight lines, left axis) for sessions R4708 (top) and R4712 (bottom). Moreover, the deviations of these residuals/clock corrections w.r.t. a linear fit are calculated (right axis of Figure A.2), and are used

to characterise the clock behaviour. Notice for instance how these residuals follow a quadratic pattern for session R4712, which suggests that modelling the clock with two clock parameters per session is not sufficient for this session. Table A.1 summarises the estimated drift and the RMS of the residuals w.r.t. the linear fit, for the sessions containing the short baseline. With clock drifts in the order of -16 to -18 ns/day, and RMS values of the same order of magnitude as residuals in Section A, these data provide clock information equivalent to the estimates of the BAS solution.

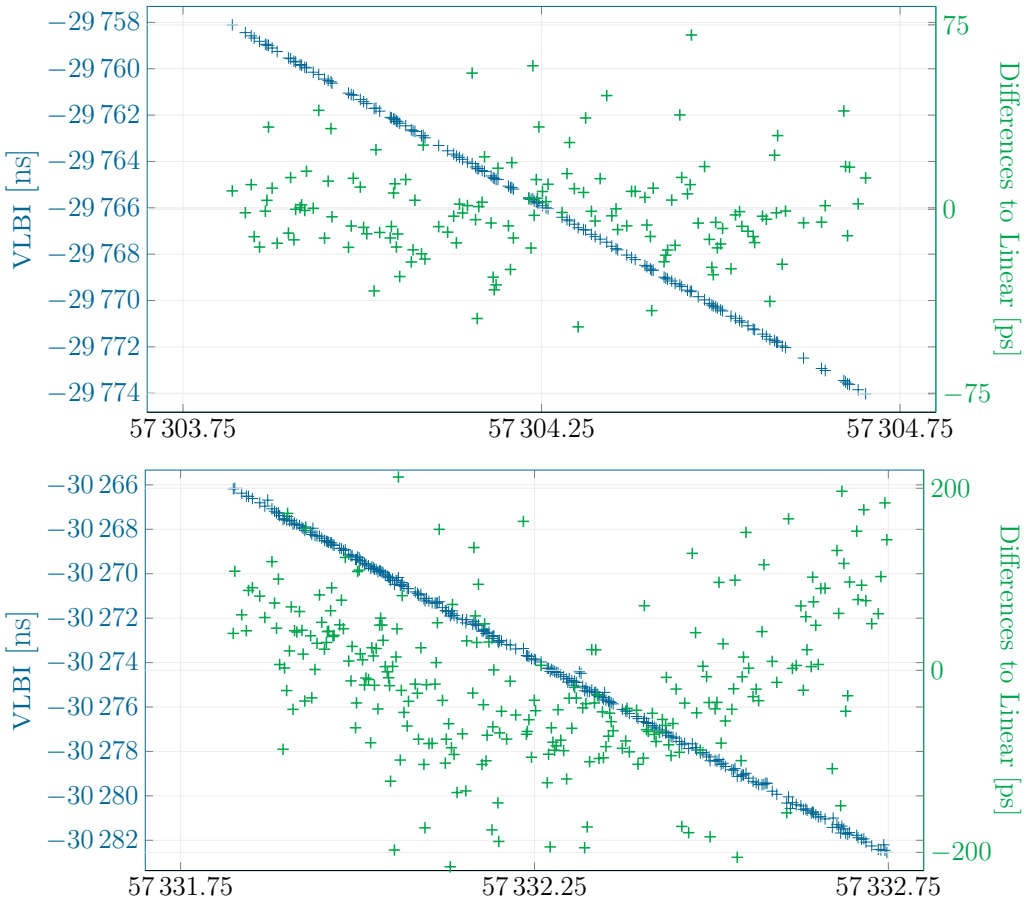

FIGURE A.2: Residuals from solutions without estimates (blue straight line) and differences to a linear fit (green scatter)

Coordinate Residuals and Repeatabilities (WETTZ13N)

The coordinate residuals w.r.t. the ITRF2008, in an ENU system, are calculated and displayed in Figure A.3. The smaller scatter is obtained, as expected, for the local baseline solutions, where north and east components display a favourable behaviour within a few mm, while the height component performs nearly twice as bad. Both global solutions (BA3 and GLO) show a significantly worse performance, due to the fact that most error sources grow with the baseline length. Nevertheless these residuals do not exceed 10 mm. Notice that Figure A.3 depicts the outlier sessions described in the previous section.

Session	VLBI Drift [ns/day]	VLBI RMS [ps]	TWOTT Drift [ns/day]	TWOTT RMS [ps]
R4708	-18.032	16.6	-18.027	3.9
R1709	-18.188	25.3	-18.154	3.0
R4710	-18.160	21.5	-18.184	2.2
R1711	-18.423	28.7	-18.378	4.6
R4712	-17.832	85.9	-17.908	55.7
R1713	-16.922	118.0	-16.811	3.6
R4714	-16.422	23.1	-16.507	7.2
R1715	-16.610	18.8	-16.586	4.1
R4716	-17.055	35.5	-17.099	3.4
R1717	-17.163	18.4	-17.179	5.3
R4718	-17.518	49.3	-17.502	6.0
R1719	-17.544	19.5	-17.534	4.8
R4720	-17.824	22.7	-17.829	4.1

TABLE A.1: Drift and RMS for VLBI and TWOTT, from a linear fit.

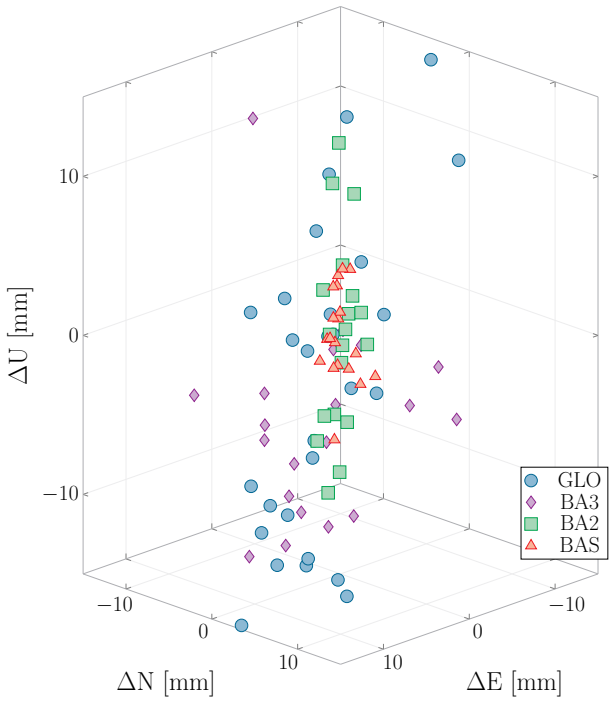

FIGURE A.3: Residuals per component [in mm].

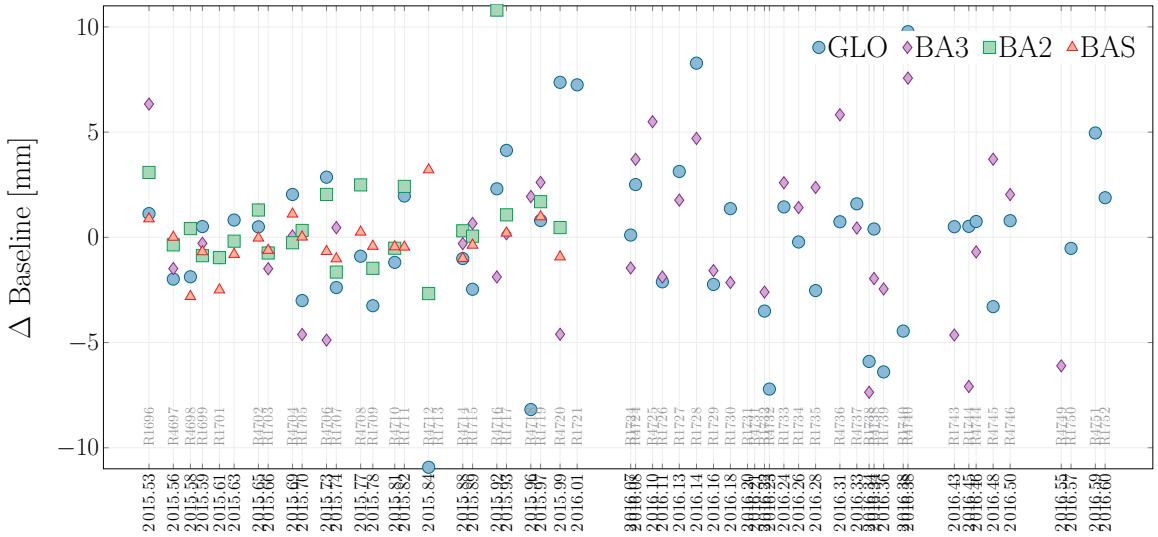

FIGURE A.4: Baseline length differences [mm] w.r.t. the local tie.

To complement this analysis, the repeatabilities of the obtained coordinates have been calculated. The obtained values, $[1.21, 0.81, 2.84]$ mm for BAS, $[1.25, 0.85, 2.88]$ mm for BA2, $[4.53, 4.16, 9.14]$ mm for BA3, and $[7.11, 6.11, 9.51]$ mm for GLO, show in general higher values for the up component. The local baseline solutions display very good performance with values close to 1 mm and 3 mm, for the horizontal and vertical components, respectively.

Comparison with the Local Tie

A set of surveyed local ties, described in (Kodet, J. et al., 2018), report a baseline length of 123.3070 m $\pm$ 0.7 mm. Baseline length differences w.r.t. these values are computed and represented in Figure A.4. Moreover, the mean value over the time series is calculated. This results in average values and standard deviations of -0.8 ± 4.9 mm for the GLO solution, -0.2 ± 4.6 mm for the BA3 solution, -0.3 ± 0.8 mm for the BAS solution, and -0.1 ± 1.3 mm for the BA2 solution. The comparison of the baseline length shows an excellent agreement with differences clearly below 1 mm, albeit the large standard deviations for the global solutions. In addition to the baseline length, the differences per component w.r.t. the local ties are analysed, in a ENU system. Figure A.5 displays these differences. Following the behaviour of the repeatabilities, the up component shows a larger scatter, while the north component displays the best performance. This behaviour is attributed to the orientation of the baseline, since RTW is located at the north of TTW1.From the 4 solutions, the BAS approach shows the best performance regarding the aforementioned indicators, on account of its parametrisation, which is based on only data of the short baseline and estimates the smallest number of parameters (coordinates and clock offsets), which strengthens the calculation of the estimated parameters. The vector of differences over the time series for this solution results in $[-2.04, -0.05, -1.60] \pm [1.2, 0.8, 2.8]$ mm.

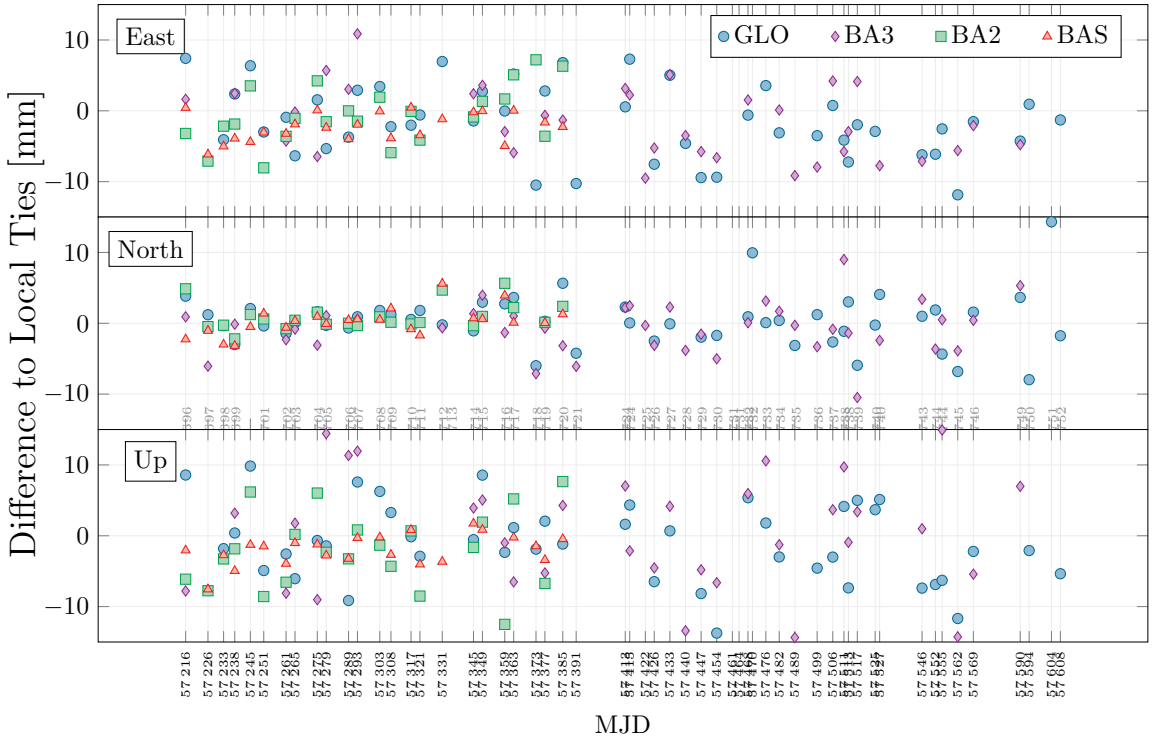

FIGURE A.5: ENU differences [mm] w.r.t the local tie.

SUMMARY AND FUTURE ACTIVITIES

This work presents investigations on a short VLBI baseline, using several processing approaches in terms of local troposphere and clock parametrisation. These solutions are subsequently compared with local ties (baseline length and components), where a sub-mm agreement of the estimated baseline with terrestrial measurements is found. The standard deviation are about 1 mm and 3 mm for the for the horizontal and vertical component, respectively. An additional analysis of the clock behaviour for the short VLBI baseline is performed, where the TWOTT data is used to replace the clock estimation. Comparable results for the clock modelling in terms of drift are obtained, with a significant improvement of the RMS. The use of TWOTT to replace the clock estimation yields comparable results in terms of station coordinates (and their comparison with the local tie) to those obtained from the VLBI estimation. However, for sessions with atypical clock behaviour (quadratic rather than linear), the use of TWOTT improves the consistency of the solutions. Future activities include variations in the clock parametrisation, the exclusion/down-weighting of outlier observations, a more detailed analysis of the residuals to detect possible systematic effects, and further test with the TWOTT data.

ACKNOWLEDGEMENTS

The authors would like to thank the IVS (Behrend, D., 2013) for providing the VLBI observations.

B

APPENDIX: PAPER III

Originally published as: ***I. D. Herrera-Pinzón*** *et al. (2020). "Co-Location of Space Geodetic Techniques: Studies on Intra-Technique Short Baselines". In:* International Association of Geodesy Symposia: Beyond 100: The Next Century in Geodesy. *Ed. by J. T. Freymueller et al. Berlin: Springer.* DOI: *https://doi.org/10.1007/1345_2020_95*

Paper III

Co-Location of Space Geodetic Techniques: Studies on Intra-Technique Short Baselines

Iván Herrera-Pinzón and Markus Rothacher
Institute for Geodesy and Photogrammetry
Swiss Federal Institute of Technology in Zurich (ETHZ)

(Author's version. It differs from the published paper only in terms of layout and formatting)

Abstract

The goal of the project "Co-location of Space Geodetic Techniques on Ground and in Space", in the DFG funded research unit on reference systems and founded by the Swiss National Foundation (SNF), is the improvement of existing and the establishment of new ties between space geodetic techniques, together with the assessment and reduction of technique-specific biases. To achieve this, the co-located instruments at the Geodetic Observatory Wettzell (Germany) are used, where hardware for new ties is being developed, and systematic errors in the space geodetic techniques are detected, assessed and removed on very short, well-known baselines. We summarise results for three *intra-technique* co-location experiments in Wettzell. Firstly, an assessment of the GNSS-to-GNSS baselines in relation to the surveyed local ties, shows discrepancies of up to 9 mm. Secondly, an analysis of the short VLBI baseline shows that the use of a clock tie achieves a sub-mm agreement with respect to the local ties. And finally, initial results on the usage of differencing approaches on the short SLR baseline show that differenced residuals of the zero-test are within 3 mm. These results of this work show the potential of intra-technique studies on short baselines for the understanding of technique-specific biases and errors and the monitoring of local ties.

INTRODUCTION

The combination of the space geodetic techniques constituting the ITRF is performed using the local ties at fundamental sites (Ray, J. et al., 2005). However, multiple sites show discrepancies beyond the requirements of the Global Geodetic Observing

System (GGOS), positions ≤ 1 mm and velocities ≤ 0.1 mm/yr (Rothacher, M. et al., 2009). For instance, based on the tie discrepancies of the ITRF2014, Figure B.1 shows that the differences in east, north and up components for a GNSS-to-GNSS baseline surpasses largely the 1 mm requirement in several sites (Altamimi, Z. et al., 2016). Same can be observed for baselines between GNSS-to-SLR and GNSS-to-VLBI where the discrepancies are in the cm level. Some sites, such as the Geodetic Observatory

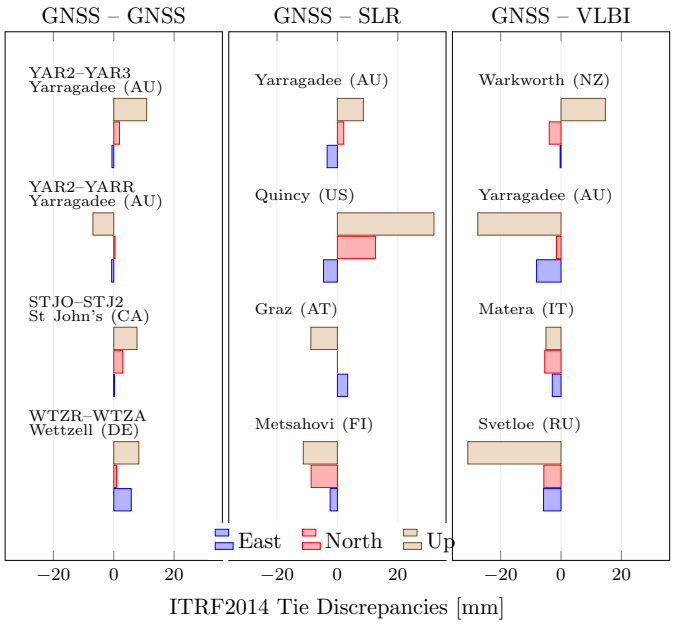

FIGURE B.1: ITRF2014 Tie Discrepancies at selected co-location sites according to Altamimi, Z. et al., 2016.

Wettzell in Germany (Figure B.2), are equipped with more than one instrument of the same technique. Thus, very short baselines of the same technique can be formed. These short baselines provide the perfect opportunity to study technique-specific systematic and time-dependent biases, as the baselines are known precisely from terrestrial measurements (local ties), the relative atmospheric delays can be modelled and a common clock can be used. In particular for Wettzell, a VLBI short baseline, a SLR short baseline, and multiple GNSS short baselines are available. Within the scope of this project, several experiments in short baselines have been performed, to continuously monitor the local ties, and detect technique-specific systematic and time-dependent biases which are affecting the performance of the different geodetic techniques. The study of intra-technique experiments is expected to lead to a better understanding of system-specific error sources, biases and delays and constitute an essential step for the realisation of highly precise terrestrial reference frame that fulfils the demanding requirements of today and the future.

MULTI-YEAR ANALYSIS OF GNSS SHORT BASELINES AT CO-LOCATION SITES

The first of these intra-technique co-location experiments deals with GNSS short baselines. For the network of GNSS stations in Wettzell, 15 year of GNSS data were reprocessed, using a tailored parameterisation, based in double differences with ambi-

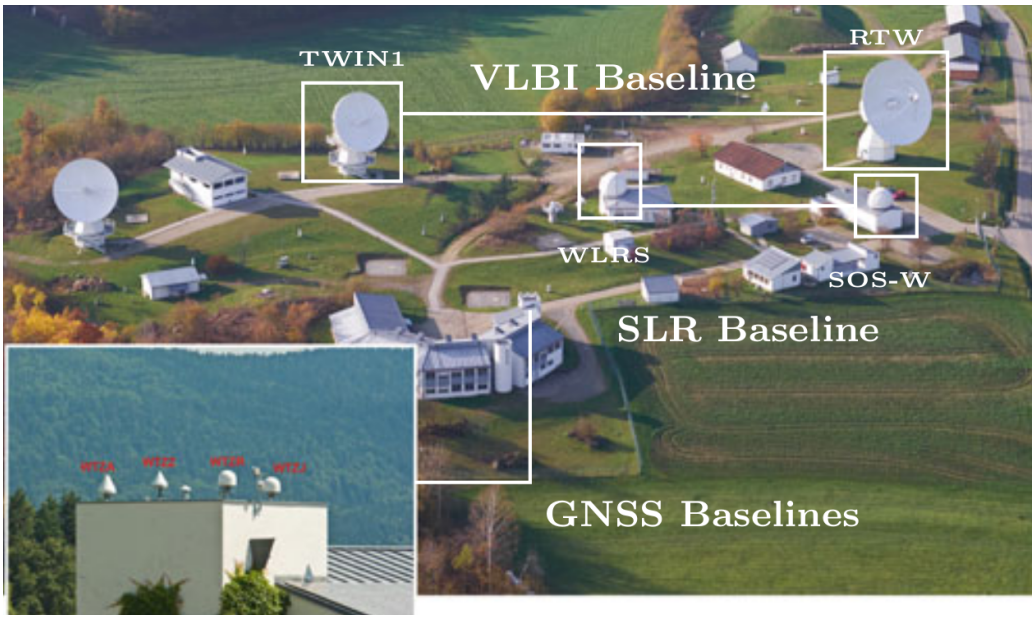

FIGURE B.2: Co-Located instruments at the Geodetic Observatory Wettzell. Credits: IAPG TU-München

guity fixing, with six different solutions: Single frequency L1 and L2, Ionosphere-free linear combination (L3), with and without the estimation of the relative troposphere, on the assumption that for such a small distance and small height difference, differences in tropospheric delays can be modelled. This reprocessing yielded highly consistent time series, with repeatabilities for the east and north component below 1 mm, and 2 mm for the up component. Figure B.3 shows the repeatabilities for the up component of the station WTZZ with respect to WTZR, for each investigated solution, where seasonal outliers associated with snow on the antennas, noise changes due to changes in the receiver and in general site-specific events can be observed. This analysis shows that the single-frequency solutions without estimation of the relative troposphere have better performance in terms of repeatabilities, than the linear combinations or the solutions with estimation of relative troposphere. In particular, the solution L3-TR shows an amplified noise and considerably larger outliers. It is worth mentioning that this solution is equivalent to the one used for the global solution, hence the relevance of its characterisation. With these solutions, we made the comparison of the GNSS based solution and the local ties at the epoch of the local tie.These ties have a precision better than 2 mm. Figure B.4 shows the differences for the different baselines at Wettzell, where the the worst performance for the baseline WTZZ-WTZR is given by the L3 based solution with troposphere estimates. The general performance at the site includes discrepancies up to the 9 mm, for the height component when the estimation of the relative troposphere is involved. The detailed parametrisation and an analysis for several other co-location sites included in the ITRF2014 solution are shown in (**Herrera-Pinzón, I. D.** et al., 2018a).

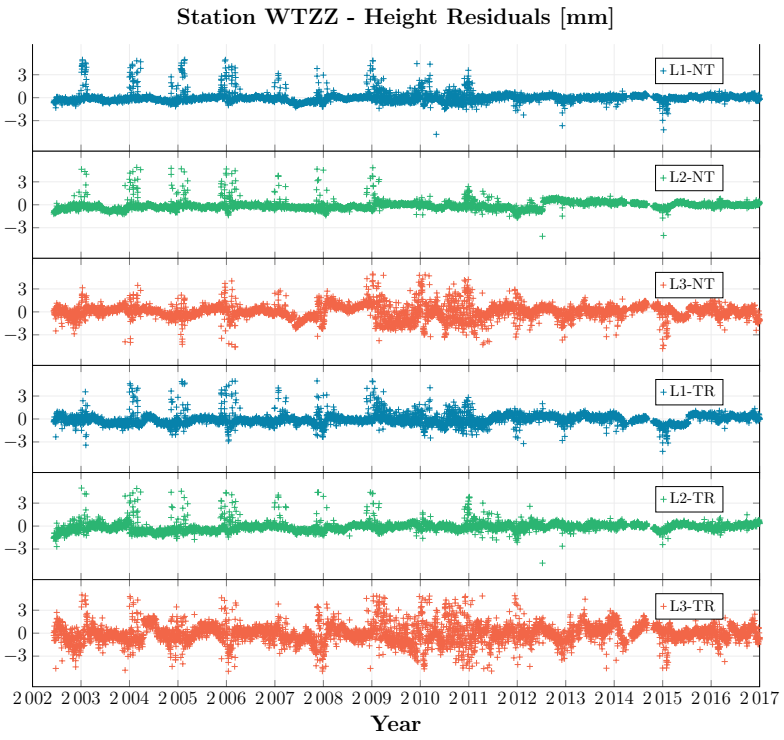

FIGURE B.3: Repeatabilities for the up component of station WTZZ (with respect to WTZR).

ASSESSMENT OF THE VLBI SHORT BASELINE AT WETTZELL

The second type of intra-technique co-location experiment performed, uses the short VLBI baseline at Wettzell, realised by the 20m RTW telescope and the 13m TWIN1 telescope. We use 57 VLBI sessions of the IVS campaign, which contain the baseline RTW–TWIN1, between July 2015 and June 2016 (Behrend, D., 2013). The local Wettzell baseline is not present after January 26th, 2016. Similarly to GNSS, 4 different approaches have been designed, where the modelling of the dry atmosphere, the solid Earth tides and ocean loading, are common for all these solutions. The first approach (GLO) is a global solution, where all VLBI observations are used. Zenith wet delays are estimated as a piece-wise linear function with 2 h intervals, using the wet VMF model for mapping. Receiver clock offsets are estimated are parametrised as a linear polynomial during the session, for each station except for RTW.

The second processing approach (BAS) is a short baseline solution, where only the RTW-TWIN1 baseline observations are used. Receiver clock offsets are calculated each 24 h for TWIN1, for each session. The main feature of this approach is that the troposphere wet delays between the two stations are not estimated, on the assumption that for such a small distance and small height difference, differences in tropospheric delays can be modelled. The third approach is a baseline solution (BA2), where only the RTW-TWIN1 baseline observations are used. Receiver clock offsets are defined as for the BAS solution. But zenith wet tropospheric delays are estimated piece-wise linearly with a time resolution of 2 h and mapped with the wet VMF model for RTW. Finally, for the outage of data in 2016, the (BA3) solution uses the station NYALES20,

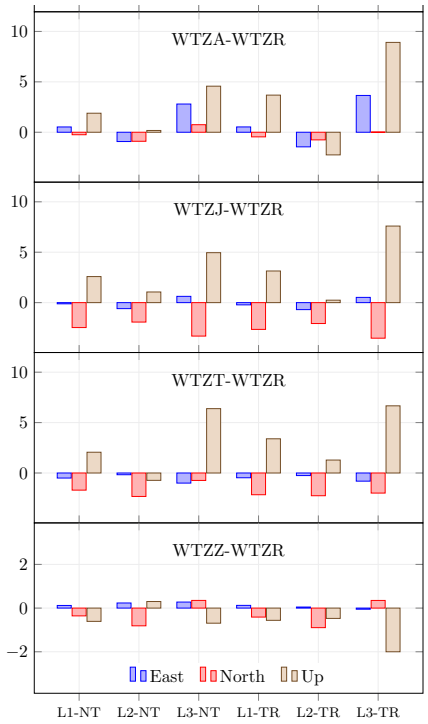

FIGURE B.4: Differences of GNSS based baselines to local ties [mm] in Wettzell, at the epoch of the local tie.

in Ny-Alesund (Svalbard, Norway), to connect the two Wettzell telescopes. Receiver clock offsets are defined as in the BA2 solution and Zenith wet tropospheric delays are set up as for the GLO solution.

Figure B.5 shows the residuals of the estimation process, where the local solutions have lower level of noise. A deeper explanation of the modelling and parameterisation used to obtain these results can be found in (**Herrera-Pinzón, I. D.** et al., 2018b). Based on these solutions, we performed the comparison of the VLBI based solution and the local ties, regarding the baseline length (123.3070 m $\pm$ 0.7 mm) (Kodet, J. et al., 2018). The differences obtained for these solutions have an overall satisfactory mean behaviour, with mean over the time series below 1 mm, even for the global solution. However, the largest difference is the scatter of these time series: The global solutions have standard deviations of ca. 5 mm, while with the local solutions display a standard deviation of around 1 mm. Similarly to the processing of GNSS short baselines, the BAS solution (without estimation of relative troposphere) shows the best time series of results (Figure B.6). The mean sub-mm differences over time for each solution are GLO: -0.8 ± 4.9, BA3: -0.2 ± 4.6, BAS: -0.3 ± 0.8, BA2: -0.1 ± 1.3. A more comprehensive discussion of these results can be found in (**Herrera-Pinzón, I. D.** et al., 2018b).

DIFFERENCING APPROACHES FOR SLR SHORT BASELINES

Double differences are an standard approach for the GNSS processing. But simultaneous SLR observations from one telescope to two satellites are impossible. How-

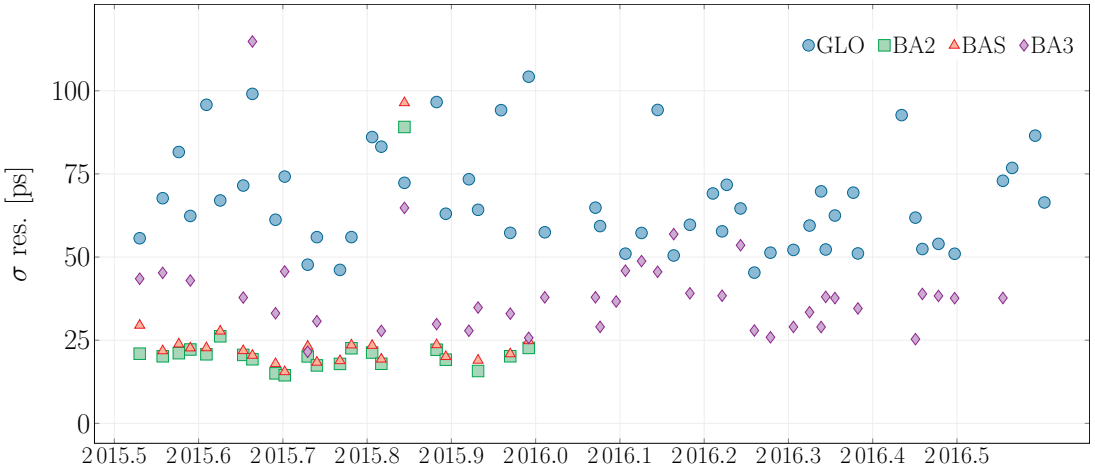

FIGURE B.5: Time series of the residuals of the VLBI processing for each investigated solution.

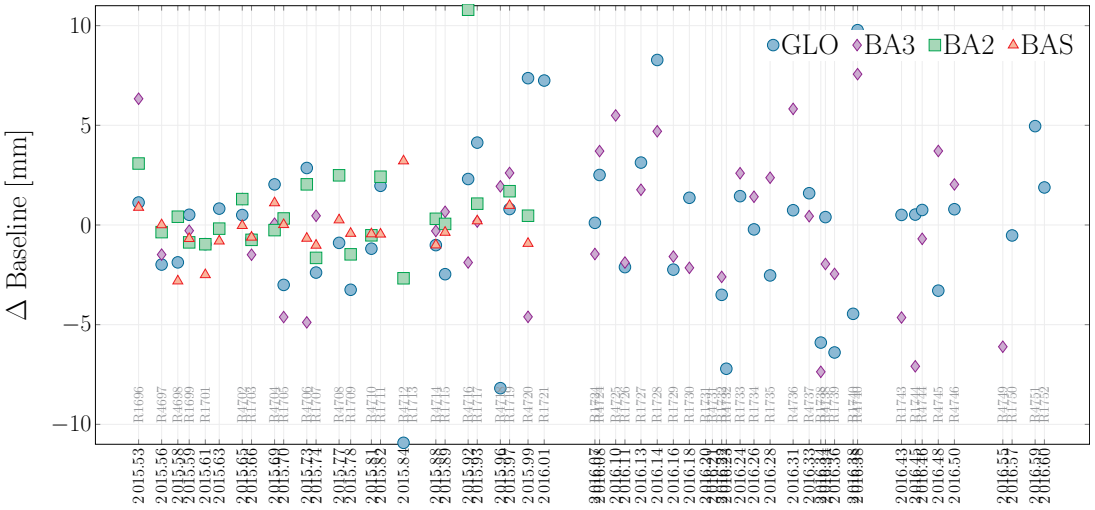

FIGURE B.6: Comparison of the VLBI-based baseline and the baseline derive from the local ties between the telescopes at Wettzell.

ever, (Pavlis, E., 1985) and (Svehla, D. et al., 2013) introduced the concept of quasi-simultaneity to build differences. Two observations are considered quasi-simultaneous if they lie within the same time window. Figure B.7 shows the concept of quasi-simultaneity for a SLR baseline, where time windows for the observation from the telescope 2 with respect to the telescope 1, are t_1 and t_2, for satellite 1 and 2 respectively. With this idea, the goal is to test the potential of the differencing approaches, namely single and double differences, for the estimation of geodetic parameters. It is expected that single-difference observations between the ranges from two stations to one satellite will remove biases related to the satellite orbit and the retro-reflectors. Similarly, two quasi-simultaneous double-differences can remove station-dependent range errors. These differences, together with the original ranges (zero-differences), are used to get estimates of both satellite- and station-specific error sources, so that systematic effects common to both stations are identified at mm-level. Moreover, this approach can be potentially used to improve the processing of classical SLR observations of GNSS and LEO satellites, and to estimate accurate local ties. As a proof of concept, the residuals

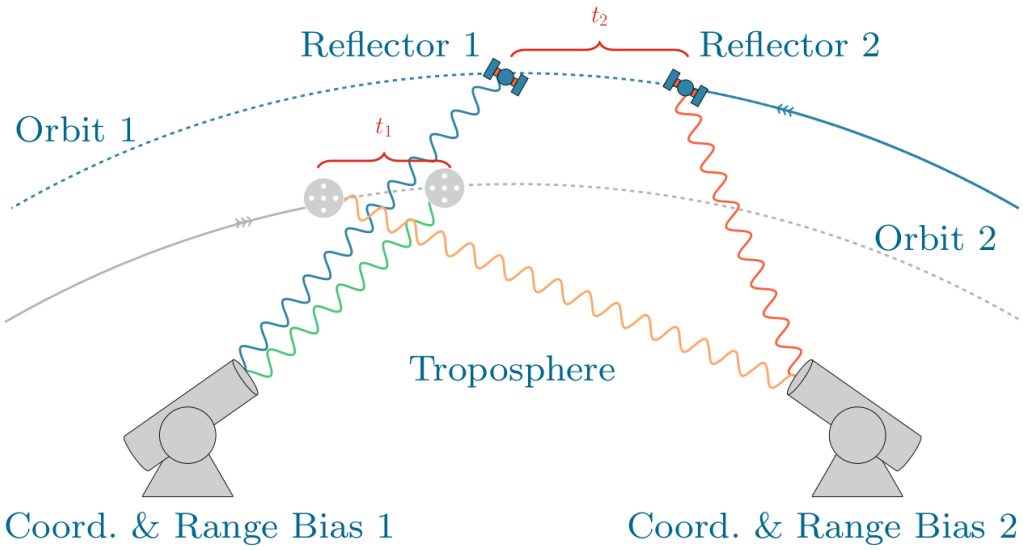

FIGURE B.7: Concept of quasi-simultaneity for differences of SLR observations, together with the error sources targeted with these approaches.

of the zero-difference process (residual of the original observables), are used to build the single and double differences. These observables are used in a so-called zero test, where geodetic parameters are not estimated. Instead, coordinates of the stations are fixed according to the local ties and the atmospheric parameters are calculated with the standard model of Marini, J. et al., 1973. The zero difference residuals for the short SLR baseline at Wettzell, realised by the telescopes WLRS and SOS-W, for the day 03.07.2018, are displayed in Figure B.8. Only GLONASS and Galileo satellites were used for this initial assessment.

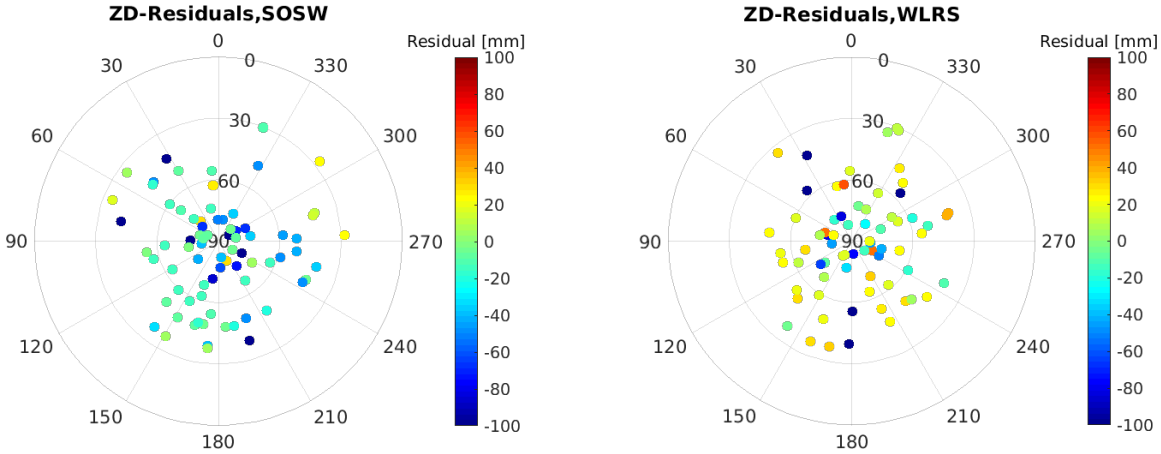

FIGURE B.8: Skyplot of the residuals of the zero-test, as seen at each SLR station, using the original observations (zero-differences).

Single Difference Residuals [2 Telescopes to 1 Satellite]

These residuals are then synchronised, considering the telescope, the satellites for which single and double differences are desired, and considering the window for quasi-

simultaneity, which in this case was 3 h. Figure B.9 shows the differenced residuals grouped by constellation. This analysis reveals that the residuals are evidently biased, with a mean value of -26.3 mm, a value related to the range biases of WLRS and SOS-W. An extensive analysis of these biases is discussed in details in Riepl, S. et al., 2019. Not

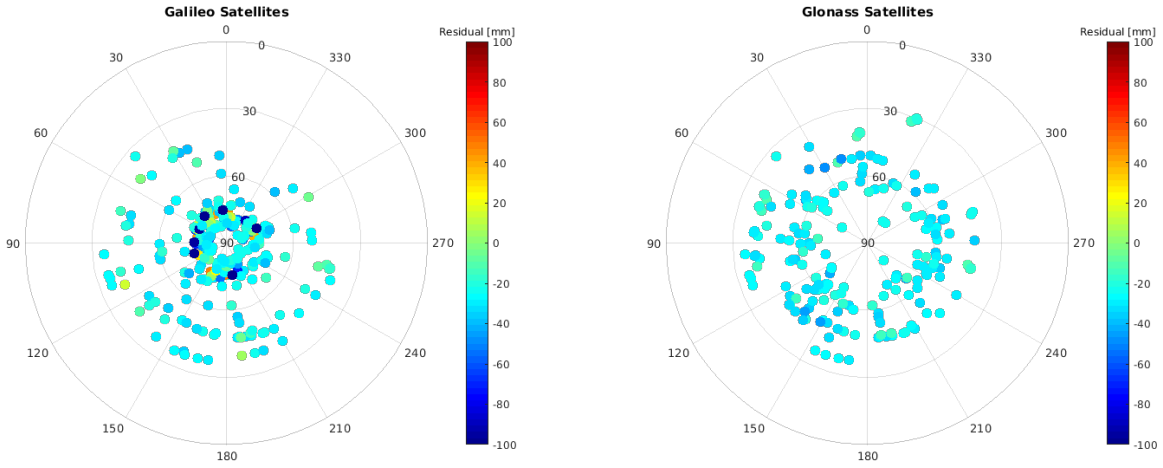

FIGURE B.9: Single differences from 2 telescopes to 1 satellite. Left: Galileo satellites. Right: GLONASS satellites.

only range biases can be observed within these differences, but after removing the mean bias, errors associated to the orbits are also noticeable (Figure B.10), especially for Galileo satellites. The identification of orbital errors is therefore an advantage of this approach.

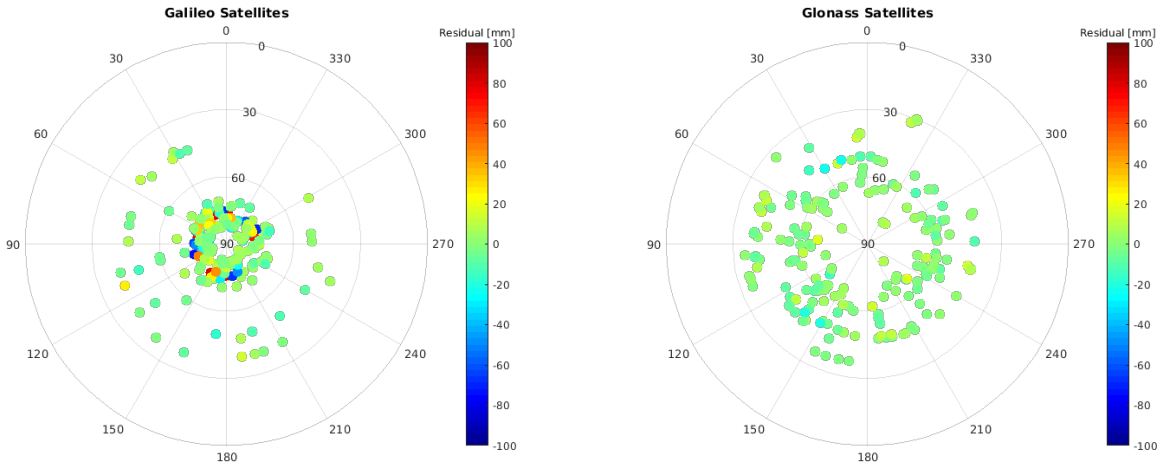

FIGURE B.10: Single differences from 2 telescopes to 1 satellite, after removing the mean bias. Left: Galileo satellites. Right: GLONASS satellites.

Single Difference Residuals [1 Telescope to 2 Satellites]

Single differences of residuals from the same telescope to the two satellites can be also built. Allowing a quasi-simultaneity of 24 h, the time series of differenced residuals per station is depicted in Figure B.11. The blue coloured residuals indicate two Galileo satellites, the red coloured two GLONASS satellites, and the green colour is used when

the difference is built using one satellite from each system. One feature stands out in the time series: the poor performance of some Galileo satellites, namely their orbits, is the responsible of the largest residuals throughout the time series. In particular Galileo satellites E01 and E05 shoe the largest residuals. This is observed for both telescopes, and is summarised in Tables B.1. This identification, and also removal, of orbital issues is a great advantage of the differencing approaches.

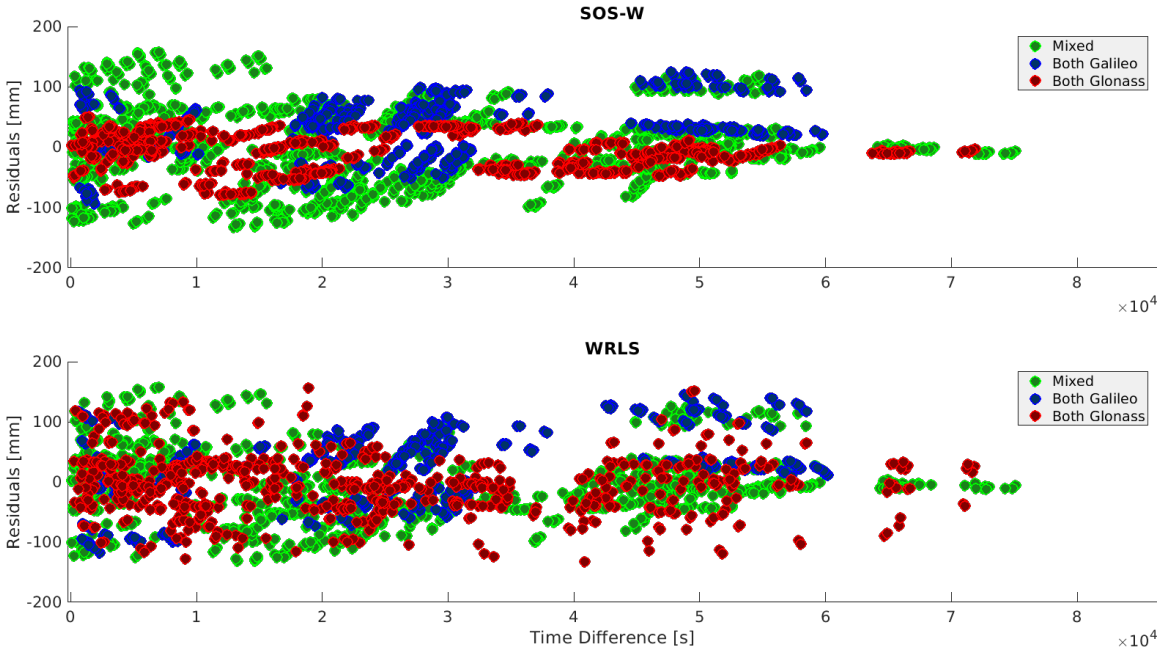

FIGURE B.11: Time series of single differences from 1 telescope to 2 satellites. Top: Telescope SOS-W. Bottom: WLRS. The x-axis indicates the time difference between the two observations used to build the differences, namely the quasi-simultaneity.

	mean	σ
GAL	32.6	47.2
GLO	-9.0	30.7
MIX	-0.4	59.8

	mean	σ
GAL	29.5	59.6
GLO	-5.3	22.6
MIX	-17.3	70.0

TABLE B.1: Summary of the statistics for single differences from 1 telescope to 2 satellites. Left: SOS-W. Right: WRLS.

Double Difference Residuals

Finally, in the same fashion, the double differenced residuals are built. Figure B.12 shows see all the possible differences that can be built when allowing a quasi-simultaneity of 24 h. Based on the single differences from one telescope to two satellites, for SOS-W in the x-axis and WLRS in the y-axis, 63452 differences were available. These residuals range from -10 to 10 cm, with a mean value of 1.2 mm and a scatter of 24 mm. This behaviour is heavily influenced by the bad performances of the aforementioned

Galileo satellites. Considering only those double differences of GLONASS satellites during the first 30 minutes of this window, Figure B.13 shows that the differenced residuals improve considerably in terms of scatter, with an standard deviation of 5.3 mm, for 150 differences, with a mean values of -0.7 mm. This results indicate that quasi-simultaneous SLR differences are feasible, and that it is possible to obtain double-difference residuals close to the sub-mm level. In turn, the use of SLR differenced observations constitutes a valuable observable for the estimation of geodetic parameters through SLR.

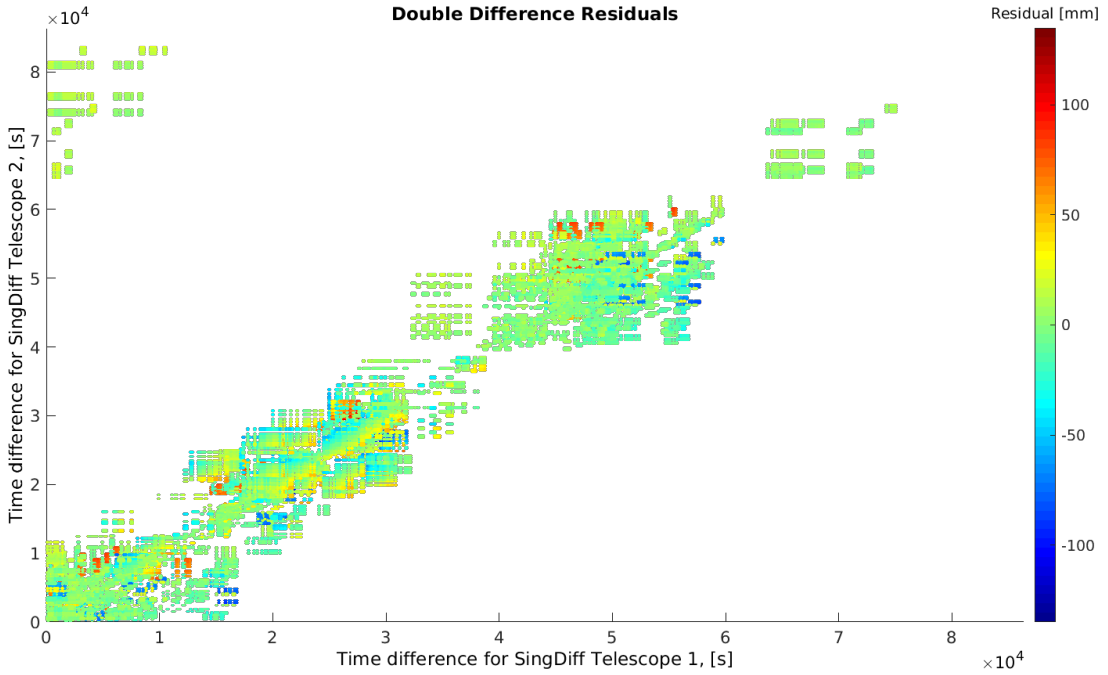

FIGURE B.12: Double differences of SLR residuals. The x-axis indicates the time difference allowed to build the single differences from the SOS-W telescope to two satellites. Similarly, the y-axis shows the time difference allowed to build the single differences from the WLRS telescope to two satellites. Finally, the colour bar indicates the value of the residual.

CONCLUSIONS AND OUTLOOK

This progress work focuses on determine the potential of intra-technique studies on short baselines for the understanding of technique-specific biases and errors and the monitoring of local ties. Experiments on GNSS-to-GNSS, SLR-to-SLR and VLBI-to-VLBI short baselines are assessed, where multiple local and environmental effects, such as snow, meteorological data, antenna phase centre variations and multipath, are investigated. In particular, the analysis of GNSS short baselines showed cm-level discrepancies with respect to local ties, for a processing strategy equivalent to those used in global solutions. On the other hand, the study of VLBI shot baselines showed mm to sub-mm agreement of estimated baseline with respect to the local ties. Within these two experiments, the benefits of the accurate and common timing estimation, for the determination of height and troposphere, were investigated. Finally, a concept

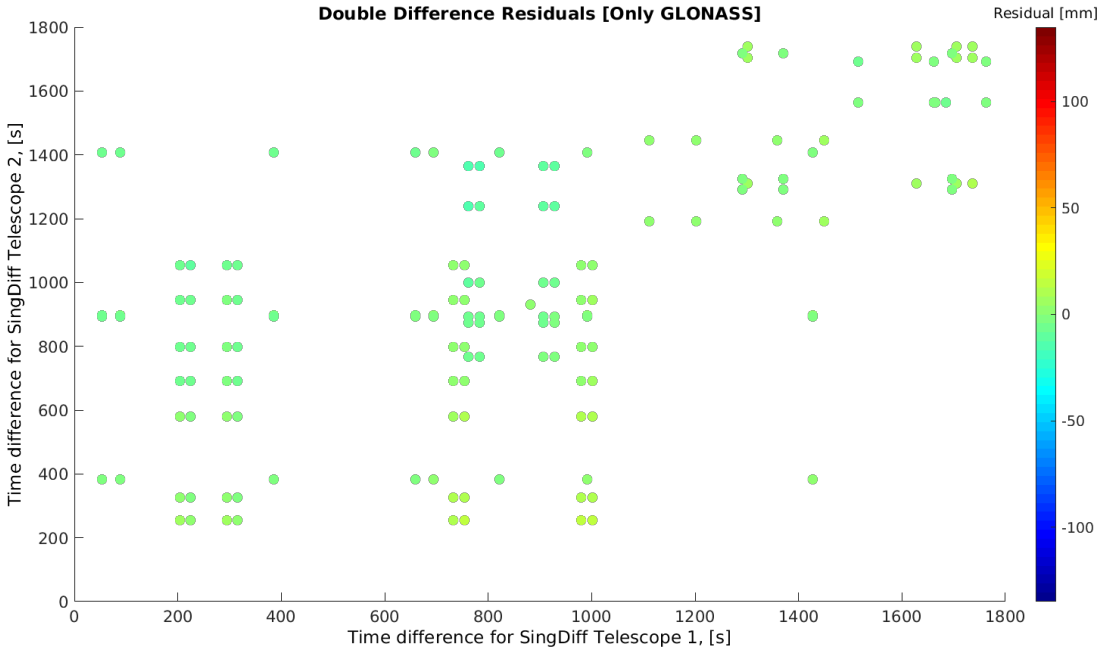

FIGURE B.13: Double differences of SLR residuals, restricted to the first 30 minutes of observations to GLONASS satellites only.

for the differencing of SLR observables was investigated, where mm-level differenced residuals were found. Besides allowing the identification of station- and orbital biases, these method proved their usability for the estimation of geodetic parameters. These findings are expected to be extended in future experiments within this project. The Unnecessary estimation of clock corrections, replaced by the a Two Way Optical Time and Frequency System is expected to make the estimation of VLBI clock corrections unnecessary. The SLR differencing approaches are expected to be used for the estimation of coordinates, and the assessment of local ties. Finally inter-technique experiments on very short baselines, including GNSS and VLBI observations are foreseen, where the tasks lie into the assessment of biases among the space geodetic techniques, and the study of the benefits from a rigorous GNSS-VLBI combination of all common parameter types.

ACKNOWLEDGEMENTS

This work has been developed within the project "Co-location of Space Geodetic Techniques on Ground and in Space" in the frame of the DFG funded research unit on reference systems, and founded by the Swiss National Foundation (SNF). Additionally, the authors would like to thank the team at the GO-Wettzell, in particular to Dr. Jan Kodet and Prof. Dr. Ulrich Schreiber, for their support in the realisation of this work.

BIBLIOGRAPHY

Abbondanza, C., Z. Altamimi, P. Sarti, M. Negusini, and L. Vittuari (2009). "Local effects of redundant terrestrial and GPS-based tie vectors in ITRF-like combinations". In: *Journal of Geodesy* 83.11, p. 1031. ISSN: 1432-1394. DOI: https://doi.org/10.1007/s00190-009-0321-6.

Abbondanza, C. and P. Sarti (2010). "Effects of illumination functions on the computation of gravity-dependent signal path variation models in primary focus and Cassegrainian VLBI telescopes". In: *Journal of Geodesy* 84.8, pp. 515–525. ISSN: 1432-1394. DOI: https://doi.org/10.1007/s00190-010-0389-z.

Altamimi, Z., P. Rebischung, L. Métivier, and X. Collilieux (2016). "ITRF2014: A new release of the International Terrestrial Reference Frame modeling nonlinear station motions". In: *Journal of Geophysical Research: Solid Earth* 121.8. 2016JB013098, pp. 6109–6131. ISSN: 2169-9356. DOI: http://dx.doi.org/10.1002/2016JB013098.

Altamimi, Z., P. Sillard, and C. Boucher (2002). "ITRF2000: A new release of the International Terrestrial Reference Frame for earth science applications". In: *Journal of Geophysical Research: Solid Earth* 107 (B10), pp. 1–19. DOI: https://doi.org/10.1029/2001JB000561.

Altamimi, Z., P. Sillard, and C. Boucher (2003). "The impact of a No-Net-Rotation Condition on ITRF2000". In: *Geophysical Research Letters* 30 (2), pp. 36-1-36–4. DOI: https://doi.org/10.1029/2002GL016279.

Angermann, D., H. Drewes, M. Krügel, B. Meisel, M. Gerstl, R. Kelm, H. Müller, W. Seemüller, and V. Tesmer (2004). *ITRS Combination Center at DGFI: A Terrestrial Reference Frame Realization 2003. Angewandte Geodäsie*. Research rep. 313. Deutshce Geodätische Kommission. ISRN: ISBN 3 7696 8593 8.

Arias, E. F., P. Charlot, M. Feissel, and J.-F. Lestrade (1995). "The extragalactic reference system of the International Earth Rotation Service, ICRS". In: *Astronomy and Astrophysics* 303, pp. 604–608.

Arias, E. F. and M. Feissel (1990). "The Celestial System of the International Earth Rotation Service". In: *Inertial Coordinate Systems on the Sky. Proceedings of the International Astronomical Union*. Ed. by J. H. Lieske and V. K. Abalakin, pp. 119–128.

Arnold, D., O. Montenbruck, S. Hackel, and K. Sośnica (2019). "Satellite laser ranging to low Earth orbiters: orbit and network validation". In: *Journal of Geodesy* 93.11, pp. 2315–2334. ISSN: 1432-1394. URL: https://doi.org/10.1007/s00190-018-1140-4.

Artz, T., A. Springer, and A. Nothnagel (2014). "A complete VLBI delay model for deforming radio telescopes: the Effelsberg case". In: *Journal of Geodesy* 88.12, pp. 1145–1161. ISSN: 1432-1394. DOI: https://doi.org/10.1007/s00190-014-0749-1.

Bar-Sever, Y. E., P. M. Kroger, and J. A. Borjesson (1998). "Estimating horizontal gradients of tropospheric path delay with a single GPS receiver". In: *Journal of Geophysical Research: Solid Earth* 103 (B3), pp. 5019–5035. DOI: https://doi.org/10.1029/97JB03534.

Behrend, D. (2013). "Data Handling within the International VLBI Service." In: *Data Science Journal*. DOI: https://doi.org/10.2481/dsj.WDS-011.

Behrend, D., C. Thomas, J. Gipson, E. Himwich, and K. Le Bail (2020). "On the organization of CONT17". In: *Journal of Geodesy* 94.10, p. 100. ISSN: 1432-1394. DOI: https://doi.org/10.1007/s00190-020-01436-x.

Bergstrand, S., M. Herbertsson, C. Rieck, J. Spetz, C.-G. Svantesson, and R. Haas (2019). "A gravitational telescope deformation model for geodetic VLBI". In: *Journal of Geodesy* 93.5, pp. 669–680. ISSN: 1432-1394. DOI: https://doi.org/10.1007/s00190-018-1188-1.

Beutler, G., W. Gurtner, I. Bauersima, and M. Rothacher (1987a). "Correlations between Simultaneous GPS Double Difference Carrier Phase Observations in the Multistation Mode: Implementation Considerations and First Experiences". In: Manuscripta Geodaetica 12, pp. 40–44.

Beutler, G., W. Gurtner, I. Bauersima, and M. Rothacher (1986). "Efficient Computation of the Inverse of the Covariance Matrix of Simultaneous GPS Carrier Phase Difference Observations". In: Manuscripta Geodaetica 11, pp. 249–255.

Beutler, G., I. Bauersima, S. Botton, W. Gurtner, M. Rothacher, T. Schildknecht, and A. Geiger (1987b). "Accuracy and Biases in the Geodetic Application of the Global Positioning System". In: *Manuscripta Geodaetica*. Vol. 1. 14. Berlin, Heidelberg, New York: Springer Verlag, pp. 28–35.

Biancale, R. and M. Rothacher (2017). *European Geodetic Reference Antenna in Space E-GRASP/Eratosthenes*. Tech. rep. Proposal for Earth Explorer Opportunity Mission EE-9.

Bilich, A., K. M. Larson, and P. Axelrad (2008). "Modeling GPS phase multipath with SNR: Case study from the Salar de Uyuni, Bolivia". In: *Journal of Geophysical Research: Solid Earth*. Geodesy and Gravity/Tectonophysics. DOI: https://doi.org/10.1029/2007JB005194.

Bloßfeld, M., V. Štefka, H. Müller, and M. Gerstl (2016). "Satellite Laser Ranging". In: *IAG 150 Years*. Ed. by C. Rizos and P. Willis. Cham: Springer International Publishing, pp. 541–547. ISBN: 978-3-319-30895-1.

Böhm, J., A. Niell, P. Tregoning, and H. Schuh (2006a). "Global Mapping Function (GMF): A new empirical mapping function based on numerical weather model data". In: *Geophysical Research Letters* 33.7. L07304. ISSN: 1944-8007. DOI: http://dx.doi.org/10.1029/2005GL025546.

Böhm, J., B. Werl, and H. Schuh (2006b). "Troposphere mapping functions for GPS and very long baseline interferometry from European Centre for Medium-Range

Weather Forecasts operational analysis data". In: *Geophysical Research* 111. B02406. DOI: https://doi.org/10.1029/2005JB003629.

Borre, K., D. M. Akos, N. Bertelsen, P. Rinder, and S. H. Jensen (2007). *A Software-Defined GPS and Galileo Receiver: Single-Frequency Approach*. ISBN-10 0-8176-4390-7, ISBN-13 978-0-8176-4390-4. Birkhaüser Boston.

Brockmann, E., D. Ineichen, and S. Schaer (2010). "Use of double stations in the Swiss Permanent GNSS Network AGNES". In: *Report on the Symposium of the IAG Subcommission for Europe (EUREF)*. URL: http://www.euref.eu/symposia/2010Gavle/Symposium2010Gavle.html.

Charlot, P., C. S. Jacobs, D. Gordon, S. Lambert, A. de Witt, J. Böhm, A. L. Fey, R. Heinkelmann, E. Skurikhina, and O. Titov (2020). "The third realization of the International Celestial Reference Frame by very long baseline interferometry". In: *Astronomy & Astrophysics* 644. DOI: https://doi.org/10.1051/0004-6361/202038368.

Chen, G. and T. Herring (1997). "Effects of atmospheric azimuthal asymmetry on the analysis of space geodetic data". In: *Journal of Geophysical Research* 102.B9, pp. 20489–20502. DOI: https://doi.org/10.1029/97JB01739.

Combrinck, L. (2010). "Satellite Laser Ranging". In: *Sciences of Geodesy - I: Advances and Future Directions*. Ed. by G. Xu. Berlin, Heidelberg: Springer Berlin Heidelberg, pp. 301–338. ISBN: 978-3-642-11741-1. DOI: https://doi.org/10.1007/978-3-642-11741-1_9.

Coulot, D., P. Berio, R. Biancale, S. Loyer, L. Soudarin, and A.-M. Gontier (2007). "Toward a direct combination of space-geodetic techniques at the measurement level: Methodology and main issues". In: *Journal of Geophysical Research: Solid Earth* 112 (B5). DOI: https://doi.org/10.1029/2006JB004336.

Dach, R., S. Lutz, P. Walser, and P. Fridez, eds. (2015). *Bernese GNSS Software Version 5.2*. Astronomical Institute. Bern University. DOI: http://dx.doi.org/10.7892/boris.72297.

Dach, R., S. Schaer, D. Arnold, L. Prange, D. Sidorov, A. Susnik, A. Villiger, and A. Jäggi (2017). "CODE final product series for the IGS". In: DOI: http://dx.doi.org/10.7892/boris.75876.2.

Dedes, G. C. and I. I. Müller (1989). "Baseline estimation with semidynamic and geometric satellite methods". In: *Bulletin géodésique* 63, pp. 99–114. DOI: https://doi.org/10.1007/BF02519145.

Diamantidis, P.-K., G. Kłopotek, and R. Haas (2021). "VLBI and GPS inter- and intra-technique combinations on the observation level for evaluation of TRF and EOP". In: *Earth, Planets and Space* 73.1, p. 68. ISSN: 1880-5981. DOI: https://doi.org/10.1186/s40623-021-01389-1.

Dilßner, F., G. Seeber, G. Wübbena, and M. Schmitz (2008). "Impact of Near-Field Effects on the GNSS Position Solution". In: *Proceedings of the International Technical Meeting, ION GNSS* (Savannah, Georgia). Institute of Navigation.

Dow, J., R. Neilan, and C. Rizos (2009). "The International GNSS Service in a changing landscape of Global Navigation Satellite Systems". In: *Journal of Geodesy* 83.3, pp. 191–198. DOI: http://dx.doi.org/10.1007/s00190-008-0300-3.

Dunn, P. (2003). "Absolute Earth Scale from SLR Measurements". In: *Proceedings of the 13th International Workshop on Laser Ranging*. Ed. by R. Noomen, S. Klosko, C. Noll, and M. Pearlman. NASA.

ECMWF (2022). *European Centre for Medium-Range Weather Forecasts*. URL: https://www.ecmwf.int/.

Exertier, P., A. Belli, and J. Lemoine (2017). "Time biases in laser ranging observations: A concerning issue of Space Geodesy". In: *Advances in Space Research* 60.5, pp. 948–968. ISSN: 0273-1177. DOI: https://doi.org/10.1016/j.asr.2017.05.016. URL: https://www.sciencedirect.com/science/article/pii/S0273117717303459.

Glaser, S., D. Ampatzidis, R. König, T. Nilsson, R. Heinkelmann, F. Flechtner, and H. Schuh (2018). "Simulation of VLBI Observations to Determine a Global TRF for GGOS". In: *International Symposium on Earth and Environmental Sciences for Future Generations*. Ed. by J. T. Freymueller and L. Sánchez. Cham: Springer International Publishing, pp. 3–9. ISBN: 978-3-319-69170-1.

Glaser, S., R. König, K. H. Neumayer, T. Nilsson, R. Heinkelmann, F. Flechtner, and H. Schuh (2019). "On the impact of local ties on the datum realization of global terrestrial reference frames". In: *Journal of Geodesy* 93.5, pp. 655–667. ISSN: 1432-1394. DOI: https://doi.org/10.1007/s00190-018-1189-0.

GSC (2021). *Signal-in-Space Interface Control Document. European GNSS (GALILEO) Open Service*. Tech. rep. European GNSS Service Centre.

GSSC (2022). *GNSS Science Support Centre: Navipedia*. Accessed: 01.06.2022. URL: https://gssc.esa.int/navipedia/index.php/Main_Page (visited on 06/01/2022).

Haas, M. and K. Meisenheimer (2003). "Sind Radiogalaxien und Quasare dasselbe? Die Antwort des Infrarotsatelliten ISO". In: *Sterne und Weltraum*. 24th ser.

Haas, R., A. Neidhardt, J. Kodet, C. Plötz, U. Schreiber, G. Kronschnabl, S. Pogrebenko, D. Duev, S. Casey, and L. Plank (2014). "The Wettzell-Onsala G0128 experiment". In: *IVS 2014 General Meeting Proceedings - "VGOS: The New VLBI Network"*. Ed. by D. Behrend, K. Baver, and K. Armstrong. 978-7-03-042974-2. Science Press, pp. 451–455. ISBN: 978-7-03-042974-2.

Halsig, S., A. Bertarini, R. Haas, A. Iddink, J. Kodet, G. Kronschnabl, A. Neidhardt, A. Nothnagel, C. Plötz, and T. Schüler (2019). "Atmospheric refraction and system stability investigations in short-baseline VLBI observations". In: *Journal of Geodesy* 93.4, pp. 593–614. ISSN: 1432-1394. DOI: https://doi.org/10.1007/s00190-018-1184-5.

Heinkelmann, R. (2013). "VLBI Geodesy: Observations, Analysis and Results". In: *Geodetic Sciences*. Ed. by S. Jin. Rijeka: IntechOpen. Chap. 3. DOI: https://doi.org/10.5772/54446.

Heinkelmann, R., P. Willis, Z. Deng, G. Dick, T. Nilsson, B. Soja, F. Zus, J. Wickert, and H. Schuh (2016). "Multi-technique comparison of atmospheric parameters at the DORIS co-location sites during CONT14". In: *Advances in Space Research* 58.12. Scientific Applications of DORIS in Space Geodesy, pp. 2758–2773. ISSN: 0273-1177. DOI: https://doi.org/10.1016/j.asr.2016.09.023. URL: https://www.sciencedirect.com/science/article/pii/S0273117716305543.

Herrera-Pinzón, I. D. and M. Rothacher (2018a). "Assessment of Local GNSS Baselines at Co-Location Sites". In: *Journal of Geodesy* 92.9, pp. 1079–1095. ISSN: 0949-7714. DOI: https://doi.org/10.1007/s00190-017-1108-9.

Herrera-Pinzón, I. D. and M. Rothacher (2020). "Co-Location of Space Geodetic Techniques: Studies on Intra-Technique Short Baselines". In: *International Association of Geodesy Symposia: Beyond 100: The Next Century in Geodesy*. Ed. by J. T. Freymueller and L. Sánchez. Berlin: Springer. DOI: https://doi.org/10.1007/1345_2020_95.

Herrera-Pinzón, I. D. and M. Rothacher (2023). "Impact of Local- and Tropospheric Ties for the Rigorous Combination of GNSS and VLBI". In: *Proceedings of the IAG International Symposium on Reference Frames for Applications in Geosciences (REFAG 2022)*. DOI: https://doi.org/10.1007/1345_2023_195.

Herrera-Pinzón, I. D., M. Rothacher, J. Kodet, and K. U. Schreiber (2018b). "Analysis of the Short VLBI Baseline at the Wettzell Observatory". In: *Proceedings of the 10th IVS General Meeting (2018)*. Kartverket, S.49. URL: https://ivscc.gsfc.nasa.gov/publications/gm2018/.

Herrera-Pinzón, I. D., M. Rothacher, and S. Riepl (2021). "Differencing strategies for SLR observations at the Wettzell observatory". In: *Journal of Geodesy* 96.4. ISSN: 1432-1394. DOI: https://doi.org/10.1007/s00190-021-01588-4.

Herring, T. A. (1992). "Modeling Atmospheric Delays in the Analysis of Space Geodetic Data". In: ed. by J. De Munck and T. Spoelstra. Geodetic Commission Publications on Geodesy, The Netherlands.

Hobiger, T. and R. Haas (2015). "CONT14 as a testbed for the combination VLBI and GPS data on the observation level". In: *EVGA Working Meeting*. Ponta Delgada.

Hofmann-Wellenhof, B., H. Lichtenegger, and E. Wasle (2008). *GNSS – Global Navigation Satellite Systems: GPS, GLONASS, Galileo, and more*. Springer-Verlag Wien. ISBN: 978-3-211-73012-6. DOI: https://doi.org/10.1007/978-3-211-73017-1.

Hsu, L.-T. (2017). "GNSS multipath detection using a machine learning approach". In: *2017 IEEE 20th International Conference on Intelligent Transportation Systems (ITSC)*, pp. 1–6. DOI: https://doi.org/10.1109/ITSC.2017.8317700.

IAU (1976). "Proceedings of the 16th General Assembly". In: *Transactions of the International Astronomical Union*. Ed. by E. A. Müller and A. Jappel, p. 31. ISSN: ISBN 90-277-0836-3.

IAU (1991). "IAU Recomendations from the Working Group on Reference Systems". In: *Transactions of the International Astronomical Union* 21 (2). Ed. by J. Bergeron.

IAU (1994). "Resolution of the 22nd General Assembly". In: The Hague, The Netherlands.

IGS (2017). *International GNSS Service*. URL: http://www.igs.org (visited on 09/01/2022).

ILRS (2022). *ILRS Normal Point Algorithm*. Ed. by A. T. Sinclair. URL: https://ilrs.gsfc.nasa.gov/data_and_products/data/npt/npt_algorithm.html.

Ineichen, D. and E. Brockmann (2015). *Geostation Zimmerwald: Einmessung 2014*. Tech. rep. 14-21. Messungen vom 10. - 14. November 2014 und. Multiepochen-Ausgleichung 1987 - 2014. Bundesamt für Landestopografie Swisstopo, p. 103.

ITRF (2020). *International Terrestrial Reference Frame 2020 (ITRF2020)*. International Earth Rotation and Reference Systems Service. URL: https://itrf.ign.fr/en/solutions/ITRF2020.

JPL (2017). *Jet Propulsory Laboratory: GPS Time Series*. Accessed: 01.05.2017. URL: https://sideshow.jpl.nasa.gov/post/series.html (visited on 05/01/2017).

Kallio, U., H. Koivula, S. Lahtinen, V. Nikkonen, and M. Poutanen (2019). "Validating and comparing GNSS antenna calibrations". In: *Journal of Geodesy* 93.1, pp. 1–18. ISSN: 1432-1394. DOI: https://doi.org/10.1007/s00190-018-1134-2.

Kallio, U. and M. Poutanen (2012). "Can We Really Promise a mm-Accuracy for the Local Ties on a Geo-VLBI Antenna". In: *Geodesy for Planet Earth*. Ed. by S. Kenyon, M. C. Pacino, and U. Marti. Berlin, Heidelberg: Springer Berlin Heidelberg, pp. 35–42. ISBN: 978-3-642-20338-1.

Kembhavi, A. K. and J. V. Narlikar (1999). *Quasars and Active Galactic Nuclei*. Inter-University Centre for Astronomy and Astrophysics. Pune 411 007, India: Cambridge University Press. URL: https://ned.ipac.caltech.edu/level5/Kembhavi/Kem_contents.html.

Kirkko-Jaakkola, M., J. Traugott, D. Odijk, J. Collin, G. Sachs, and F. Holzapfel (2009). "A raim approach to GNSS outlier and cycle slip detection using L1 carrier phase time-differences". In: *2009 IEEE Workshop on Signal Processing Systems*, pp. 273–278. DOI: https://doi.org/10.1109/SIPS.2009.5336264.

Klügel, T., S. Mähler, and C. Schade (2012). "Ground Survey and Local Ties at the Geodetic Observatory Wettzell". In: *Proceedings 17th International Workshop on Laser Ranging* (Frankfurt). 48. Bundesamt für Kartographie und Geodäsie, pp. 127–131.

Koch, K.-R. (1999). *Parameter Estimation and Hypothesis Testing in Linear Models*. 2nd ed. ISBN: 978-3-540-65257-1. DOI: https://doi.org/10.1007/978-3-662-03976-2.

Kodet, J., K. U. Schreiber, C. Plötz, A. Neidhardt, G. Kronschnabl, R. Haas, G. Molera Calvés, S. Pogrebenko, M. Rothacher, B. Männel, and L. Plank (2014). "Co-locations of Space Geodetic Techniques on Ground and in Space". In: *IVS 2014 General Meeting Proceedings: "VGOS: The New VLBI Network"*. Ed. by D. Behrend, K. Baver, and K. Amstrong. International VLBI Service for Geodesy and Astrometry. Science Press, pp. 446–450.

Kodet, J., K. Schreiber, J. Eckl, C. Plötz, S. Mähler, T. Schüler, T. Klügel, and S. Riepl (2018). "Co-location of space geodetic techniques carried out at the Geodetic Observatory Wettzell using a closure in time and a multi-technique reference target". In: *Journal of Geodesy* 92, pp. 1097–1112. DOI: doi.org/10.1007/s00190-017-1105-z.

Kodet, J., U. Schreiber, P. Panek, I. Prochazka, B. Männel, and T. Schüler (2016). "Optical Two-Way Timing System for Space Geodesy Applications". In: *European Frequency and Time Forum (EFTF)*, pp. 1–6. DOI: https://doi.org/10.1109/EFTF.2016.7477788.

Landskron, D. and J. Böhm (2018). "VMF3/GPT3: refined discrete and empirical troposphere mapping functions". In: *Journal of Geodesy* 92.4, pp. 349–360. ISSN: 1432-1394. DOI: https://doi.org/10.1007/s00190-017-1066-2.

Langley, R. B. (2017). "Innovation: GLONASS — past, present and future". In: *GPS World*.

Lösler, M., R. Haas, and C. Eschelbach (2019). "Gravitational deformation of ring-focus antennas for VGOS: first investigations at the Onsala twin telescopes project". In: *Journal of Geodesy* 93.10, pp. 2069–2087. ISSN: 1432-1394. DOI: https://doi.org/10.1007/s00190-019-01302-5.

Luceri, V., M. Pirri, J. Rodríguez, G. Appleby, E. Pavlis, and H. Müller (2019). "Systematic errors in SLR data and their impact on the ILRS products". In: *Journal of Geodesy* 93, pp. 2357–2366. DOI: https://doi.org/10.1007/s00190-019-01319-w.

Lyard, F., F. Lefevre, T. Letellier, and O. Francis (2006). "Modelling the global ocean tides: modern insights from FES2004". In: *Ocean Dynamics* 56.5, pp. 394–415. ISSN: 1616-7228. DOI: http://dx.doi.org/10.1007/s10236-006-0086-x.

Männel, B. (2016). "Colocation of Space Geodetic Techniques". PhD thesis. Swiss Federal Institute of Technology in Zurich (ETHZ).

Männel, B. and M. Rothacher (2016a). "Ionospheric corrections for single-frequency tracking of GNSS satellites by VLBI based on co-located GNSS". In: *Journal of Geodesy* 90.2, pp. 189–203. ISSN: 1432-1394. DOI: https://doi.org/10.1007/s00190-015-0865-6.

Männel, B., M. Rothacher, P. Jetzer, S. Lecomte, and P. Rochat (2016b). "E-GRIP: A Highly Elliptical Orbit Satellite Mission for Co-location in Space". In: *IVS 2016 General Meeting Proceedings*. Ed. by D. Behrend, K. Baver, and K. Amstrong. International VLBI Service for Geodesy and Astrometry, pp. 368–372.

Marini, J. and C. Murray (1973). "Correction of Laser Range Tracking Data for Atmospheric Refraction at Elevations above 10 Degrees". In: NASA-TM-X-70555. NASA Tech. Memo., 60 p.

Marques, H. A., J. F. G. Monico, G. P. S. Rosa, M. L. Chuerubim, and M. Aquino (2012). "Second and Third Order Ionospheric Effects on GNSS Positioning: A Case Study in Brazil". In: *Geodesy for Planet Earth*. Ed. by S. Kenyon, M. C. Pacino, and U. Marti. Berlin, Heidelberg: Springer Berlin Heidelberg, pp. 619–625. ISBN: 978-3-642-20338-1.

Mendes, V. B. and E. C. Pavlis (2004). "High-accuracy zenith delay prediction at optical wavelengths". In: *Geophysical Research Letters* 31.14. DOI: https://agupubs.onlinelibrary.wiley.com/doi/abs/10.1029/2004GL020308.

Minster, J. B., Z. Altamimi, G. Blewitt, W. E. Carter, A. Cazenave, H. Dragert, T. A. Herring, K. M. Larson, J. C. Ries, D. T. Sandwell, J. M. Wahr, and J. L. Davis (2010). *Precise Geodetic Infrastructure: National Requirements for a Shared Resource*. Washington, DC: The National Academies Press. ISBN: 978-0-309-15811-4. DOI: 10.17226/12954. URL: https://nap.nationalacademies.org/catalog/12954/precise-geodetic-infrastructure-national-requirements-for-a-shared-resource.

Montenbruck, O. and E. Gill (2000). *Satellite Orbits*. ISBN-3-540-67280-X. Springer.

Moore, T. (1986). "Satellite Laser Ranging and the Determination of Earth Rotation Parameters". PhD thesis. University of Nottingham.

Nerem, R., Y. E. Bar-Sever, and G. Team (2011). "The Geodetic Reference Antenna in Space (GRASP) - A Mission to Enhance the Terrestrial Reference Frame". In: *AGU Fall Meeting Abstracts*.

Neubert, R. and T. Otsubo (2012). "The Centre of Mass Correction of LARES and LAGEOS". In: *International Technical Laser Workshop 2012 (ITLW-12)*.

Nilsson, T., K. Balidakis, R. Heinkelmann, and H. Schuh (2019). "Earth Orientation Parameters from the CONT17 Campaign". In: *Geophysica* 54.1, pp. 19–25.

Nothnagel, A. (2009). "Conventions on thermal expansion modelling of radio telescopes for geodetic and astrometric VLBI". In: *Journal of Geodesy* 83.8, pp. 787–792. ISSN: 1432-1394. DOI: https://doi.org/10.1007/s00190-008-0284-z.

Otsubo, T. and G. M. Appleby (2003). "System-dependent center-of-mass correctionfor spherical geodetic satellites". In: *Journal of Geophysical Research* 108.B4. DOI: https://doi.org/10.1029/2002JB002209.

Otsubo, T., R. A. Sherwood, G. M. Appleby, and R. Neubert (2015). "Center-of-mass corrections for sub-cm-precision laser-ranging targets: Starlette, Stella and LARES". In: *Journal of Geodesy* 89.4, pp. 303–312. ISSN: 1432-1394. URL: https://doi.org/10.1007/s00190-014-0776-y.

Padovani, P. and P. Giommi (1995). "A Sample-oriented catalogue of BL Lacertae objects". In: *Monthly Notices of the Royal Astronomical Society* 277 (4), pp. 1477–1490. DOI: https://doi.org/10.1093/mnras/277.4.1477.

Panek, P., J. Kodet, and I. Prochazka (2013). "Accuracy of two-way time transfer via a single coaxial cable". In: *Metrologia* 53.1.

Panek, P., I. Prochazka, and J. Kodet (2010). "Time measurement device with four femtosecond stability". In: *Metrologia* 47.5, pp. L13–L16. ISSN: 1681-7575. URL: http://dx.doi.org/10.1088/0026-1394/47/5/L01.

Paolozzi, A., G. Sindoni, F. Felli, D. Pilone, A. Brotzu, I. Ciufolini, E. C. Pavlis, and C. Paris (2019). "Studies on the materials of LARES 2 satellite". In: *Journal of Geodesy*

93.11, pp. 2437–2446. ISSN: 1432-1394. DOI: https://doi.org/10.1007/s00190-019-01316-z.

Pavlis, E. (1985). "On the geodetic applications of simultaneous range differences to LAGEOS". In: *Journal of Geophysical Research* 90, pp. 9431–9438. DOI: http://doi.org/doi:10.1029/JB090iB11p09431.

Pearlman, M., D. Arnold, M. Davis, F. Barlier, R. Biancale, V. Vasiliev, I. Ciufolini, A. Paolozzi, E. C. Pavlis, K. Sośnica, and M. Blossfeld (2019a). "Laser geodetic satellites: a high-accuracy scientific tool". In: *Journal of Geodesy* 93, pp. 2181–2194. DOI: https://doi.org/10.1007/s00190-019-01228-y.

Pearlman, M., C. Noll, E. Pavlis, F. Lemoine, L. Combrink, J. Degnan, G. Kirchner, and U. Schreiber (2019b). "The ILRS: approaching 20 years and planning for the future". In: *Journal of Geodesy* 93, pp. 2161–2180. DOI: https://doi.org/10.1007/s00190-019-01241-1.

Petit, G. and B. Luzum (2010). *IERS Conventions (2010). International Earth Rotation and Reference Systems Service (IERS). Technical Note No. 36*. Tech. rep. ISBN 3-89888-989-6. Frankfurt am Main: Verlag des Bundesamts für Kartographie und Geodäsie, p. 179. URL: http://www.iers.org/IERS/EN/Publications/TechnicalNotes/tn36.html/.

Petrachenko, W. T., A. E. Niell, B. E. Corey, D. Behrend, H. Schuh, and J. Wresnik (2012). "VLBI2010: Next Generation VLBI System for Geodesy and Astrometry". In: *Geodesy for Planet Earth*. Ed. by S. Kenyon, M. C. Pacino, and U. Marti. Berlin, Heidelberg: Springer Berlin Heidelberg, pp. 999–1005. ISBN: 978-3-642-20338-1.

Petrovski, I. and T. Tsujii (2012). *Digital Satellite Navigation and Geophysics*. ISBN 978-0-521-76054-6. Cambridge.

Plag, H.-P. and M. Pearlman, eds. (2009). *Global Geodetic Observing System: Meeting the Requirements of a Global Society on a Changing Planet in 2020*. Springer Berlin Heidelberg. ISBN: ISBN: 978-3-642-02687-4. DOI: http://dx.doi.org/10.1007/978-3-642-02687-4_9.

Plank, L., A. Hellerschmied, J. McCallum, J. Böhm, and J. Lovell (2017). "VLBI observations of GNSS-satellites: from scheduling to analysis". In: *Journal of Geodesy* 91.7, pp. 867–880. ISSN: 1432-1394. DOI: https://doi.org/10.1007/s00190-016-0992-8.

Plank, L., J. Lovell, J. McCallum, and D. Mayer (2016). "Observing with Sibling and Twin Telescopes". In: *IVS 2016 General Meeting Proceedings*. Ed. by D. Behrend, K. Baver, and K. Amstrong. International VLBI Service for Geodesy and Astrometry, pp. 87–91.

Ray, J. and Z. Altamimi (2005). "Evaluation of co-location ties relating the VLBI and GPS Reference Frames". In: *Journal of Geodesy* 79.4, pp. 189–195. ISSN: 1432-1394. DOI: http://dx.doi.org/10.1007/s00190-005-0456-z.

Riepl, S., H. Müller, and S. Mähler (2019). "Operating two SLR systems at the Geodetic Observatory Wettzell: from local survey to space ties". In: *Journal of Geodesy*. DOI: https://doi.org/10.1007/s00190-019-01243-z.

Riepl, S. and W. Schlüter (2001). "Normal Point Algorithm For Reduction Of Two Colour Slr Observations". In: *Surveys in Geophysics* 22.5, pp. 581–588. ISSN: 1573-0956. URL: https://doi.org/10.1023/A:1015696907252.

Rodríguez, J., G. Appleby, and T. Otsubo (2019). "Upgraded modelling for the determination of centre of mass corrections of geodetic SLR satellites: impact on key parameters of the terrestrial reference frame". In: *Journal of Geodesy* 93.12, pp. 2553–2568. ISSN: 1432-1394. DOI: https://doi.org/10.1007/s00190-019-01315-0.

Rothacher, M. (2017). *Lecture Notes: Space Geodesy*. Ed. by M. Rothacher. Institute of Geodesy and Photogrametry. ETH Zurich.

Rothacher, M., G. Beutler, and J. Hefty (2001). "High-frequency variations in Earth rotation from Global Positioning System data". In: *Journal of Geophysical Research. Solid Earth* 106, pp. 13711–13738. DOI: https://doi.org/10.1029/2000JB900393.

Rothacher, M., G. Beutler, D. Behrend, A. Donnellan, J. Hinderer, C. Ma, C. Noll, J. Oberst, M. Pearlman, H.-P. Plag, B. Richter, T. Schöne, G. Tavernier, and P. L. Woodworth (2009). "The future Global Geodetic Observing System". In: *Global Geodetic Observing System: Meeting the Requirements of a Global Society on a Changing Planet in 2020*. Ed. by H.-P. Plag and M. Pearlman. Berlin, Heidelberg: Springer Berlin Heidelberg, pp. 237–272. ISBN: 978-3-642-02687-4. DOI: http://dx.doi.org/10.1007/978-3-642-02687-4_9.

Rothacher, M., H. Drewes, A. Nothnagel, and B. Richter (2010). "Integration of Space Geodetic Techniques as the Basis for a Global Geodetic-Geophysical Observing System (GGOS-D): An Overview". In: *System Earth via Geodetic-Geophysical Space Techniques*. Ed. by F. M. Flechtner, T. Gruber, A. Güntner, M. Mandea, M. Rothacher, T. Schöne, and J. Wickert. Berlin, Heidelberg: Springer Berlin Heidelberg, pp. 529–537. ISBN: 978-3-642-10228-8. DOI: https://doi.org/10.1007/978-3-642-10228-8_43.

Rothacher, M. and **I. D. Herrera-Pinzón** (2019). *Important aspects of a rigorous combination of space geodetic techniques*. EGU General Assembly 2019; Conference Location: Vienna, Austria; Conference Date: April 7-12, 2019; Presented on Tuesday, 9. April 2019. Göttingen. DOI: https://doi.org/10.3929/ethz-b-000396065.

Rothacher, M., V. Lechner, and W. Schlüter (2004). "Local Monitoring of a Fundamental GPS Site". IGS Workshop & Symposium. URL: http://kb.igs.org/hc/en-us/articles/202507558-IGS-Workshop-2004-proceedings.

Saastamoinen, J. (1972). "Atmospheric correction for the troposphere and stratosphere in radio ranging of satellites". In: ed. by A. M. W. Henriksen and B. Chovitz. Vol. Volume 15. The Use of Artificial Satellites for Geodesy, Geophys. Monogr. AGU, Washington, D.C.

Santamaría-Gómez, A. (2013). "Very Short Baseline Interferometry: Assessment of the Relative Stability of the GPS Stations at the Yebes Observatory (Spain)". In: *Studia Geophysica et Geodaetica* 57.2, pp. 233–252. ISSN: 1573-1626. DOI: http://dx.doi.org/10.1007/s11200-012-1146-y.

Santerre, R., G. Beutler, and A. Geiger (1990). "GPS Error Analysis and Modelling". In: *Second International Symposium on Precise Positioning with the Global Positioning System*. Ottawa, Canada, pp. 356–372.

Sarti, P., C. Abbondanza, and Z. Altamimi (2013). "Local Ties and Co-Location Sites: Some Considerations After the Release of ITRF2008". In: *Reference Frames for Applications in Geosciences*. Ed. by Z. Altamimi and X. Collilieux. Berlin, Heidelberg: Springer Berlin Heidelberg, pp. 75–80. ISBN: 978-3-642-32998-2. DOI: https://doi.org/10.1007/978-3-642-32998-2_13.

Schartner, M., L. Kern, A. Nothnagel, J. Böhm, and B. Soja (2021). "Optimal VLBI baseline geometry for UT1-UTC Intensive observations". In: *Journal of Geodesy* 95.7, p. 75. ISSN: 1432-1394. DOI: https://doi.org/10.1007/s00190-021-01530-8.

Schartner, M., C. Plötz, and B. Soja (2022). "Improvements and comparison of VLBI INT2 and INT3 session performance". In: *Journal of Geodesy* 96.4, p. 26. ISSN: 1432-1394. DOI: https://doi.org/10.1007/s00190-022-01621-0.

Schmid, R. (2009). "Zur Kombination von GPS und VLBI". PhD thesis. Technische Universität München.

Schuh, H. and J. Böhm (2013). "Very Long Baseline Interferometry for Geodesy and Astrometry". In: *Sciences of Geodesy - II: Innovations and Future Developments*. Ed. by G. Xu. Berlin, Heidelberg: Springer Berlin Heidelberg, pp. 339–376. ISBN: 978-3-642-28000-9. DOI: https://doi.org/10.1007/978-3-642-28000-9_7.

Schüler, T., G. Kronschnabl, C. Plötz, A. Neidhardt, A. Bertarini, S. Bernhart, L. Porta, S. Halsig, and A. Nothnagel (2015). "Initial Results Obtained with the First TWIN VLBI Radio Telescope at the Geodetic Observatory Wettzell". In: *Sensors*. Vol. 15, pp. 18767–18800. DOI: https://doi.org/10.3390/s150818767.

Seidelmann, P. K. (1982). "1980 IAU Theory of Nutation: The final report of the IAU Working Group on Nutation". In: *Celestial mechanics* 27.1, pp. 79–106. ISSN: 1572-9478. DOI: https://doi.org/10.1007/BF01228952.

Seitz, M. (2009). "Kombination geodätischer Raumbeobachtungsverfahren zur Realisierung eines terrestrischen Referenzsystems". PhD thesis. Technical University Munich.

Seitz, M. (2015). "Comparison of Different Combination Strategies Applied for the Computation of Terrestrial Reference Frames and Geodetic Parameter Series". In: *The 1st International Workshop on the Quality of Geodetic Observation and Monitoring Systems (QuGOMS'11)*. Ed. by H. Kutterer, F. Seitz, H. Alkhatib, and M. Schmidt. Cham: Springer International Publishing, pp. 57–64. ISBN: 978-3-319-10828-5. DOI: https://doi.org/10.1007/978-3-319-10828-5_9.

Seitz, M., D. Angermann, M. Gerstl, M. Bloßfeld, L. Sánchez, and F. Seitz (2020). "Geometrical Reference Systems". In: *Handbook of Geomathematics*. Ed. by W. Freeden, M. Z. Nashed, and T. Sonar. Berlin, Heidelberg: Springer Berlin Heidelberg, pp. 1–35. ISBN: 978-3-642-27793-1. DOI: https://doi.org/10.1007/978-3-642-27793-1_79-2.

Soja, B., T. Nilsson, M. Karbon, C. Lu, X. Li, K. Balidakis, J. Anderson, S. Glaser, L. Liu, J. Mora-Díaz, M. Xu, R. Heinkelmann, and H. Schuh (2015). "Comparison of Tropospheric Delays from GPS and Kalman Filtered VLBI Data". In: *Proceedings of the 22nd European VLBI Group for Geodesy and Astrometry Working Meeting*, pp. 240–244.

Steigenberger, P., U. Hugentobler, R. Schmid, U. Hessels, T. Klügel, and M. Seitz (2013). "GPS-Specific Local Effects at the Geodetic Observatory Wettzell". In: *Reference Frames for Applications in Geosciences*. Ed. by Z. Altamimi and X. Collilieux. Berlin, Heidelberg: Springer Berlin Heidelberg, pp. 125–130. ISBN: 978-3-642-32998-2. DOI: http://dx.doi.org/10.1007/978-3-642-32998-2_20.

Svehla, D., R. Haagmans, R. Floberghagen, L. Cacciapuoti, B. Sierk, G. Kirchner, J. Rodriguez, M. Wilkinson, G. Appleby, M. Ziebart, U. Hugentobler, and M. Rothacher (2013). "Geometrical SLR Approach for Reference Frame Determination: The First SLR Double-Difference Baseline". In: *IAG Scientific Assembly 2013*. Potsdam.

Svehla, D. (2018). "The SLR/LLR Double-Difference Baseline". In: *Geometrical Theory of Satellite Orbits and Gravity Field*. https://doi.org/10.1007/978-3-319-76873-1_17. Cham: Springer International Publishing, pp. 223–249. ISBN: 978-3-319-76873-1. DOI: https://doi.org/10.1007/978-3-319-76873-1_17.

Tang, G., J. Sun, X. Li, S. Liu, G. Chen, T. Ren, and G. Wang (2016). "APOD Mission Status and Observations by VLBI". In: *IVS 2016 General Meeting Proceedings*. Ed. by D. Behrend, K. Baver, and K. Amstrong. International VLBI Service for Geodesy and Astrometry, pp. 87–91.

Teke, K., J. Böhm, T. Nilsson, H. Schuh, P. Steigenberger, R. Dach, R. Heinkelmann, P. Willis, R. Haas, S. García-Espada, T. Hobiger, R. Ichikawa, and S. Shimizu (2011). "Multi-technique comparison of troposphere zenith delays and gradients during CONT08". In: *Journal of Geodesy* 85.7. ISSN: 1432-1394. DOI: https://doi.org/10.1007/s00190-010-0434-y.

Teke, K., T. Nilsson, J. Böhm, T. Hobiger, P. Steigenberger, S. García-Espada, R. Haas, and P. Willis (2013). "Troposphere delays from space geodetic techniques, water vapor radiometers, and numerical weather models over a series of continuous VLBI campaigns". In: *Journal of Geodesy* 87.10, pp. 981–1001. ISSN: 1432-1394. DOI: https://doi.org/10.1007/s00190-013-0662-z.

Teunissen, P. (1998). "On the integer normal distribution of the GPS ambiguities". In: *Artificial Satellites* 33.2, pp. 49–64.

Thaller, D. (2008). "Inter-technique combination based on homogeneous normal equation systems including station coordinates, Earth orientation and troposphere parameters". PhD thesis. Technical University Munich.

Thaller, D., R. Dach, M. Seitz, G. Beutler, M. Mareyen, and B. Richter (2011). "Combination of GNSS and SLR observations using satellite co-locations". In: *Journal of Geodesy* 85.5, pp. 257–272. ISSN: 1432-1394. URL: https://doi.org/10.1007/s00190-010-0433-z.

Torge, W. (2001). *Geodesy - 3rd edition*. ISBN: 3-11-017072-8. Springer Walter de Gruyter - Berlin - New York.

Tornatore, V., R. Haas, S. Casey, D. Duev, S. Pogrebenko, and G. M. Calvés (2014a). "Direct VLBI Observations of Global Navigation Satellite System Signals". In: *Earth on the Edge: Science for a Sustainable Planet: Proceedings of the IAG General Assembly, Melbourne, Australia, June 28 - July 2, 2011*. Ed. by C. Rizos and P. Willis. Berlin, Heidelberg: Springer Berlin Heidelberg, pp. 247–252. ISBN: 978-3-642-37222-3. DOI: https://doi.org/10.1007/978-3-642-37222-3_32.

Tornatore, V., R. Haas, D. Duev, S. Pogrebenko, S. Casey, G. M. Calvés, and A. Keimpem (2014b). "Single Baseline GLONASS Observations with VLBI: Data Processing and First Results". In: *20th Meeting of the European VLBI Group for Geodesy and Astrometry*. Ed. by D. Behrend, K. Baver, and K. Amstrong. International VLBI Service for Geodesy and Astrometry, pp. 446–450.

Wang, J., M. Ge, S. Glaser, K. Balidakis, R. Heinkelmann, and H. Schuh (2022). "Improving VLBI analysis by tropospheric ties in GNSS and VLBI integrated processing". In: *Journal of Geodesy* 96.4, p. 32. ISSN: 1432-1394. DOI: https://doi.org/10.1007/s00190-022-01615-y.

Wilkinson, M., G. Appleby, R. Sherwood, and V. Smith (2013). "Monitoring Site Stability at the Space Geodesy Facility, Herstmonceux, UK". In: *Reference Frames for Applications in Geosciences*. Ed. by Z. Altamimi and X. Collilieux. Berlin, Heidelberg: Springer Berlin Heidelberg, pp. 95–102. ISBN: 978-3-642-32998-2. DOI: http://dx.doi.org/10.1007/978-3-642-32998-2_16.

Wilkinson, M., U. Schreiber, I. Procházka, C. Moore, J. Degnan, G. Kirchner, Z. Zhongping, P. Dunn, V. Shargorodskiy, M. Sadovnikov, C. Courde, and H. Kunimori (2019). "The next generation of satellite laser ranging systems". In: *Journal of Geodesy* 93.11, pp. 2227–2247. ISSN: 1432-1394. URL: https://doi.org/10.1007/s00190-018-1196-1.

Wresnik, J., R. Haas, J. Böhm, and H. Schuh (2007). "Modeling thermal deformation of VLBI antennas with a new temperature model". In: *Journal of Geodesy* 81.6, pp. 423–431. ISSN: 1432-1394. DOI: https://doi.org/10.1007/s00190-006-0120-2.

Xu, G. (2008). *Orbits*. ISBN: 978-3-540-78521-7 e-ISBN: 978-3-540-78522-4. Springer.